UNIVERSITA' DEGLI STUDI DI PADOVA

FACOLTA' DI SCIENZE MM. FF. NN.

DIPARTIMENTO DI SCIENZE CHIMICHE

SCUOLA DI DOTTORATO IN SCIENZE MOLECOLARI
INDIRIZZO SCIENZE CHIMICHE
CICLO XX

THEORETICAL AND COMPUTATIONAL METHODS FOR SOFT MATTER PROBLEMS

DIRETTORE DELLA SCUOLA: CH. MO PROF MAURIZIO CASARIN

SUPERVISORE: PROF.SA ALBERTA FERRARINI

DOTTORANDO: FABIO TOMBOLATO

DATA CONSEGNA TESI
31 GENNAIO 2008

Contents

Foreword

The present thesis deals with the development and implementation of models for problems in soft condensed matter, at the interface between biology and material science. In particular, two projects have been carried out. The first focuses on the molecular origin of chirality in liquid crystalline solutions of semiflexible polyelectrolytes like DNA, columnar aggregates of deoxyguanosine tetramers (G-wires) and filamentous becteriophages. The second project deals with the integration between theoretical and experimental methods for the study of membrane-proteins systems, starting from the analysis of ESR spectra of spin labelled proteins. Both projects have been carried out in collaboration with experimental groups.

This thesis is organised in two parts. In the first part, from chapter 1 to chapter 4, the work on chiral amplification in liquid crystalline solutions of polyelectrolytes is presented. In chapter 1, the phenomenon of chiral amplification is introduced and the main properties of liquid crystals are summarised. In chapters 2 and 3 the theoretical model which has been developed to connect the molecular and phase chirality of rigid polyelectrolytes is presented, together with its application to solutions of B-DNA and colloidal suspensions of M13 virus. In chapter 4, this model is extended to semiflexible polymers.

The second part, from chapter 5 to chapter 9, deals with the theoretical and computational methods used to analyse ESR experiments on spin labeled proteins. Chapter 5 is a short introduction to peripheral proteins, the Site-Directed Spin Labelling (SDSL) technique and ESR lineshape simulations. In chapters 6 and 7, a method for the analysis of the ESR spectra of spin labeled proteins is proposed, based on the structural and motional characteristics of typical spin labels in their environment. In chapter 9, the model is applied to the investigation of controversial aspects of α-Synuclein binding to lipid bilayers. Chapter 8 reports on Molecular Dynamics simulations of a fragment α-Synuclein, in the presence of a POPC bilayer.

Finally, chapter 10 presents a summary of the two projects, with some highlights on the relevant results obtained in this thesis.

Chapter 1

Chiral liquid crystal phases of polyelectrolyte suspensions

1.1 Chirality at different levels

Chirality in molecules leads to a myriad of macroscopic chiral structures [Pasteur, 1848]. The term chirality was first coined by Lord Kelvin [Thomson, 1893]:

> *" I call any geometrical figure, or group of points, chiral, and say it has chirality if its image in a plane mirror, ideally realized, cannot be brought to coincide with itself."*

According to this definition, a molecule is chiral if its mirror image cannot be rotated to replicate itself. More rigorously, an object is chiral if its symmetry group does not contain the element $\mathbf{S}_n$, a rotation around an S_n axis by $2\pi/n$ followed by a reflection through a plane perpendicular to that axis. This definition is general, and can be used to identify chirality both in molecules and in phases of matter. A chiral object and its mirror image are called enantiomorphs, or when referring to molecules, *enantiomers*. It is interesting to note that chirality is defined not on the base on the presence, but rather on the absence of a property. Chirality of a structure can be quantified in different ways [Harris, 1999].

An important phenomenon that pervades the world of chemistry and biology is *chiral amplification*. In chemistry, chiral amplification is defined as the selection of an enantiomeric product molecule with respect to the mirror image in the presence of an enantiomeric excess of catalyst [Soai, 1995]. In supramolecular chemistry, chiral amplification is the transmission of chirality from molecular building blocks to supramolecular architectures. Typical examples of chiral amplification are the formation in water solutions of helical columnar aggregates, in which the chirality of one chiral discotic molecule is transferred to the whole structure [Brunsveld, 2000], or the chiral organization of polymers due to the interaction with small amount of chiral dopants [Nagai, 2005]. Supramolecular organization and chirality permeates also the biological world. The function of fundamental components of the cell, like actin, myosin, proteins and DNA relies upon their being supramolecular chiral structures. Other systems that use supramolecular organization and chirality for their functions are viruses. A spectacular example is represented by inoviruses, or filamentous phages, like *fd,* M13, Pf1 and TMV. These are monodisperse rod-like macromolecules made of a single DNA or RNA filament enclosed in a cylindrical capsid formed by thousands of identical proteins [Wang, 2006; Nave, 1979; Marvin, 2006]. In Fig. 1.1 a scheme of chiral amplification for DNA and for viruses *fd* and M13[1] is reported. In both systems, chirality originates at the atomic level

[1] M13 differs from *fd* for replacement of a negatively charged Aspartate with a neutral Asparagine in the coat proteins.

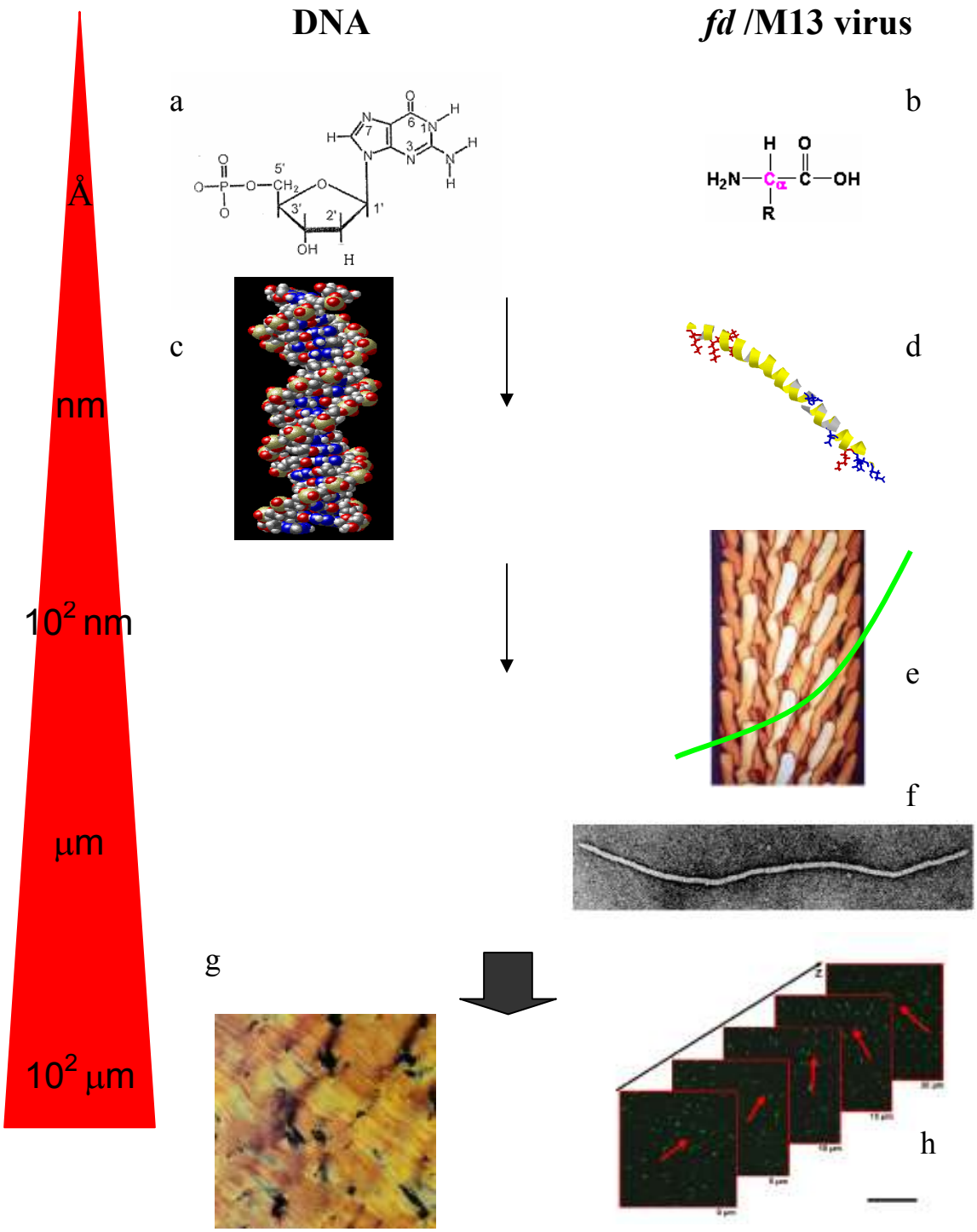

Figure 1.1 Chiral amplification for DNA and *fd* (M13) virus. This scheme is described in the text.

(Ångstrom length-scale), from the asymmetrically substituted carbons of sugar rings in nucleotides (fig 1.1.a) and from the C_α carbons of amino acids (fig.1.1.b).

Chirality is then transferred to the nanometer length-scale, in the right-handed double helix of B-DNA (fig.1.1.c) and in the right-handed α-helix structure of proteins that build the viral capsid (fig.1.1.d). In the case of viruses, we have another example of chiral amplification on the 10^2 nm length-scale, coming from the helical wrapping of proteins along the virus capsid (fig.1.1.e). It has been suggested that, by virtue of their flexibility (fig.1.1.f), viruses could bend to form "supra-helices", where chirality is amplified at the micrometer length-scale [Dogic, 2000]. Both DNA and viruses at suitable concentrations, give rises to chiral liquid crystal phases (fig.1.1.g; fig.1.1.h), so transferring the chirality from the molecular to the phase level [Proni, 2000; Dogic, 2000].

1.2 Liquid crystals and the chiral nematic (cholesteric) phase

Liquid crystals are phases of matter whose order is intermediate between that of liquids and that of crystals. For instance, liquid crystals can flow like liquids, but have the molecules oriented in a crystal-like way. The simplest liquid crystal phase is called *nematic*, and is characterized by long-range uniaxial orientational order (fig. 1.2). The constituent molecules, which typically have anisotropic shape, have the centres of mass homogeneously distributed as in an isotropic fluid, but one of their anisotropy axes aligns, on the average, along a common direction, called the *director* (usually represented by the unit vector **n**).

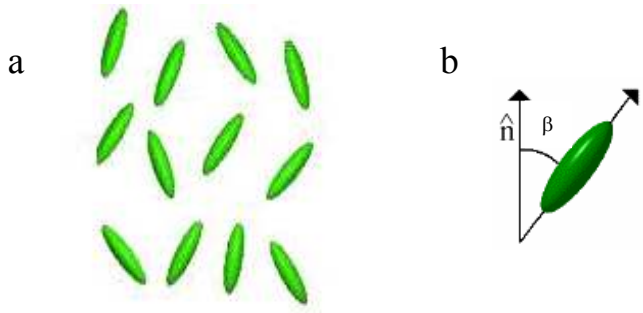

Figure 1.2 a) Schematic representation of molecules in the nematic phase; the long molecular axes align on the average along the director **n**. b) Angle β used to quantify the degree of order in the nematic phase.

The degree of order of a nematic phase is quantified by the order parameter $\overline{P_2} = (3\overline{\cos^2 \beta} - 1)/2$, where β is the angle between the long molecular axis and the director, as

shown in fig. 1.2.b. The value of $\overline{P_2}$ is equal to zero for an isotropic liquid, and equal to one in a perfect crystal. In liquid crystals, typical values of $\overline{P_2}$ are between 0.4 and 0.8.

Liquid crystal are usually distinguished in *thermotropic* and *lyotropic*. The former are constituted by pure compounds or mixtures and exhibit the isotropic-liquid crystal phase transition as temperature is changed. The latter are generally represented by solutions of anisometric molecules and undergo the phase transition under a change of concentration.

If the constituting molecules are chiral the director **n** twists, so creating the *chiral nematic* (or *cholesteric*) phase. The same effect is obtained when chiral solutes are added to an achiral nematic phase. Cholesterics were the first liquid crystals to be discovered [Reinitzer, 1888]. In the chiral nematic phase the director rotates in space in helical fashion (fig. 1.3.); sign (handedness) and magnitude of the helical pitch fully characterize the cholesteric organization. The pitch p, or correspondingly the wavenumber $q=2\pi/p$, is defined as positive or negative, according to the right- or left-handedness of the cholesteric helix, respectively.

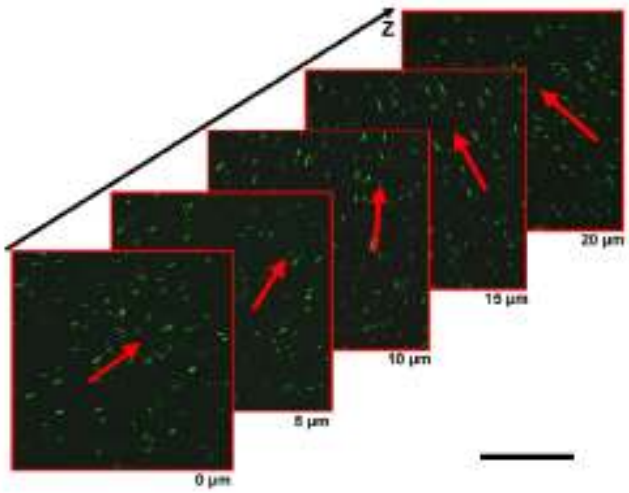

Figure 1.3 Direct visualization by confocal fluorescence microscopy of the cholesteric helix in solutions of M13 viruses. The sequence of images follows the director, represented by red arrows, through the sample thickness. In this system, the director rotates in a left-handed sense through the sample. Green spots are labelled viruses.

The deformation of a nematics or cholesterics is decribed the the *director field* **n**(**r**). The free energy associated with the deformation depends on the gradient of the director. For small

distorsions, the power expansion of the free energy density can be truncated at the quadratic term; symmetry considerations lead to the Frank-Oseen form [de Gennes, 1993]:

$$f_{el} = K_t \mathbf{n} \cdot (\nabla \cdot \mathbf{n}) + \frac{1}{2} K_{11} (\nabla \cdot \mathbf{n})^2 + \frac{1}{2} K_{22} (\mathbf{n} \cdot (\nabla \times \mathbf{n}))^2 + \frac{1}{2} K_{33} |\mathbf{n} \times (\nabla \times \mathbf{n})|^2$$

where K_{11} , K_{22} and K_{33} are the *elastic constants* for the three fundamental modes, denoted as *splay*, *twist* and *bend*, respectively. The parameter K_t , which vanises in the achiral nematic phase, is denoted as the *chiral strength*.

1.3 Chiral nematic phases of suspensions of polyelectrolytes

Solutions of rod-like charged polymers (polyelectrolytes) at suitable concentration can exhibit chiral nematic phases. Examples are represented by B-DNA [Podgornik, 1998], filamentous viruses [Dogic, 2000] and columnar aggregates of deoxyguanosine tetramers (G-wires) [Proni, 2000]. It is interesting to note that cholesteric phases have been observed both *in vitro* and *in vivo* [Livolant, 1991]. We can find some analogies between the molecular structures of these polymers. They are all rigid or semiflexible, with helical shape and high aspect ratio; they present a net surface charge with helical symmetry.

Although the phase chirality originates from the chirality of the constituent molecules, any simple correlation (molecular helix →phase helicity) fails. Two examples can illustrate this point. B-DNA is organized in a right-handed double helix and forms a left-handed cholesteric phase, whose pitch increases with temperature. G-wires constituted by the oligodeoxyguanylates denoted as dG_4, self-assemble in right-handed columns, like B-DNA; however, they form a right-handed cholesteric phase, with a pitch which decreases with temperature [Proni, 2000]. Another puzzling example is provided by Pf1 and *fd* bacteriophages, which have similar structures and slightly different arrangements of proteins in the capsid [Marvin, 2006]: *fd* exhibits a cholesteric phase, whereas only a nematic phase has been found for Pf1 [Dogic, 2000].

1.4 Theoretical models for the molecular origin of chiral nematic phases

The main reasons for the difficulty in correlating molecular and phase chirality are the smallness of the chiral contribution to intermolecular interactions and its subtle dependence on details. It can change dramatically even for small structural variations, so predictions require accurate modelling of the system. Solutions of polyelectrolytes are particularly complex, because of their intrinsic multicomponent nature; they are characterized by a variety of interactions covering a wide range of length-scales.

The first attempt to correlate molecular and phase chirality traces back to Straley [Straley, 1976], who considered an ideal system of hard helices, experiencing only steric interactions. In this system the cholesteric organization is determined by the best packing of helices. According the Straley model, B-DNA and M13 virus should form right-handed cholesteric phases, with a pitch independent of temperature, in complete contrast with experiments.

The failure of the Straley theory is not surprising, in view of the neglect of electrostatic interactions, which are expected to play a role for polyelectrolytes. The electrostatic interactions between stiff polyelectrolytes have been thoroughly investigated by Kornyshev and coworkers; a recent review of this work appeared [Kornyshev, 2006]. The theory for the electrostatic interactions between pairs of cylinders with helical charge patterns on their surface was applied to B-DNA and guanosine quadruplexes. A deep insight into the effects of the charge distribution on the pair interactions was reached; however, a proper statistical-thermodynamics treatment, required to bridge these and the cholesteric organisation, is still lacking.

In this thesis the molecular mechanism underlying the formation of cholesteric phases by polyelectrolytes has been investigated. In chapter 2 we shall present a theoretical method and a numerical procedure which, starting from the geometry and charges of rigid polyelectrolytes, lead to the prediction of the cholesteric pitch. Molecular expressions for the free energy of the system are obtained on the basis of steric and electrostatic interactions between pairs of polymers; the former are described in terms of excluded volume, while the Poisson-Boltzmann theory is used for the latter. The model has been applied to the cholesteric phase formed by solutions of B-DNA and suspensions of M13 virus. The latter study, which is presented in chapter 3, has been carried out in parallel with experiments. A limit of the model which has been developed is the neglect of the flexibility of polyelectrolytes. This approximation, if probably acceptable for 130 base-pair B-DNA fragments, becomes questionable for the M13 virus. Indeed, molecular flexibility has been invoked as the responsible for the chirality exhibited by liquid crystal phases of M13 and *fd* viruses [Grelet, 2003]. In chapter 4 a model will be presented, which has been developed to explore the possible role of shape fluctuations in the formation of cholesteric phases. A Monte Carlo method sampling of configurations of the virus, described as a worm-like polymer [Kratky, 1949], is associated with a mean field model for its orientational distribution in the chiral nematic phase.

1.5 References

Brunsveld, L., Lohmeijer B.G.G., Vekemans J.A.J.M., Meijer E.W. *Chem. Comm.* , 2305 (2000).

di Matteo A., Todd S.M., Gottarelli G., Solladié G., Williams V.E., Lemieux R.P., Ferrarini A., Spada G.P. *J. Am. Chem. Soc.* **123**, 7842 (2001).

de Gennes P.G., Prost J. *The Physics of Liquid Crystals* , 2nd edition (Clarendon Press, Oxford, 1993).

Dogic Z., Fraden S. *Langmuir* **16**, 7820 (2000).

Grelet E., Fraden S. *Phys. Rev. Lett.* **90**, 198302 (2003).

Harris A.B., Kamien R.D., Lubensky T. *Rev. Mod. Phys.* **71**, 1745 (1999).

Kornyshev A.A., Lee D.J., Leikin S., Wynveen A. *Rev. Mod. Phys.*, **79,** 943 (2007).

Kratky O., Porod D. *Rec. Trav. Chim*. **68**, 1106 (1949).

Livolant F. *Physica A* **176**, 117 (1991).

Marvin D.A., Welsh L.C., Symmons M.F., Scott W.R.P., Straus S.K. *J. Mol. Biol.* **235**, 260 (2006).

Nagai K., Maeda K., Takeyama Y., Sakajiri K., Yashima E. *Macromolecules* **38,** 5444 (2005).

Nave C., Fowler A.G., Malsey S., Marvin D.A., Siegrist H., Wachtel E.J. *Nature* **281**, 232 (1979).

Pasteur L. *Ann. Chim. Phys.* **24**, 442 (1848).

Pieraccini S., Ferrarini A., Fuji K., Gottarelli G., Lena S., Tsubaki K., Spada G.P. *Chem. Eur. J.* **12**, 1121 (2006).

Podgornik R, Strey H.H., Parsegian V.A. *Curr. Opin. Coll. & Interf. Sci.* **3**, 534 (1998).

Proni G., Gottarelli G., Mariani P., Spada G.P. *Chem. Eur. J.* **6**, 3249 (2000).

Reinitzer F. *Monatshefte fur Chemie* **9**, 421 (1888).

Soai K., Shibata T., Marioka H., Choji K. *Nature* **378**, 767 (1995).

Straley J.P. *Phys. Rev. A* **14**, 1835 (1976).

Thomson W. *The Robert Boyle Lecture, Oxford University Junior Scientific Club,* (1893), reprinted in *Baltimore Lectures*, (C.J. Clay & Sons, London).

Wang Y.A., Yu X., Overman S., Tsuboi M., Thomas G.J., Hegelman E.H. *J. Mol. Biol.* **361**, 209 (2006).

Chapter 2

From the double-stranded helix to the chiral nematic phase of B-DNA: a theoretical model

From the double-stranded helix to the chiral nematic phase of B-DNA: A molecular model

Fabio Tombolato and Alberta Ferrarini
Dipartimento di Scienze Chimiche, Università di Padova, via Marzolo 1, 35131 Padova, Italy

(Received 29 September 2004; accepted 3 November 2004; published online 21 January 2005)

B-DNA solutions of suitable concentration form left-handed chiral nematic phases (cholesterics). Such phases have also been observed in solutions of other stiff or semiflexible chiral polymers; magnitude and handedness of the cholesteric pitch are uniquely related to the molecular features. In this work we present a theoretical method and a numerical procedure which, starting from the structure of polyelectrolytes, lead to the prediction of the cholesteric pitch. Molecular expressions for the free energy of the system are obtained on the basis of steric and electrostatic interactions between polymers; the former are described in terms of excluded volume, while a mean field approximation is used for the latter. Calculations have been performed for 130 base pair fragments of B-DNA. The theoretical predictions provide an explanation for the experimental behavior, by showing the counteracting role played by shape and charge chirality of the molecule. © *2005 American Institute of Physics.* [DOI: 10.1063/1.1839859]

I. INTRODUCTION

Solutions of B-DNA display a rich polymorphism as a function of concentration, which comprises the formation of chiral phases.[1] Many aspects of such behavior are still unexplained, as well as unexplained are most phenomena involving DNA-DNA interactions:[2–4] the most striking and biologically significant effect is the dense packing of DNA in chromatin. This paper deals with the chiral nematic (cholesteric) phase, which has been observed *in vivo* and *in vitro*.[5–9]

Cholesteric phases are also formed by solutions of other stiff or semiflexible chiral polyelectrolytes, e.g., filamentous viruses,[10] polysaccharides such as xanthan,[11] or columnar aggregates of deoxyguanosine tetramers (*G* wires).[9] The latter can have different organizations depending on the chemical structure of the monomeric units; accordingly, cholesteric phases with different features are formed. In all cases the relation between molecular and macroscopic chirality is unknown, and any simple correlation (molecular helix↔phase helicity) fails. An example can illustrate this point. B-DNA helices are right-handed and form a left-handed cholesteric phase, whose pitch increases with temperature. *G* wires constituted by the oligodeoxyguanylates denoted as d(GpGpGpG), or dG_4, self-assemble in right-handed columns, like B-DNA; however, unlike B-DNA, they form a right-handed cholesteric phase with a pitch which decreases with temperature.[9] Yet the two molecular systems have similar chemical structure and their chiral nematic phases are formed under analogous conditions.

The stability of the chiral nematic phase is explained by the elastic continuum theory in terms of the competition between chiral forces, which favor a twist deformation of the director, and restoring elastic torques, which oppose the deformation.[12] The two contributions reflect the intermolecular interactions specific of each system. The elastic term has a weaker dependence on molecular structure, and reasonable estimates, at least of its order of magnitude, can be obtained even in simple ways. On the contrary, magnitude and sign of the chiral contribution can change dramatically even for small structural variations; therefore predictions require a detailed modeling of the system. This is a general feature of chiral properties, which are determined by a tiny fraction of the whole intermolecular interactions, with a subtle dependence on the molecular structure.[13] Nevertheless, molecular theories[14,15] and simulation methods[16] that are able to provide reliable predictions of the cholesteric pitch of thermotropic cholesterics on the basis of the structure of the chiral molecules have been developed. The case of polyelectrolyte solutions is more complicated, because these are multicomponent systems characterized by a variety of interactions covering a wide range of lengthscales. The early theory by Straley deals with a system of hard helices, whose free energy is calculated according to the virial expansion truncated at the second term.[17] The organization of the cholesteric phase is then determined by the best packing of helices. For instance, B-DNA should form a right-handed cholesteric phase, with a pitch independent of temperature, in full contrast with experiment. Subsequently, the additional effect of dispersion interactions between macromolecules in a solvent, treated as a dielectric continuum, was introduced.[18] However, a theory for polyelectrolytes cannot ignore interactions between charges. For example, in the case of DNA each phosphate group has a net charge of $-1e$ at $p\mathrm{H}\sim 6-7$, which corresponds to a high surface charge density of about $-1e/\mathrm{nm}^2$. Recently a thorough analysis of electrostatic interactions between stiff polyelectrolytes has been presented, based on a detailed description of screened electrostatic interactions between cylinders with arbitrary surface charge patterns, embedded in a solvent containing microions.[19] This theory provides a deep insight into the effects of the charge distribution on interactions between charged helices. Information about the preferred twist between B-DNA helices can be inferred from the analysis of the potential energy surface

as a function of the interhelix angle and distance.[20]

In this paper we present a molecular theory for the cholesteric pitch of solutions of stiff polyelectrolytes, which differs from previous treatments for two main reasons. A statistical-mechanics analysis is performed, which allows a consistent description of the system properties, comprising orientational order, elastic constants, and chiral strength, and of their temperature dependence. Moreover, both steric and electrostatic interactions are considered, according to the same picture which underlies theories developed for the nematic phase of solutions of rodlike polyelectrolytes, following the Onsager suggestion.[21] Such theories are able to explain the orientational order and the features of the isotropic-nematic transition,[22] as well as the elastic properties[23] of cholesteric solutions of stiff chiral polyelectrolytes, approximated as uniformly charged rods. However, the chirality of shape and charge distribution cannot be neglected if chiral properties are investigated. The smallness of chiral effects and their dependence on molecular details pose serious problems to the possibility of getting reliable predictions. On one side an accurate representation of the molecular structure is required, but on the other side a detailed description, e.g., at the atomistic level, is unfeasible for the complex systems under examination. We have considered the case of B-DNA solutions by taking into account the chirality of shape and charge distribution by a coarse-grained representation, which, however, preserves the main features of the molecular structure.

The paper is organized as follows: In the following section the theoretical framework is presented and general expressions for the free energy of the system and the cholesteric pitch in terms of steric and electrostatic intermolecular interactions are reported. Then expressions suitable for numerical calculations, in terms of orientational order parameters, are derived through expansion of the density function on a set of basis functions. In Sec. IV the modeling of the B-DNA structure and of intermolecular interactions is described, while in Sec. V the computational aspects of the method are summarized. Then the results obtained are reported and discussed, and conclusive remarks are presented by pointing out achievements and limits of this work. To avoid making the text unnecessarily heavy, derivations have been confined to Appendixes.

II. THEORY

The twist deformation characterizing a chiral nematic phase is specified by sign and magnitude of the pitch of the helix formed in space by the mesophase director $\hat{n}$. The pitch p, or correspondingly the wave number $q=2\pi/p$, is defined as positive or negative, according to the right or left handedness of the cholesteric helix, respectively.

The continuum elastic theory can justify the stability of the cholesteric phase and provides an expression for the equilibrium pitch in terms of macroscopic properties of the system. Let us consider the Helmholtz free energy density f, which is related to the free energy F of the system by the integral

$$F=\int d\mathbf{R} f(\mathbf{R}). \tag{1}$$

For small deformations, the expansion of the Helmholtz free energy density f in a power series of the deformation q can be truncated at the quadratic contribution,

$$f\approx f^u+K_t q+\tfrac{1}{2}K_{22}q^2, \tag{2}$$

where f^u is the free energy density of the undeformed nematic phase, and

$$K_t=\left(\frac{\partial f}{\partial q}\right)_{q=0}, \tag{3a}$$

$$K_{22}=\left(\frac{\partial^2 f}{\partial q^2}\right)_{q=0} \tag{3b}$$

are, respectively, the chiral strength and the twist elastic constant.[12] At given (T,V) values, equilibrium corresponds to the minimum of the Helmholtz free energy; by imposing the condition $(\partial f/\partial q)_{T,V}=0$, the equilibrium wave number is obtained,

$$q=-\frac{K_t}{K_{22}}. \tag{4}$$

The cholesteric pitch vanishes if the mesophase is formed by achiral molecules or by a racemic mixture (with no enantiomeric excess), in which cases $K_t=0$; it has opposite handedness for pairs of mesophases formed by enantiomers, because these have opposite K_t values. The purpose of a molecular theory is the derivation of expressions for chiral strength and twist elastic constant in terms of the intermolecular interactions.

A. Free energy of the undeformed nematic phase

Let us take a system of N identical particles in the volume V at temperature T, interacting through hard core repulsions and electrostatic interactions. Manageable expressions for the Helmoltz free energy of the system are obtained by using a variational approach, based on the Gibbs–Bogoliubov inequality:[24]

$$F\leqslant F_0+\langle H_1\rangle_0, \tag{5}$$

where F_0 is the Helmholtz free energy of a model system with Hamiltonian H_0 and $H_1=H-H_0$ is the difference between the Hamiltonian of the system and that of the model. The angular brackets with the zero subscript denote the average value calculated over the distribution function of the model system,

$$\langle H_1\rangle_0=\frac{\int d\mathbf{\Gamma}^N (H-H_0)\exp(-H_0/k_BT)}{\int d\mathbf{\Gamma}^N \exp(-H_0/k_BT)}. \tag{6}$$

In this expression k_B is the Boltzmann constant and $\mathbf{\Gamma}^N$ is a collective notation for all the degrees of freedom of the system, $\mathbf{\Gamma}^N=(\mathbf{R}^N,\Omega^N)$, with the vector $\mathbf{R}$ and the Euler angles $\Omega=(\alpha,\beta,\gamma)$ specifying position and orientation of a particle.

We shall now derive expressions for the two contributions in Eq. (5), starting from the case of a uniform system. A

reasonable choice for the model is represented by a system of hard particles, whose free energy, according to the second virial approximation, is given by[21]

$$F_0 = Nk_BT[\ln(\Lambda_{tr}^3\Theta_{or}) - 1] + k_BTV\int d\Omega\,\rho(\Omega)\ln\rho(\Omega) + \frac{k_BTV}{2}\int d\Omega_A d\Omega_B \rho(\Omega_A)\rho(\Omega_B)\nu_{excl}(\Omega_{AB}). \quad (7)$$

The first two terms are ideal gas contributions; $\Lambda_{tr} = (h^2/2\pi k_BTm)^{1/2}$ is the de Broglie wavelength and $\Theta_{or} = (h^2/2\pi k_BTI_x)^{1/2}(h^2/2\pi k_BTI_y)^{1/2}(h^2/2\pi k_BTI_z)^{1/2}$, with h, m and $I_{x,y,z}$ representing the Planck constant, the mass, and the principal components of the inertia tensor.[25] The third term in Eq. (7) is the second virial contribution, with the function $\nu_{excl}(\Omega_{AB})$ representing the volume excluded to the B particle by the A particle; this is defined as

$$v_{excl}(\Omega_{AB}) = -\int d\mathbf{R}_{AB} e_{AB}(\mathbf{R}_{AB},\Omega_{AB}), \quad (8)$$

where the vector $\mathbf{R}_{AB}$ is defined as $\mathbf{R}_{AB} = \mathbf{R}_B - \mathbf{R}_A$, while Ω_{AB} are the Euler angles for the rotation from the molecular frame of particle A to that of particle B (see scheme). The function e_{AB} is the Mayer function[25]

$$e_{AB}(\mathbf{R}_{AB}\Omega_{AB}) = \exp\{-U_h(\mathbf{R}_{AB},\Omega_{AB})/k_BT\} - 1 \quad (9)$$

with $U_h(\mathbf{R}_{AB},\Omega_{AB})$ being the hard core potential between the A and B particles,

$$U_h(\mathbf{R}_{AB},\Omega_{AB}) = \begin{cases} \infty & \text{if } A,B \text{ overlap} \\ 0 & \text{if } A,B \text{ do not overlap.} \end{cases} \quad (10)$$

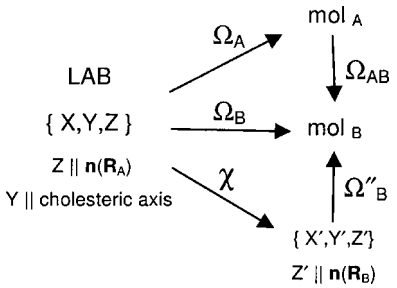

Scheme 1

The function $\rho(\Omega,\mathbf{R})$ is the single particle density function,[26] which satisfies the normalization condition

$$\int d\mathbf{R}\, d\Omega \rho(\mathbf{R},\Omega) = N. \quad (11)$$

The density function reflects the particle and phase symmetry properties. In a uniform system the density function is independent of the molecular position; if furthermore the phase is isotropic, it is also independent of orientation, and is simply given by $\rho_{iso} = 1/8\pi^2\nu$, with $\nu = V/N$ being the available volume per molecule.

Electrostatic interaction between particles are introduced in a mean field way, according to Eq. (6). By taking into account the pairwise additivity of electrostatic interactions and the independence of position of the density function, we can write for a homogeneous system

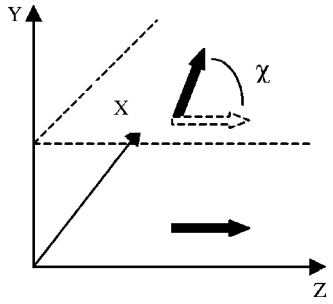

FIG. 1. Definition of the twist angle χ. Black arrows indicate the orientation of the director $\hat{n}$ at different positions along cholesteric axis (Y).

$$\langle H_1\rangle_0 \approx \frac{1}{2}\int d\mathbf{R}_A d\mathbf{R}_B d\Omega_A d\Omega_B \rho(\Omega_A)\rho(\Omega_B) \times g_h(\mathbf{R}_{AB},\Omega_{AB})U_{el}(\mathbf{R}_{AB},\Omega_{AB}) \quad (12)$$

with the hard particle pair distribution function $g_h(\mathbf{R}_{AB},\Omega_{AB})$ approximated as

$$g_h(\mathbf{R}_{AB},\Omega_{AB}) = \begin{cases} 0 & \text{if } A,B \text{ overlap} \\ 1 & \text{if } A,B \text{ do not overlap.} \end{cases} \quad (13)$$

By collecting the contributions in Eqs. (7) and (12) we can write the free energy density of the system as

$$f = f^{id} + f^{ex} \quad (14)$$

with f^{id} representing the ideal term

$$f^{id} = \frac{N}{V}k_BT[\ln(\Lambda_{tr}^3\Theta_{or}) - 1] + k_BT\int d\Omega\,\rho(\Omega)\ln\rho(\Omega) \quad (15)$$

and the excess contribution

$$f^{ex} = \frac{1}{2}\int d\mathbf{R}_B d\Omega_A d\Omega_B \rho(\Omega_A)\rho(\Omega_B)u(\mathbf{R}_{AB},\Omega_{AB}), \quad (16)$$

where the pair interaction is defined as

$$u(\mathbf{R}_{AB},\Omega_{AB}) = \{-k_BTe_{AB}(\mathbf{R}_{AB},\Omega_{AB}) + g_h(\mathbf{R}_{AB},\Omega_{AB})U_{el}(\mathbf{R}_{AB},\Omega_{AB})\}. \quad (17)$$

We have found an expression for the approximate free energy $F_{app} = F_0 + \langle H_1\rangle_0$ as a functional of the density function ρ, $F_{app}[\rho]$; according to the Gibbs–Bogoliubov inequality the best approximation to the free energy of the system can be found by functional minimization.

B. Free energy of the twisted nematic phase and cholesteric pitch

In the twisted nematic phase the density function depends also on the particle position, and we can write $\rho = \rho[\Omega,\chi(\mathbf{R})]$, where χ is the angle between the local director at the particle position $\mathbf{R}$ and the director at the origin of the laboratory frame, as shown in Fig. 1. The lengthscale of the twist deformation is orders of magnitude larger than the molecular dimension and the lengthscale of intermolecular interactions. As a consequence, the local phase properties are hardly distinguishable from those of the corresponding nem-

atic phase, and the density function in the cholesteric phase can be reasonably assumed to be the same as that in the undeformed nematic phase, with respect to the local director $\hat{n}$.[27]

Thus, the free energy density of the cholesteric phase can be expressed as the sum of an ideal contribution with the form of Eq. (15), with the Euler angles Ω expressing the molecular orientation with respect to the local director, along with an excess term which has the form

$$f^{ex}=\frac{1}{2}\int d\mathbf{R}_B d\Omega_A d\Omega_B \rho(\Omega_A)\rho[\Omega_B,\chi(\mathbf{R}_B)]u(\mathbf{R}_{AB},\Omega_{AB}) \tag{18}$$

having chosen a laboratory frame with the Z axis parallel to the local director at the position of the A particle.

Then, by reminding the free energy expansion Eq. (2), we obtain molecular expressions for the chiral strength

$$K_t=\left(\frac{df^{ex}}{dq}\right)_{q=0}=\frac{1}{2}\int d\mathbf{R}_B d\Omega_A d\Omega_B \rho(\Omega_A) \times\left(\frac{d\rho[\Omega_B,\chi(R_B)]}{dq}\right)_{q=0} u(\mathbf{R}_{AB},\Omega_{AB}) \tag{19}$$

and the twist elastic constant

$$K_{22}=\left(\frac{d^2f^{ex}}{dq^2}\right)_{q=0}=\frac{1}{4}\int d\mathbf{R}_B d\Omega_A d\Omega_B \rho(\Omega_A) \times\left(\frac{d^2\rho[\Omega_B,\chi(\mathbf{R}_B)]}{dq^2}\right)_{q=0} u(\mathbf{R}_{AB},\Omega_{AB}). \tag{20}$$

The helical wave number can then be obtained as the ratio between chiral strength and twist elastic constant, according to Eq. (4). By distinguishing steric and electrostatic contribution and recalling the form of the pair potential Eq. (17), we can write

$$q=-\frac{\tilde{K}_t^h+\dfrac{K_t^{el}(T)}{k_BT}}{\tilde{K}_{22}^h+\dfrac{K_{22}^{el}(T)}{k_BT}}, \tag{21}$$

where the apices el or h denote electrostatic and hard core contribution, respectively, and $\tilde{K}^h=K^h/k_BT$ is independent of temperature.

III. FREE ENERGY IN TERMS OF ORDER PARAMETERS

A convenient route for the numerical solution of the problem rests on the technique of expansion of the density function on a basis of orthogonal functions. In this case the appropriate functions are the Wigner rotation matrices $D^j_{lm}(\Omega)$.[28]

By taking into account the $D_{\infty h}$ symmetry of the undeformed nematic phase and approximating particles as axially symmetric, we can write

$$\rho(\Omega)=\frac{1}{8\pi^2\nu}\sum_{j=0,2,4...}(2j+1)\langle D^j_{00}\rangle D^j_{00}(\Omega) \tag{22}$$

with the expansion coefficients $\langle D^j_{00}\rangle$ defined as

$$\langle D^j_{00}\rangle=\nu\int d\Omega\rho(\Omega)D^j_{00}(\Omega). \tag{23}$$

Such coefficients are the nematic order parameters.

For the density function in the chiral nematic phase we can write

$$\rho[\Omega,\chi(\mathbf{R})]=\frac{1}{8\pi^2\nu}\sum_{j=0,1,2,...}(2j+1) \times\sum_{l=-j}^{j}\langle D^j_{l0}[\chi(\mathbf{R})]\rangle D^j_{l0}(\Omega) \tag{24}$$

with the coefficients $\langle D^j_{l0}[\chi(\mathbf{R})]\rangle$ defined by an expression analogous to Eq. (23). By using the transformations reported in Scheme I and exploiting the addition theorem of Wigner matrices[28] we can write

$$\langle D^j_{l0}[\chi(\mathbf{R})]\rangle=\nu\sum_{n=-j}^{j}D^j_{ln}(0,\chi,0)\int d\Omega''\rho(\Omega'')D^j_{n0}(\Omega''), \tag{25}$$

where the Euler angles Ω'' specify the molecular orientation with respect to the local director in $\mathbf{R}$.

By using the relation $D^j_{ln}(0,\chi,0)=d^j_{ln}(\chi)$, where $d^j_{ln}(\chi)$ are reduced Wigner rotation matrices,[28] and recognizing that the integrals in Eq. (25) are the nematic order parameters, Eq. (23), we can write

$$\langle D^j_{l0}[\chi(\mathbf{R})]\rangle=d^j_{l0}(\chi)\langle D^j_{00}\rangle, \quad j \text{ even}. \tag{26}$$

The density function in the twisted nematic phase can then be expressed as

$$\rho[\Omega,\chi(\mathbf{R})]=\frac{1}{8\pi^2\nu}\sum_{j=0,2,4,...}(2j+1)\langle D^j_{00}\rangle \times\sum_{l=-j}^{j}d^j_{l0}[\chi(\mathbf{R})]D^j_{l0}(\Omega). \tag{27}$$

If a laboratory frame with the Y axis along the cholesteric axis is chosen, as in Fig. 1 and Scheme I, we can write

$$\chi(\mathbf{R})=qY, \tag{28}$$

where q is the wave number of the twist deformation; therefore $\rho=\rho(\Omega,qY)$, and explicit expressions for the derivatives in Eqs. (19) and (20) can be obtained (see Appendix A for the derivation):

$$\left(\frac{\partial\rho[\Omega_B,\chi(\mathbf{R})]}{\partial q}\right)_{q=0} = -\frac{1}{16\pi^2 v}\sum_{j=2,4,\ldots}(2j+1)\sqrt{\frac{(j+1)!}{(j-1)!}}\langle D^j_{00}\rangle \times[D^j_{10}(\Omega)-D^j_{-10}(\Omega)]Y, \tag{29a}$$

$$\left(\frac{\partial^2\rho[\Omega_B,\chi(\mathbf{R})]}{\partial q^2}\right)_{q=0} = \frac{1}{32\pi^2 v}\sum_{j=2,4,\ldots}(2j+1)\langle D^j_{00}\rangle\left\{-2j(j+1)D^j_{00}(\Omega) + \sqrt{\frac{(j+2)!}{(j-2)!}}[D^j_{20}(\Omega)+D^j_{-20}(\Omega)]\right\}Y^2. \tag{29b}$$

By introducing Eqs. (22) and (29a) into Eq. (19) for the chiral strength, the following expression is obtained (for the derivation see Appendix C):

$$K_t=\frac{1}{3\sqrt{2}}\frac{1}{8\pi^2 v^2}\sum_{j_A=2,4,\ldots}(2j_A+1)\langle D^{j_A}_{00}\rangle\sum_{j_B=2,4,\ldots}(2j_B+1) \times\sqrt{\frac{(j_B+1)!}{(j_B-1)!}}C^2(j_A,j_B,1;0,1,1)\langle D^{j_B}_{00}\rangle \times\left\{\int d\Omega_{AB}\int d\mathbf{R}_{AB}\,\mathrm{Im}\{D^{j_B}_{10}(\Omega_{AB})T^{11}_{AB}\}u(\mathbf{R}_{AB},\Omega_{AB})\right\}. \tag{30}$$

Analogously, as shown in Appendix D, by substituting Eqs. (22) and (29b) into Eq. (20) we can express the twist elastic constant as

$$K_{22}=[K_{22}]_{T^{00}}+[K_{22}]_{T^{20}}+\sum_{p=1,2}[K_{22}]_{T^{2p}} \tag{31}$$

with

$$[K_{22}]_{T^{00}}=\frac{1}{8}\left(\frac{1}{8\pi^2\nu}\right)^2\sum_{j_A=0,2,4,\ldots}(2j_A+1)\langle D^{j_A}_{00}\rangle \times\sum_{j_B=2,4,\ldots}(2j_B+1)\langle D^{j_B}_{00}\rangle\delta_{j_Aj_B} \times\left\{\left(-\frac{16\pi^2}{\sqrt{3}}\right)j_B(j_B+1)C^2(j_A,j_B,0;0,0,0)\right\} \times\int d\mathbf{R}_{AB}\int d\Omega_{AB}D^{j_B}_{00}(\Omega_{AB})T^{00}_{AB}u(\mathbf{R}_{AB},\Omega_{AB}), \tag{32a}$$

$$[K_{22}]_{T^{20}}=\frac{1}{8}\left(\frac{1}{8\pi^2\nu}\right)^2\sum_{j_A=0,2,4,\ldots}(2j_A+1)\langle D^{j_A}_{00}\rangle \times\sum_{j_B=2,4,\ldots}(2j_B+1)\langle D^{j_B}_{00}\rangle\frac{8\pi^2}{5} \times\left[j_B(j_B+1)C(j_A,j_B,2;0,0,0)\left(\frac{2}{\sqrt{6}}\right) - \sqrt{\frac{(j_B+2)!}{(j_B-2)!}}C(j_A,j_B,2;0,2,2)\right] \times C(j_A,j_B,2;0,0,0)\int d\mathbf{R}_{AB} \times\int d\Omega_{AB}D^{j_B}_{00}(\Omega_{AB})T^{20}_{AB}u(\mathbf{R}_{AB},\Omega_{AB}), \tag{32b}$$

$$[K_{22}]_{T^{2p}}=\frac{1}{8}\left(\frac{1}{8\pi^2\nu}\right)^2\sum_{j_A=0,2,4,\ldots}(2j_A+1)\langle D^{j_A}_{00}\rangle \times\sum_{j_B=2,4,\ldots}(2j_B+1)\langle D^{j_B}_{00}\rangle\frac{8\pi^2}{5} \times\left[j_B(j_B+1)C(j_A,j_B,2;0,0,0)\left(\frac{2}{\sqrt{6}}\right) - \sqrt{\frac{(j_B+2)!}{(j_B-2)!}}C(j_A,j_B,2;0,2,2)\right] \times 2C(j_a,j_B,2;0,p,p)\int d\mathbf{R}_{AB}\int d\Omega_{AB} \times\mathrm{Re}\{D^{j_B}_{10}(\Omega_{AB})T^{2p}_{AB}\}u(\mathbf{R}_{AB},\Omega_{AB}),\quad p=1,2. \tag{32c}$$

In the above expressions $C(j_A,j_B,j;0,m,m)$ are Clebsch–Gordan coefficients,[28] while $\mathrm{Im}\{\cdot\}$ and $\mathrm{Re}\{\cdot\}$ denote the imaginary and real part of the function within brackets, respectively. The symbol T^{1p} is used for the irreducible spherical components of the first rank tensor $\mathbf{R}_{AB}$, while T^{00} and T^{2p} are used for the zeroth and second rank irreducible spherical components of the tensor $\mathbf{R}_{AB}\otimes\mathbf{R}_{AB}$ (see Appendix B).

According to Eqs. (30) and (32), calculation of chiral strength and twist elastic constant requires the order parameters $\langle D^j_{00}\rangle$. These can be obtained by minimization of the free energy of the undeformed nematic phase which, by virtue of Eq. (22), can be expressed as a function of the order parameters. Namely, by substituting Eq. (22) into Eqs. (15) and (16), the following expressions for the ideal and excess contribution to the free energy density of the nematic phase, in k_BT unit, are obtained:

$$\frac{f^{id}}{k_BT}=\frac{1}{v}\ln(\Lambda_{tr}^3\Theta_{or})-\frac{1}{v}\{1+\ln(8\pi^2 v)\}+\frac{1}{8\pi^2 v}$$
$$\times\sum_{j=0,2,4,\ldots}(2j+1)\langle D_{00}^{j}\rangle\int d\Omega D_{00}^{j}(\Omega)$$
$$\times\left\{\ln\sum_{j'=0,2,4,\ldots}(2j'+1)\langle D_{00}^{j'}\rangle D_{00}^{j'}(\Omega)\right\}, \quad (33)$$

$$\frac{f^{ex}}{k_BT}=\frac{1}{16\pi^2 v^2}\sum_{j_A=0,2,4,\ldots}(2j_A+1)(\langle D_{00}^{j_A}\rangle)^2$$
$$\times\int d\mathbf{R}_{AB}d\Omega_{AB}D_{00}^{j_A}(\Omega_{AB})\frac{u(\mathbf{R}_{AB},\Omega_{AB})}{k_BT}. \quad (34)$$

IV. MODELING OF B-DNA AND INTERMOLECULAR INTERACTIONS

Calculation of chiral strength K_t, elastic constant K_{22}, and order parameters $\langle D_{00}^{j}\rangle$ requires evaluation of integrals of the general form

$$\int_0^\infty dR_{AB}R_{AB}^2\int_0^{2\pi}d\phi_{AB}\int_0^{\pi}d\vartheta_{AB}\sin\vartheta_{AB}\int_0^{2\pi}d\alpha_{AB}$$
$$\times\int_0^{\pi}d\beta_{AB}\sin\beta_{AB}\int_0^{2\pi}d\gamma_{AB}$$
$$\times u(R_{AB},\phi_{AB},\vartheta_{AB},\alpha_{AB},\beta_{AB},\gamma_{AB})$$
$$\times\Xi(R_{AB},\phi_{AB},\vartheta_{AB},\alpha_{AB},\beta_{AB}), \quad (35)$$

where $\mathbf{R}_{AB}$, the vector position of molecule B with respect to molecule A, is expressed in spherical coordinates and $\Xi(R_{AB},\phi_{AB},\vartheta_{AB},\alpha_{AB},\beta_{AB})$ denotes a generic function whose specific form depends upon the property we are dealing with. In particular, we have

$$\Xi(\mathbf{R}_{AB},\Omega_{AB})$$
$$=\begin{cases}\mathrm{Im}\{D_{10}^{j_B}(\Omega_{AB})R_{AB}^1\} & \rightarrow K_t \quad (36a)\\ \mathrm{Re}\{D_{i0}^{j_B}(\Omega_{AB})T_{AB}^i\} & \rightarrow K_{22} \quad (36b)\\ D_{00}^{j_A}(\Omega_{AB}) & \rightarrow \text{order parameters.} \quad (36c)\end{cases}$$

The cost of the calculation can be very high since a large number of pair configurations has to be sampled. In particular, high accuracy is required in evaluating K_t, because this is a small quantity resulting from the sum of integrals which are large in value and opposite in sign. As will be shown below, each integral requires evaluation of the integrand function for a number of pair configurations of the order of 10^9. If the molecule is represented as an assembly of N spheres with M point charges, a number of operations proportional to N^2 and M^2 is required for each configuration. It follows that the feasibility of calculations depends on the level of detail employed in modeling the molecular features.

A. Modeling the shape of B-DNA

The function in Eq. (36a) extracts the chiral part of intermolecular interactions. Of course, steric interactions will have a chiral component only if the two interacting particles have a chiral shape. On the contrary, the presence of a chiral charge distribution is not a sufficient condition for a nonvanishing electrostatic contribution to the chiral strength. Namely, on the basis of symmetry considerations it can be demonstrated that the electrostatic contribution to K_t vanishes for cylinders with a helical charge distribution on their surface (see Appendix E). So a chiral shape is necessary to have not only a steric, but also an electrostatic contribution to K_t.

We have modeled double stranded B-DNA in the following way: a base pair is represented by five spheres, one corresponds to the aromatic cores, two to the sugar, and two to the phosphate groups. The centers of all spheres lie on the same plane, perpendicular to the helix axis (see Fig. 2). The DNA helix is obtained by a 3.4 Å translation of the center of the spheres representative of the aromatic cores along a common axis and a 36° right-handed rotation of the base pair plane about such an axis. The geometry parameters are reported in Table I; a fragment of about 30 bp of our model B-DNA is shown in Fig. 3. Despite its simplicity, this model can reproduce the main features of B-DNA, with realistic dimensions of major and minor groove. This model has been proposed by Montoro and Abascal[29] and subsequently used by other authors[30] to simulate the distribution of microions around B-DNA.

For polymers with a strong shape anisotropy, like DNA fragments, the elastic constant K_{22} and the order parameters weekly depend on molecular details. So, with the aim of reducing the computational cost, we have calculated these properties by approximating a DNA molecule as an assembly of fused spheres of radius equal to 11.9 Å, with the centers aligned along a common axis at a distance of 3.4 Å from each other. Because of its shape this model will be henceforth denoted as the "spherocylinder."

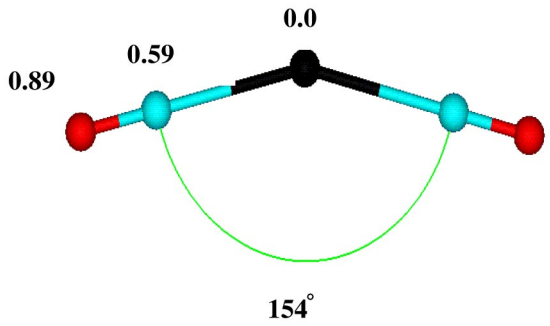

FIG. 2. Geometry and charges assumed for a B-DNA base pair. Angles are expressed in degrees and lengths in nanometers.

TABLE I. Parameters for the spheres used for modeling the shape of B-DNA.

Group	Sphere diameter σ (nm)	Distance of sphere center from helical axis (nm)
Base pairs	1.0	0.0
Sugar	0.6	0.59
Phosphate	0.6	0.89

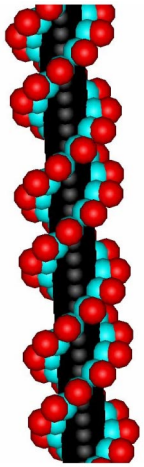

FIG. 3. Model of a B-DNA fragment of about 30 base pairs.

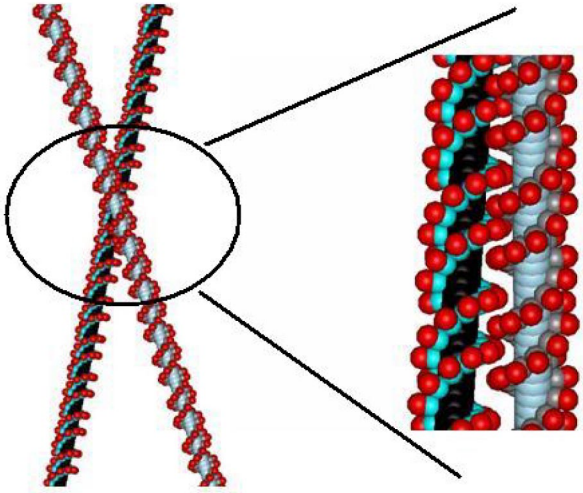

FIG. 4. A pair configuration with B-DNA molecules at close distance.

B. Intermolecular electrostatic potential and charge parameterization

Electrostatic interactions between polyelectrolytes are mediated by solvent, counterions, and salt; this makes their description a formidable task. According to the linearized Poisson-Boltzmann theory, screened Coulomb interactions between polyelectrolytes can be considered; thus, we can write for a pair of polyelectrolytes, say A and B,

$$U_{el}^{AB}(\mathbf{R}_{AB},\Omega_{AB})=\frac{e^2}{4\pi\varepsilon_0\varepsilon}\sum_{i=1}^{M_A}\zeta_{Ai}\sum_{j=1}^{M_B}\zeta_{Bj}\times\frac{\exp(-\kappa_D|\mathbf{r}_{Ai}-\mathbf{r}_{Bj}|)}{|\mathbf{r}_{Ai}-\mathbf{r}_{Bj}|},\tag{37}$$

where M_A (M_B) is the number of point charges in polyelectrolyte A (B), $e\zeta_{Ai}$ ($e\zeta_{Bj}$) is the ith (jth) charge on molecule A (B) and $\mathbf{r}_{Ai}$ ($\mathbf{r}_{Bj}$) is its position, ε is the dielectric permittivity of the solvent, and ε_0 that of vacuum. The parameter κ_D^{-1} is the so-called Debye screening length: $\kappa_D=(2Ie^2/\varepsilon_0\varepsilon k_BT)^{1/2}$, with the ionic strength $I=(10^{-3}/2\mathcal{N})\Sigma_\alpha z_\alpha^2\rho_\alpha^0$ (mol/l). Here $\mathcal{N}$ is the Avogadro number, z_α is the valence of α ions, and ρ_α^0 their concentration in bulk solution. Equation (37), which derives from a mean field treatment of the microion atmosphere, is more satisfactory in the case of monovalent microions, which are characterized by weak correlations; moreover, it is reasonable only for low values of the surface charge density on polyelectrolytes. Actually, at sufficient distance between the polymers it can still be used for higly charged polyelectrolytes, like DNA, provided that effective charges are used.

We have used Eq. (37) with effective charges defined according to the Manning theory.[31] So, the fraction of uncompensated charge is given by $\delta=1/|z|\xi$, with z equal to the counterion valence and the parameter $\xi(>1)$ defined as $\xi=e^2/(4\pi\varepsilon_0\varepsilon bk_BT)$, where b is the average charge spacing along the helix axis. For DNA, $b=(0.34\,\text{nm})/2$ (two phosphate groups with charge $-1e$ at distance 0.34 nm); for monovalent counterions in water at 25 °C, we obtain $\xi=4.2$ and $\delta=-0.24$.

As will be emphasized below, most configurations important for the emergence of chiral effects are characterized by the presence of small portions of the two polyectrolytes in close proximity; an example is shown in Fig. 4. The underlying assumptions of Eq. (37) are certainly inappropriate for interactions between charges located in such regions. With the purpose of taking into account this effect, while keeping the simple form necessary in the present framework, we have introduced a phenomenological hybrid potential, defined as follows. The electrostatic interaction between the ith charge (belonging to the A molecule) and the jth charge (in the B molecule) is assumed to have the Coulomb form if their distance (r_{ij}) is equal to the contact distance between the spheres bearing them (σ_{ij}). For distances larger than a given reference distance (r_0), the form of Eq. (37) is assumed, and a linear interpolation between the boundary values is taken for intermediate distances:

$$U_{ij}^{el}(\mathbf{r})=\begin{cases}\dfrac{e^2\zeta_{Ai}\zeta_{Bj}}{4\pi\varepsilon_0\varepsilon' r_{ij}}, & r_{ij}=\sigma_{ij}\\ \dfrac{e^2\zeta_{Ai}\zeta_{Bj}}{4\pi\varepsilon_0\varepsilon r_{ij}}\exp(-\kappa_D r_{ij}), & r_{ij}\geqslant r_0\\ \dfrac{U_{ij}^{el}(r_0)-U_{ij}^{el}(\sigma_{ij})}{r_0-\sigma_{ij}}(r_{ij}-\sigma_{ij}), & \sigma_{ij}>r_{ij}>r_0,\end{cases}\tag{38}$$

where the symbol ε' denotes an effective dielectric permittivity.

In our calculations for B-DNA, negative effective charges of magnitude δe have been located at the centers of the spheres representing phosphate groups in the model used for calculation of the chiral strength K_t (see Fig. 2).

V. COMPUTATIONAL METHODS

Calculation of the cholesteric pitch at given temperature, concentration, and ionic strength requires the following.

(i) Evaluation of integrals of the general form Eq. (35).
(ii) Calculation of order parameters.

As explained at the beginning of the preceding section, the first step is computationally demanding and calculations are only feasible if efficient algorithms and optimized procedures are used. Sensible choices have enabled a sizable reduction of computing time; calculation of the cholesteric pitch can be carried out in about a week on a 2000 MHz desktop computer. The strategy adopted will be outlined in the following. Calculation of the electrostatic contribution is the most time consuming step. It turns out to be convenient to store the electrostatic potential generated by molecule A on a grid; this allows a reduction of the number of computational steps, which in this way scale with the number of point charges in the polymer M, rather than with M^2. The need of a grid dense enough to ensure a satisfying degree of accuracy requires the storage of a huge array. In the case of the spherocylinder model, further advantage can be derived from the fact that integration on the γ_{AB} variable in Eq. (35) can be avoided. Namely, it can be shown that this integration has the effect of transforming the interaction between a point charge on molecule A and all the M discrete charges on molecule B in the interaction between the charge on A and M/m uniformly charged rings on B, where m is the number of charges which are located at the same height and distance from the cylinder axis. In this case each point of the grid represents the electrostatic potential integrated over the γ_{AB} angle.

According to Eq. (35), each term requires evaluation of sixfold integrals (fivefold in the case of the spherocylinders). The following integration order is employed:

$$\int_0^{\pi} d\vartheta_{AB} \sin\vartheta_{AB} \int_0^{2\pi} d\alpha_{AB} \int_0^{\pi} d\beta_{AB} \sin\beta_{AB} \times \int_0^{2\pi} d\phi_{AB} \int_0^{2\pi} d\gamma_{AB} \int_0^{\infty} dR_{AB} R_{AB}^2. \tag{39}$$

The innermost integral is over the R_{AB} variable; calculation of both electrostatic and steric interactions requires the identification of the closest approach distance R_{AB}^0 for all possible pair configurations. This has been accomplished by using the algorithm outlined in Appendix F. The number of checks, thus the computing time, can be significantly reduced in the following way: a first estimate of the closest approach distance is obtained for spherocylinders; once identified the large spheres in contact, a finer evaluation of the contact distance is performed on a restricted region of the helices. Typically, about 40 base pairs (bp) above and 40 below that corresponding to the large sphere are taken.

The excluded volume integral is analytical and is calculated between the integration limits 0 and R_{AB}^0. On the contrary, the electrostatic contribution has to be evaluated numerically. Because of the regular form of the integrand function, integration has been simply performed by using the trapezoidal rule.[32] In principle, calculations should be performed for R_{AB} ranging from R_{AB}^0 to infinity. In practice, the upper integration limit is given a finite value R_{AB}^1. For the calculation of contributions to order parameters and twist elastic constants we have assumed $R_{AB}^1 = R_{AB}^0 + 10\kappa_D^{-1}$, a value large enough to ensure that the integrand is negligible, and 60 integration points have been taken. In the case of contributions to the chiral strength K_t, the integration can be truncated at the value R_{AB}^1 equal to the closest approach distance between the spherocylinders enclosing the helices. Namely, for larger distances any chiral contribution is excluded for symmetry reasons, as mentioned above. Because of the smallness of the integration range, about some angstroms, it is sufficient to use only three integration points; this is a considerable advantage from the point of view of computing time.

The dependence of the integrand on the γ_{AB} angle is quite irregular for the helical particles, with sharp maxima, especially in the case of chiral contributions. A convenient quadrature algorithm has been devised in the Romberg method, which allows a nonuniform spacing of abscissas.[32] Integrals on the variables ϑ_{AB}, β_{AB}, α_{AB}, and ϕ_{AB} have been calculated using the Gauss algorithm, with integration points and weights determined by the zeros of the Legendre (for the ϑ_{AB} and β_{AB} variables) and the Chebyshev polynomials (for the α_{AB} and ϕ_{AB} variables).[32] For the ϕ_{AB} function, characterized by rapid oscillations between positive and negative values, 192 integration points have been used. On the contrary, for the ϑ_{AB} and β_{AB} variables only 12 points have been taken for calculating K_t, while 12 and 24 integration points, respectively, have been used to evaluate order parameters and elastic constant. Only a single value was sufficient for the α_{AB} angle because of the scarce dependence of the integrals upon this variable.

For given thermodynamic conditions, i.e., given the values of the variables (N,V,T), the equilibrium order parameters of the nematic phase are obtained by minimization of the approximate Helmholtz free energy F_{app} $(\langle D_{00}^2\rangle, \langle D_{00}^4\rangle, \ldots)$, as explained in Appendix G. In principle, the stability against phase separation should be checked; however, we have neglected this possibility, in view of our aim, which is not an accurate description of the features of the phase transition, but rather a reasonable estimate of order parameters, consistent with the choices made for the calculation of elastic constants and chiral strength. The free energy density has been minimized by using the Powell algorithm.[32]

VI. RESULTS AND DISCUSSION

Calculations have been performed for an aqueous solution of 130 bp fragments of B-DNA for which pitch values at different temperatures and ionic strengths are available.[8,9] Two temperatures, 286 and 323 K, and three different ionic strengths, $I = 0.1$, 0.2, and 0.5 mol/l have been considered. The concentration parameters used for the calculations are reported in Table II. It has to be mentioned that in evaluating the ionic strength counterions are also taken into account; so, in the absence of added salt we have $I = 0.1$ mol/l for a DNA concentration equal to 200 mg/ml. This point has to be taken into account when theoretical predictions are compared with experimental values, because in most cases the concentration of added salt is reported. The parameters required to specify

TABLE II. Characteristics of B-DNA solutions considered in our calculations.

Molecular weight (Dalton/130 bp)	Molecular volume ν_0 (nm^3)	Concentration (mg/ml)	Concentration (mol/l)	Solution volume for molecule ν (nm^3)
8.45×10^4	1.64×10^2	200	2.37×10^{-3}	7.0×10^2

TABLE IV. Order parameters calculated for the system of hard helices.

$\langle D^2_{00}\rangle$	0.89
$\langle D^4_{00}\rangle$	0.68
$\langle D^6_{00}\rangle$	0.43

the electrostatic interaction, i.e., the Debye screening constant κ_D and the fraction of uncompensated charge δ, are shown in Table III; they have been calculated at different temperatures and ionic strengths according to the expressions reported in Sec. IV B, by taking into account the temperature dependence of the dielectric constant of the solvent. We can see that, as a result of two compensating temperature effects, κ_D is practically the same at $T=286$ K and $T=323$ K. The dielectric constant ε' appearing in Eq. (38) has been given the value 2, while the reference distance $r_0=8$ Å has been assumed. This choice corresponds to a distance of 2 Å between the surface of the spheres representing phosphate groups.

We shall start considering a hypotetical DNA solution with purely steric interactions. Of course, this is not an appropriate model for a strong polyelectrolyte like DNA, but it will be useful to understand the results obtained for the more realistic model reported henceforth. Table IV displays the predicted order parameters; only values up to the sixth rank have been calculated since, as will be discussed in more detail below, truncation at this level of the summations in Eqs. (30)–(34) guarantees a good compromise between accuracy and computing speed. We can see that, under the conditions chosen for the calculations, a high order is predicted, with order parameters which decrease with increasing rank, but remain non-negligible even at the sixth rank. Table V reports the twist elastic constant K_{22}, the chiral strength K_t, and the cholesteric wave number q. Experimental order parameters and elastic constant are not available, but the values obtained for $\langle D^2_{00}\rangle$ and K_{22} appear reasonable for nematic solutions of stiff polymers.[23] The chiral strength K_t is negative, this means that steric interactions drive the formation of a right-handed cholesteric helix phase. This result, in agreement with the Straley theory, can be explained by considering that the cholesteric handedness is determined by configurations with molecules fitting into each other grooves (see Fig. 4). So, a right-handed cholesteric phase is predicted for the system of hard helices; the calculated cholesteric pitch, of about 35 μm, is about 15 times longer than the experimental value. Of course, no temperature dependence is predicted for the hard particle system, in clear contrast with experiment.

When the electrostatic interactions are switched on, the results reported in Tables VI and VII are obtained. We can see that electrostatic interactions have a very small effect on order parameters and elastic constants, which can be summarized by saying that the mesophase becomes slightly less ordered and more easily deformable. The reason is that electrostatic interactions between equally charged molecules oppose their parallel alignment.[23] On the contrary, electrostatic interactions have a dramatic effect on the cholesteric pitch, since they give a large contribution to the chiral strength K_t, opposite in sign to the steric term. This fact can be explained considering that electrostatic repulsions are maximized in those configurations which are favored for sterical reasons, because charges of equal sign lie at close distance. The electrostatic contribution to chiral strength largely overcomes the steric one; therefore a left-handed cholesteric phase is predicted, as experimentally observed. Also magnitude and temperature dependence of the pitch are in agreement with experiment, as appears from Fig. 5, where the theoretical predictions are compared with the experimental data reported in Ref. 9 (calculations and measurements refer to constant V and constant p, respectively, but this difference can be neglected for our system in the temperature range under investigation). The pitch lengthens with increasing temperature (the wave number q decreases), and the reason can be easily understood with the aid of Eq. (21). We should recall that the excluded volume contribution is independent of T. The electrostatic term at the denominator is small; so, as a first approximation, the temperature dependence of the denominator can be neglected. The ratio $K^{el}(T)/k_BT$ at the numerator decreases with increasing temperature. It follows that the relative weight of the steric contribution, which plays against a left-handed distortion of the nematic phase, becomes stronger at higher temperature. Tables VI and VII also report the values of order parameters, elastic constants, chiral strengths, and cholesteric wave numbers predicted at $T=323$ K and different ionic strengths. We can see that the electrostatic contribution to order parameters and elastic constants de-

TABLE III. Values of Debye screening length κ_D^{-1}, dielectric constant ε, and fraction of uncompensated charge fraction δ employed for calculations at different temperatures and ionic strengths.

	$T=286$ K			$T=323$ K		
I (mol/l)	0.1	0.2	0.5	0.1	0.2	0.5
κ_D^{-1} (nm)	0.94	0.66	0.42	0.93	0.66	0.42
ε[a]	82	82	82	70	70	70
δ	0.24	0.24	0.24	0.23	0.23	0.23

[a]Reference 44.

TABLE V. Elastic constant, chiral strength, and cholesteric wave number predicted for a system of hard helices

K_{22} (10^{-12} N)	K_t (10^{-6} N/m)	q (μm^{-1})
1.00	−0.21	0.21

creases with increasing ionic strength; thus, their values get even closer to those obtained for the system of hard helices. Also the electrostatic contribution to K_t decreases with increasing ionic strength, but it remains much larger then the steric contribution; as a result, a pitch variation of the about 30% is predicted on going from $I=0.1$ and $I=0.5$ mol/l, a result compatible with experimental data.[8,9]

It is now worth considering the effect of some assumptions and approximations used in our calculations. We shall start from the form of the electrostatic potential, Eq. (38). The introduction of the short-range Coulomb form is only a simple way to correct for the unrealistic screening of electrostatic interactions between regions of polymers at very short distance, and the dielectric constant ε' and reference distance r_0 should be taken as phenomenological parameters. The choice of their values affects the magnitude of the electrostatic contribution to K_t and its dependence on the ionic strength. The electrostatic contribution to the chiral strength at $T=323$ K and $I=0.2$ mol/l is equal to 1.50×10^{-6} N/m when calculated with $\varepsilon'=2$ and $r_0=8$ Å, and drops to 0.23×10^{-6} N/m if a purely screened Coulomb potential is used. This corresponds to a larger value of the predicted cholesteric pitch. Actually, ε' and r_0 could be taken as adjustable parameters to be determined from comparison with experimental data. The values obtained in this way would be very close to those we have taken in our calculations, on the basis of the reasonable assumptions that ε' should be similar to the dielectric constant of an organic medium, while r_0 should roughly correspond to a distance comparable with the dimension of a water molecule between the surfaces of two polyelectrolytes.

Another point to be checked is the effect of truncation in the summations appearing in Eqs. (30)–(34). The magnitude of terms decreases with increasing values of the indices j_A, j_B, and the series can be truncated at a finite value $j^{\max}$. This can be estimated by taking into account that (i) high accuracy is required because the integrands are oscillating functions with a number of zeroes increasing with rank, (ii) integrals are multiplied by coefficients that increase with rank. We have taken $j_A^{\max}=j_B^{\max}=6$; the contributions of different rank to twist elastic constant and chiral strength are shown in Tables VIII and IX. These are defined in such a way that

TABLE VI. Order parameters predicted for B-DNA solutions at different temperatures and ionic strengths.

	$T=286$ K	$T=323$ K		
I (mol/l)	0.2	0.1	0.2	0.5
$\langle D_{00}^2\rangle$	0.87	0.83	0.86	0.88
$\langle D_{00}^4\rangle$	0.62	0.55	0.63	0.65
$\langle D_{00}^6\rangle$	0.38	0.30	0.39	0.41

TABLE VII. Electrostatic contributions to elastic constants and chiral strengths (the steric contributions are reported in Table V), along with cholesteric wave numbers predicted for B-DNA solutions at different temperatures and ionic strengths.

	$T=286$ K	$T=323$ K		
I (mol/l)	0.2	0.1	0.2	0.5
K_{22} (10^{-12} N) electrostatic	−0.16	−0.16	−0.09	−0.01
K_t (10^{-6} N/m) electrostatic	1.79	1.71	1.50	1.41
q (μm^{-1})	−1.65	−1.80	−1.42	−1.20

$K_{22}=\Sigma_{j_Aj_B}K_{22}^{j_Aj_B}$ and $K_t=\Sigma_{j_A}K_t^{j_Aj_A}$. It appears that even the sixth rank contributions do not vanish; anyway the magnitude of terms decreases with rank, with a rate which depends on the kind of interaction and property. We can see that $K_{22}^{j_Aj_B}=K_{22}^{j_Bj_A}$; this result, which is in accordance with symmetry requirements, gives an indication on the accuracy of our calculations. The effect of truncation on twist elastic constant, chiral strength, and cholesteric wave number is shown in Table X. The non-negligible contribution of terms of rank higher than the second appears; namely, truncation at the second rank would give an error of about 100% on the predicted pitch.

VII. CONCLUSION

We have presented a molecular theory and a numerical procedure for the prediction of the pitch of chiral nematic solutions of stiff polyelectrolytes on the basis of their structure. A statistical-mechanics approach is used to connect phase properties and intermolecular interactions. The challenge is represented by the need of combining a coarse-grained description, imposed by the complexity of the system, with a sufficiently detailed representation of the chiral molecular properties at the origin of the macroscopic phenomenon.

To this purpose several approximations have been taken. First of all, the intermolecular interactions between polyelectrolytes have simply been described as the superposition of excluded volume and electrostatic contributions, with the

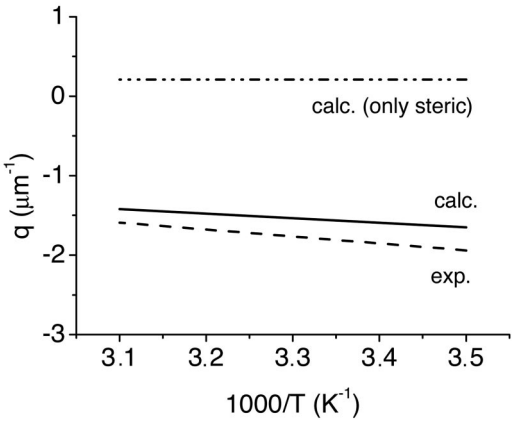

FIG. 5. Predicted cholesteric wave number as a function of the inverse temperature (solid line). Steric contribution and experimental results (Ref. 9) are shown by the dot-dashed and the dashed line, respectively.

TABLE VIII. Contributions of different rank to twist elastic constants; steric and electrostatic parts are reported. Values are calculated for the temperature $T=323$ K and the ionic strength $I=0.2$ mol/l.

$K_{22}^{j_A j_B}$ (10^{-12} N)	Steric	Electrostatic
K_{22}^{22}	2.27	−0.21
K_{22}^{24}	−0.95	0.13
K_{22}^{42}	−0.95	0.13
K_{22}^{44}	0.88	−0.19
K_{22}^{46}	−0.29	0.08
K_{22}^{64}	−0.30	0.08
K_{22}^{66}	0.34	−0.11

solvent regarded as a dielectric continuum and ions viewed as an ionic density which screens interactions between polymer charges. Moreover, charge interactions are simply treated at the level of the linearized Poisson–Boltzmann equation, with the use of renormalized charges, defined according to the Manning theory; a phenomenological correction has been introduced for nonscreened interactions between the small portions of polymers which are at very short distance. Effects of dielectric discontinuity have been fully neglected.

Calculations have been performed for 130 bp fragments of B-DNA by using a representation of the molecule as a regular rigid helix, so neglecting the deviations resulting from its flexibility and from the presence of different base pairs. Relaxing the approximations would certainly affect the numerical results; however, the picture emerging from our work should not change, since this depends on the physical ingredients present in the model.

In view of all the underlying approximations, we cannot expect a strict agreement between theoretical predictions and experimental data, but this is not our scope. We rather intend to provide some insight into the mechanisms, up to now unclear,[2] driving the formation of chiral nematic phases in solutions of polyelectrolytes, on the basis of a physically reasonable picture.

The main results of this work can be summarized in the following way.

(a) A model based on steric and electrostatic interactions between polyelectrolytes correctly predicts the organization of the cholesteric phase of B-DNA solutions. It provides and explanation for the observed left-handed helicity and for the temperature dependence of the pitch. We would like to stress here the importance of handedness in characterizing a cholesteric phase; this point seems sometimes to be undervalued, as though it were obvious. On the contrary, it has been seen experimentally and explained theoretically that the relation between cholesteric handedness and molecular structure is by no way simple, and small structural changes, sometimes occurring even in the same molecules as a consequence of a change of temperature or solvent, can be associated with pitch inversion.[33–35] Thus, sign is an important piece of information, which should always accompany the magnitude of the cholesteric pitch (although experimental determination might be a nontrivial task) and should not be ignored by theories for chiral nematic phases. By assuming reasonable values of the parameters describing electrostatic interactions, we predict for the cholesteric phase of B-DNA a pitch of a few micrometers, which increases with temperature, in agreement with experiment. As pointed out by some authors,[36] knowledge of the temperature dependence of the cholesteric pitch can be extremely useful for understanding the mechanism underlying this phenomenon of chirality amplification.

TABLE IX. Contributions of different rank to chiral strength; steric and electrostatic parts are reported. Values are calculated for the temperature $T=323$ K and the ionic strength $I=0.2$ mol/l.

$K_t^{j_A j_A}$ (10^{-6} N/m)	Steric	Electrostatic
K_t^{22}	−0.34	1.79
K_t^{44}	0.15	−0.38
K_t^{66}	−0.02	0.11

(b) Steric and electrostatic interactions are generally recognized as responsible for order and elastic properties of nematic solutions of stiff polyelectrolytes;[22,23,37] they also determine the alignment of proteins in nematic suspensions of filamentous viruses.[38,39] In both cases theoretical models based on the excluded volume representation of steric repulsions and a mean field description of electrostatic interactions between charged macromolecules have been shown to be able to explain the experimental data. Depending on the property under investigation, a greater or lesser detail is required in the description of molecular shape and charges. A simple representation of cylinders as uniformly charged rods is sufficient in the former case, while in the latter a realistic account of the protein structure and charge distribution is necessary. For the prediction of the cholesteric pitch, the chirality of both shape and charge pattern have to be taken into account.

(c) The shape chirality plays a crucial role in our description. Not only it is at the origin of the steric contribution to the cholesteric pitch, but it is also responsible for the emergence of the electrostatic contribution. Namely, as already pointed out by some authors,[40,41] chiral interactions would be washed out if averaged over a uniaxial distribution. Within our model it is the shape chirality which breaks the axial symmetry of the pair distribution function at short distances. It follows from this issue that chiral effects are determined by those pair configurations in which at least parts of the polymers lie at short distance, so that they can feel each others shape chirality.

(d) Calculations show that steric and electrostatic interactions have a counteracting effect in the case of B-DNA, which can be simply explained in the following way. Steric interactions would lead to the formation of a right-handed cholesteric phase, as a consequence of the good packing of helices fitting into each others grooves. However such configurations are also characterized by strong repulsions between the charges of polyelectrolytes; therefore they are unfavorable for electrostatic reasons. Since for B-DNA solutions the latter effect prevails, a left-handed cholesteric phase results.

TABLE X. Effect of truncation at different ranks on elastic constant, chiral strength, and cholesteric wave number, calculated at the temperature $T=323$ K and ionic strength $I=0.2$ mol/l.

Rank		2	4	6
K_{22} (10^{-12} N)	Steric	2.27	1.25	1.00
	Electrostatic	−0.21	−0.14	−0.1
K_t (10^{-6} N/m)	Steric	−0.34	−0.19	−0.21
	Electrostatic	1.79	1.39	1.50
q (μm^{-1})		−0.70	−1.08	−1.42

It is experimentally observed that the cholesteric pitch of B-DNA solutions is strongly affected by intercalators, groove binders, and polycations such as spermidine.[42,43] The presence of molecules interacting with DNA is likely to change the parameters of the molecular helix and influence the effective charges of DNA. So, according to our model a change of steric and electrostatic contributions to chiral strength and twist elastic constant is expected, with strong effects on the cholesteric pitch.

The approach developed in this work is not restricted to the case of DNA and could be applied to the chiral nematic phase of other polyelectrolytes. In particular, it would be interesting to investigate the case of G wires. On the basis of the results obtained for B-DNA, we can attempt an explanation for behavior of dG_4 aggregates mentioned in the Introduction: as for B-DNA, we expect that steric and electrostatic interactions should favor a right-handed and a left-handed cholesteric phase, respectively. However, unlike the case of B-DNA, the former contribution would prevail for dG_4. Such a picture should be checked with calculations; a practical difficulty derives form the uncertainty about the aggregate geometry, which has to be known with a certain level of detail for reliable predictions of the cholesteric phase organization.

ACKNOWLEDGMENTS

This work was supported by the Italian Ministry for University and Research (MIUR) through projects PRIN2003 (''Cristalli Liquidi e Macromolecole per Nanostrutture Organizzate'') and FIRB2001 (Grant No. RBNE01P4JF). The authors gratefully thank Professor Gian Piero Spada and Dr. Stefano Moro for stimulating discussions.

APPENDIX A: DERIVATION OF THE EXPRESSION FOR THE q DERIVATIVES OF THE DENSITY FUNCTION, EQS. (29a)–(29c)

By using the expansion of the density function, Eq. (27), the q derivatives in Eqs. (19) and (20) can be expressed as

$$\left(\frac{\partial\rho[\Omega_B,\chi(\mathbf{R}_B)]}{\partial q}\right)_{q=0} = \frac{1}{8\pi^2\nu}\sum_{j=0,2,4,\ldots}(2j+1)\langle D^j_{00}\rangle \times\sum_{l=-j}^{j}\left(\frac{d d^j_{l0}[\chi(\mathbf{R}_B)]}{d\chi}\right)_{\chi=0} D^j_{l0}(\Omega_B)Y_B, \tag{A1a}$$

$$\left(\frac{\partial^2\rho[\Omega_B,\chi(\mathbf{R}_B)]}{\partial q^2}\right)_{q=0} = \frac{1}{8\pi^2\nu}\sum_{j=0,2,4,\ldots}(2j+1)\langle D^j_{00}\rangle \times\sum_{l=-j}^{j}\left(\frac{d^2 d^j_{l0}[\chi(\mathbf{R}_B)]}{d\chi^2}\right)_{\chi=0} D^j_{l0}(\Omega_B)Y^2_B. \tag{A1b}$$

So, the χ derivatives of the reduced Wigner matrices have to be calculated. The following expression has been used:[28]

$$d^j_{l0}(\chi)=[(j+l)!(j-l)!j!j!]^{1/2}\sum_k(-1)^k \times\frac{\left(\cos\frac{\chi}{2}\right)^{2j-2k+l}\left(\sin\frac{\chi}{2}\right)^{2k-l}}{k!(j+l-k)!(j-k)!(-l+k)!} \tag{A2}$$

with the summation extended to all k values which allow non-negative values for the argument of the factorials.

By taking into account the condition on the factorials and those of vanishing exponents of the $\sin(\chi/2)$ powers in the χ derivatives of the reduced Wigner matrices, it follows:

$$\frac{d}{d\chi/2}d^j_{l,0}(\chi)=-\frac{1}{2}\sqrt{\frac{(j+1)!}{(j-1)!}}(\delta_{l,1}-\delta_{l,-1}), \tag{A3a}$$

$$\frac{d^2}{d(\chi/2)^2}d^j_{l,0}(\chi)=\frac{1}{4}\left[-2j(j+1)\delta_{l,0} + \sqrt{\frac{(j+2)!}{(j-2)!}}(\delta_{l,2}+\delta_{l,-2})\right], \tag{A3b}$$

where δ is the Kronecker symbol.

APPENDIX B: EXPRESSION FOR Y_B AND Y^2_B IN TERMS OF IRREDUCIBLE SPHERICAL COMPONENTS

The Cartesian component Y_B and its square can be expressed as the following linear combinations[28]

$$Y_B=(\tfrac{1}{2})^{1/2}i(T^{11}_B+T^{1-1}_B), \tag{B1a}$$

$$Y^2_B=-\frac{1}{\sqrt{3}}T^{00}_B-\frac{1}{\sqrt{6}}T^{20}_B-\frac{1}{2}T^{22}_B-\frac{1}{2}T^{2-2}_B, \tag{B1b}$$

where T^{1p} are the irreducible spherical components of the first rank tensor $\mathbf{R}_B$, while T^{00} and T^{2p} are the zeroth and second rank irreducible spherical components of the tensor $\mathbf{R}_B\otimes\mathbf{R}_B$. All tensors in this equation are expressed in the

laboratory frame; if instead a reference frame fixed on the A particle is considered (the corresponding tensor components will be hereafter indicated with the AB subscript), the following forms are obtained:

$$Y_B = \frac{i}{\sqrt{2}} \sum_{p=-1}^{1} [D^{1*}_{1p}(\Omega_A) + D^{1*}_{-1p}(\Omega_A)] T^{1p}_{AB}, \tag{B2a}$$

$$Y^2_B = -\frac{1}{\sqrt{3}} D^0_{00} T^{00}_{AB} + \sum_{p=-2}^{2} \left[-\frac{1}{\sqrt{6}} D^{2*}_{0p}(\Omega_A) - \frac{1}{2} D^{2*}_{2p}(\Omega_A) - \frac{1}{2} D^{2*}_{-2p}(\Omega_A) \right] T^{2p}_{AB}, \tag{B2b}$$

where D^j_{pq} are Wigner rotation matrices,[28] Ω_A are Euler angles defining the orientation of the A particle in the laboratory frame, and the star denotes the complex conjugate. The components T^{1p}_{AB}, T^{00}_{AB} e T^{2p}_{AB} have the following expressions in terms of spherical coordinates $\mathbf{R}_{AB} = (R_{AB}, \phi_{AB}, \vartheta_{AB})$:

$$T^{1\pm1}_{AB} = -(\tfrac{1}{2})^{1/2} (R_{AB} \sin\vartheta_{AB} \cos\phi_{AB} + \pm i R_{AB} \sin\vartheta_{AB} \sin\phi_{AB}), \tag{B3a}$$

$$T^{00}_{AB} = -\frac{1}{\sqrt{3}} R^2_{AB}, \tag{B3b}$$

$$T^{20}_{AB} = \frac{1}{\sqrt{6}} R^2_{AB} (-\sin^2\vartheta_{AB} + 2\cos^2\vartheta_{AB}), \tag{B3c}$$

$$T^{2\pm1}_{AB} = -R^2_{AB} \sin\vartheta_{AB} \cos\vartheta_{AB} (\cos\phi_{AB} \pm i \sin\phi_{AB}), \tag{B3d}$$

$$T^{2\pm2}_{AB} = R^2_{AB} \sin^2\vartheta_{AB} \left[\frac{1}{2} (\cos^2\phi_{AB} - \sin^2\phi_{AB}) \pm i \cos\phi_{AB} \sin\phi_{AB} \right]. \tag{B3e}$$

APPENDIX C: DERIVATION OF THE EXPRESSION FOR THE CHIRAL STRENGTH EQ. (31)

If the expansions, Eqs. (23) and (30a), for the density function and its first derivative are substituted into Eq. (20), and the expression for Y_B in terms of the irreducible spherical components, Eq. (B1a), is used, we obtain

$$K_t = -\frac{i}{4\sqrt{2}} \frac{1}{(8\pi^2 v)^2} \sum_{j_A=0,2,4,\ldots} (2j_A+1) \langle D^{j_A}_{00} \rangle \sum_{j_B=2,4,\ldots} (2j_B+1) \sqrt{\frac{(j_B+1)!}{(j_B-1)!}} \langle D^{j_B}_{00} \rangle \times \int d\mathbf{R}_B d\Omega_A d\Omega_B D^{j_A}_{00}(\Omega_A) [D^{j_B}_{10}(\Omega_B) - D^{j_B}_{-10}(\Omega_B)] (T^{11}_B + T^{1-1}_B) u(\mathbf{R}_{AB}, \Omega_{AB}). \tag{C1}$$

It is convenient to change the integration variables $R_B \to R_{AB}$, $\Omega_B \to \Omega_{AB}$ (see Scheme I); then, by using the addition theorem for Wigner rotation matrices,[28] Eq. (C1) becomes

$$K_t = -\frac{i}{4\sqrt{2}} \frac{1}{(8\pi^2 v)^2} \sum_{j_A=0,2,4,\ldots} (2j_A+1) \langle D^{j_A}_{00} \rangle \sum_{j_B=2,4,\ldots} (2j_B+1) \sqrt{\frac{(j_B+1)!}{(j_B-1)!}} \langle D^{j_B}_{00} \rangle \sum_{p=-1}^{1} \sum_{r=-j_B}^{j_B} \int d\Omega_A D^{j_A}_{00}(\Omega_A) \times [D^{j_B}_{1r}(\Omega_A) - D^{j_B}_{-1r}(\Omega_A)] [D^1_{1,p}{}^*(\Omega_A) + D^1_{-1,p}{}^*(\Omega_A)] \int d\Omega_{AB} D^{j_B}_{r0}(\Omega_{AB}) \int d\mathbf{R}_{AB} \mathbf{R}^p_{AB} u(\mathbf{R}_{AB}, \Omega_{AB}). \tag{C2}$$

By exploiting the orthogonality of Wigner matrices and using the coupled representation, the integral over Ω_A can be expressed as

$$\int d\Omega_A D^{j_A}_{00}(\Omega_A) [\mathrm{D}^{j_B}_{1r}(\Omega_A) - \mathrm{D}^{j_B}_{-1r}(\Omega_A)] [\mathrm{D}^1_{1,p}{}^*(\Omega_A) + \mathrm{D}^1_{-1,p}{}^*(\Omega_A)] = \frac{16\pi^2}{3} C^2(j_A, j_B, 1; 0, 1, 1) \delta_{p,r} (\delta_{p,1} - \delta_{p,-1}), \tag{C3}$$

where $C(j_A, j_B, 1; 0, 1, 1)$ are Clebsch–Gordan coefficients[28] and δ is the Kronecker symbol. If Eq. (C3) is substituted into Eq. (C2), after some algebraic manipulation the expression Eq. (30) is obtained for the chiral strength K_t.

APPENDIX D: DERIVATION OF THE EXPRESSION FOR THE TWIST ELASTIC CONSTANT EQS. (31)–(32)

If the expansions Eqs. (22) and (29b) for the density function and its second derivative are substituted into Eq. (20), we obtain

$$K_{22} = \frac{1}{8} \left(\frac{1}{8\pi^2 \nu} \right)^2 \sum_{j_A=0,2,4,\ldots} (2j_A+1) \langle \mathrm{D}^{j_A}_{00} \rangle \sum_{j_B=2,4,\ldots} (2j_B+1) \langle \mathrm{D}^{j_B}_{00} \rangle \int d\mathbf{R}_B \int d\Omega_A \int d\Omega_B \mathrm{D}^{j_A}_{00}(\Omega_A) \times \left\{ -2j_B(j_B+1) \mathrm{D}^{j_B}_{00}(\Omega_B) + \sqrt{\frac{(j_B+2)!}{(j_B-2)!}} [\mathrm{D}^{j_B}_{20}(\Omega_B) + \mathrm{D}^{j_B}_{-20}(\Omega_B)] \right\} Y^2_B u(\mathbf{R}_{AB}, \Omega_{AB}). \tag{D1}$$

It is convenient to change the integration variables $R_B \rightarrow R_{AB}$, $\Omega_B \rightarrow \Omega_{AB}$ (see Scheme I); then, by using the addition theorem for Wigner rotation matrices,[28] and the expression for Y_B^2 in terms of the irreducible spherical components, Eq. (B1b), Eq. (D1) becomes

$$K_{22}=\frac{1}{8}\left(\frac{1}{8\pi^2\nu}\right)^2 \sum_{j_A=0,2,4\ldots} (2j_A+1)\langle D_{00}^{j_A}\rangle \sum_{j_B=2,4,\ldots} (2j_B+1)\langle D_{00}^{j_B}\rangle \sum_{r=-j_B}^{j_B} \int d\Omega_A \int d\mathbf{R}_{AB} D_{00}^{j_A}(\Omega_A)$$
$$\times\left\{-2j_B(j_B+1)D_{0r}^{j_B}(\Omega_A)+\sqrt{\frac{(j_B+2)!}{(j_B-2)!}}[D_{2r}^{j_B}(\Omega_A)+D_{-2r}^{j_B}(\Omega_A)]\right\}\left\{-\frac{2}{\sqrt{12}}D_{00}^{0*}(\Omega_A)T_{AB}^{00}\right.$$
$$\left.+\sum_{p=-2}^{2}\left[-\frac{1}{\sqrt{6}}D_{0p}^{2*}(\Omega_A)-\frac{1}{2}D_{2p}^{2*}(\Omega_A)-\frac{1}{2}D_{-2p}^{2*}(\Omega_A)\right]T_{AB}^{2p}\right\}\int d\Omega_{AB} D_{r0}^{j_B}(\Omega_{AB})u(\mathbf{R}_{AB},\Omega_{AB}). \tag{D2}$$

The integrals in the Ω_A variables can be evaluated by exploiting the orthogonality of Wigner matrices and using the coupled representation. We can then write

$$\int d\Omega_A D_{00}^{j_A}(\Omega_A)\left\{-2j_B(j_B+1)D_{0r}^{j_B}(\Omega_A)+\sqrt{\frac{(j+2)!}{(j-2)!}}[D_{2r}^{j_B}(\Omega_A)+D_{-2r}^{j_B}(\Omega_A)]\right\}\left(-\frac{2}{\sqrt{12}}D_{00}^{0*}(\Omega_A)\right)$$
$$=\sqrt{\frac{4}{3}}8\pi^2 j_B(j_B+1)C^2(j_A,j_B,0;0,0,0), \tag{D3a}$$

$$\int d\Omega_A D_{00}^{j_A}(\Omega_A)\left\{-2j_B(j_B+1)D_{0r}^{j_B}(\Omega_A)+\sqrt{\frac{(j+2)!}{(j-2)!}}[D_{2r}^{j_B}(\Omega_A)+D_{-2r}^{j_B}(\Omega_A)]\right\}$$
$$\times\left(\sum_{p=-2}^{2}-\frac{1}{\sqrt{6}}D_{0p}^{2*}(\Omega_A)-\frac{1}{2}D_{2p}^{2*}(\Omega_A)-\frac{1}{2}D_{-2p}^{2*}(\Omega_A)\right)$$
$$=\frac{8}{5}\pi^2 C(j_A,j_B,2;0,r,r)\delta_{rp}\left\{+\sqrt{\frac{2}{3}}j_B(j_B+1)C(j_A,j_B,2;0,0,0)-\frac{1}{2}\sqrt{\frac{(j+2)!}{(j-2)!}}[C(j_A,j_B,2;0,2,2)\right.$$
$$\left.+C(j_A,j_B,2;0,-2,-2)]\right\}, \tag{D3b}$$

where $C(j_A,j_B,j;0,p,p)$ are Clebsch–Gordan coefficients. By substituting these espressions in Eq. (D2) and separating the terms containing the irreducible tensors of zeroth and second rank we obtain

$$[K_{22}]_{T^0}=\frac{1}{8}\left(\frac{1}{8\pi^2\nu}\right)^2 \sum_{j_A=0,2,4,\ldots} (2j_A+1)\langle \mathrm{D}_{00}^{j_A}\rangle \sum_{j_B=2,4,\ldots} (2j_B+1)\langle \mathrm{D}_{00}^{j_B}\rangle \int d\mathbf{R}_{AB}\int d\Omega_{AB}\delta_{j_A j_B}$$
$$\times\left\{-2j_B(j_B+1)C^2(j_A,j_B,0;0,0,0)8\pi^2 \mathrm{D}_{00}^{j_B}(\Omega_{AB})\left(-\frac{2}{\sqrt{12}}\right)T_{AB}^{00}u(\mathbf{R}_{AB},\Omega_{AB}),\right. \tag{D4a}$$

$$[K_{22}]_{T^2}=\frac{1}{8}\left(\frac{1}{8\pi^2\nu}\right)^2 \sum_{j_A=0,2,4,\ldots} (2j_A+1)\langle D_{00}^{j_A}\rangle \sum_{j_B=2,4,\ldots} (2j_B+1)\langle D_{00}^{j_B}\rangle \int d\mathbf{R}_{AB}\int d\Omega_{AB}$$
$$\times\left\{\sum_{p=-2}^{2}\frac{8\pi^2}{5}\left[-2j_B(j_B+1)C(j_A,j_B,2;0,0,0)C(j_A,j_B,2;0,p,p)\left(-\frac{1}{\sqrt{6}}\right)\right.\right.$$
$$\left.\left.-\sqrt{\frac{(j_B+2)!}{(j_B-2)!}}C(j_A,j_B,2;0,2,2)C(j_A,j_B2;0,p,p)\right]D_{p0}^{j_B}(\Omega_{AB})T_{AB}^{2p}\right\}u(\mathbf{R}_{AB},\Omega_{AB}). \tag{D4b}$$

If the summation over the p index is made explicit and the terms with $p=1$, -1, $p=2$, -2 are collected, Eqs. (32) are obtained.

APPENDIX E: DEMONSTRATION OF THE VANISHING CHIRAL ELECTROSTATIC CONTRIBUTION WHEN AVERAGED OVER A CYLINDRICALLY SYMMETRIC PAIR DISTRIBUTION

A generic integral in the electrostatic part of Eq. (30) can be written as

$$\int_0^\infty dR_{AB}R_{AB}^3\int_0^\pi d\vartheta_{AB}\sin\vartheta_{AB}\int_0^\pi d\beta_{AB}\sin\beta_{AB}d_{10}^j(\beta_{AB})\int_0^{2\pi}d\phi_{AB}\int_0^{2\pi}d\alpha_{AB}\sin(\alpha_{AB}-\phi_{AB})$$

$$\int_0^{2\pi}d\gamma_{AB}g_h(R_{AB},\phi_{AB},\vartheta_{AB},\alpha_{AB},\beta_{AB},\gamma_{AB})U_{el}(R_{AB},\phi_{AB},\vartheta_{AB},\alpha_{AB},\beta_{AB},\gamma_{AB}). \tag{E1}$$

For cylinders the correlation function g_h is independent of the angle γ_{AB}, so we can write

$$\int_0^\infty dR_{AB}R_{AB}^3\int_0^\pi d\vartheta_{AB}\sin\vartheta_{AB}\int_0^\pi d\beta_{AB}\sin\beta_{AB}d_{10}^j(\beta_{AB})\int_0^{2\pi}d\phi_{AB}\int_0^{2\pi}d\alpha_{AB}\sin(\alpha_{AB}-\phi_{AB})$$

$$\times g_h(R_{AB},\phi_{AB},Z_{AB},\alpha_{AB},\beta_{AB})\overline{U_{el}}(R_{AB},\phi_{AB},Z_{AB},\alpha_{AB},\beta_{AB}), \tag{E2}$$

where $\overline{U_{el}}(R_{AB},\phi_{AB},\vartheta_{AB},\alpha_{AB},\beta_{AB})$ represents the electrostatic interaction between charges on molecule A and charged rings on molecule B. After a change in the integration variables we obtain

$$\int_0^\infty dR_{AB}R_{AB}^3\int_0^\pi d\vartheta_{AB}\sin\vartheta_{AB}\int_0^\pi d\beta_{AB}\sin\beta_{AB}d_{10}^j(\beta_{AB})\int_0^{2\pi}d\phi_{AB}\int_0^{2\pi}d\alpha'_{AB}\sin(\alpha'_{AB})g_h(\alpha'_{AB}$$

$$+\phi_{AB},\beta_{AB},R_{AB},\vartheta_{AB},\phi_{AB})\overline{U_{el}}(\alpha'_{AB}+\phi_{AB},\beta_{AB},R_{AB},\vartheta_{AB},\phi_{AB}), \tag{E3}$$

which can be rearranged as

$$\int_0^\infty dR_{AB}R_{AB}^3\int_0^\pi d\vartheta_{AB}\sin\vartheta_{AB}\int_0^\pi d\beta_{AB}\sin\beta_{AB}d_{10}^j(\beta_{AB})\int_0^\pi d\alpha'_{AB}\sin(\alpha'_{AB})\int_0^{2\pi}d\phi_{AB}[g_h(\alpha'_{AB}+\phi_{AB},\beta_{AB},R_{AB},\vartheta_{AB},\phi_{AB})$$

$$\times\overline{U_{el}}(\alpha'_{AB}+\phi_{AB},\beta_{AB},R_{AB},\vartheta_{AB},\phi_{AB})-g_h(\alpha'_{AB}+\phi_{AB}+\pi,\beta_{AB},R_{AB},\vartheta_{AB},\phi_{AB})$$

$$\times\overline{U_{el}}(\alpha'_{AB}+\phi_{AB}+\pi,\beta_{AB},R_{AB},\vartheta_{AB},\phi_{AB})]. \tag{E4}$$

The correlation function g_h is independent of the ϕ_{AB} angle for two cylinders. Therefore integration over this variable is equivalent to calculation of the interaction between charged rings on molecule A with charged rings on molecule B. As a consequence the two integrals over the angle ϕ_{AB} are equal and their sum vanishes for any value of the variables α'_{AB}, β_{AB}, R_{AB}, and ϑ_{AB}.

APPENDIX F: ALGORITHM FOR THE CALCULATION OF THE CLOSEST APPROACH DISTANCE BETWEEN POLYELECTROLYTES

For given values of the variables α_{AB}, β_{AB}, γ_{AB}, ϑ_{AB}, and ϕ_{AB}, for each pair of spheres (i,j) the following calculations are performed:

(1) The distance between the two spheres (r_{ij}) is expressed in terms of the intermolecular vector $\mathbf{R}_{AB}$.

(2) Condition of contact is imposed: $r_{ij}=\sigma_{ij}$, with $\sigma_{ij}=(\sigma_i+\sigma_j)/2$, and the closest approach distance for the two spheres, R_{AB}^{ij}, is stored.

At the end of the cycle the largest value of R_{AB}^{ij} is taken as the closest approach distance R_{AB}^0.

APPENDIX G: MINIMIZATION OF THE FREE ENERGY

In practice, it is convenient to choose as variational parameters, in place of the order parameters, the expansion coefficients of the mean field potential $U^{mf}(\Omega_B)$. This is derived by imposing the stationarity condition to the free energy density:

$$\frac{\delta}{\delta\rho(\Omega_B)}\left\{\frac{f[\rho]}{k_BT}-\lambda\int d\Omega_B\rho(\Omega_B)\right\}=0, \tag{G1}$$

where λ is a Lagrange undetermined multiplier, introduced to take into account the normalization condition on the density function, Eq. (11). By calculating the functional derivative with the expressions for the free energy density, Eqs. (33) and (34), we can write

$$\rho(\Omega_B)=\frac{\exp\left\{-\dfrac{U^{mf}(\Omega_B)}{k_BT}\right\}}{\displaystyle\int d\Omega_B\exp\left\{-\frac{U^{mf}(\Omega_B)}{k_BT}\right\}} \tag{G2}$$

with the mean field potential

$$U^{mf}(\Omega_B)=\int d\mathbf{R}_{AB}d\Omega_A\rho(\Omega_A)u(\mathbf{R}_{AB},\Omega_{AB}). \tag{G3}$$

This can be expressed by an expansion on a basis of Wigner rotation matrices:

$$\frac{U^{mf}(\Omega_B)}{k_BT} = \sum_{j=2,4,\ldots} u_j D^j_{00}(\Omega_B). \tag{G4}$$

After substitution of this expression into Eq. (G2) we can rewrite the free energy density of the undeformed nematic phase, Eqs. (33) and (34), in the form

$$\frac{f(\{u_j\})}{k_BT} = -\frac{1}{v}\sum_{j=2,4,\ldots} u_j\langle D^j_{00}\rangle - \frac{1}{v}(\ln v - \ln Z) + \frac{1}{16\pi^2 v^2} \times \sum_{j_A=0,2,4,\ldots} (2j_A+1)\langle D^j_{00}\rangle^2 \times \int d\mathbf{R}_{AB} d\Omega_{AB} D^{j_A}_{00}(\Omega_{AB}) \frac{u(\mathbf{R}_{AB},\Omega_{AB})}{k_BT}, \tag{G5}$$

with the partition function

$$Z = \int d\Omega_B \exp\left\{-\sum_j u_j D^j_{00}(\Omega_B)\right\} \tag{G6}$$

and the order parameters

$$\langle D^j_{00}\rangle = \frac{\int d\Omega_B \exp\{-\Sigma_j u_j D^j_{00}(\Omega_B)\} D^j_{00}(\Omega_B)}{Z}. \tag{G7}$$

The free energy Eq. (G5), is thus expressed as a function of the coefficients $\{u_j\}$, and its equilibrium value can be obtained by minimizing with respect to these parameters. The use of the coefficients $\{u_j\}$ as variational parameters has a twofold advantage: (i) the expansion of the mean field potential, Eq. (G4), converges faster than that of the density function Eq. (22) and (ii) the parameters $\{u_j\}$ are unconstrained, unlike order parameters, which are restricted to the range $-1/2 \leqslant \langle D^j_{00}\rangle \leqslant 1$.

[1] R. Podgornik, H. H. Strey, and V. A. Parsegian, Curr. Opin. Colloid Interface Sci. **3**, 534 (1998).
[2] H. M. Harreis, C. N. Likos, and H. Löwen, Biophys. J. **84**, 3607 (2003).
[3] W. M. Gelbart, R. F. Bruinsma, P. A. Pincus, and V. A. Parsegian, Phys. Today **53**, 38 (2000).
[4] R. D. Kamien and S. Fraden, Biophys. J. **78**, 2189 (2000).
[5] F. Livolant, Physica A **176**, 117 (1991).
[6] F. Livolant and A. Leforestier, Prog. Polym. Sci. **21**, 115 (1996).
[7] Yu. M. Yevdokimov, S. G. Skurdin, and V. I. Salyanov, Liq. Cryst. **3**, 115 (1988).
[8] D. H. van Winkle, M. W. Davidson, W. X. Chen, and R. L. Rill, Macromolecules **23**, 4140 (1990).
[9] G. Proni, G. Gottarelli, P. Mariani, and G. P. Spada, Chem.-Eur. J. **6**, 3249 (2000).
[10] S. Fraden and Z. Dogic, Langmuir **16**, 7820 (2000).
[11] T. Sato, T. Kakihara, and A. Teramoto, Polymer **31**, 824 (1990).
[12] G. W. Vertogen and W. de Jeu, *Thermotropic Liquid Crystals. Fundamentals* (Springer, Berlin, 1988).
[13] K. B. Lipkowitz, Acc. Chem. Res. **33**, 555 (2000).
[14] A. Ferrarini, G. J. Moro, and P. L. Nordio, Phys. Rev. E **53**, 681 (1996); S. M. Todd, A. Ferrarini, and G. J. Moro, Phys. Chem. Chem. Phys. **3**, 5535 (2001).
[15] A. V. Emelayenko, M. A. Osipov, and D. A. Dunmur, Phys. Rev. E **62**, 2340 (2000).
[16] D. J. Earl and M. R. Wilson, J. Chem. Phys. **120**, 9679 (2004).
[17] J. P. Straley, Phys. Rev. A **14**, 1835 (1976).
[18] M. A. Osipov, in *Liquid Crystalline and Mesomorphic Polymers*, edited by V. Shibaev and L. Lam (Springer, Berlin, 1994).
[19] A. A. Kornyshev and S. Leikin, J. Chem. Phys. **107**, 3656 (1997); **108**, 7035(E) (1998).
[20] A. A. Kornyshev, S. Leikin, and S. V. Malinin, Eur. Phys. J. E **7**, 83 (2002); A. A. Kornyshev and S. Leikin, Phys. Rev. E **62**, 2576 (2000).
[21] L. Onsager, Ann. N.Y. Acad. Sci. **51**, 627 (1949).
[22] A. Stroobants, H. N. W. Lekkerkerker, and Th. Odijk, Macromolecules **19**, 2232 (1986).
[23] G. J. Vroege and Th. Odijk, J. Chem. Phys. **87**, 4223 (1987).
[24] M. D. Girardeau and R. M. Mazo, Adv. Chem. Phys. **24**, 187 (1973).
[25] D. A. McQuarrie, *Statistical Mechanics* (Harper & Row, New York, 1976).
[26] J. P. Hansen and I. R. Mc Donald, *Theory of Simple Liquids* (Academic, London, 1986).
[27] W. M. Gelbart and A. Ben-Shaul, J. Chem. Phys. **77**, 916 (1982).
[28] A. D. Varshalovich, N. A. Moskalev, and V. K. Kersonskii, *Quantum Theory of Angular Momentum* (World Scientific, New York, 1995).
[29] J. C. G. Montoro and J. L. F. Abascal, J. Chem. Phys. **103**, 8273 (1995); **109**, 6200 (1998); **114**, 4277 (2001).
[30] E. Allahyarov, G. Gompper, and H. Löwen, Phys. Rev. E **69**, 041904 (2004); E. Allahyarov, H. Löwen, and G. Gompper, *ibid.* **68**, 061903 (2003).
[31] G. Manning, J. Chem. Phys. **51**, 924 (1969).
[32] W. H. Press, B. P. Flannery, S. A. Teukolsky, and W. T. Vettering, *Numerical Recipes* (Cambridge University Press, Cambridge, 1986).
[33] A. di Matteo, S. M. Todd, G. Gottarelli, G. Solladié, V. E. Williams, R. P. Lemieux, A. Ferrarini, and G. P. Spada, J. Am. Chem. Soc. **123**, 7842 (2001).
[34] A. V. Emelayenko, Phys. Rev. E **67**, 031704 (2003).
[35] K. Yoshiba, A. Teramoto, N. Nakamura, and T. Sato, Macromolecules **36**, 2108 (2003).
[36] T. Sato, Y. Sato, Y. Umemura *et al.*, Macromolecules **26**, 4551 (1993).
[37] H. Graf and H. Löwen, Phys. Rev. E **59**, 1932 (1999).
[38] A. Ferrarini, J. Phys. Chem. B **107**, 7923 (2004).
[39] M. Zweckstetter, G. Hummer, and A. Bax, Biophys. J. **86**, 3444 (2004).
[40] A. B. Harris, R. D. Kamien, and T. C. Lubensky, Rev. Mod. Phys. **71**, 1745 (1999).
[41] S. A. Issaenko, A. B. Harris, and T. C. Lubensky, Phys. Rev. E **60**, 578 (1999); S. A. Issaenko and A. B. Harris, *ibid.* **61**, 2777 (2000).
[42] J. Pelta, D. Durand, J. Doucet, and F. Livolant, Biophys. J. **71**, 48 (1996).
[43] F. Cesare-Marincola, G. Saba, and A. Lai, Phys. Chem. Chem. Phys. **5**, 1678 (2003).
[44] R. C. Weast, *Handbook of Chemistry and Physics* (CRC, Cleveland, 1975).

Chapter 3

Chiral nematic phases of suspensions of rodlike viruses: left-handed phase helicity from a right-handed molecular helix

Chiral Nematic Phase of Suspensions of Rodlike Viruses: Left-Handed Phase Helicity from a Right-Handed Molecular Helix

Fabio Tombolato,[1] Alberta Ferrarini,[1] and Eric Grelet[2]

[1]*Dipartimento di Scienze Chimiche, Università di Padova, via Marzolo 1, 35131 Padova, Italy*

[2]*Centre de Recherche Paul Pascal, CNRS UPR 8641, Université Bordeaux 1, 115 Avenue Albert Schweitzer, 33600 Pessac, France*

(Received 13 April 2006; published 28 June 2006)

We report a study on charged, filamentous virus called M13, whose suspensions in water exhibit a chiral nematic (cholesteric) phase. In spite of the *right*-handed helicity of the virus, a *left*-handed phase helicity is found, with a cholesteric pitch which increases with temperature and ionic strength. Several sources of chirality can be devised in the system, ranging from the subnanometer to the micrometer length scale. Here an explanation is proposed for the microscopic origin of the cholesteric organization, which arises from the helical arrangement of coat proteins on the virus surface. The phase organization is explained as the result of the competition between contributions of opposite handedness, deriving from best packing of viral particles and electrostatic interparticle repulsions. This hypothesis is supported by calculations based on a coarse-grained representation of the virus.

DOI: 10.1103/PhysRevLett.96.258302 PACS numbers: 82.70.−y, 61.30.−v, 61.30.Cz, 61.30.St

Filamentous viruses are long and thin polyelectrolytes, made of a filament of nucleic acid, enclosed in a cylindrical wrapping of proteins (capsid). Features like monodispersity, some degree of stiffness, and the ability to organize in ordered structures motivate the strong interest they have raised as model systems for soft condensed matter physics [1]. Filamentous viruses form liquid crystalline phases [2], whose general behavior, i.e., transition properties and degree of order, can be explained in terms of a few parameters, as density, contour length (L), diameter (D), and surface charge density, according to theories developed for colloidal dispersions of rodlike polyelectrolytes that experience steric and screened electrostatic interactions [3,4]. Ion mediated electrostatic interactions between virions can also explain the bundling behavior of M13 and *fd* viruses [5]. However, the connection between chirality at the molecular scale and the macroscopic chiral organization of liquid crystalline phases is not understood, and the prediction of twist handedness and periodicity (cholesteric pitch) based on molecular features remains a challenge [6,7]. A puzzling example is provided by Pf1 and *fd* bacteriophages, which have similar structures and slightly different arrangements of proteins on the surface [8,9]: *fd* exhibits a cholesteric phase, whereas only a nematic phase has been found for Pf1 [10]. Another surprising result is the persistence of phase chirality when filamentous viruses are sterically stabilized with a thick coat of neutral polymer [7]. If, in general, the connection between molecular and phase chirality is not straightforward [6], the complexity becomes even higher in the case of viruses, due to the simultaneous presence of several levels of chirality. These range from the asymmetry of C_α atoms in the coat proteins, to the α-helical structure of these proteins and their helical arrangement on the virus surface. The observation of phase chirality for polymer stabilized viruses led to the suggestion of an influence of chiral fluctuations of the virus shape [7].

In this Letter, we shall focus on the cholesteric phase formed by M13 virus [8]. In addition to the dependence of the cholesteric pitch on temperature and ionic strength, we have measured the handedness, which is essential to fully characterize a chiral system, but is sometimes neglected. An explanation for the origin of the phase chirality is proposed and tested with the help of a molecular model.

M13 is a charged monodisperse bacteriophage with a high aspect ratio ($L = 880$ nm, $D = 6.6$ nm); M13 is semiflexible (persistence length $\xi = 2200$ nm) and has a molecular weight of $M_W = 1.64 \times 10^7$ g/mol [10]. M13 is formed by a single stranded DNA, around which about 2700 identical coat proteins are helicoidally wrapped following a fivefold rotation axis combined with a twofold screw axis [8,11]. The model of the M13 virus surface is shown in Fig. 1. A coat protein is formed by 50 amino acids, which provide M13 with a helical charge distribution; a net charge (carried by ionic amino acids) of $-2.4e$ per protein in water at $p\mathrm{H} = 8.2$ is estimated, i.e., a linear charge density of about $7e/\mathrm{nm}$ [8,12]. Taking advantage of the colloidal scale, which allows the visualization by fluorescence microscopy of a *single* rodlike virus, the cholesteric handedness of aqueous suspensions of M13 rods has been determined [13]. Relatively thick glass cells made by cover slip and slide have been used, with mylar spacers of different thicknesses (50 and 100 μm) to avoid boundary effects. Samples are equilibrated for 24 hours, which leads to planar cholesteric domains (cholesteric helix axis parallel to the incident light) with a size of a few hundred μm (Fig. 2). *Left*-handed supramolecular helicity is observed, whereas *right* handedness would be expected for purely sterical reasons. Indeed, a simple steric model, extended from Straley's work for the packing of helical structures

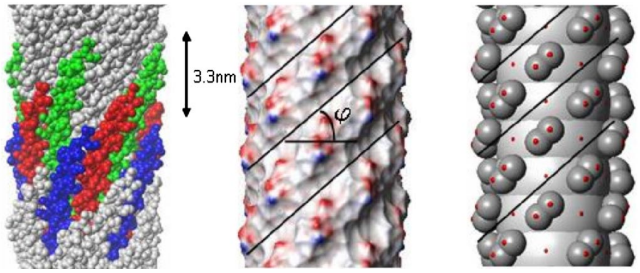

FIG. 1 (color online). Surface of the M13 virus [24], generated from the 2C0X.pdb capsid protein structure [8]. (a) All-atom representation; proteins with a given color are related by a fivefold symmetry axis. The distance of 3.3 nm corresponds to the periodicity, i.e., the separation between pairs of proteins with the same coordinates in the plane perpendicular to this symmetry axis. (b) Surface accessible to a sphere of radius 0.5 nm, rolling on the all-atom representation. Colors correspond to the electrostatic potential (red: negative, blue: positive). (c) Coarse-grained representation. Stacked light gray spheres (radius of 2.5 nm) represent the core of the virus, while dark gray spheres (radius of 0.6 nm) represent protruding amino acids (each sphere corresponds to 4 amino acids). Red spots correspond to point charges (located at 0.1 nm distance from the virus surface). Black lines show the tangent to a right-handed molecular helix identified on the virus surface ($\varphi \sim 41°$).

[14], shows that right-handed screws pack in a right-handed way for $\varphi < 45°$, whereas a left-handed superhelix is generated for $\varphi > 45°$ [Fig. 1(b)] [6]. The cholesteric pitch p, or correspondingly the wave number $q = 2\pi/p$, is defined as positive or negative, according to the right or left handedness of the cholesteric helix, respectively. Its experimental dependence upon temperature and ionic strength has also been measured (Table I), using polarization microscopy [7,10].

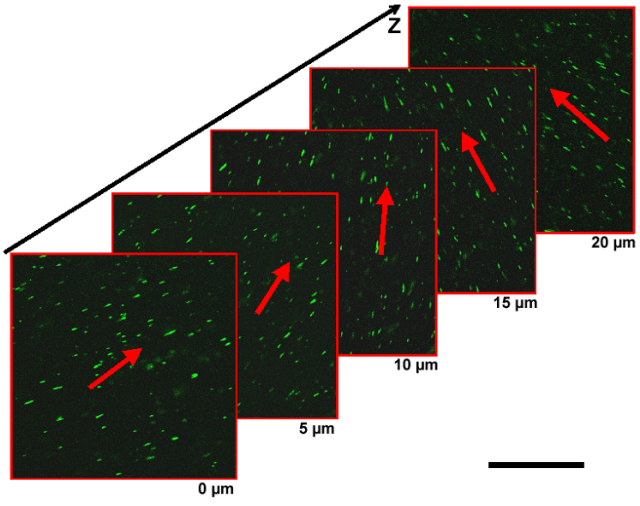

FIG. 2 (color online). Direct visualization by confocal fluorescence microscopy of the left-handed cholesteric helix in M13 virus suspensions, at concentration $C_{M13} = 49$ mg/ml and ionic strength $I = 110$ mM. The sequence of images follows the virus director, represented by red arrows, through the sample thickness (Z). One M13 virus out of 10^4 has been labeled with a fluorescein dye. The scale bar indicates 50 μm.

The cholesteric phase of M13 shares some similarity with that of right-handed B-DNA, where a left-handed helicity has been found by circular dichroism [15]. Recently, a model for the latter has been proposed, interpreting the cholesteric organization as the result of the competition of steric and electrostatic repulsion between charged helices [16]. The main responsibility for the chiral supramolecular organization has been ascribed to the shape chirality, which would also modulate the electrostatic repulsion between DNA molecules. We have hypothesized a similar mechanism for M13. Although not so clearly defined as in the case of DNA, a right-handed helix can be identified on the surface structure of M13 (Fig. 1). As a consequence of the geometrical arrangement of the major coat proteins and the mobility of their solvent exposed N-terminal portion [8,11], grooves as deep as about 1 nm appear on the virus surface. Their presence and dimension is supported by x-ray data, showing that pentapeptides can be inserted between two adjacent α helices on the surface of the virion [17]. Since each protein bears some ionic charges, the chiral arrangement of the coat implies a helical charge distribution (Fig. 1). The possibility that shape and charge chirality deriving from the protein arrangement can be responsible for the cholesteric organization has been explored with a theoretical approach. According to the continuum elastic theory, the Frank free energy density f can be expanded in a power series of the twist deformation of the mesophase director: $f \approx f^u + K_t q + \frac{1}{2} K_{22} q^2$, where f^u is the free energy density of the undeformed nematic phase [18]. The equilibrium wave number is obtained by minimization of the free energy: $q = -K_t/K_{22}$, with the chiral strength $K_t = (\partial f/\partial q)_{q=0}$ and the twist elastic constant $K_{22} = (\partial^2 f/\partial q^2)_{q=0}$. K_t accounts for the intrinsic propensity to twist deformations, as a consequence of the chirality of intermolecular interactions; it has opposite signs for enantiomers, and vanishes in the absence of molecular chirality. K_{22} describes the resistance of the system to the director deformation. A molecular expression for the free energy has been developed with a pair potential consisting of steric repulsions and electrostatic interactions between virus particles in an ionic water solution [16]. The former are treated at the level of the second virial term, while the latter have been included by averaging over the hard-particle pair distribution function, according to the mean field approximation. The excess Helmholtz free energy of a suspension of N virus particles can then be expressed as:

$$F^{\mathrm{ex}} = \frac{1}{2} \int d\mathbf{R}_A d\mathbf{R}_B d\Omega_A d\Omega_B \rho(\Omega_A, \mathbf{R}_A) \times \rho(\Omega_B, \mathbf{R}_B) u(\mathbf{R}_{AB}, \Omega_{AB}), \quad (1)$$

where $\mathbf{R}$ and Ω denote position and orientation of a virion

TABLE I. Order parameter ($\overline{P_2}$), twist elastic constant (K_{22}), steric (K_t^h), and electrostatic (K_t^{el}) contributions to the chiral strength, and cholesteric wave number: q^{calc} (calculated), q_h^{calc} (calculated for purely hard-core interactions), and q^{exp} (experimental). T is temperature and I the ionic strength. The virus concentration is $C_{\mathrm{M13}} = 53$ mg/ml.

T (K)	I (mM)	$\overline{P_2}$	K_{22} (pN)	K_t^h (nN/m)	K_t^{el} (nN/m)	q^{exp} ($\mu\mathrm{m}^{-1}$)	q^{calc} ($\mu\mathrm{m}^{-1}$)	q_h^{calc} ($\mu\mathrm{m}^{-1}$)
296	30	0.94	0.9	−3.2	+83	−0.143	−0.09	+0.003
296	110	0.95	1.1	−3.2	+81	−0.097	−0.07	+0.003
323	110	0.95	1.2	−3.5	+81	−0.066	−0.06	+0.003

and $\rho(\Omega, \mathbf{R})$ is the single particle density function, which satisfies the normalization condition $\int d\mathbf{R} d\Omega \rho(\mathbf{R}, \Omega) = N$. The interaction between virions is described by the function

$$u(\mathbf{R}_{AB}, \Omega_{AB}) = -k_B T e_{AB}^h(\mathbf{R}_{AB}, \Omega_{AB}) + g_h(\mathbf{R}_{AB}, \Omega_{AB}) U^{\mathrm{el}}(\mathbf{R}_{AB}, \Omega_{AB}), \quad (2)$$

were e_{AB}^h is the Mayer function for a pair of hard particles [19], g_h is the hard-particle pair distribution function, and $U^{\mathrm{el}}(\mathbf{R}_{AB}, \Omega_{AB})$ is the electrostatic potential between a pair of polyelectrolytes. The density function $\rho(\Omega, \mathbf{R})$ can be written in terms of the orientation of the local director in $\mathbf{R}$, thus of the twist wave number q, and of orientational order parameters with respect to the director, $\overline{P_J}$ (even J). It follows that the free energy can in turn be expressed as a function of twist deformation and orientational order parameters. In view of their large length scale, twist deformations can be assumed to negligibly disturb the local order; $\overline{P_J}$ values can then be obtained by minimizing the free energy of the undeformed nematic phase. Finally, chiral strength and twist elastic constant are evaluated as derivatives of the free energy density with respect to the twist deformation.

A coarse-grained representation of the virus structure has been used to parametrize interactions. Starting from atomic coordinates [8], the model shown in Fig. 1(c) has been built. Three negative point charges have been placed on each protein. Two of them, located on outer spheres, roughly correspond to protruding ionic amino acids, while the third, placed within the groove, accounts for the excess of electron density on solvent exposed oxygen atoms in the protein backbone. For simplicity, the three charges have been assumed to be equivalent. The electrostatic interaction between a pair of virus particles can be approximated as the superposition of screened Coulomb interactions between their (renormalized) charges [20]. However, this is not appropriate for charges at short distance and solvent confined between close surfaces. At the contact distance between the spheres bearing a pair of interacting charges, the electrostatic potential seems better expressed by the Coulomb law in a nonpolar medium. To keep calculations feasible, a simple choice has been made: the electrostatic potential between two charges is assumed to have the Coulomb form at the contact separation and the screened Coulomb form beyond a reference distance, r_0; for intermediate distances, an interpolation between the boundary values is performed [16]. In view of the dimension of the grooves, r_0 has been given the value of 1 nm. The integrals over mutual orientations and distances of a pair of virions, necessary for obtaining the free energy and its derivatives, are calculated numerically. The full virion is considered and, given the form of the Mayer function, the excluded volume contribution only needs to be evaluated over overlapping configurations. In the electrostatic part, the pair distribution function is simply chosen equal to the step function: $g_h = 0$ or $g_h = 1$, for overlapping and nonoverlapping pair configurations, respectively; thus, electrostatic integrals are evaluated over nonoverlapping pair configurations. Computing time is significantly reduced by exploiting symmetries and introducing cutoff distances for the screened electrostatic interactions. Moreover, a simplified virus model has been adopted to calculate order parameters and twist elastic constant, which are scarcely affected by the short length scale features of the system: a virus has been represented as a rod of fused spheres, while keeping the charge distribution shown in Fig. 1(c).

Experimental and theoretical results are collected in Table I. Electrostatic interactions have a small effect on order parameters and twist elastic constant, which substantially are of steric nature. High $\overline{P_2}$ values are obtained, slightly larger than those determined for M13 under analogous conditions by birefringence measurements [21]. Experimental K_{22} data are available for *fd* virus; $K_{22} \sim 0.4$ pN has been reported from measurements of the critical magnetic field [10], which is about half the predicted value. Electrostatic (K_t^{el}) and steric (K_t^h) contributions to the chiral strength have *opposite* sign; the latter yields a right-handed supramolecular helix which, in agreement with Straley's model [14], provides the best packing of a system of hard right-handed helices like those outlined in Fig. 1. Electrostatic interactions give an antagonist contribution to the chiral strength, which can be interpreted as the result of the repulsions arising when helices fit into each other's grooves. Indeed, electrostatic repulsions are maximized in those configurations which are favored for sterical reasons, because charges of equal sign lie at close distance. The electrostatic term largely overcomes the steric one; therefore, a left-handed cholesteric phase is predicted, as experimentally observed. The electrostatic contributions to the free energy and to its derivatives scale as Q^2, the square of point charges. The values reported in

Table I have been obtained with $Q = -0.3e$, i.e., one fourth of the bare charges. This corresponds to a degree of charge compensation which is a little lower than predictions of the Manning theory [22]; however, the model of a uniform line charge distribution can only yield very approximate estimates for the system under investigation. The cholesteric wave number, $q = -(K_t^{\mathrm{el}} + K_t^h)/K_{22}$, is also reported in Table I. In agreement with experiment, the cholesteric pitch is predicted to increase with increasing temperature and ionic strength. In the case of a purely entropic mechanism the pitch would be independent not only of ionic strength, but also of temperature, since elastic constant and chiral strength would have the same linear dependence of T.

In summary, we have experimentally investigated the cholesteric phase of M13 virus and we have shown that the main findings can be explained by a model accounting for steric and electrostatic interactions between rigid chiral rods. The model relies on a realistic representation, although at a coarse-grain level, of what are deemed to be the relevant molecular features for chirality amplification: the shape chirality deriving from the arrangement of the coat proteins, and the associated helical distribution of charges. The predicted pitch and handedness depend on the structure of the coat proteins, and are expected to change with it. It must be mentioned that in the model presented here some simplifying assumptions have been taken. Beside the simple treatment of electrostatics, a major approximation is the neglect of virus flexibility, which is expected to affect order and elastic properties of the system and to introduce its own dependence on temperature and ionic strength. Moreover, changes in the physicochemical conditions are likely to bring about modifications in structure and arrangement of coat proteins, which are not accounted for by our model. This work singles out a general feature in the phenomenon of chirality amplification, i.e., *the simultaneous presence of oppositely handed contributions at the molecular scale* [6,23]. Only in the particular and rather unrealistic case of hard-core interactions between screwlike molecules, a simple link from molecular to phase helicity exists [14].

E. G. warmly thanks G. Gourges and P. Sirand-Pugnet from I.N.R.A. for their assistance in the preparation of the viruses. F. T. and A. F. acknowledge financial support by MIUR (No. PRIN 2005).

[1] Z. Dogic and S. Fraden, in *Soft Matter*, edited by G. Gompper and M. Schick (Wiley-VCH, Weinheim, 2006), Vol. 2.
[2] J. Lapointe and D. A. Marvin, Mol. Cryst. Liq. Cryst. **19**, 269 (1973).
[3] L. Onsager, Ann. N.Y. Acad. Sci. **51**, 627 (1949).
[4] A. Stroobants *et al.*, Macromolecules **19**, 2232 (1986).
[5] A. P. Lyubartsev *et al.*, Phys. Rev. Lett. **81**, 5465 (1998).
[6] A. B. Harris *et al.*, Rev. Mod. Phys. **71**, 1745 (1999).
[7] E. Grelet and S. Fraden, Phys. Rev. Lett. **90**, 198302 (2003).
[8] D. A. Marvin *et al.*, J. Mol. Biol. **355**, 294 (2006). M13 differs from *fd* for replacement of a negatively charged Aspartate with a neutral Asparagine in the coat protein.
[9] D. S. Thiriot *et al.*, J. Mol. Biol. **341**, 869 (2004).
[10] Z. Dogic and S. Fraden, Langmuir **16**, 7820 (2000).
[11] S. Bhattacharjee *et al.*, Biophys. J. **61**, 725 (1992); A. C. Zeri *et al.*, Proc. Natl. Acad. Sci. U.S.A. **100**, 6458 (2003); L. C. Welsh *et al.*, Macromolecules **29**, 7075 (1996).
[12] K. Zimmermann *et al.*, J. Biol. Chem. **261**, 1653 (1986).
[13] M13 was grown using the XL1-Blue strain of *E. Coli* as the host bacteria and purified following standard biological protocols [1]. To vary the ionic strength, viruses have been dialyzed against a 20 m*M* TRIS-HCl buffer at $p\mathrm{H} = 8.2$ with an adjusted amount of NaCl. Virus concentrations have been measured by spectrophotometry. For fluorescence microscopy experiments, M13 has been labeled with fluorescein isothiocyanate (FITC).
[14] J. P. Straley, Phys. Rev. A **14**, 1835 (1976).
[15] D. H. Van Winkle *et al.*, Macromolecules **23**, 4140 (1990); F. Livolant and A. Leforestier, Prog. Polym. Sci. **21**, 1115 (1996).
[16] F. Tombolato and A. Ferrarini, J. Chem. Phys. **122**, 054908 (2005).
[17] G. Kishchenko *et al.*, J. Mol. Biol. **241**, 208 (1994).
[18] P. G. de Gennes and J. Prost, *The Physics of Liquid Crystals* (Clarendon, Oxford, 1993).
[19] J. P. Hansen and I. R. McDonald, *Theory of Simple Liquids* (Academic, New York, 1986).
[20] J.-P. Hansen and H. Löwen, Ann. Rev. Phys. Chem. **51**, 209 (2000).
[21] K. R. Purdy and S. Fraden, Phys. Rev. E **70**, 061703 (2004).
[22] G. Manning, J. Chem. Phys. **51**, 924 (1969).
[23] R. L. B. Selinger *et al.*, Phys. Rev. Lett. **93**, 158103 (2004).
[24] Surface generated using DS ViewerPro 5.0 software.

Chapter 4

Chapter 4 Model for the chiral nematic phase of semiflexible polymers

4.1 Introduction

In chapter 3 the chiral and elastic properties of the cholesteric phase of suspensions of the M13 virus were explained by a model based on the continuum elastic theory and the classical density functional theory, to connect intermolecular interactions (on the nanometer scale) and director deformations (on a micrometer scale). A crucial point of the model is the description of pair interactions in terms of steric repulsions between hard particles, treated at the excluded volume level, and electrostatic interactions, introduced according to the Poisson-Boltzmann theory. Calculations were performed with a coarse grained representation of the virus and good predictions of handedness and pitch of the chiral nematic phase were obtained. In this model viruses are represented as rigid particles and their flexibility, which clearly appears from the electron micrograph image shown in fig. 4.1, is completely neglected.

Figure 4.1 Electron micrograph image of the *fd* virus (from http://www.rowland.harvard.edu/ rjf/dogic/ fdvirus.php)

Recently Purdy and Fraden found that the flexibility has to be invoked to explain the features of the isotropic-nematic transition of suspensions of *fd* and M13 viruses [Purdy, 2004]. Fraden and Grelet, studying the concentration dependence of the isotropic-nematic transition exhibited by suspensions of *fd* viruses coated with PEG[1] at different ionic strengths, suggested that the virus flexibility could be responsible for the formation of the cholesteric phase [Grelet, 2003]. Their hypothesis is based on the consideration that viruses grafted with polymers cannot 'feel' the details of each other surface, therefore the phase chirality cannot originate from short-range electrostatic and steric interactions, which are sensitive to such details. The authors proposed that thermal fluctuations can induce 'supra-helical' structures in the shape of the viruses. The intrinsic chirality of the virus would bias the handedness of these helices and the enantiomeric excess would be at the origin of the cholesteric phase. Recently, the same interpretation was proposed by other authors who investigated the chiral nematic phase of several viruses belonging to the same family as *fd* and M13 [Tomar, 2007]. Up to now,

[1] PEG: polyethylene glycol.

however, the role of chiral fluctuations in the shape of viruses has remained at the level of hypothesis. Indeed, it has never been characterised experimentally and it is not even clear what, in the virus structure, should be responsible for it. Interest on filamentous viruses as templates in nanomaterial science has recently stimulated the study of the flexibility of M13 by single molecule experiments [Khalil, 2007], but the information obtained in this way does not go beyond the level of the isotropic bending elasticity. Furthermore, it is not obvious whether chiral shape fluctuations, even though present, would be able to induce the chiral organization of the nematic phase.

To explore this possibility, we have developed a theoretical approach that couples a Monte Carlo sampling of conformations of the virus, described as a worm-like polymer, to a mean field model for its orientational distribution in the chiral nematic phase. In the next section, a form for the single molecule distribution function of semiflexible polymers in nematics will be proposed. Then, expressions for the chiral and elastic parameters of the cholesteric phase will be derived, in terms of the virus elasticity and of the orienting mean field. In the fourth section the model for the virus elasticity will be presented. Then a coarse grained representation of the virus will be introduced and the methods employed for the calculations will be summarised. The results obtained for some selected cases will be reported and discussed in the seventh section; finally conclusions and future outlooks will be presented.

4.2 Orientational distribution function for a semiflexible polymer in the nematic phase

The statistical thermodynamic model developed in this thesis to describe the properties of a liquid crystal solution of semiflexible polymers starts from the expression for the single molecule orientational distribution function. The case of the nematic phase will be considered first, than the derivation will be extended to the cholesteric phase.

Let us consider a nematic solution of N polymers at constant volume V and temperature T. A polymer is approximated as a sequence of M segments of fixed length l (see fig. 4.2). We define a laboratory frame (LAB), with the Z axis parallel to the director **n**, and M local frames, (i), each having the z_i axis parallel to a segment of the polymer. The vector $\boldsymbol{r_i}$ defines the position of centre of mass of i-th segment in the LAB frame; the orientation of the i-th segment segment is specified by the unit vector $\boldsymbol{t_i}$.

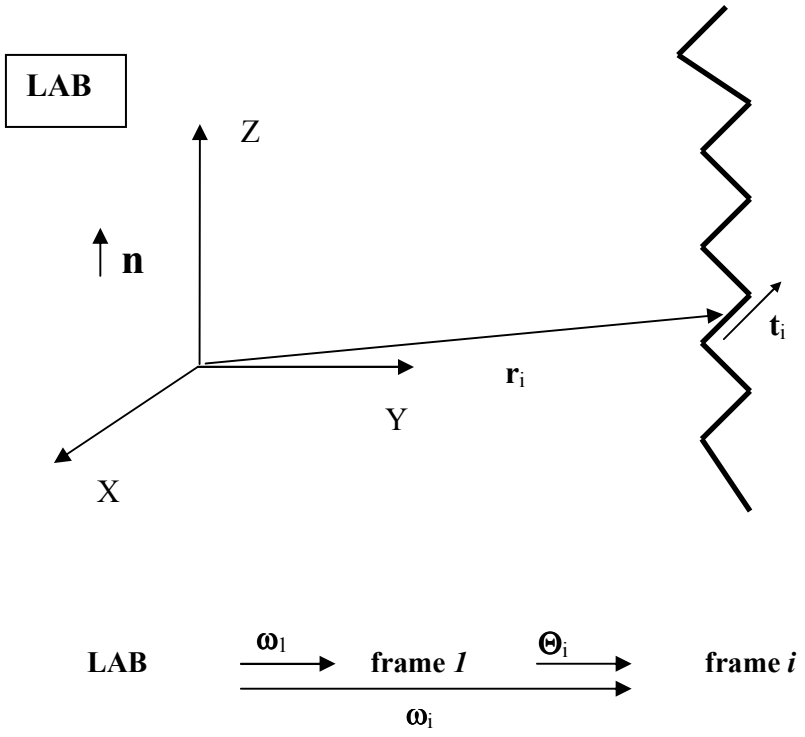

Figure 4.2 Reference systems and variables used to define conformation and orientation of a semiflexible polymer in the nematic phase.

The conformation of a polymer is defined by the set of variables $\boldsymbol{\omega} \equiv (\omega_1,...,\omega_M)$ and $\mathbf{r} \equiv (\mathbf{r}_1,...\mathbf{r}_M)$, that specify orientation and position, respectively, of each segment in the LAB frame. A (uniform) nematic phase is translationally invariant, therefore the average properties do not depend on the translational degrees of freedom. We can define the orientational distribution function of the polymer:

$$p(\boldsymbol{\omega}) = \frac{\exp\left[-U(\boldsymbol{\omega})/k_B T\right]}{\int d\boldsymbol{\omega} \exp\left[-U(\boldsymbol{\omega})/k_B T\right]} \tag{4.1}$$

where k_B is the Boltzmann constant and $U(\boldsymbol{\omega})$ can be seen as a potential accounting for the anisotropy of interactions in the nematic phase and the internal forces which oppose polymer deformations. The function $p(\boldsymbol{\omega})$ is normalized as:

$$\int d\boldsymbol{\omega} p(\boldsymbol{\omega}) = 1 \tag{4.2}$$

It is convenient to introduce the set of internal variables $\boldsymbol{\Theta} \equiv (\boldsymbol{\Theta}_2,...,\boldsymbol{\Theta}_M)$, which specify the polymer conformation. The orientation of *i*-th segment in the LAB frame can then be specified by ω_1, the orientation of segment 1 in the LAB frame, and the set of angles $\boldsymbol{\Theta}_i$, each defining the orientation of *i* local frame in the (*i*-1) frame (see fig. 4.2). Using these variables, the potential $U(\boldsymbol{\omega})$ can be approximated as the sum of two contributions:

$$U(\boldsymbol{\omega}) \equiv U(\boldsymbol{\Theta}, \omega_1) \approx U^{bend}(\boldsymbol{\Theta}) + U^{or}(\boldsymbol{\Theta}, \omega_1) \tag{4.3}$$

The former, $U^{bend}(\boldsymbol{\Theta})$, is the *bending elastic energy* of the polymer; it depends only on the internal variables $\boldsymbol{\Theta}$ and accounts for the energetic cost associated with polymer bending. This term will be discussed in detail in section 4.3. The second term, $U^{or}(\boldsymbol{\Theta}, \omega_1)$, is the potential of mean torque experienced by a polymer in the conformation specified by the $\boldsymbol{\Theta}$ angles, with the first segment in the orientation ω_1, by virtue of the anisotropy of the interactions with the environment. In principle, this contribution could be calculated starting from pair interactions between polymers, as done in the model for rigid polymers which has been adopted in chapters 2 and 3. The polymer flexibility, however, introduces a dependence on the conformation that makes this approach unfeasible. So, we have adopted a simplified treatment, in the spirit of the Maier-Saupe theory for the orientational order in nematics [Maier, 1959], which assumes for the orienting potential experienced by rigid, axially symmetric molecules the simple form: $U^{or} = -a\,k_B T P_2(\mathbf{t}\cdot\mathbf{n})$, where P_2 is the second Legendre polynomial[2] and $\mathbf{t}$ is a unit vector, parallel to the molecular axis. The adimensional parameter a defines the strength of the orienting field and vanishes in the isotropic phase. The Maier-Saupe form can be extended to flexible molecules, represented as assemblies of rigid segments [Emsley, 1982; Ferrarini, 1995]; thus, for our model polymer we can write:

$$U^{or}(\boldsymbol{\Theta}, \omega_1) = -a\,k_B T \sum_{i=1}^{M} P_2(\mathbf{t}_i \cdot \mathbf{n}) \tag{4.4}$$

where the sum is extended to all the segments. For positive values of the orienting strength *a*, the minimum of the potential of mean torque, U^{or}, corresponds to the perfectly aligned polymer, with all segments parallel to the director.

Once obtained an expression for the orientational distribution function, the average value of the arbitrary function $g(\boldsymbol{\Theta}, \omega_1)$ in the nematic phase can be calculated as :

$$\overline{g} = \frac{\int d\boldsymbol{\Theta}\, d\omega_1\; g(\boldsymbol{\Theta}, \omega_1) \exp\left[-U(\boldsymbol{\Theta}, \omega_1)/k_B T\right]}{\int d\boldsymbol{\Theta}\, d\omega_1\; \exp\left[-U(\boldsymbol{\Theta}, \omega_1)/k_B T\right]} \tag{4.5}$$

[2] $P_2(x) = 1.5x^2 - 0.5$

In the cholesteric phase, the director rotates around a perpendicular axis in helical way. The director field $\mathbf{n} = \mathbf{n}(\mathbf{R})$ has to be introduced and in principle the space dependence of properties should be taken into account. However, if the length-scale of the twist deformation is much longer than the molecular dimension, which is the general case of cholesterics, the orientational distribution with respect to the local director can be assumed to be the same as in the nematic phase. Therefore the expressions which have been derived for nematics can be extended to cholesterics, by only taking into account the space dependence of the director. This can be simply introduced in a parameteric way, through the wavenumber q (the corresponding pitch being $p=2\pi/q$).

4.3 Statistical thermodynamic derivation of chiral and elastic parameters of the cholesteric phase

According to the Frank-Oseen elastic theory, the free energy density, f, of a nematic phase in the presence of small distortions of the director field can be expressed by a power series expansion of three deformation modes (splay, bend, twist), truncated at quadratic term [de Gennes, 1993]. For a twist deformation with wavenumber q, we can write:

$$f(q) \cong f_u + \left(\frac{\partial f}{\partial q}\right)_{q=0} q + \frac{1}{2}\left(\frac{\partial^2 f}{\partial q^2}\right)_{q=0} q^2 = f_u + K_t q + \frac{1}{2} K_{22} q^2 \tag{4.6}$$

Here f_u is the free energy density of undeformed phase,

$$K_t = \left(\frac{\partial f}{\partial q}\right)_{q=0} \tag{4.7}$$

is the *chiral strength* and

$$K_{22} = \left(\frac{\partial^2 f}{\partial q^2}\right)_{q=0} \tag{4.8}$$

is the *twist elastic constant* [Vertogen, 1988]. The equilibrium wavenumber is obtained by minimization of the free energy, $\frac{\partial f(q)}{\partial q} = 0$, which leads to the relation:

$$q = -\frac{K_t}{K_{22}} \tag{4.9}$$

Here we want to connect the equilibrium pitch to the features of the virus suspensions, as described by the distribution function, eq. (4.1). To this purpose, an expression for the Helmholtz free energy density of the system on the basis of the orientational distribution function will be derived. The Helmholtz free energy density of the nematic phase can be expressed as:

$$f_{Nem} = f_{Iso} + \Delta f_{nem} \tag{4.10}$$

where f_{Iso} refers to the isotropic phase and Δf_{nem} is the free energy difference between nematic and isotropic phase. We can write Δf_{nem} as

$$\Delta f_{Nem} = \Delta u_{nem} + T\Delta s_{nem} \tag{4.11}$$

where *u* and *s* are the density of internal energy and entropy, respectively. Given the form of the potential U(**ω**), eq. (4.3), the former can be expressed as

$$\Delta u_{Nem} = \frac{N}{V}\left(\overline{U_{nem}^{bend}} - \overline{U_{iso}^{bend}} + \frac{1}{2}\overline{U_{nem}^{or}}\right) \tag{4.12}$$

where $\overline{U_{iso}^{bend}}$, $\overline{U_{nem}^{bend}}$ and $\overline{U_{nem}^{or}}$ are average values calculated according to eq. (4.5), with the labels *nem* and *iso* indicating that the average is performed over the nematic and isotropic (*a*=0) distribution function, respectively. The factor 1/2 in the last term of eq. (4.12) corrects for the over-counting of intermolecular interactions.

The orientational entropy density is written in the Gibbs form:

$$s = -\frac{Nk_B}{V}\int d\boldsymbol{\omega}\, p(\boldsymbol{\omega}) \ln p(\boldsymbol{\omega}) \tag{4.13}$$

So, using eq. (4.1) and eq. (4.13) and reminding that in the isotropic phase the only term in eq. (4.3) is that associated to the bending energy, we can write:

$$\Delta s_{nem} = -\frac{Nk_B}{V}\left(\frac{\overline{U_{nem}^{bend}}}{k_B T} - \frac{\overline{U_{iso}^{bend}}}{k_B T} + \frac{\overline{U_{nem}^{or}}}{k_B T} + \ln Z_{nem} - \ln Z_{iso}\right) \tag{4.14}$$

where $Z = \int d\boldsymbol{\omega} \exp\left[-U(\boldsymbol{\omega})/k_B T\right]$ is the configuration integral. Summing eq. (4.12) and eq. (4.14) we obtain the following expression for Δf_{nem}:

$$\Delta f_{nem} = -\frac{1}{2}\frac{N}{V}\overline{U_{nem}^{or}} - \frac{Nk_B T}{V}\ln Z_{nem} \tag{4.15}$$

For the chiral nematic phase, the parametric dependence upon the wavenumber must be included, so we can write:

$$\Delta f_{nem}(q) = -\frac{1}{2}\frac{N}{V}\overline{U_{nem}^{or}(q)} - \frac{Nk_B T}{V}\ln Z_{nem}(q) \tag{4.16}$$

According to eq. (4.7), the chiral strength K_t can now be obtained as the first derivative of free energy density with respect to the wavenumber, calculated at vanishing deformation (*q*=0):

$$K_t = -\frac{N}{2V}\frac{\partial}{\partial q}\overline{U_{nem}^{or}(q)}\bigg|_{q=0} - \frac{Nk_B T}{V}\frac{\partial \ln Z_{nem}(q)}{\partial q}\bigg|_{q=0} \tag{4.17}$$

As shown in appendix A, the first term in eq. (4.17) can be written as:

$$\left.\frac{\partial}{\partial q}\overline{U_{nem}^{or}(q)}\right|_{q=0} = \overline{U_{nem}^{or\ 1}(\boldsymbol{\Theta},\omega_0;q)}^{0} - \frac{1}{k_B T}\overline{U_{nem}^{or}(\boldsymbol{\Theta},\omega_1;q)U_{nem}^{or\ 1}(\boldsymbol{\Theta},\omega_1;q)}^{0} + \tag{4.18}$$

$$+\frac{1}{k_B T}\overline{U_{nem}^{or}(\boldsymbol{\Theta},\omega_1;q)}^{0}\overline{U_{nem}^{or\ 1}(\boldsymbol{\Theta},\omega_1;q)}^{0}$$

The superscript zero indicates that the average has to be taken at vanishing deformation (q=0). $U_{nem}^{or\ 1}(\boldsymbol{\Theta},\omega_1;q)$ is the first derivative of the orienting field with respect to the deformation.

The second term in eq. (4.17) gives the contribution:

$$\left.\frac{\partial}{\partial q}\overline{\ln Z_{nem}(q)}\right|_{q=0} = \left.\frac{1}{Z_{nem}(q)}\frac{\partial Z_{nem}(q)}{\partial q}\right|_{q=0} = -\frac{1}{k_B T}\overline{U_{nem}^{or\ 1}(\boldsymbol{\Theta},\omega_1;q)}^{0} \tag{4.19}$$

From eq. (4.18) and eq. (4.19) we obtain the following compact expression for the chiral strength K_t:

$$K_t == \frac{N}{2V}\left[\begin{array}{l}\overline{U_{nem}^{or\ 1}(\boldsymbol{\Theta},\omega_1;q)}^{0} + \frac{1}{k_B T}\overline{U_{nem}^{or}(\boldsymbol{\Theta},\omega_1;q)U_{nem}^{or\ 1}(\boldsymbol{\Theta},\omega_1;q)}^{0} + \\ -\frac{1}{k_B T}\overline{U_{nem}^{or}(\boldsymbol{\Theta},\omega_1;q)}^{0}\overline{U_{nem}^{or\ 1}(\boldsymbol{\Theta},\omega_1;q)}^{0}\end{array}\right] \tag{4.20}$$

Using now the definition of the twist elastic constant K_{22} , eq. (4.8), we can write:

$$K_{22} = \frac{N}{V}\left[\begin{array}{l}\overline{U_{nem}^{or\ 2}(\boldsymbol{\Theta},\omega_1;q)}^{0} + \\ +\frac{1}{k_B T}\left(\overline{U_{nem}^{or}(\boldsymbol{\Theta},\omega_1;q)U_{nem}^{or\ 2}(\boldsymbol{\Theta},\omega_1;q)}^{0} - \overline{U_{nem}^{or}(\boldsymbol{\Theta},\omega_1;q)}^{0}\overline{U_{nem}^{or\ 2}(\boldsymbol{\Theta},\omega_1;q)}^{0}\right) + \\ -\frac{1}{2(k_B T)^2}\left(\overline{U_{nem}^{or}(\boldsymbol{\Theta},\omega_1;q)U_{nem}^{or\ 1}(\boldsymbol{\Theta},\omega_1;q)^2}^{0} - \overline{U_{nem}^{or}(\boldsymbol{\Theta},\omega_1;q)}^{0}\overline{U_{nem}^{or\ 1}(\boldsymbol{\Theta},\omega_1;q)^2}^{0}\right) + \\ +\frac{1}{(k_B T)^2}\overline{U_{nem}^{or\ 1}(\boldsymbol{\Theta},\omega_1;q)}\left(\overline{U_{nem}^{or}(\boldsymbol{\Theta},\omega_1;q)U_{nem}^{or\ 1}(\boldsymbol{\Theta},\omega_1;q)}^{0} - \overline{U_{nem}^{or}(\boldsymbol{\Theta},\omega_1;q)}^{0}\overline{U_{nem}^{or\ 1}(\boldsymbol{\Theta},\omega_1;q)}^{0}\right)\end{array}\right] \tag{4.21}$$

where $U_{nem}^{or\ 2}(\boldsymbol{\Theta},\omega_1)$ is the second derivative of orienting potential with respect to the deformation.

The equilibrium pitch of the cholesteric helix is then obtained from the ratio of eq. (4.20) and eq. (4.21).

4.4 Virus elasticity: a modified worm-like model including chirality

The simplest model that captures the most relevant statistical properties of semiflexible polymers is the *worm-like chain model* (WLC) [Kratky, 1949]: polymers are considered as inextensible particles, whose bending is opposed by an elastic energy cost which, per unit

length, is proportional to the square of the curvature. In the continuum version of the model, the bending free energy of a polymer of contour length L can be written as [Wilhelm, 1996]:

$$\frac{U^{bend}}{k_B T} = \frac{\kappa}{2}\int_0^L ds\left[\frac{\partial \mathbf{t}(s)}{\partial s}\right]^2 \tag{4.22}$$

where $\mathbf{t}(s)$ is the tangent vector at position s along the polymer and κ is the bending elastic constant.

For our calculations, it is convenient to use the discretized form of the WLC model:

$$\frac{U^{bend}}{k_B T} = -\kappa\sum_{i=1}^{M-1} \mathbf{t}_i \cdot \mathbf{t}_{i+1} \tag{4.23}$$

where M is the number of segments used to represent the polymer.

The WLC model has been extensively used to describe the statistical properties of polymers like elastomers [Kovac, 1982]. Recently it has been used to interpret the elasticity of biopolymers like DNA [Rivetti, 1996; Wiggins, 2006], viruses [Maeda, 1985; Wang, 2006] and giant worm-like micelles [Cannavacciuolo, 2000]. It has also been used to analyse the fluctuations of semiflexible polymers in ordered solvents [Dogic, 2004]. The WLC model is able to capture many of the features of the long length-scale behaviour of polymers; in some cases, however, its limits appear. Let us take the case of DNA. Starting from a symmetry analysis, Marko and Siggia [Marko, 1994], showed that the bending free energy of DNA has a form more complex than eq. (4.31). In particular, they found that, in addition to the bending elastic constant, also a twist constant that opposes changes of the double helix periodicity and a coupled bend-twist elastic constant should be introduced. After the theoretical predictions of Marko and Siggia, these constants were measured [Smith, 1996; Strick, 1996]. Subsequently, some attempts to improve the model proposed by Marko and Siggia were done by Kamien and others [Kamien, 1996; O'Hern, 1997]; they tried to insert more molecular details into the description of DNA elasticity and they obtained other elastic constants, coupling for example twist and stretching modes.

According to the model proposed by Marko and Siggia, the bending elastic modulus of DNA is a function of the direction of bending;

$$\kappa(\gamma) = \kappa_{iso} - \kappa_{aniso}\sin(2\gamma) \tag{4.24}$$

where κ_{iso} and κ_{aniso} are the isotropic and the anisotropic component of the bending modulus. The factor 2 derives from an assumption of the model: no distinction between minor and major groove is made, therefore locally there are two equivalent bending directions.

The generalization of this result to the M13 and *fd* viruses is not straightforward. As described in chapter 3, these are long polymers (about 800 nm) made by a single DNA strand inserted into a capsid of about 2750 identical proteins. These are organized in a well defined pattern (see fig. 4.3): they lie at the vertices of a pentagon, and proceeding along the virus axis,

a pentamer is related to the next one by a cork-screw axis, with a translation of 1.6 nm and a rotation of 180° (for a total of 540 pentamers).

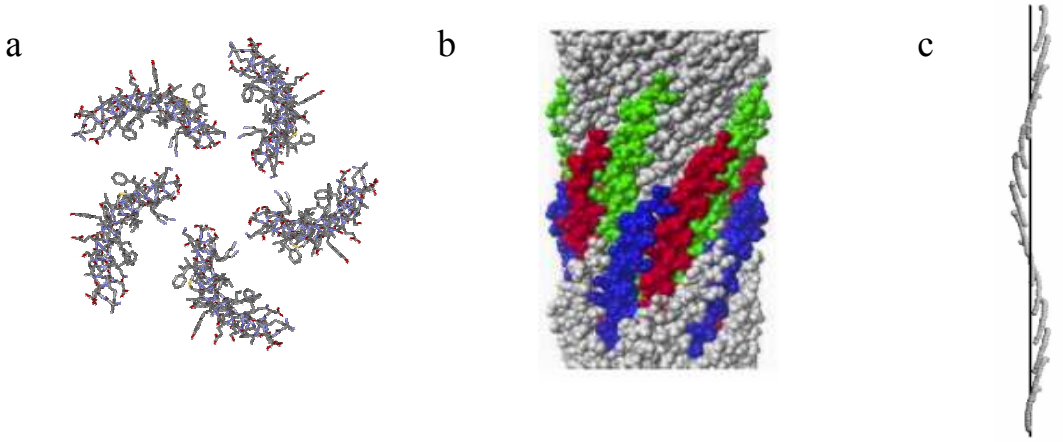

Figure 4.3 Structure of the M13 (or the *fd*) virus. (a) The building block of the capsid is a pentamer of proteins. The five proteins lie roughly at the vertices of a pentagon. (b) All-atom representation of the virus surface. Proteins with a given colour are related by a five-fold symmetry axis. (c) Helical wrapping of capsid proteins.

Up to now there are only limited experimental data on the flexibility of viruses; only the persistence length L_p [3] has been determined and the reported values oscillate between 2.2μm [Maeda, 1985] and 1.0μm [Wang, 2006]. Therefore, we can only make some hypothesis: we shall assume that the only relevant elasticity contribution comes from bending (twist and stretch-coupled terms are neglected). In contrast to the case of DNA, the symmetry constraints are not obvious. Namely, different sources of bending anisotropy could be devised. One can be found in the chirality of the capsid; on the other hand, recent experiments on Class I and II symmetry viruses suggest that bending asymmetry could originate from the organization of DNA [Tomar, 2007]. In the absence of any precise information, we have explored the effect of different choices, using a trial form for $\kappa(\gamma)$:

$$\kappa(\gamma) = \kappa_{iso} - \kappa_{aniso} \sin\left(i\frac{2\pi}{j} + m\gamma_i \right) \tag{4.25}$$

with the parameters m , which we call *local symmetry parameter*, and j , henceforth denoted as *bending periodicity*. The former accounts for the existence of m preferred bending directions (in the case of an ideal DNA double helix, with two equivalent grooves, m=2). As a consequence of

[3] The persistence length L_p is a property related to the stiffness of a polymer. Formally, it is defined as the length over which the correlation of vectors tangent to the polymer is lost: $\langle \mathbf{t}(s) \cdot \mathbf{t}(s') \rangle = \exp(-L/L_p)$ where L is the contour length of the polymer.

chirality, such bending preferred directions are not the same for all segments, but rotate in space according to a helical pattern with periodicity $2\pi/j$, on going from a segment to the next one. In the case of DNA, the periodicity corresponds to 10 base pairs (each base pair rotates of about 36° with respect to the previous one), and $j = 10$. Combining eq. (4.22) and eq. (4.25), we obtain the following expression for the bending elastic energy:

$$U^{bend}(\boldsymbol{\Theta}) = -k_B T \sum_{i=1}^{M} \left[\kappa_{iso} - \kappa_{aniso} \sin\left(i\frac{2\pi}{j} + m\gamma_i \right) \right] \cos\theta_i \tag{4.26}$$

where $\boldsymbol{\Theta}$ is a vector with elements $\Theta_i = (\theta_i, \gamma_i)$, θ_i being is the bending angle between two consecutive segments i and i+1, and γ_i the angle that identifies the bending direction (see fig. 4.5).

4.5 Coarse grained representation of the virus

We have used the following coarse grained description of the M13/*fd* virus: each pentamer of proteins is represented by a sphere of radius $r = 7$ nm, for a total of 540 spheres (see fig. 4.4). The distance between the centre of adjacent spheres is equal to 1.6 nm. Thus, a number of segments M=539 of length l=1.6 nm has been assumed. The angles θ_i, γ_i appearing in eq. (4.26) are shown in fig. 4.5.

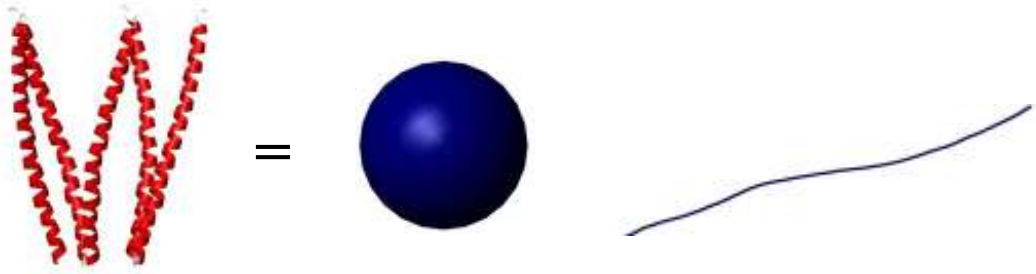

Figure 4.4 In our coarse grained description, a pentamer of proteins is represented by a sphere of radius 7 nm. A virus (right) is made of 540 spheres.

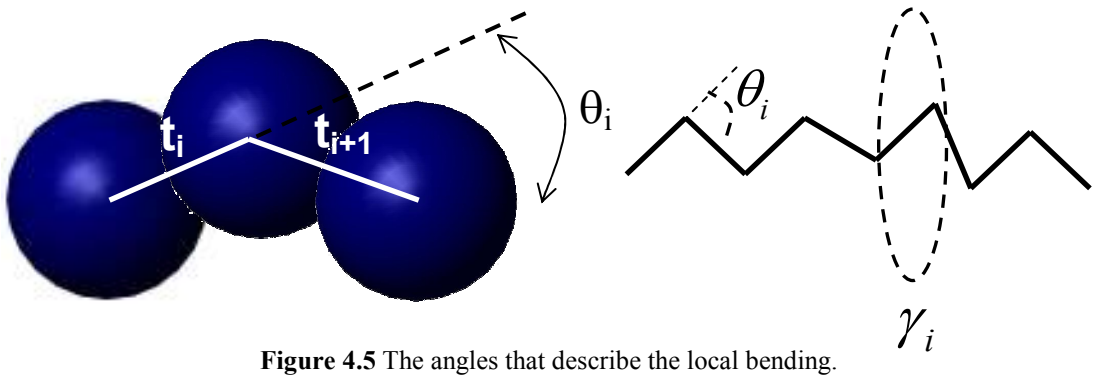

Figure 4.5 The angles that describe the local bending.

4.6 Numerical methods

We can see that calculation of the chiral strength K_t and the elastic constant K_{22} requires the evaluation of integrals with the general form

$$\overline{g} = \frac{\int d\theta_2 ... d\theta_M d\gamma_2 ... d\theta_M d\beta_1 d\gamma_1 \; g(\mathbf{\Theta}, \omega_1) \exp\left[-\left(U^{or}(\mathbf{\Theta}, \omega_1) + U^{bend}(\mathbf{\Theta})\right)\right]}{\int d\theta_2 ... d\theta_M d\gamma_2 ... d\theta_M d\beta_1 d\gamma_1 \exp\left[-\left(U^{or}(\mathbf{\Theta}, \omega_1) + U^{bend}(\mathbf{\Theta})\right)\right]} \tag{4.27}$$

with M=539. The angles β_1, γ_1 define the orientation of segment 1 in the LAB frame.

The integrals over the internal variables $\mathbf{\Theta}$ have been evaluated by Monte Carlo sampling, with the Metropolis algorithm [Metropolis, 1953]. Trial polymer conformations were generated by the PIVOT method [Stellman, 1971]: any new conformation is defined by choosing at random a pivotal segment $i \in [1,538]$ and two rotational increments: $\Delta\theta \in [-3°, +3°]$ and $\Delta\gamma \in [-5°, +5°]$. The increments are then added to the old angles ($\theta_i^{old}, \gamma_i^{old}$), generating the new values θ_i^{new} and γ_i^{new}; this produces a rotation of all segments from $i+1$ to 539. The acceptance probability W of any conformation characterised by a new set of internal variables $\mathbf{\Theta}^{new}$ is given by:

$$W = \min\left[\exp\left(-U^{bend}(\mathbf{\Theta}^{new}) + U^{bend}(\mathbf{\Theta}^{old})\right), 1\right] \tag{4.28}$$

The selected increments $\Delta\beta$, $\Delta\gamma$ were chosen to have an acceptance probability of about 50%. Before acceptance, all new conformations were checked with an excluded volume criterion to avoid overlapping structures: the new configuration was only accepted if the distance between the centres of the *i*-th and the *j*-sphere, with $|j-i| > 5$ was greater than $2r$, with r being the radius of the sphere.

Using this probability acceptance, the average value of any function can be obtained as:

$$\overline{g} = \frac{\sum_{x=1}^{conformers} \int d\beta_1 d\gamma_1 \; g(\mathbf{\Theta}_x, \omega_1) \exp\left[-\left(U^{or}(\mathbf{\Theta}_x, \omega_1)\right)\right]}{\sum_{x=1}^{conformers} \int d\beta_1 d\gamma_1 \exp\left[-\left(U^{or}(\mathbf{\Theta}_x, \omega_1)\right)\right]} \tag{4.29}$$

where the sum runs over all the accepted conformers. This expression can be rewritten as:

$$\overline{g} = \sum_{x=1}^{conformers} w_x \overline{g_x} \tag{4.30}$$

with the weight w_x defined as:

$$w_x = \frac{\int d\beta_1 d\gamma_1 \; \exp\left[-\left(U^{or}(\mathbf{\Theta}_x, \omega_1)\right)\right]}{\sum_{x=1}^{conformers} \int d\beta_1 d\gamma_1 \exp\left[-\left(U^{or}(\mathbf{\Theta}_x, \omega_1)\right)\right]} \tag{4.31}$$

and the orientationally averaged function for the *x* conformer:

$$\overline{g}_x = \frac{\int d\beta_1 d\gamma_1 \; g(\boldsymbol{\Theta}_x, \omega_1) \exp\left[-\left(U^{or}(\boldsymbol{\Theta}_x, \omega_1)\right)\right]}{\int d\beta_1 d\gamma_1 \exp\left[-\left(U^{or}(\boldsymbol{\Theta}_x, \omega_1)\right)\right]} \tag{4.32}$$

The integrals over the β_1, γ_1 angles were evaluated with the Gauss quadrature algorithm [Press, 1986].

4.7 Results and discussion

In this section, we will discuss the results obtained for a few choices of the parameters in eq. (4.26) : κ_{iso} , κ_{aniso} , j and m. The results of our calculations refer to virus suspensions of concentration equal to 50 mg/ml (that means that the factor N/V in eqs. (4.20) and (4.21) is equal to $2 \cdot 10^{-9} Å^{-3}$) and temperature T=298 K.

The value of the elastic bending constant κ_{iso} was chosen on the basis of the available data on the persistence length of the M13 virus. For the discretized classical WLC model, the bending elastic constant and the persistence length are related as:

$$\kappa = \frac{L_p}{l} \tag{4.33}$$

where l is the length of a segment. Assuming L_p equal to 2.2 μm [Maeda, 1985], with l=1.6 nm, the value κ_{iso} =1375 is obtained. Eq. (4.33) does not hold in the presence of anisotropic bending elasticity ($\kappa_{aniso} \neq 0$). In this case, the value κ_{iso} was chosen with the criterion of getting the same end-to-end distribution as for the classical WLC model with κ_{iso} =1375 and κ_{aniso}=0 (see fig.4.6).

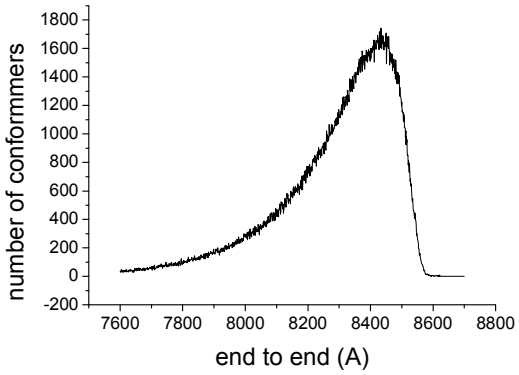

Figure 4.6 End-to-end distribution obtained for the classical WLC model, with κ_{iso} =1375. This curve represents the distribution of distances between head and tail of the virus.

The strength of the orienting potential, a, was chosen to reproduce the experimental value of order parameter $\overline{P_2}$, that for a virus solution at the concentration 50 mg/ml is about 0.8 [Purdy, 2004]. The order parameter $\overline{P_2}$ is equal to the major principal value of the Saupe ordering matrix [Vertogen, 1988]; this is calculated as:

$$\overline{\mathbf{S}} = \sum_{x=1}^{conformers} w_x \overline{\mathbf{S}}_x \tag{4.34}$$

where $\overline{\mathbf{S}}_x$ is the ordering matrix for the x conformer, those elements are defined as:

$$\overline{S_{\alpha\beta}}^x = \left(3\overline{\cos\theta_\alpha \cos\theta_\beta}^x - \delta_{\alpha\beta}\right)/2 \tag{4.35}$$

where θ_α are the angles between the director and the axes of the frame fixed on segment 1.

For all set of parameters a statistical sample of $2\cdot10^6$ conformers was analysed. This huge number is necessary to get reliable estimates of the chiral strength K_t. Chiral properties are strongly dependent on molecular details and contributions of opposite sign can be found for similar structures; namely, strong oscillation of K_t were found, especially with certain sets of parameters, as discuss below. On the contrary, the twist elastic constant K_{22} is less sensitive to molecular details, and stable results could be obtained for statistical samples of the order of $5\cdot10^4$ conformers.

In the following, when presenting the results, the quantities K_{22x} and K_{tx} will be reported. They are defined according to eq. (4.32) and can be seen as the twist elastic constant and the chiral strength in a suspensions where all the viruses have the x conformation. Correspondingly, the cholesteric wavenumber $q_x = -K_{tx}/K_{22x}$ can be defined.

Isotropic bending: κ_{iso}=1375, κ_{aniso}=0 We shall start from the case of a polymer with isotropic bending. Taking κ_{iso}=1375 we obtain an order parameter $\overline{P_2} = 0.8$ with a=0.035. Fig. 4.7 shows the conformer dependence of K_{22x} and the corresponding distribution. WE can see that most values lie in the range between $3\cdot10^{-12}$ N and $3\cdot10^{-13}$ N; after averaging over all conformers, the elastic constant $K_{22} = 1.09\cdot10^{-12}$ N is obtained. Experimental data are available for the *fd* virus; $K_{22} \sim 0.4\cdot10^{-12}$ N has been reported [Dogic, 2000], which is about one half of the value predicted here.

Fig. 4.8 shows the conformer dependence of the cholesteric wavenumber q_x and the corresponding distribution. It can be seen that a wide range of possible q_x values is predicted, both positive and negative; some values are extremely huge. For the sake of comparison, we can mention that typical experimental values for suspensions of M13 virus range between -0.1 and -0.065 μm^{-1}. In fig. 4.8 two conformers are shown, which give q_x=14 μm^{-1} and q_x=-10 μm^{-1}.

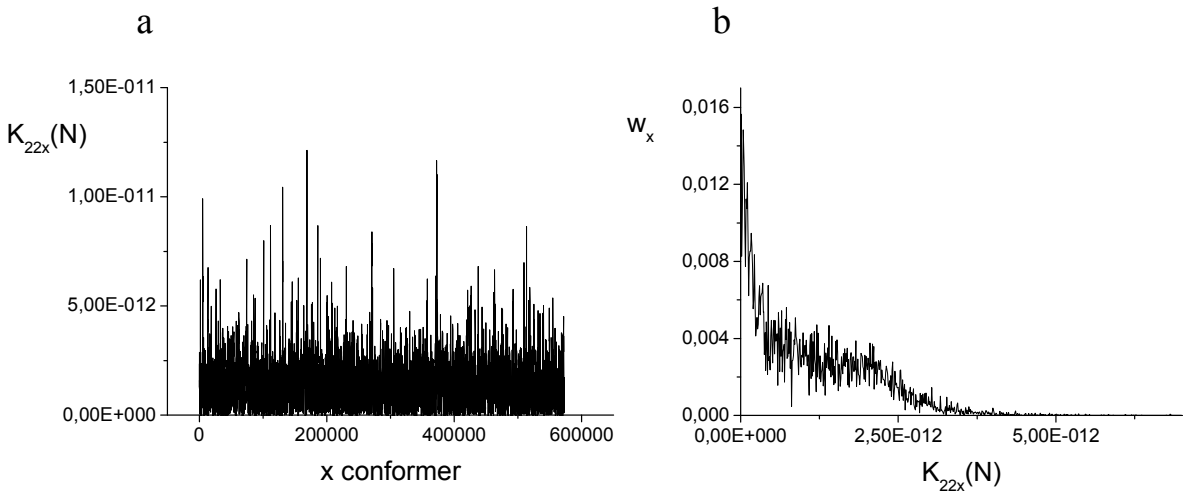

Figure 4.7 a) Values of the twist elastic constants in a sample of $6 \cdot 10^5$ conformers. b) Distribution of the twist elastic constant in a sample of $2 \cdot 10^6$ conformers. (κ_{iso}=1375, κ_{aniso}=0)

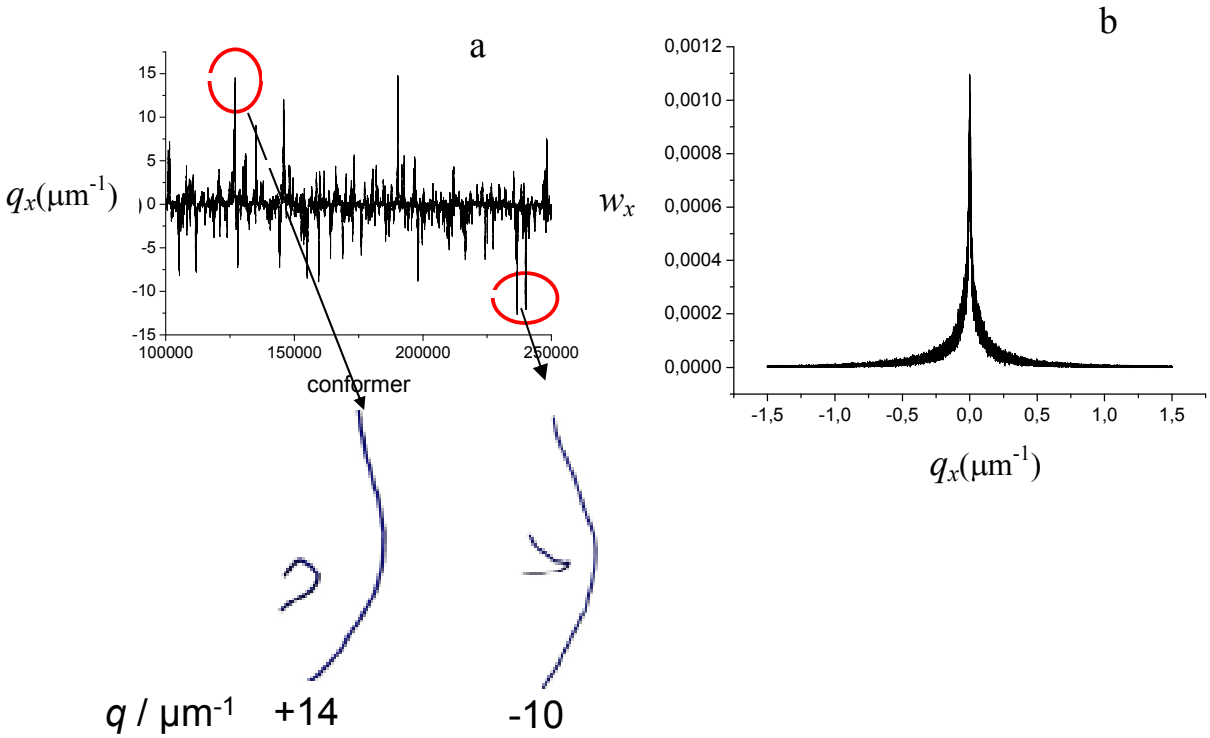

Figure 4.8 a) Values of the wavenumber in a sample of $2.5 \cdot 10^5$ conformers. b) Distribution of the wavenumber in a sample of $2 \cdot 10^6$ conformers. (κ_{iso}=1375, κ_{aniso}=0)

From fig. 4.8.b, however, we can infer that conformers with a q_x value outside the range between -1 μm^{-1} and +1 μm^{-1} have negligible statistical weight. In fact, conformers with very high chirality are strongly curved and they are not favoured in an ordered phase where, on the contrary, straight conformers, which can be well aligned to the director, are stabilised. As we can see from fig.4.8.b, the q_x values are symmetrically distributed with respect to zero; as a consequence a vanishing phase chirality (q=0) is predicted, after averaging over all the conformers in the sample. This situation is typical of a racemic mixture of chiral molecules. With κ_{aniso}=0 the virus lacks any intrinsic chirality; therefore, each conformer with a given q_x value has an enantiomer which is equally probable and has opposite q_x. In this way all chiral effects are washed out.

Anisotropic bending: κ_{iso}=7000, κ_{aniso}=50, j=269, m=1 Here an anisotropic contribution is introduced in the bending elasticity. In the absence of any experimental information on what reasonable choices of the parameters might be, a κ_{aniso} / κ_{iso} ratio lower than 1% is taken, with the criterion that chiral contributions generally are only a weak perturbation in comparison to the whole energetics. The local symmetry parameter m=1 is chosen; that means that only one preferred bending direction is assumed for each segment. This direction rotates in helical way along the axis of the virus, with periodicity equal to half the virus length (j=269). For this system, the strength of the orienting potential must be given the value a=0.050, to obtain an order parameter $\overline{P_2} = 0.8$.

Fig. 4.9 shows fluctuations and distribution of the twist elastic constant as a function of the virus conformation. The K_{22x} values lie in the range between between $3 \cdot 10^{-12}$ N and $3 \cdot 10^{-14}$ N, and there is a stronger dependence on conformation than in the case of isotropic bending elasticity considered above. After averaging over all conformers, $K_{22}=7.2 \cdot 10^{-13}$ N is obtained.

In fig. 4.10 fluctuations and distribution of the wavenumber q_x are reported. We can see that, with the new set of bending parameters, there is a strong selection of possible q_x values. These can range approximately between -1.0 μm^{-1} and +1.5μm^{-1}; again both positive and negative values are present, but they are not symmetrically distributed. The introduction of the anisotropic term in the bending elasticity breaks the symmetry: virus conformers that give positive q_x are preferred (about 85% of the total number). After averaging, q=+0.53μm^{-1} is obtained, which is about an order of magnitude bigger than the experimental values for *fd* [Grelet, 2003] and M13 viruses (see chapter 3). We can notice that a right-handed chiral nematic phase is predicted (positive value of q); the opposite handedness would be obtained with j=-1.

In fig. 4.10 two conformers are shown; both have a clear left-handed helicity, but one gives q_x =+0.5 μm^{-1} , and the other q_x =-0.3μm^{-1}.

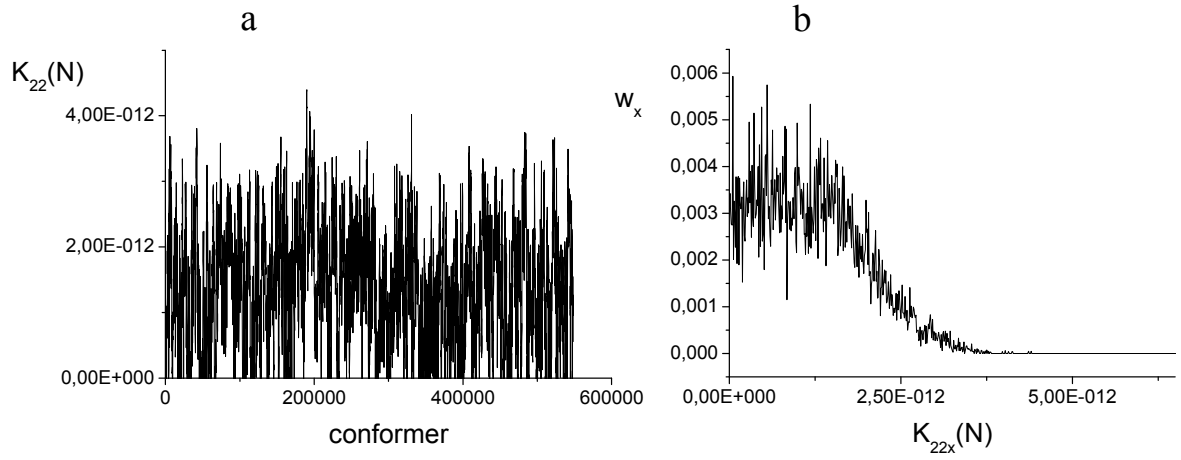

Figure 4.9 a) Values of the twist elastic constants in a sample of $6 \cdot 10^5$ conformers. b) Distribution of the twist elastic constant in a sample of $2 \cdot 10^6$ conformers. (κ_{iso}=7000, κ_{aniso}=50, j=269, m=1).

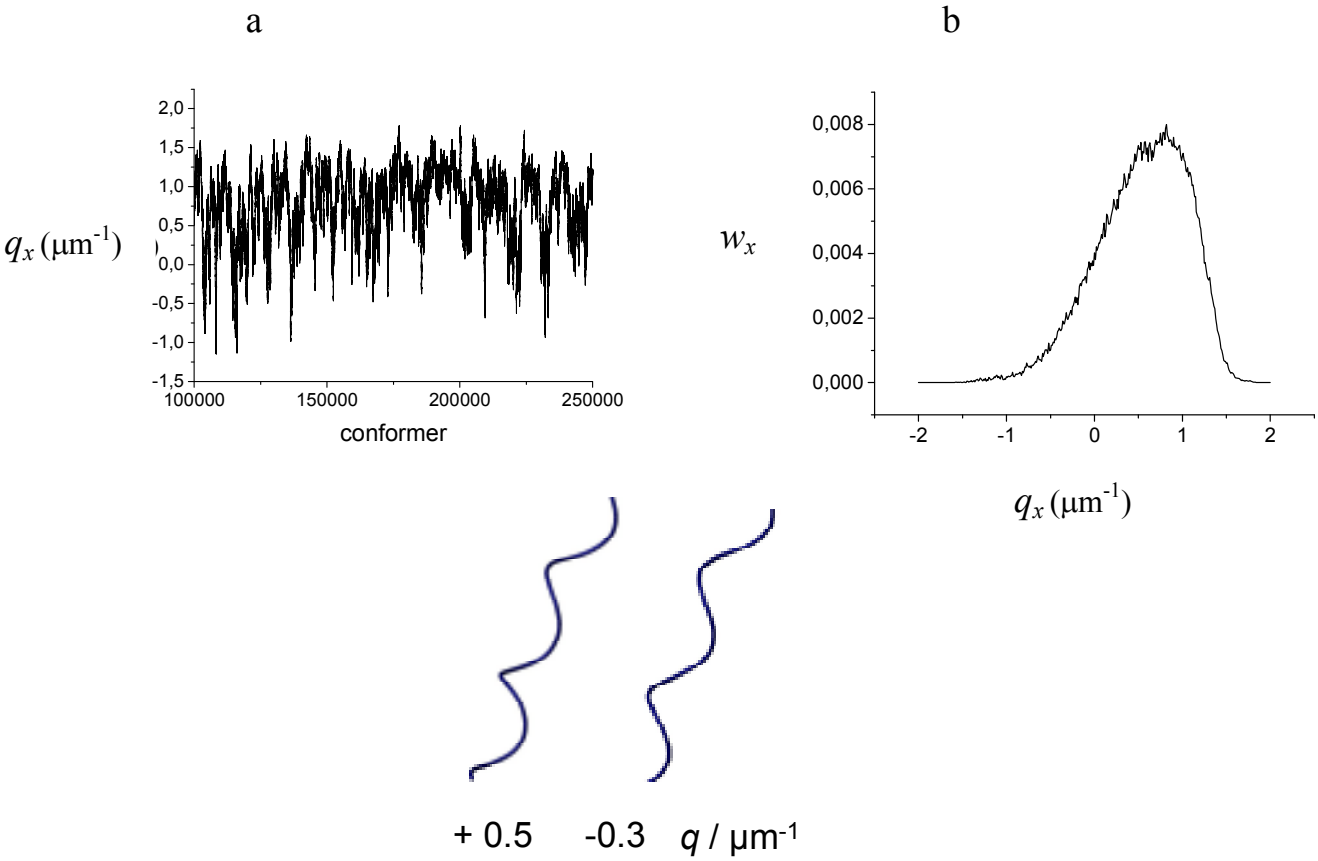

Figure 4.10 a) Values of the wavenumber in a sample of $2.5 \cdot 10^5$ conformers. b) Distribution of the wavenumber in a sample of $2 \cdot 10^6$ conformers. Blue structures correspond to virus conformers with q equal to +0.5 and -0.3μm^{-1}. (κ_{iso}=7000, κ_{aniso}=50, j=269, m=1).

Anisotropic bending: κ_{iso}=1500, κ_{aniso}=50, j=269, m=2 This situation differs from the previous one because now two preferred bending directions are assumed. Again these preferred orientations rotate along virus axis in a helical way, with periodicity equal to half the length of the virus. We can see that the value of κ_{iso} is not far from that used for the isotropic case. Also orienting strength required to get the order parameter $\overline{P_2} = 0.8$, i.e. a=0.038, is close to the value used for the isotropic case. The anisotropic model tends to the classical WLC model for increasing m.

Fig. 4.11 shows fluctuations and distribution of the twist elastic constant as a function of the virus conformation. With this set of bending parameters, we find for the twist elastic constants K_{22x} results similar to those obtained for the classical WLC model. Again, most of the values lie in the range between $3 \cdot 10^{-12}$ N and $3 \cdot 10^{-14}$ N. We obtain an average value of K_{22} =$1.05 \cdot 10^{-12}$ N, that is very close to the result of the classical WLC model.

Fig. 4.12. shows fluctuations and distribution of the wavenumbers q_x. Also for this property, the analogy with the classical WLC model appears. The strong selection of allowed q_x values, obtained for the case with m=1, has disappeared. Again, there are conformers with huge q_x values, but they have a negligible statistical weight in an ordered phase. The q_x distribution is less asymmetric than in the case with m=1, though not perfectly symmetric (there is a prevalence of negative values, about 60%). For this system we obtain q=-0.007 μm^{-1}; a left-handed cholesteric phase is predicted, with a wavenumber q which is about one order of magnitude smaller than the measured values for suspensions of *fd* and M13 viruses. It is interesting to note that the average q is significantly smaller than the q_x values of the single conformers which contribute to it.

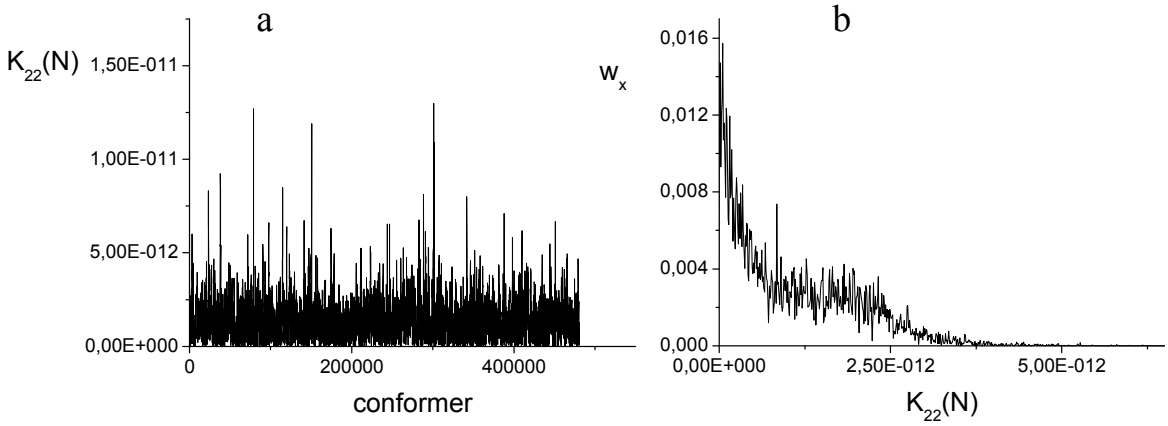

Figure 4.11 a) Values of the twist elastic constants in a sample of $6 \cdot 10^5$ conformers. b) Distribution of the twist elastic constant in a sample of $2 \cdot 10^6$ conformers. (κ_{iso}=1500, κ_{aniso}=50, j=269, m=2).

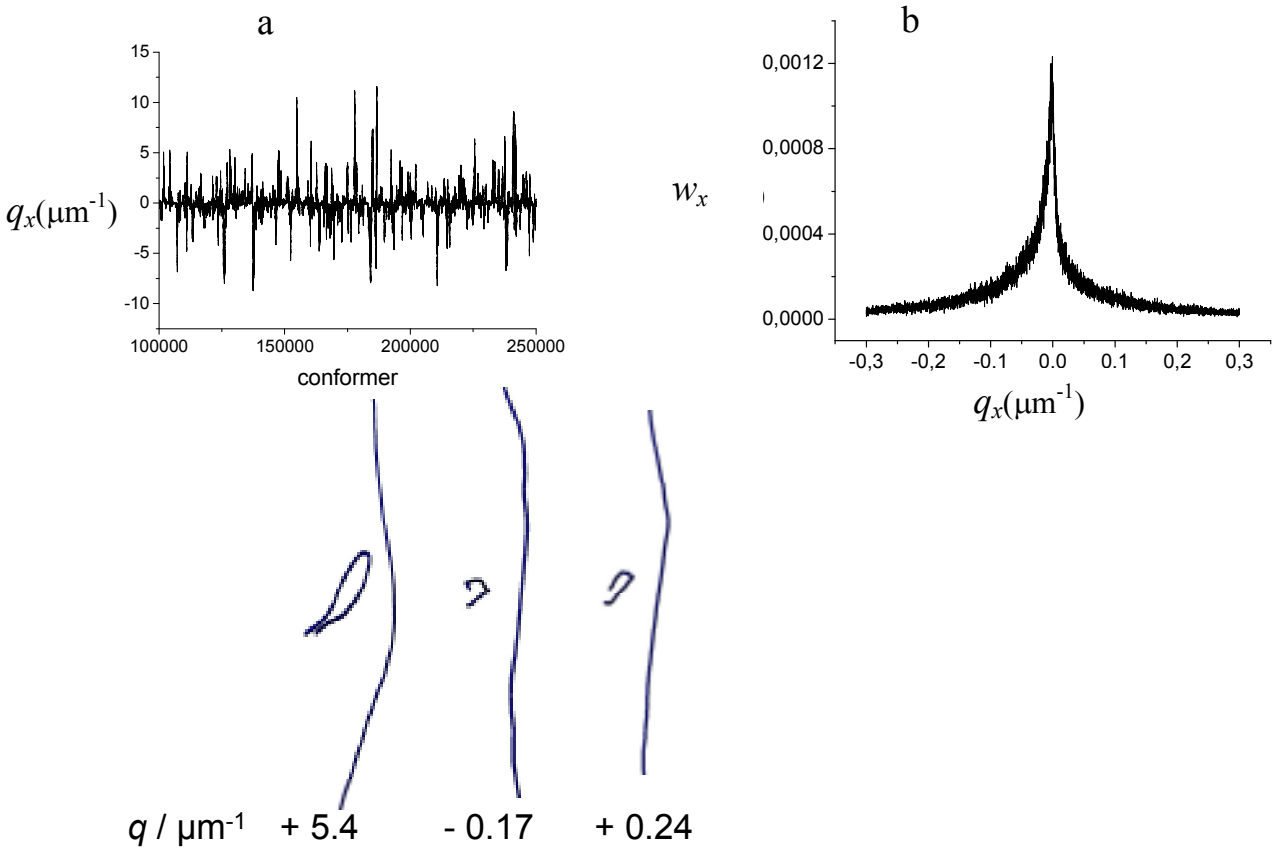

Figure 4.12 a) Values of the wavenumber in a sample of $2.5 \cdot 10^5$ conformers. b) Distribution of the wavenumber in a sample of $2 \cdot 10^6$ conformers. Blue structures correspond to virus conformers with q equal to +5.4, -0.17 and +0.24μm^{-1}. (κ_{iso}=7000, κ_{aniso}=50, j=269, m=2).

4.8 Conclusions

In this chapter a model has been presented, to explore the possibility that bending fluctuations of semiflexible polymers can be responsible for the formation of chiral nematic phases. The model has been thought in particular for the case of the *fd* and M13 filamentous viruses, but could be applied to the study of other semiflexible polymers.

A theoretical framework has been set up, to establish a clear link, based on statistical thermodynamics, between the virus elasticity and the elastic and chiral property of the nematic phase. One of the key issues concerns the elastic behaviour of viruses. In some analogy with the model developed for DNA [Marko, 1994], the classical WLC model was modified, introducing into the bending elasticity an anisotropic contribution that should account for the molecular chirality. However, in the case of DNA the relatively simple molecular shape has permitted a derivation of the anisotropic bending terms on the basis of symmetry. Furthermore, the abundance of experimental data gave the possibility of checking and supporting the model. In the case of *fd* and M13 viruses, the derivation of a sensible form for the bending elasticity is made difficult by the higher structural complexity on one side, and the lack of detailed experimental data on the other side. Therefore we could only perform a preliminary investigation, aimed at investigating whether the introduction of a chiral bias at the level of bending fluctuations could result in the stabilization of a chiral nematic phase.

A simple form for the virus bending energy has been proposed, which contains four parameters: isotropic bending constant κ_{iso}, anisotropic bending constant κ_{aniso}, local symmetry parameter m and bending periodicity j. The first parameter, κ_{iso}, describes the isotropic contribution to the bending energy, and is the only term of the classical WLC model. The second parameter, κ_{aniso} , quantifies the bending anisotropy. The third parameter, m, describes the number of local preferred directions of bending, while the fourth, j, describes the periodicity of the preferred bending direction along the virus axis. Even if the results strongly depend on the choices for these parameters, some general considerations can be made.

We have seen that the elastic constant K_{22}, which opposes twist director deformations in the nematic phase, does not strongly depend on the details of the bending elasticity of the polymer. With different choices for bending parameters, we obtained twist elastic constants in the range between $10^{-13} \div 10^{-12}$N; these values are comparable with experimental data for *fd* viruses [Dogic, 2000]. In chapters 2 and 3 it was already noticed that the twist elastic constants are not very sensitive to molecular details.

On the contrary, the chiral strength K_t , and then cholesteric pitch p, are strongly affected by the anisotropy features of the bending elasticity of viruses. In a statistical sample, virus conformers that could give a chiral nematic phase are present. The range of possible pitch values can be very large, and increases with the flexibility of viruses. However, the global effect can be washed out by the simultaneous presence of conformers with opposite twisting

ability (that will give cholesterics of opposite handedness). In the absence of any chiral bias in the bending elasticity, a racemic mixture of conformers is obtained without any net chiral effect. The introduction of an anisotropic bending contribution breaks the symmetry and, for suitable choices, the unbalance between conformers with opposite twisting power could be sufficient to stabilize a cholesteric phase with pitch comparable with the values measured for suspensions of *fd* and M13 viruses. Presently, the lack of detailed experimental data on the flexibiilty of viruses makes it impossible to go beyond this qualitative level. Very recent single molecule experiments provided some information [Wang, 2006; Khalil, 2007]; hopefully, a more detailed knowledge will be available in the future.

As reported in chapter 3, the cholesteric pitch of suspensions of *fd* and M13 viruses exhibits some dependence upon temperature and ionic strength. Both effects could be introduced in our model, through the persistence length [Skolnick, 1977]. Their inclusion should be relatively straightforward; this is planned for the next future and could give other criteria to evaluate the reliability of our model.

Appendix A Derivation of eq. (4.18)

$$\left.\frac{\partial}{\partial q}\overline{U_{nem}^{or}(q)}\right|_{q=0} = \frac{\partial}{\partial q}\frac{\int d\boldsymbol{\Theta}\, d\omega_1\, U_{nem}^{or}(\boldsymbol{\Theta},\omega_1;q)\exp\left[-U(\boldsymbol{\Theta},\omega_1;q)/k_BT\right]}{\int d\boldsymbol{\Theta}\, d\omega_1\, \exp\left[-U(\boldsymbol{\Theta},\omega_1;q)/k_BT\right]} = \tag{A.1}$$

$$\left.\frac{\int d\boldsymbol{\Theta}\, d\omega_1\, U_{nem}^{or\,1}(\boldsymbol{\Theta},\omega_1;q)\exp\left[-U(\boldsymbol{\Theta},\omega_1;q)/k_BT\right]}{\int d\boldsymbol{\Theta}\, d\omega_1\, \exp\left[-U(\boldsymbol{\Theta},\omega_1;q)/k_BT\right]}\right|_{q=0} -$$

$$-\frac{1}{k_BT}\left.\frac{\int d\boldsymbol{\Theta}\, d\omega_1\, U_{nem}^{or}(\boldsymbol{\Theta},\omega_1;q)U_{nem}^{or\,1}(\boldsymbol{\Theta},\omega_1;q)\exp\left[-U(\boldsymbol{\Theta},\omega_1;q)/k_BT\right]}{\int d\boldsymbol{\Theta}\, d\omega_1\, \exp\left[-U(\boldsymbol{\Theta},\omega_1;q)/k_BT\right]}\right|_{q=0} +$$

$$\int d\boldsymbol{\Theta}\, d\omega_1\, U_{nem}^{or}(\boldsymbol{\Theta},\omega_1;q)\exp\left[-U(\boldsymbol{\Theta},\omega_1;q)/k_BT\right]\times$$

$$\times\left.\frac{\partial}{\partial q}\frac{1}{\int d\boldsymbol{\Theta}\, d\omega_1\, \exp\left[-U(\boldsymbol{\Theta},\omega_1;q)/k_BT\right]}\right|_{q=0}$$

Substituting the following expression:

$$\left.\frac{\partial}{\partial q}\frac{1}{\int d\boldsymbol{\Theta}\, d\omega_1\, \exp\left[-U(\boldsymbol{\Theta},\omega_1;q)/k_BT\right]}\right|_{q=0} = \left(\frac{1}{\int d\boldsymbol{\Theta}\, d\omega_1\, \exp\left[-U(\boldsymbol{\Theta},\omega_1;q)/k_BT\right]}\right)^2 \times \tag{A.2}$$

$$\times\frac{1}{k_BT}\int d\boldsymbol{\Theta}\, d\omega_1\, U_{nem}^{or\,1}(\boldsymbol{\Theta},\omega_1;q)\exp\left[-U(\boldsymbol{\Theta},\omega_1;q)/k_BT\right]$$

into eq. A.1 we obtain the compact form:

$$\left.\frac{\partial}{\partial q}\overline{U_{nem}^{or}(q)}\right|_{q=0} = \overline{U_{nem}^{or\,1}(\boldsymbol{\Theta},\omega_1;q)}^{0} - \frac{1}{k_BT}\overline{U_{nem}^{or}(\boldsymbol{\Theta},\omega_1;q)U_{nem}^{or\,1}(\boldsymbol{\Theta},\omega_1;q)}^{0} + \tag{A.3}$$

$$+\frac{1}{k_BT}\overline{U_{nem}^{or}(\boldsymbol{\Theta},\omega_1;q)}^{0}\overline{U_{nem}^{or\,1}(\boldsymbol{\Theta},\omega_1;q)}^{0}$$

4.9 References

Cannavacciuolo L., Sommer C., Pedersen J.S., Schurtenberger P. *Phys. Rev. E* **62**, 5409 (2000).

de Gennes P.G., Prost J. *The Physics of Liquid Crystals* , 2nd edition (Clarendon Press, Oxford, 1993).

Dogic Z., Fraden S. *Langmuir* **16**, 7820 (2000).

Dogic Z., Zhang J., Lau A.W.C., Arada-Espinoza H., Dalhaimer P., Discher D.E., Janmey P.A., Kamien R.D., Lubensky T.C., Yodh A.G. *Phys. Rev. Lett.* **92**, 125503 (2004).

Emsley J.W., Luckhurst G.R., Stockley C.P. *Proc. R. Soc. Lond.A* **381**, 117 (1982).

Ferrarini A., Luckhurst G.R., Nordio P.L. *Molec. Phys.* **85**, 131 (1995).

Grelet E., Fraden S. *Phys. Rev. Lett.* **90**, 198302 (2003).

Kamien R., Lubensky T.C., Nelson P., O'Hern C.S. *Europhys. Lett.* **38**, 237 (1997).

Khalil A.S., Ferrer J.M., Brau R.R., Kottmann S.T., Noren C.J., Lang M.J., Belcher A.M. *PNAS* **104**, 4892 (2007).

Kovac J., Crabb C.C. *Macromolecules* **15**, 537 (1982).

Kratky O., Porod D. *Rec. Trav. Chim*. **68**, 1106 (1949).

Maeda T., Fujime S. *Macromolecules* **18**, 2430 (1985).

Maier W., Saupe A. Z. *Naturforsch.* **14a**, 882 (1959).

Marko J.F., Siggia E.D. *Macromolecules* **27**, 981 (1994).

Metropolis N., Rosenbluth A.W., Rosenbluth. M.N., Teller A.H., Teller E. *J. Chem. Phys*. **21**, 1087 (1953).

O'Hern C.S., Kamien R.D., Lubensky T.C., Nelson P. *Europ. Phys. J. B* **1**, 95 (1997).

Press W.H., Flannery B.P., Teukolsky S.A., Vetterling W.T. *Numerical Recipes* (Cambridge Univerity Press, Cambridge, 1986)

Purdy K.R., Fraden S. *Phys. Rev. E* **70**, 061703 (2004).

Rivetti C., Guthold M., Bustamante C., *J. Mol. Biol.* **264**, 919 (1996).

Skolnick J., Fixman M. *Macromolecules* **10**, 944 (1977).

Smith S.B., Cui Y.J., Bustamante C. *Science* **271**, 795 (1996).

Stellman S.D., Gans P.J. *Macromolecules* **5**, 516 (1972).

Strick T.R., Allemand J.F., Bensimon D., Bensimon A., Croquette V. *Science* **271**, 1835 (1996).

Tang J., Fraden S. *Biopolimers* **39**, 13 (1996).

Tomar S., Green M.M. Day L.A. *J. Am. Chem. Soc.* **129**, 3367 (2007).

Vertogen G., de Jeu W.H. *Thermotropic Liquid Crystals, Fundamentals* (Springer, Berlino, 1988)

Wiggins P.A., Van Der Heijden T., Moreno-Herrero F., Spakowitz A., Phillips R., Widom J., Dekker C., Nelson P.C. *Nature* 1, 137 (2006).

Wang Y.A., Yu X., Overman S., Tsuboi M., Thomas G.J., Egelman E.H. *J. Mol. Biol.* **361**, 209 (2006).

Wilhelm J., Frey E. *Phys. Rev. Lett.* **77**, 2581 (1996).

Chapter 5

Chapter 5 ESR lineshape simulation and Molecular Dynamics to study membrane-protein interaction

5.1 Membrane-protein interaction: the case of α-Synuclein

The interaction between proteins and cell membranes, which plays a crucial role in many biological processes, is governed by subtle rules which are not fully understood. A variety of behaviours can be found, whose origin is encoded in the protein sequence. An interesting example is represented by proteins which undergo interconversion between two forms: they are unstructured in solution and fold when binding to cell membranes. Controversial issues concern the structural and dynamic aspects of folding, the mechanism and depth of protein insertion, the delicate interplay of specific interactions and more generic hydrophobic and electrostatic interactions and the role of membrane features like curvature and packing stress, as well as the change of protein and membrane properties upon binding. α-Synuclein, a 140 amino acid protein involved in Parkinson's disease, belongs to this class. In the last few years this system has been investigated by spectroscopic [Jao, 2004; Bisaglia, 2005; Ulmer, 2005] and computational [Mihajlovich, 2007] techniques, but there are a number of unresolved issues, and between them the possibility of the dependence of the protein structure on the nature of the binding interface.

In collaboration with experimentalists, we have performed a joint investigation aimed at shedding light on some aspects of the interaction of α-Synuclein with membranes. Using SDLS and ESR spectroscopy, we have studied structure and binding of α-synuclein in phospholipid vesicles and SDS micelles. The experimental work has been accompanied by lineshape simulation and modeling of the spin labeled protein, as described in chapter 9. In parallel, the mutual effects of protein-membrane interactions have been explored by atomistic Molecular Dynamics simulations of a fragment of α-synuclein in the presence of a lipid bilayer; chapter 8 reports on this study.

The spectral analysis has required a preliminary work, for the set up of the methodological tools needed for a proper interpretation of ESR experiments on paramagnetic spin labels attached by side chains to proteins. This work is presented in chapters 6 and 7.

5.2 The Site-Directed Spin Labeling (SDSL) technique

Site-Directed Spin Labeling (SDSL) [Hubbel, 1994] is a powerful tool for probing structure and conformational dynamics of proteins. SDSL utilizes site-directed mutagenesis to replace one or more amino acids in a domain of interest with a cysteine. This residue is then modified with a sulphydryl-specific nitroxide reagent to introduce a paramagnetic side-chain [Todd, 1989]. The spin label methanetiosulphonate is one of the most used, due to its similarity to triptophan or phenilalanine. Once added to cysteine, methanetiosulphonate I yields the so called R1 side chain (fig.5.1).

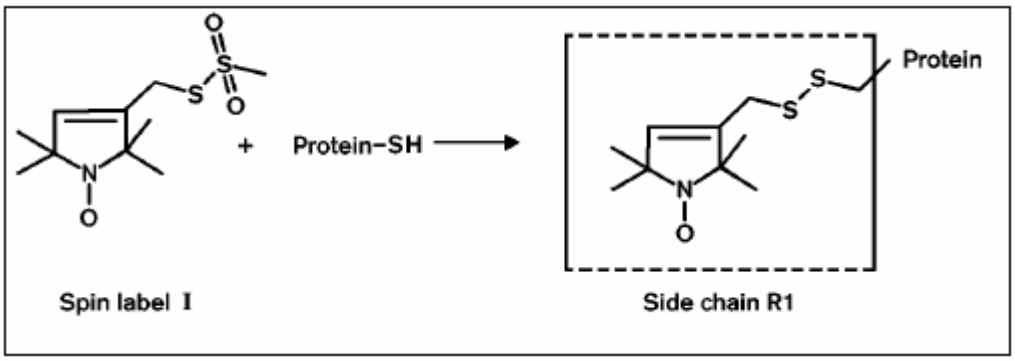

Figure 5.1 Schematic representation of the insertion of the spin label into a cysteine containing protein.

The nitroxide spin label has an unpaired electron and can be studied by Electron Paramagnetic Resonance (ESR) spectroscopy. In an EPR experiment, transitions between electron spin states induced by an oscillating magnetic field, in the presence of an additional static magnetic field, are revealed. The spin Hamiltonian is the sum of two contributions: the Zeeman term, that accounts for the interaction between electron spin magnetic moment and static magnetic field, and the hyperfine contribution, accounting for the interaction between the electron spin magnetic moment and the nuclear spin magnetic moment of nitrogen. Zeeman and hyperfine interactions are described by two tensorial quantities: $\boldsymbol{g}$ and $\boldsymbol{A}$, respectively (for a detailed introduction to ESR spectroscopy, see [Athernon, 1993]). The ESR spectrum of a nitroxide is given by three lines (fig.5.2). The lineshape reflects all the motions which mediate the magnetic tensors. In the presence of very fast dynamics (this situation is typical of samples at high temperature), the spectrum presents three similar sharp lines, which broaden as motions slow down.

The popularity of SDSL has grown for many reasons. The technique can be used for problems in protein structure determination that cannot be solved by other powerful techniques, like NMR and X-ray diffraction. Notable examples are the study of the structure and dynamics of high molecular weight proteins in solution and the investigation of conformational transitions and protein folding in real time. In addition, the technique can be applied to the study of membrane proteins, protein-membrane interactions and protein complexes, because there is no correlation time limit due to the tumbling of the labelled protein. Furthermore, SDSL is a sensitive technique, requiring samples of only a few tens of picomoles.

Three kinds of information can be obtained from the analysis of the ESR spectrum of a nitroxide probe in a protein: its accessibility to collision with paramagnetic reagents in solution [Farahbakhsh, 1992]; its distance from a second nitroxide or bound metal ion in the protein [Altenbach, 2001]; its dynamics. Measures of solvent accessibility and environment polarity give information on the local secondary structure [Gross, 1999]. The motions of the spin label reflect structural and dynamic features of the protein itself. However, it is not easy to discriminate the contribution to the spectral lineshape deriving from the different motions responsible for reorientation of the spin label; these comprise protein tumbling, backbone fluctuations, dynamics of the side chain bearing the spin label itself. Recent experimental advances, such as multi-frequency ESR, allow to separate different dynamic modes in biomolecules on the basis of time scale resolution; using high-frequency spectra [Liang, 2004] fast snapshots of molecular motions are captured (such as localized backbone and side

chain fluctuations), whereas slower snapshots obtained with X-band[1] ESR give information on the overall protein tumbling.

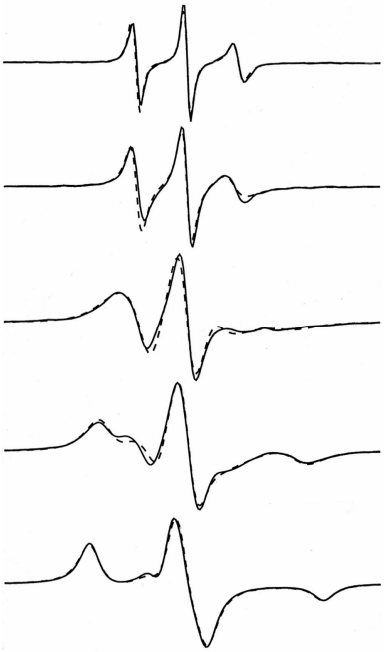

Figure 5.2 Typical X-band ESR spectra of a nitroxide spin label. Lineshape reflects all the motions which mediate magnetic tensors. Here, the effect of slowing down dynamics (from top to bottom) is shown.

5.3 ESR lineshape simulation

Simulation of ESR lineshapes based on a realistic modelling of the system can be extremely useful to fully exploit experimental data, extracting from them parameters with a clear physical meaning. The difficult task is to obtain a realistic description of dynamics of molecular systems that, typically, have many degrees of freedom. Different approaches can be used to solve this problem. The dynamics of classical degrees of freedom can be obtained in the form of trajectories, by Molecular Dynamics simulations [Stoica, 2004]. In principle, Molecular Dynamics trajectories could be used to solve the Liouville equation and obtain the Free Induction Decay; however extremely long trajectories are needed.

An alternative and very successful approach for the lineshape simulation is based on the Stochastic Liouville Equation (SLE) formalism [Schwartz, 1982], to describe the time evolution of the spin degrees of freedom (treated in a quantum-mechanical way) coupled to the molecular orientational degrees of freedom (described classically). In the SLE the Fokker-Plank equation is solved to describe

[1] Microwave frequency of 9.5 GHz, magnetic field of 0.34 T.

the time evolution of the probability density function for the orientational variables. This method is practicable for a few bodies, but becomes unfeasible in the case of many degrees of freedom (actually, the most advanced programs can simulate ESR spectra of systems modelled as one or two bodies). The advantage of the SLE approach is an easy description of some physical properties of the system, that can be introduced in a parametric way. These parameters are then optimized by a best fitting process. However, due to the high number of parameters of simulation, a large number of experimental data are needed. Moreover, it could be difficult to correlate these parameters to physical properties of the system. The problem can be simplified in the presence of motions occurring on different time-scales. For example, in the case of a protein, fast modes, like backbone fluctuations or side-chain isomerizations, are superimposed to slow dynamics, like overall protein tumbling or refolding processes. In this situation line-shape analysis can be simplified if fast and slow motion effects on ESR lineshape can be treated separately. In this case, partially averaged magnetic tensors and T_2 relaxation times can be calculated for the fast motions and spectral lineshapes are then obtained by introducing such parameters in the stochastic Liouville equation for the slow protein tumbling [Cassol, 1997].

5.4 References

Altenbach C., Oh K.J., Trabanino R.J., Hideg K., Hubbell W.L. *Biochemistry* **40**, 15471 (2001).

Atherton N.M. *Principles of Electron Spin Resonance* (Ellis Horwood, New York, 1993)

Bisaglia M., Tessari I., Pinato L., Bellanda M., Girando. S., Fasano M., Bergantino E., Bubacco L., Mammi S. *Biochemistry* **44**, 329 (2005).

Borbat P., Ramlall T.F., Freed J.H., Eliezer D. *J. Am. Chem. Soc.* **128**, 10004 (2006).

Cassol R., Ge M.T., Ferrarini A., Freed J.H., *J. Phys. Chem.B* **101**, 8782 (1997).

Farahbakhsh Z., Altenbach C., Hubbell W.L. *Photochem. Photobiol.* **56**, 1019 (1992).

Freed J.H. in *Spin Labeling: Theoy and Application* (Berliner, L.J., ed., Academic Press, New York, 1976)

Gross A., Columbus L., Hideg K., Altenbach C., Hubbell W.L., *Biochemistry* **38**, 10344 (1999).

Hubbel W., Altenbach C. *Curr. Opin. Struct. Biol*. **4** , 566 (1994).

Jao C.C., Der-Sarkissian A., Chen J., Langen R. *PNAS* **101**, 8331 (2004).

Liang Z., Lou Y, Columbus L., Hubbell L., Freed J., *J. Phys. Chem. B* **108**, 17649 (2004).

Mchaourab H., Lietzow M.L., Hubbell H.W. *Biochemistry* **35**, 7692 (1996)

Mihajlovich M., Lazaridis T. *Proteins* **70**, 761 (2007).

Schwartz L.J., Sillman A.E., Freed J.H., *J. Chem. Phys*. **77**, 5410 (1982).

Stoica I., *J. Phys. Chem. B* **108**, 1771 (2004).

Todd A., Cong J., Levinthal F., Hubbell W.L. *Proteins* **6**, 294 (1989).

Ulmer T.S., Bax A., Cole N.B., Nussbaum R.L. *J. Biol. Chem.* 280, 9595 (2005).

Chapter 6

Dynamics of the nitroxide side chain in spin-labeled proteins

Dynamics of the Nitroxide Side Chain in Spin-Labeled Proteins

Fabio Tombolato and Alberta Ferrarini*

Dipartimento di Scienze Chimiche, Via Marzolo 1, Università di Padova, 35131 Padova, Italy

Jack H. Freed

Baker Laboratory of Chemistry and Chemical Biology, Cornell University, Ithaca, New York 14853-1301

Received: May 15, 2006; In Final Form: August 21, 2006

The dynamics of the tether linking methanethiosulfonate (MTSSL) spin probes to α-helices has been investigated with the purpose of rationalizing its effects on ESR line shapes. Torsional profiles for the chain bonds have been calculated ab initio, and steric interactions with the α-helix and the neighboring residues have been introduced at the excluded-volume level. As a consequence of the restrictions deriving from chain geometry and local constraints, a limited number of allowed conformers has been identified that undergo torsional oscillations and conformational jumps. Torsional fluctuations are described as damped oscillations, while transition rates between conformers are calculated according to the Langer multidimensional extension of the Kramers theory. The time scale and amplitude of the different motions are compared; the major role played by rotations of the outermost bonds of the side chain emerges, along with the effects of substituents in the pyrroline ring on the conformer distribution and dynamics. The extent and symmetry of magnetic tensor averaging produced by the side chain motions are estimated, the implications for the ESR spectra of spin-labeled proteins are discussed, and suggestions for the introduction of realistic features of the spin probe dynamics into the line shape simulation are presented.

I. Introduction

ESR spectroscopy of nitroxide spin probes introduced by site-directed mutagenesis (site-directed spin labeling, SDSL) has become a valuable tool for the investigation of protein structure and dynamics.[1−5] Spectra reflect mobility and chemical environment of the spin label; if, as shown in several cases, the mutation does not significantly perturb the system, information on the nitroxide label yields useful insights on the protein. However, given the variety of processes that can produce nitroxide reorientation, this information cannot be easily extracted from line shapes. Namely, different motions, covering a wide range of amplitudes and different time scales, are simultaneously present in the system: they comprise overall protein tumbling and refolding processes, backbone fluctuations, and side chain isomerizations. Recognition of the role played by the spin label, even though it is not the objective of the investigation, is a prerequisite for extracting from experimental data useful information on structural and dynamical properties of proteins.

In this study, we have performed a conformational analysis of the side chain of a nitroxide spin label with the purpose of characterizing the geometrical and motional parameters of the tether. In this way we intend to identify any general features, which can be helpful for the interpretation of ESR spectra of spin-labeled proteins. We have focused on the methanethiosulfonate (MTSSL) spin label, whose structure is shown in Figure 1. This is the most widely used spin probe, which has been successfully employed in a variety of studies; a few significant examples are represented by the structural rearrangements associated with the gating mechanisms of the KscA potassium channel[6] and the mechanosensitive MscL channel,[7] the structure of SNARE proteins involved in membrane fusion,[8] the interaction of α-synuclein with membranes,[9,10] structure and helix motions in the light-driven proton pump bacteriorhodopsin[11] and in the photoreceptor rhodopsin,[12,13] and reconstruction of the chemotaxis receptor−kinase assembly.[14]

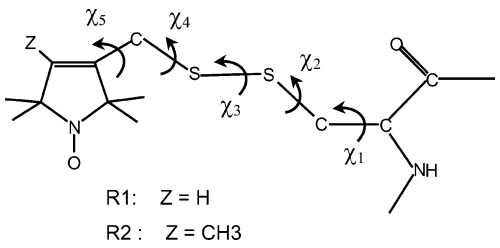

Figure 1. Structure of the spin labels considered in this study. They are obtained by reaction of the sulfhydryl group of a cysteine with 1-oxyl-2,2,5,5-tetramethyl-3-pyrroline-3-(methyl)methanethiosulfonate (R1) and 1-oxyl-2,2,4,5,5-pentamethyl-3-pyrroline-3-(methyl)-methanethiosulfonate (R2). The five dihedral angles defining the chain conformation are shown.

We have examined the internal motions of MTSSL attached to a model α-helix. Torsional energy profiles have been obtained by quantum mechanical methods, with a proper account of the constraints imposed by the local environment. Knowledge of the potential energy is a requirement for modeling the internal dynamics; the features of the energy landscape allow the description of the system in terms of a limited number of rotamers undergoing conformational jumps and librations about the minima of the side chain torsional potential. A diffusive treatment of the dynamics is used, which, although approximate, retains a realistic account of energetic and frictional features of the flexible tail.[15−18] As a result of this analysis, the amplitude and time scale of the chain motions can be estimated, and some

* Corresponding author. E-mail: alberta.ferrarini@unipd.it.

10.1021/jp0629487 CCC: $33.50
Published on Web 12/21/2006

general consideration on the effect of the tether dynamics on ESR spectra can be derived. The question might arise whether the results obtained from a model system can be extended to peptides or proteins, where the spin label is inserted into a given amino acid residue pattern. Actually, it has been shown that the main features of the ESR line shape are preserved under mutation of residues in the proximity of the spin label, with minor differences deriving from the specific environment.[19]

An account of the dynamics of the spin probe beyond the simplifying assumptions used here could be obtained in the form of trajectories by molecular dynamics (MD) or Brownian dynamics simulations.[20−25] A detailed picture of the local environment probed by the spin label and of the various processes modulating its orientations can be attained by such means, but at a computational cost which can be very great due to the huge number of degrees of freedom. Conformational transitions in the side chain occur on the nanosecond time scale; therefore, even long trajectories can sample just a few conformations. A more effective sampling can be achieved, e.g., by suitable Monte Carlo techniques[26,27] or by MD simulations under nonrealistic conditions such as very high temperature; with these choices, however, information on the time dependence of the processes is lost. Also, the use of MD trajectories with frozen protein degrees of freedom has been proposed for the study of the dynamics of the spin label.[28] The present work should not be intended as an alternative to these simulation techniques, but rather as a complementary method. The study of the system under the simpler approach we use directly provides useful physical insights, and these can also yield suggestions for sampling the side chain conformational space and extracting magnetically relevant parameters from trajectories. The results of this study can also be used to directly introduce the nitroxide dynamics in line shape analysis: in a companion paper, they will be exploited in the framework of line shape theory to interpret the ESR spectra of mutants of T4 lysozyme.[29]

The paper is organized in the following way. In the next section (II), the model for the conformational dynamics of the nitroxide side chain is presented. Then the results of the conformational study and the dynamical analysis are reported and the averaging of magnetic tensors produced by side chain motions is examined (Section III). In the final section (IV), the results of our investigation are discussed, stressing their implication for the ESR spectra of spin-labeled proteins, and the conclusions of this work are summarized.

II. Conformational Dynamics of a Nitroxide Side Chain Linked to an α-Helix

A. Torsional Potential and Distribution. Under the assumption of fixed bond lengths and bond angles, the geometry of the MTSSL spin label, whose structure is reported in Figure 1, is specified by the values of the five dihedral angles denoted as $\boldsymbol{\chi} = (\chi_1, ..., \chi_5)$. The potential energy of the nitroxide chain linked to an α-helix is expressed as

$$V(\boldsymbol{\chi}) = V'(\boldsymbol{\chi}) + V''(\boldsymbol{\chi}) \tag{1}$$

where V' is the torsional potential of the isolated chain, while V'' accounts for interactions of the chain with its neighborhood in the protein, i.e., the α-helix backbone and the side chains of the nearby residues. The former term is approximated as a sum of single bond contributions:

$$V'(\boldsymbol{\chi}) \approx V^{(1)}(\chi_1) + ... + V^{(5)}(\chi_5) \tag{2}$$

If the potential energy is characterized by minima separated by sufficiently high barriers of at least a few k_BT units, a simplified description can be adopted in terms of a finite number of rotational isomers (rotamers),[30] each corresponding to a given energy minimum. The geometry of the Jth conformer is defined by the five-dimensional vector $\boldsymbol{\chi}^J = (\chi_1^J, ..., \chi_5^J)$, with χ_i^J being the value of the ith dihedral for this conformer. Namely, the torsional angle distribution

$$p(\boldsymbol{\chi}) = \frac{\exp[-V(\boldsymbol{\chi})/k_BT]}{\int d\boldsymbol{\chi} \exp[-V(\boldsymbol{\chi})/k_BT]} \tag{3}$$

can be approximated as the sum:

$$p(\boldsymbol{\chi}) \approx \sum_J p_J(\delta\boldsymbol{\chi}^J) \tag{4}$$

with $\delta\boldsymbol{\chi}^J = \boldsymbol{\chi} - \boldsymbol{\chi}^J$ and $p_J(\delta\boldsymbol{\chi}^J)$ being the torsional angle distribution for the Jth conformer:

$$p_J(\delta\boldsymbol{\chi}^J) = \frac{\exp[-V(\delta\boldsymbol{\chi}^J)/k_BT]}{\sum_J \int d(\delta\boldsymbol{\chi}^J) \exp[-V(\delta\boldsymbol{\chi}^J)/k_BT]} \tag{5}$$

The function $V(\delta\boldsymbol{\chi}^J)$ represents the torsional potential of the chain in the neighborhood of the Jth minimum, which can be approximated by a harmonic expansion:

$$V(\delta\boldsymbol{\chi}^J) \approx V_J + \frac{1}{2}(\delta\boldsymbol{\chi}^J)\cdot\mathbf{V}_J^{(2)}\cdot(\delta\boldsymbol{\chi}^J) \tag{6}$$

where V_J is the potential energy of the chain in the conformation specified by the dihedral angles $\boldsymbol{\chi} = \boldsymbol{\chi}^J$, and $\mathbf{V}_J^{(2)}$ is the matrix of the second derivatives of the potential energy at the same point. Thus, the torsional distribution for the Jth conformer, eq 5, can be rewritten as:

$$p_J(\delta\boldsymbol{\chi}^J) \approx \frac{\exp\{-[V_J + (\delta\boldsymbol{\chi}^J)\cdot\mathbf{V}_J^{(2)}\cdot(\delta\boldsymbol{\chi}^J)/2]/k_BT\}}{(2\pi k_BT)^{5/2}\sum_J (\det\mathbf{V}_J^{(2)})^{-1/2}} \tag{7}$$

where $\det\mathbf{V}_J^{(2)}$ indicates the determinant of the matrix.

By integrating this multivariate Gaussian distribution over the $\delta\boldsymbol{\chi}^J$ variables, the probability of the Jth conformer can be defined:

$$P_J = \frac{\exp(-E_J/k_BT)}{\sum_J \exp(-E_J/k_BT)} \tag{8}$$

where E_J is the free energy:[31]

$$E_J = V_J + \frac{k_BT}{2}\ln\frac{\det\mathbf{V}_J^{(2)}}{(2\pi k_BT)^5} \tag{9}$$

B. Dynamics. In the presence of sufficiently high energy barriers between conformers, the chain dynamics can be described in terms of jumps between stable conformers and torsional oscillations in the minima of the potential.[16] In view of the time scale separation, the two motions can be treated separately. For long chains, simultaneous small rotations around several bonds can produce large amplitude displacements of the

tail end, with characteristic times comparable to isomerization times.[32] However, couplings can be neglected for short chains, like that of MTSSL.[18] Thus, conformational jumps can be simply described by the master equation:

$$\frac{\partial P_J(t)}{\partial t} = -\sum_{J'} W_{JJ'} P_{J'}(t) \tag{10}$$

where $P_J(t)$ is the time-dependent probability of the Jth conformer and $-W_{JJ'}$, with $J \neq J'$, represents the $J \leftarrow J'$ transition rate. If multiple transitions are neglected, in view of their high activation energy, the only nonvanishing matrix elements are those between conformers connected by single bond rotations. In the viscous regime characterizing chain motions in water solutions, where inertial effects are damped out, bond rotations can be described as diffusive processes, and transition rates can be expressed in terms of potential energy and friction opposing such rotations, according to the Kramers theory.[33] For barrier crossing in a system with several degrees of freedom, the following expression is obtained:[15,16,34]

$$W_{JJ'} = \frac{\lambda}{2\pi} \exp\left[-\frac{E_S - E_{J'}}{k_B T}\right] \qquad J \neq J' \tag{11}$$

Here $E_{J'}$ is the free energy of the J' conformer, defined in eq 9, and E_s is that at the saddle point, defined in an analogous way, with $\mathbf{V_s}^{(2)}$ the matrix of the second derivatives of the potential energy at the saddle point. The parameter λ is the unique negative eigenvalue of the matrix $\mathbf{D_s V_s}^{(2)}/k_B T$, where $\boldsymbol{D}_\mathbf{s}$ is 5×5 diffusion matrix calculated for the chain geometry at the saddle point. It is related to the friction matrix, $\boldsymbol{\xi}_s$, by the Stokes−Einstein relation, $\mathbf{D_s} = k_B T \boldsymbol{\xi}_s^{-1}$. It is worth emphasizing that transition rates calculated in this way take into account the coupling between reaction coordinate (the rotating dihedral) and nonreactive modes; barrier crossing occurs through cooperative small rotations of bonds adjacent that undergoing the conformational change in such a way as to optimize frictional and energetic effects at barrier crossing. The diagonal terms of the transition matrix are obtained by the detailed balance condition, which guarantees the existence of a stationary solution, equal to the equilibrium distribution, eq 8:

$$W_{JJ} = -P_J^{-1} \sum_{J' \neq J} W_{JJ'} P_{J'} \tag{12}$$

It is convenient to work with the symmetrized form of the transition matrix, which will be denoted as $\tilde{\mathbf{W}}$, and whose elements are defined as:

$$\tilde{W}_{JJ'} = P_J^{-1/2} W_{JJ'} P_{J'}^{1/2} = \frac{\lambda}{2\pi} \exp\left[-\frac{E_S - E_J/2 - E_{J'}/2}{k_B T}\right] \tag{13}$$

Within the harmonic approximation, damped oscillations within the potential well corresponding to the Jth conformer are described by the time-dependent probability density $p_J(\delta\boldsymbol{\chi}^J,t)$, which evolves in time according to the multivariate Fokker−Planck−Smoluchowski equation:

$$\frac{\partial p_J(\delta\boldsymbol{\chi}^J,t)}{\partial t} = \left(\frac{\partial}{\partial(\delta\boldsymbol{\chi}^J)}\right) \cdot \mathbf{D}_J \cdot \left[\left(\frac{\partial}{\partial(\delta\boldsymbol{\chi}^J)}\right) + \left(\frac{\mathbf{V}_J^{(2)} \cdot \delta\boldsymbol{\chi}^J}{k_B T}\right)\right] p_J(\delta\boldsymbol{\chi}^J,t) \tag{14}$$

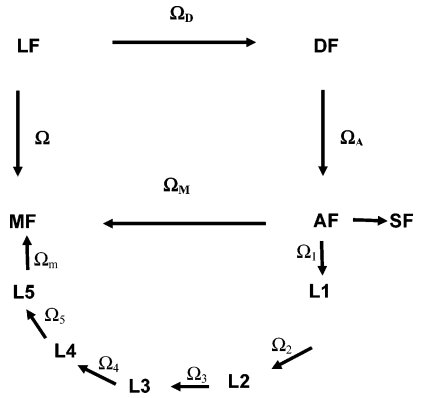

Figure 2. Reference frames considered in this work. LF: laboratory frame, with $Z_L \parallel B_0$. DF: Principal axis system (PAS) of the rotational diffusion tensor of the protein. AF: amino acid residue frame, with the origin on the C_α bringing the nitroxide side chain, the z_A axis perpendicular to the plane of the N−C_α−CO atoms, and the x_A axis on the plane containing the z_A axis and C_α−C_β bond. L_i: local frame, with $z_{L_i} \parallel i$th chain bond and x_{L_i} in the plane of the preceding chain bond when $\chi_{i-1} = 0°$. MF: magnetic frame, with the origin on the nitroxide N nucleus, the z_M axis along the N-p_z orbital, and the x_M axis parallel to the N−O bond. SF: ordering frame, with the axes parallel to the principal ordering axes.

where $\mathbf{D}_J = k_B T \boldsymbol{\xi}_J^{-1}$ is the diffusion matrix calculated for the geometry of the Jth conformer. This equation can be easily solved by a normal mode transformation:[35,36]

$$\frac{\partial p_J(\mathbf{y},t)}{\partial t} = \sum_i \frac{\partial}{\partial y_i}\left(\frac{\partial}{\partial y_i} + \Lambda_i^J y_i\right) p_J(\mathbf{y},t) \tag{15}$$

with $\delta\boldsymbol{\chi}^J = \mathbf{U}\mathbf{y}$ and $\mathbf{U}^{-1}\mathbf{D}_J\mathbf{V}_J^{(2)}\mathbf{U} = k_B T \boldsymbol{\Lambda}^J$. Correlation functions for normal modes decay as simple exponentials, with time constants equal to the inverse of the eigenvalues Λ_i^J:

$$\overline{y_i(0)y_i(t)}/\overline{y_i(0)y_i(0)} = e^{-\Lambda_i^J t} \tag{16}$$

C. Orientational Distribution of the Spin Label. Amplitude and symmetry of the orientational distribution of the spin label produced by the side chain dynamics can be quantified by the order parameters:

$$\overline{D_{qk}^L(\Omega_M)} = \int \mathrm{d}\Omega_M D_{qk}^L(\Omega_M) p(\Omega_M) \tag{17}$$

where $D_{qk}^L(\Omega_M)$ are Wigner matrix elements, $p(\Omega_M)$ is the orientational distribution function, and Ω_M are the Euler angles defining the orientation of the spin label in a frame fixed on the C_α atom bringing the spin label (the frame of the amino acid residue, according to the notation used in Figure 2). The nonvanishing order parameters depend on the symmetry of the orientational distribution of the spin probe; all order parameters vanish if orientations are isotropically sampled. In principle, Wigner matrices of any rank L could be needed; here, we shall limit our consideration to second-rank matrices, which are involved in the transformation of the magnetic tensors. Some general considerations on second-rank order parameters are presented in the Appendix. In the following, the expressions used to calculate the order parameters of the spin label in the presence of torsional oscillations and conformational jumps are reported. For this purpose, it is convenient to introduce the coordinate transformations shown in Figure 2.

Average values of Wigner rotation matrices for the Jth conformer are obtained by integrating over the torsional distribution eq 7. Under the assumption of independent bond

contributions, this can be expressed as the product of the single bond probabilities:

$$p_{J,i}(\delta\chi_i^J) \approx \frac{\exp[-V_{J,i}^{(2)}(\delta\chi_i^J)^2/2k_BT]}{(2\pi k_BT/V_{J,i}^{(2)})^{1/2}} \quad (18)$$

with $V_{J,i}^{(2)}$ being the second derivative of the chain potential energy with respect to the χ_i variable, calculated for $\chi_i = \chi_i^J$. Then, the addition theorem for Wigner matrices[38] can be exploited to decompose the AF → MF rotation into a set of local transformations, and the order parameters for the Jth conformers can be expressed as:

$$\overline{D^2_{qk}(\Omega_M^J)} = \sum_{q_1,q_2,q_3,q_4,q_5} D^2_{q,q_1}(\Omega_1^J)\,\overline{D^2_{q_1,q_2}(\tilde{\Omega}_2^J)}\ldots \overline{D^2_{q_4,q_5}(\tilde{\Omega}_5^J)}\,\overline{D^2_{q_5,k}(\tilde{\Omega}_m^J)} \quad (19)$$

Here the Euler angles $\Omega_{i+1}^J = (\chi_i^J, \beta_{i+1}^J, \gamma_{i+1}^J)$, $\tilde{\Omega}_{i+1}^J = (\chi_i^J + \delta\chi_i^J, \beta_{i+1}^J, \gamma_{i+1}^J)$ and $\tilde{\Omega}_m^J = (\chi_5^J + \delta\chi_5^J, \beta_m^J, \gamma_m^J)$ appear, which describe the local transformations $L_i \rightarrow L_{i+1}$, with the chain in the Jth conformation (see Figure 2). The single bond averages have the form:

$$\overline{D^2_{q_i,q_{i+1}}(\tilde{\Omega}_{i+1}^J)} = \overline{e^{-iq_i\delta\chi_i^J}}\, D^2_{q_i,q_{i+1}}(\Omega_{i+1}^J) \quad (20)$$

with

$$\overline{e^{-iq_i\delta\chi_i^J}} = \int \mathrm{d}(\delta\chi_i^J)\, p_{J,i}(\delta\chi_i^J) e^{-iq_i\delta\chi_i^J} \approx \exp\left(-\frac{q_i^2}{2}\overline{(\delta\chi_i^J)^2}\right) \quad (21)$$

where $\overline{(\delta\chi_i^J)^2}$ is the mean square amplitude of the single bond torsional distribution:

$$\overline{(\delta\chi_i^J)^2} = \int \mathrm{d}(\delta\chi_i^J)\, p_{J,\,i}(\delta\chi_i^J)\,(\delta\chi_i^J)^2 \approx \left(\frac{k_BT}{V_{J,i}^{(2)}}\right) \quad (22)$$

For a set of conformers which in addition to torsional oscillations undergo conformational jumps, the order parameters can be obtained as

$$\overline{D^2_{q,k}(\Omega_M)} = \sum_J P_J\,\overline{D^2_{q,k}(\Omega_M^J)} = \frac{\sum_J e^{-V_J/k_BT}(\det\mathbf{V}_J^{(2)})^{-1/2}\,\overline{D^2_{q,k}(\Omega_M^J)}}{\sum_J e^{-V_J/k_BT}(\det\mathbf{V}_J^{(2)})^{-1/2}} \quad (23)$$

with the average Wigner matrix elements calculated according to eq 21 and the sum extended to all interconverting conformers.

The magnetic tensors partially averaged by chain motions can be expressed in terms of these order parameters:

$$\overline{F_{\mu;AF}^{(2,q)}} = \sum_k \overline{D^2_{q,k}{}^*(\Omega_M)}\, F_{\mu;MF}^{(2,k)} \quad (24)$$

where $\mu = g$ or $\mu = A$, for the **g** and the **A** hyperfine tensor, respectively.

III. Results: Nitroxide Chain Motions

A. Conformational Analysis. The single bond contributions to the torsional potential, $V^{(i)}(\chi_i)$, for the MTSSL chain have been obtained by considering the subsystems that are shown in Figure 3. Ab initio calculations in a vacuum have been performed at the HF/6-31G** level (ROHF/6-31G** for the subsystem containing the nitroxide).[39] The torsional potential for a given bond was obtained by relaxed scan in the range −180° to +180°. Figure 3 shows the torsional profiles as a function of the dihedral angles. The following convention is used: a right-handed rotation, with the rotation axis directed toward the chain end, is taken as positive. Using the notation adopted for alkyl chains, minima close to 180° will be designed as t states, whereas the labels $g_\pm$ will be used for minima characterized by dihedrals ranging between ±40° and ±120°.[30]

For the χ_1 dihedral, rotation of the $-CH_2-S-SH$ group, linked at the C_α atom of a $CH_3-NH-C_\alpha H-CO-CH_3$ fragment frozen in the standard α-helix geometry, has been examined. The torsional potential shown in Figure 3A was obtained by taking the $C_\alpha-C_\beta-S_\gamma-S_\delta$ dihedral in the t conformation and the $C_\beta-S_\gamma-S_\delta-H$ dihedral close to +90°; analogous profiles were found with the former in $g_\pm$ states and/or the latter close to −90°. The features of the torsional potential are in accordance with the results of the conformational analysis of the cysteine sulfhydryl in proteins.[40,41] There are two roughly equivalent minima corresponding to staggered configurations with the $N-C_\alpha-C_\beta-S_\gamma$ dihedral equal to 180° in one ($C_\beta-S_\gamma$ bond between the $C_\alpha-CO$ and the $C_\alpha-H$ bonds) and to +65° in the other ($C_\beta-S_\gamma$ bond between the $C_\alpha-NH$ and the $C_\alpha-CO$ bonds); a lower minimum is found for a dihedral equal to −60° ($C_\beta-S_\gamma$ bond between the $C_\alpha-H$ and the $C_\alpha-NH$ bonds). The minima are separated by high barriers, corresponding to eclipsed configurations; a significantly lower barrier is obtained for the configuration with the $C_\beta-S_\gamma$ bond over the $C_\alpha-H$ bond.

The rotation of the central bond of the CH_3-CH_2-S-SH model system has been considered to calculate the torsional profile for the χ_2 and χ_4 dihedral angles (Figure 3C). The resulting profile is similar in shape to that for the central C−C bond of *n*-butane; it is symmetric with respect to $\chi_2(\chi_4) = 0°$, with the absolute minimum at 180° (t), and two equivalent relative minima at ±75° ($g_\pm$). Barriers on the order of a few k_BT units at room temperature separate t and $g_\pm$ minima.

The $CH_3-S-S-CH_3$ fragment has been studied to obtain the $V^{(3)}(\chi_3)$ torsional potential (Figure 3B). Only two minima are found for values of the $CH_3-S-S-CH_3$ dihedral equal to ±90°, separated by high barriers.

Finally, the torsional potential for the χ_5 dihedral has been calculated as a function of the angle about the bond connecting the pyrroline ring to the tether, in the system $CH_3-S-S-CH_2$-sl, with sl = 1-oxy-2,2,5,5-tetramethylpyrroline (R1 spin probe) and sl = 1-oxy-2,2,4,5,5-pentamethylpyrroline (R2 spin probe). Calculations for R1 have been performed with the $S-S-CH_2-C$ dihedral angle constrained either in the t or in the g state. In the former case (Figure 3D), configurations with the $S-CH_2-C-CH$ dihedral angle significantly larger than ∼+120° or smaller than ∼−120° have very high energy. For values falling within the range of ±120° the energy profile becomes rather flat, with two minima at $\chi_5 \sim \pm 77°$, separated by a shallow barrier, whose size and shape is very sensitive to the level of calculation. On the contrary, when the $S-S-CH_2-C$ dihedral is in the $g_\pm$ state, the torsional profile for $S-CH_2-C-CH$ has two minima, at ±10° and −100°, with a barrier of a few k_BT at room temperature (Figure 3E). In the case of the R2 spin probe, the presence of the methyl substituent at the 4-position in the pyrroline ring prevents the possibility of configurations with the $S-S-CH_2-C$ dihedral in g states. When

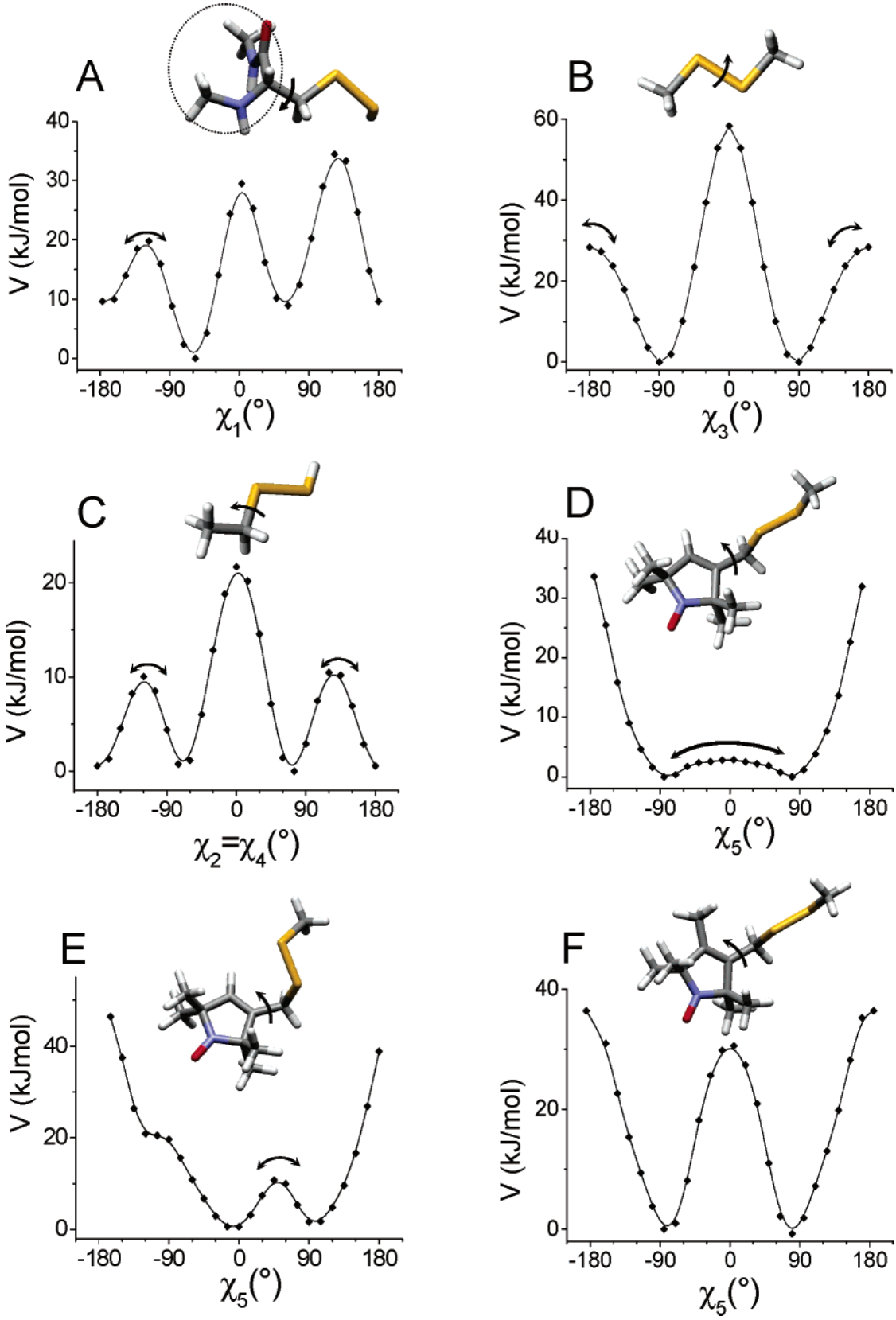

Figure 3. Torsional potentials and model subsystems considered for calculating them. Arrows indicate the rotating bonds, with the convention used to define the sense of rotation: a right-handed rotation, with the rotation axis directed toward the chain end, is taken as positive. For χ_1, the value $\chi_1 = 0°$ corresponds to the eclipsed configuration with the $C_\beta-S_\gamma$ bond over the $C_\alpha-N$ bond. For χ_5, the value $\chi_5 = 0°$ corresponds to the eclipsed configuration with the C−CH double bond of the pyrroline ring over the CH_2-S_δ bond. The dashed circle shows atoms that have been kept frozen in the α-helix configuration in calculations for χ_1. Arrows in the torsional profiles show transitions between the allowed conformers, which are listed in Table 2. The solid line is a guide to the eye.

this angle is in the *t* state, two minima are found, with $\chi 5 = \pm 85°$, separated by very high barriers (Figure 3F).

Values of the dihedral angles at the minima of the torsional potentials are collected in Table 1. For the χ_1 to χ_4 dihedrals,

TABLE 1: Values of the Dihedral Angles at the Minima of the Torsional Potentials $V^{(i)}(\chi_i)$

χ_1	$-60°$ (g_-), $+65°$ (g_+), $180°$ (t)
$\chi_2 \equiv \chi_4$	$-75°$ (g_-), $+75°$ (g_+), $180°$ (t)
χ_3	$-90°$ (g_-), $+90°$ (g_+)
χ_5[a]	$-77°$ (g_-), $+77°$ (g_+)
χ_5[b]	$\pm 8°$, $\mp 100°$

[a] χ_4 in the t state. [b] χ_4 in the $g_\pm$ state.

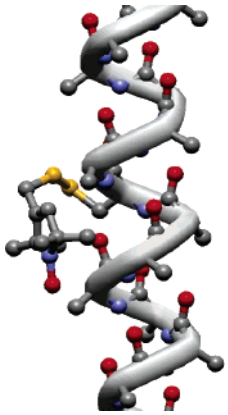

Figure 4. Poly-Ala α-helix with the R1 spin label in a sterically forbidden conformation ($\chi_1 = -60°$, $\chi_2 = -75°$, $\chi_3 = -90°$, $\chi_4 = +75°$).

the minima are separated by high barriers, which range from about $4k_BT$ for the $g \rightleftharpoons t$ transitions of χ_2 or χ_4, to more than 10 k_BT for the $-90° \rightleftharpoons +90°$ transitions of χ_3. Analogous considerations hold for the χ_5 dihedral of R2 and also for that of R1 if χ_4 is in the g state. It follows that, in all these cases, the nitroxide side chain can be described in terms of a finite number of stable rotamers.[30] From eq 22, we can estimate root-mean-square fluctuations of about 12.5° for the χ_2 and χ_4 dihedrals, and 8.5° for χ_1 and χ_3, at $T = 298$ K. An increase of about 5% can be estimated under a 10° increase in temperature. A root-mean-square amplitude of 12.5° is appropriate also for the χ_5 dihedral of R2 and for that of R1 when χ_4 is in the g state ($\chi_5|_{\chi4=g}$). The situation for the χ_5 dihedral of R1 can be quite different when χ_4 is in the t state ($\chi_5|_{\chi4=t}$); from the torsional potential shown in Figure 3D, a wider distribution of χ_5 values about the minima is inferred, and the simple description in terms of a few conformational states may not be fully satisfactory.

Taking the minima of the single bond torsional potentials, a total number of 108 and 54 conformers can be estimated for R1 and R2, respectively. This number is reduced by interactions of the spin label with its environment, i.e., backbone and side chains of nearby residues. We have introduced such effects, described by the V'' contribution in eq 1, at the level of steric interactions, which have been modeled in terms of excluded volume. For this purpose, each of the possible conformers of the nitroxide side chain was inserted in a poly-Ala α-helix and was excluded if the distance between any pair of atoms was shorter than the sum of their van der Waals radii. The following values have been used: $r_C = 1.5$ Å, $r_O = 1.35$ Å, $r_N = 1.4$ Å, $r_S = 1.8$ Å. It is worth mentioning that the choice of these values is not critical for the determination of the excluded conformers because these do suffer severe hindrance; as an example, Figure 4 shows a forbidden conformer of R1. After the steric control, the number of allowed conformers is reduced from 108 to 18 for R1 and from 54 to 10 for R2; values of the dihedral angles defining their geometry are listed in Table 2. The conformers possible for R2 are denoted by an asterisk in the Table. The

TABLE 2: Torsional Angles and Probabilities for the Sterically Allowed Conformers of the Nitroxide Side Chain of the R1 Spin Label, at a Site Located in the Middle of a Poly-Ala Helix[a]

conformer	χ_1 (deg)	χ_2 (deg)	χ_3 (deg)	χ_4 (deg)	χ_5 (deg)	P_J
C1*	−60	−75	−90	180	+77 (+85)	0.143 (0.201)
C2*	−60	−75	−90	180	−77 (−85)	0.143 (0.201)
C3	−60	−75	−90	−75	+100	0.045
C4	−60	−75	−90	−75	−8	0.074
C5*	−60	180	90	180	+77 (+85)	0.187 (0.263)
C6*	−60	180	90	180	−77 (−85)	0.187 (0.263)
C7	−60	180	90	+75	−100	0.059
C8	−60	180	90	+75	+8	0.098
C9*	180	180	−90	180	+77 (+85)	0.009 (0.013)
C10*	180	180	−90	180	−77 (−85)	0.009 (0.013)
C11	180	180	−90	−75	+100	0.003
C12	180	180	−90	−75	−8	0.005
C13*	180	180	90	180	+77 (+85)	0.009 (0.013)
C14*	180	180	90	180	−77 (−85)	0.009 (0.013)
C15*	180	75	90	180	+77 (+85)	0.007 (0.010)
C16*	180	75	90	180	−77 (−85)	0.007 (0.010)
C17	180	75	90	+75	−100	0.002
C18	180	75	90	+75	+8	0.004

[a] Statistical weights were calculated at $T = 298$ K on the basis of the single bond torsional potential, V' in eq 1. Conformers allowed for the R2 spin probe are denoted by an asterisk; probability and χ_5 values for these are reported in parentheses.

geometry of the allowed conformers is displayed in Figure 5; here, a compact representation is adopted, with each structure corresponding to a set of conformers connected by χ_4 and χ_5 jumps. Inspection of Table 2 shows that some single bond conformational states, predicted for the isolated chain, are forbidden by the α-helix environment. This is the case, for instance, of the g_+ state, which according to Figure 3A should be as populated as the t state for the χ_1 dihedral, but never appears in Table 2. This very low probability of the g_+ state of the $N-C_\alpha-C_\beta-S_\gamma$ dihedral in α-helices is confirmed by the analysis of the conformers of cysteine, as shown, e.g., in ref 43.

Table 2 also reports the conformer probabilities, P_J, calculated at $T = 298$ K according to eq 8. Root-mean-square fluctuations $\overline{(\delta\chi_5^J)^2}^{1/2} = 20°$ were assumed for conformers of R1 with χ_4 in the t state. We can see that the overall weight of conformers with χ_1 in the g_- state greatly exceeds that of conformers having χ_1 in the t state. Of course, the probabilities reported in Table 2 should be considered as only a first-order estimate; indeed, the primary result of our analysis is the identification of a restricted number of allowed conformers and of their geometry. The actual probabilities for MTSSL at a given helical site could be significantly affected by local effects, depending on the nature of the nearby residues and/or the presence of attractive interactions involving the spin label, which are not taken into account in our present model. In the companion paper,[29] where the effects of the chain dynamics on the ESR spectra are investigated, it is shown that the presence of conformers with different mobility do yield the appropriate spectral contributions, but with weights that are different from those predicted by the calculated probabilities.

The geometry we have predicted for the conformers of R1 is in general agreement with the values determined from X-ray structures of four spin-labeled T4L mutants.[41,42] The g_-g_-, g_-t, and tg_+ configurations for $\chi_1\chi_2$, which were found in the crystal structures, also appear in Table 2. For the latter, we predict a very low probability; actually, the interaction with a nearby residue was suggested as the reason for its stabilization in the

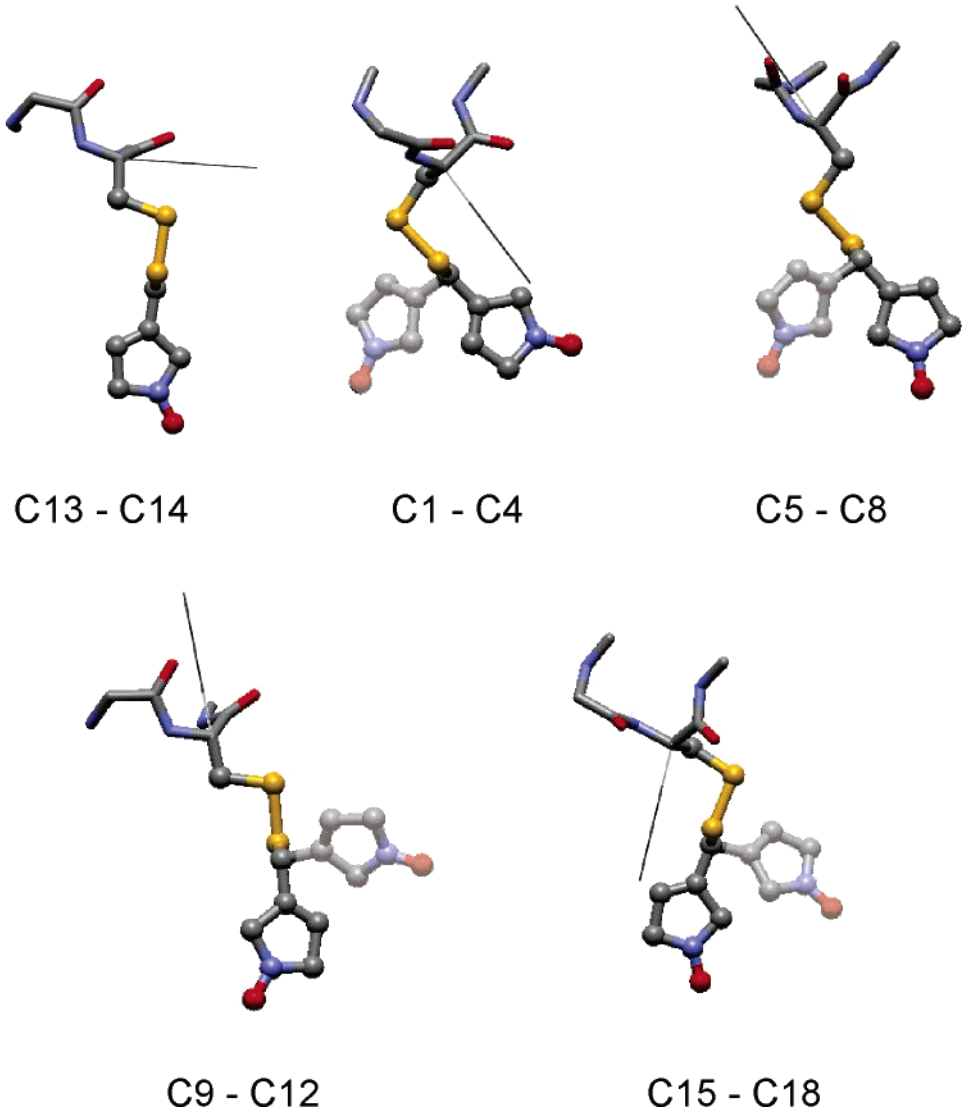

Figure 5. Geometry of the allowed conformers of the R1 spin label listed in Table 2. Each figure corresponds to a set of interconverting conformers. Only half of the conformers are shown, which correspond to one of the two possible χ_5 states compatible with a given χ_4 state. Conformers connected by a χ_4 rotation are superimposed on the same structure. To avoid crowding, the methyl substituents in the pyrroline ring have been eliminated. The ball-and-stick representation is used for the side chain, while simple sticks indicate backbone bonds. The black line shows the orientation of the *Y*-ordering axis; the *Z*-ordering axis is perpendicular to the plane of the figure.

crystal. No experimental data confirm the *tt* configuration, which from our analysis is sterically allowed, although with very low weight.

B. Dynamics. We start by considering the R1 spin label; Table 3 reports the elements of the symmetrized transition matrix $\tilde{\mathbf{W}}$, calculated according to eq 13, in water solution at $T = 298$ K. Given the 18 conformers listed in Table 2, the possible single bond transitions are those indicated by arrows in Figure 3. Our simple picture of conformational jumps is not strictly valid in the absence of a sufficiently high barrier, as in the case of the $\chi_5|_{\chi4=t}$ dihedral, in which case the whole torsional distribution should be taken into account. On the other hand, a detailed description is prevented by the degree of uncertainty affecting the shape of this torsional profile, which, as already mentioned, also depends on the computational method; moreover, the possibility of high barriers can be hypothesized due to interactions involving the pyrroline ring.[42] Therefore, we have adopted also for χ_5 the description in terms of jumps between the minima of the torsional potential, which, in addition to the advantage of simplicity, allows us to obtain quantitative results without the need of a detailed knowledge of the torsional potential, as we shall see below.

According to eq 11, calculation of the transition rates requires the evaluation of the friction matrix accounting for the viscous torques opposing bond rotations.[15] For a given transition, the 5 $\times$ 5 friction matrix is evaluated for the saddle point geometry of the side chain.[44] A united atom representation has been used: the nitroxide side chain is described as a collection of spheres, corresponding to the N, O, S, and C atoms and the CH, CH_3, and CH_2 groups. For the sake of simplicity, identical spheres of hydrodynamic radius equal to 1 Å have been taken. With these choices, a value of 10^{10} s^{-1} is predicted for the $g \rightarrow t$ transition rate of *n*-butane at room temperature.[15]

It appears clearly from Table 3 that a limited number of single bond jumps is possible. To understand the results reported in the Table, it is worth reminding the reader that the transition rate between a pair of conformers is determined by energetic and frictional effects, i.e., the height of the barrier that has to be crossed and the friction opposing the chain motion in the solution environment. Rotation about a given bond can be slower

TABLE 3: Off-Diagonal Elements of the Symmetrized Transition Matrix $\tilde{W}$, Calculated for Water Solution at $T = 298$ K[a]

	C1	C2	C3	C4	C5	C6	C7	C8	C9	C10	C11	C12	C13	C14	C15	C16	C17	C18
C1		**>10** (χ_5)	**1.5** (χ_4)															
C2	**>10** (χ_5)																	
C3	**1.5** (χ_4)			**1.5** (χ_4)														
C4			**1.5** (χ_5)															
C5						**>10** (χ_5)							0.01 (χ_1)					
C6					**>10** (χ_5)		**0.36** (χ_4)							0.01 (χ_1)				
C7						**0.36** (χ_4)		**1.5** (χ_5)										
C8							**1.5** (χ_5)											
C9										**>10** (χ_5)	**0.36** (χ_4)		0.002 (χ_3)					
C10									**>10** (χ_5)					0.002 (χ_3)				
C11									**0.36** (χ_4)			**1.5** (χ_5)						
C12											**1.5** (χ_5)							
C13					0.01 (χ_1)				0.002 (χ_3)					**>10** (χ_5)	0.05 (χ_2)			
C14						0.01 (χ_1)				0.002 (χ_3)			**>10** (χ_5)			0.05 (χ_2)		
C15													0.05 (χ_2)			**>10** (χ_5)		
C16														0.05 (χ_2)	**>10** (χ_5)		**1.5** (χ_4)	
C17																**1.5** (χ_4)		**1.5** (χ_5)
C18																	**1.5** (χ_5)	

[a] The matrix elements are reported, in units of 10^9 s^{-1}. Rates higher than 10^8 s^{-1} are shown in boldface. Under each transition rate, the dihedral angle involved in the conformational jump is reported in parenthesis.

or faster, depending on the chain geometry, which affects the friction opposing such rotations and the degree of bond cooperativity in the barrier crossing. We can see that interconversions involving the χ_3 and χ_1 dihedrals are predicted to be very slow by virtue of the high barriers and the large friction accompanying the displacements of bulky chain portions. Higher rates are obtained for χ_2 and χ_4 rotations because lower barriers have to be crossed. The latter are predicted to be about 1 order of magnitude faster than the former, and this can be explained by considering that they produce displacement of a smaller chain portion, therefore they are characterized by lower friction. In view of the arguments presented above, only a lower bound for $\chi_5|_{\chi4=t}$ transitions is reported, which would correspond to a barrier comparable to that for $\chi_5|_{\chi4=g}$ transitions. Anyway, as a consequence of the relatively low friction, high rates are predicted for χ_5 jumps.

The χ_4 and χ_5 dynamics occur on the time scale of standard X-band ESR; therefore, it should have appreciable effects on line shapes. The χ_2 and χ_3 transitions are expected to be much less effective, not only because they are slower, but mainly because the large amplitude chain displacements they would produce are likely to be sterically hindered in the α-helix environment. If such transitions are ignored, the 18 conformers of R1 can be grouped into four independent blocks, each containing four rotamers connected by χ_4 and χ_5 transitions: (C1−C4), (C5−C8), (C9−C12), and (C15−C18), in addition to a block of a pair of conformers, interconverting only through χ_5 jumps (C13 and C14).

If the same considerations are applied to the R2 spin label, 10 noninterconverting conformers are found, all having χ_4 in the *t* state and the pyrroline ring perpendicular to the $S_\delta CC$ plane, i.e., χ_5 equal to ±85°. These conformers can only undergo oscillations about the minima of the torsion potential. The characteristic frequencies of such motions, calculated according to eq 14, range from 10^9 s^{-1} to 10^{11} s^{-1} and, given the small amplitude of motions, are expected to have scarce effects on ESR line shapes.

C. Order Parameters and Partially Averaged Magnetic Tensors. Order parameters for the spin label orientational distribution and magnetic tensors partially averaged by the chain motions of the spin labels R1 and R2 are reported in Tables 4 and 5, respectively. The Cartesian representation is used; the relationships between irreducible spherical and Cartesian representation are reviewed in the Appendix, together with some general definitions. Table 4 reports the order parameters calculated for a few representative cases. Capital letters are used for the reference axes of the so-called ordering frame (SF), whereas small letters are used for the molecular axes, which correspond to the coordinate axes of the magnetic frame; $z = z_M$ is along the N-p_z orbital and $x = x_M$ is parallel to the N−O bond. Using liquid crystal terminology, the *X*, *Y*, and *Z* axes can be denoted as "directors". So S_{zz}^{KK}, with $K = X, Y, Z$, gives the degree of alignment of the z_M axis to the *K* director. The S_{ii}^{ZZ} order parameter, with $i = x, y, z$, accounts for the alignment of the *i*th magnetic axis with respect to the *Z* director. According to the usual convention, in the ordering frame, we shall denote as *Z* the axis with the highest order parameter, i.e., the axis to which z_M preferentially aligns. If the orientational distribution of the z_M axis, produced by chain

TABLE 4: Order Parameters for the Orientational Distribution of MTSSL Produced by the Side Chain Motions, Calculated for Selected Conformers at $T = 298$ K, under Different Conditions[a]

conformer	S_{zz}^{XX}	S_{zz}^{YY}	S_{zz}^{ZZ}	S_{xx}^{ZZ}	S_{yy}^{ZZ}	S_{xy}^{ZZ}	S_{xz}^{ZZ}	S_{yz}^{ZZ}	
C13	−0.44	−0.37	0.81	−0.44	−0.38	0.02	−0.01	0.01	
C13−C14	−0.44	−0.24	0.67	−0.37	−0.30	0.09	−0.01	−0.01	(a)
C13−C14	−0.44	0.03	0.47	−0.30	−0.17	0.19	−0.01	0.01	(b)
C1−C4	−0.28	−0.22	0.51	−0.25	−0.26	0.14	−0.05	0.02	(a)
C1−C4	−0.23	−0.12	0.35	−0.20	−0.15	0.22	−0.05	0.01	(b)

[a] The *X*, *Y*, *Z* axes are the so-called directors. For C13, only torsional oscillations are assumed, while for C13−C14 and C1−C4, conformational jumps are also taken into account, as explained in the text. Labels denote different choices for the $\chi_5|_{\chi 4=t}$ distribution. (a) Gaussian distribution of root-mean-square amplitude $\overline{(\delta\chi_5)^2}^{1/2} = 20°$; (b) distribution in the range 0° to ±120° under the torsional potential shown in Figure 3D.

TABLE 5: Magnetic Tensors Partially Averaged by Side Chain Motions, Calculated for Selected Conformers of MTSSL at $T = 298$ K, under Different Conditions (Same as in Table 4)[a]

conformers	g_{XX}	g_{YY}	g_{ZZ}	A_{XX}	A_{YY}	A_{ZZ}	A_{XY}	A_{XZ}	A_{YZ}	
C13	2.00767	2.00561	2.00275	7.74	8.46	32.00	0.47	−0.06	−0.10	
C13−C14	2.00708	2.00580	2.00315	7.56	11.32	29.32	−0.12	−1.14	−0.02	(a)
C13−C14	2.00710	2.00521	2.00372	7.71	15.35	25.14	−0.03	−1.91	−0.04	(b)
C1−C4	2.00628	2.00603	2.00372	11.77	10.43	26.00	−0.004	−1.21	0.59	(a)
C1−C4	2.00632	2.00557	2.00414	11.86	13.60	22.75	−0.59	−1.65	0.58	(b)

[a] Both tensors are expressed in the principal axis system of **g**. The following values before averaging have been assumed: $g_{xx} = 2.00803$, $g_{yy} = 2.00582$, $g_{zz} = 2.00218$, $A_{xx} = 6.42$ G, $A_{yy} = 5.95$ G, $A_{zz} = 35.83$ G.[47]

dynamics, has axial symmetry, the relation $S_{zz}^{XX} = S_{zz}^{YY} = -S_{zz}^{ZZ}/2$ holds, and a single director can be considered, i.e., the *Z* director, parallel to the C_∞ axis. For a perfectly rigid chain, the result $S_{zz}^{XX} = S_{zz}^{YY} = -1/2$ and $S_{zz}^{ZZ} = 1$ would be obtained, i.e., perfect order, with the *Z* axis parallel to the N-p_z orbital.

The first line of Table 4 reports the order parameters calculated for the C13 conformer experiencing only torsional oscillations; for the χ_5 dihedral, fluctuations with root-mean-square amplitude of 12.5° have been assumed, as in the case of the R2 spin label. The orientation of the *Z* and *Y* directors is similar to that shown in Figure 5 for the C13−C14 pair. In view of the strong confinement of motions, the order parameters are very high, with some biaxiality, i.e., the degree of alignment of the N-p_z orbital in the plane perpendicular to the *Z* director is anisotropic, with a preference of this orbital to lie on the *YZ* plane.[45]

The effect of χ_5 jumps is illustrated by the results reported in Table 4 for the C13−C14 pair. In this example, all dihedrals experience torsional oscillations; in addition, conformational jumps are possible for χ_5. Two different choices for the $\chi_5|_{\chi 4=t}$ distribution have been considered. In case (a), a Gaussian distribution centered in the minima of the single bond torsional potential is assumed, with root-mean-square amplitude $\overline{(\delta\chi_5)^2}^{1/2} = 20°$; this value is estimated from the curvature in the minima of the torsional potential, Figure 3D. In case (b), wider oscillations are allowed: for each minimum, the full distribution in the range 0° to ±120°, under the torsional potential shown in Figure 3D, is taken into account; analogous results would be obtained with a Gaussian distribution of root-mean-square amplitude $\overline{(\delta\chi_5)^2}^{1/2} \simeq 35-40°$. The orientation of the directors, which is imposed by the chain geometry, is shown in Figure 5; it is similar to that obtained for C13 in the absence of χ_5 jumps, with the *Z* axis not far from parallel to the S_δ−C bond. We can see from Table 4 that the presence of extended χ_5 motions has a twofold effect. One is that it reduces the orientational order, and the decrease is greater as the amplitude of fluctuations is greater about the minima of the torsional potential. On the other side, it increases the biaxiality of the distribution: the N-p_z orbital is more and more confined on the *YZ* plane, i.e., perpendicular to the S_δ−C bond. Considering now the S_{ii}^{ZZ} values, we can see that also the difference in alignment of the x_M and y_M axes to the *Z* director increases with increasing amplitude of χ_5 rotations. Moreover, the x_M and y_M axes no longer correspond to principal alignment directions in the magnetic frame.

The two bottom lines of Table 4 report the order parameters calculated for the C1−C4 set of interconverting conformers. Again, torsional fluctuations occur for all dihedrals, with the additional possibility of χ_4 and χ_5 conformational jumps. For the $\chi_5|_{\chi 4=t}$ distribution, the same two choices denoted above as (a) and (b) have been assumed. Comparison with the results obtained for the C13−C14 pair shows that the occurrence of χ_4 jumps has the effect of reducing not only the degree of order, but also the biaxiality in the distribution of both the ordering and magnetic axes. The orientation of the directors can be inferred from Figure 5; the *Z* and *Y* axes are roughly parallel to the S_δ−C bond and the C−S_γ bond, respectively.

The restricted chain motions are not very effective in averaging out the magnetic tensors of the spin probe, as shown in Table 5, which reports the components of the partially averaged **g** and hyperfine **A** tensors, both expressed in the principal axis system (PAS) of the former. In all cases, the partially averaged **A** tensor is not far from diagonal in the principal frame of the partially averaged **g** tensor, and the axes of this frame are close to the *X*, *Y*, *Z* directors. Again a clear dependence on the nature and amplitude of the side chain motions is found. Even conformational jumps, although they are more effective than torsional librations, are not able to fully average out the magnetic anisotropies. Interestingly, as a consequence of the lack of any symmetry in the distribution of the N-p_z orbital, the partially averaged hyperfine tensor loses its quasi-axial symmetry.

The considerations presented here for C13, for the C13−C14 pair and for the C1−C4 block could be extended to other isolated and interconverting conformers, respectively. Because of the change in the chain geometry, the orientation of the ordering frame (SF) in the molecular frame (AF) depends on the conformer, but both order parameters and partially averaged tensors are similar for all isolated conformers on one side, and for all blocks of interconverting conformers on the other side.

In the context of ESR line shape analysis, order parameters or coefficients related to them are often introduced to specify the motional restrictions experienced by the spin probe, and in

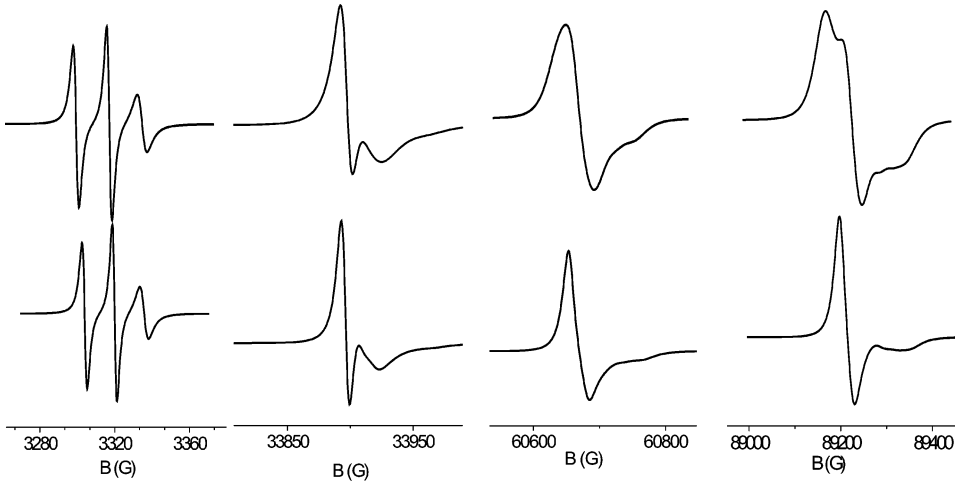

Figure 6. ESR spectra at different frequencies calculated for the R2 spin probe with partially averaged magnetic tensors, undergoing overall rotational diffusion with an isotropic diffusion coefficient $D_0 = 10^8\ s^{-1}$. Top: the partially averaged tensors reported in Table 5 for C13 have been used. Bottom: axial partially averaged tensors have been used, which have been obtained from the values reported in Table 5 for C13, taking indentical *X* and *Y* components, equal to the mean of the values *X* and *Y* values appearing in the Table. The examples correspond to 9.4, 95, 170, and 250 GHz from left to right.

general some simplifying assumptions are made. In all cases, axial symmetry of the orientational distribution of z_M is assumed. At the lowest level, e.g., in the model of diffusion in a cone, also the equivalence of the x_M and y_M axes is assumed, and the single-order parameter $S^{2,0} = \overline{D^2_{0,0}(\Omega_M)}$ is used. The additional order parameter $S^{2,2} = 2\mathrm{Re}\ \overline{D^2_{0,2}(\Omega_M)}$ is introduced by more general approaches, which however make the simplifying assumptions that the principal alignment axes of the magnetic frame coincide with the x_M, y_M, z_M axes, and that any biaxiality of the z_M distribution may be neglected.[46−49] The inadequacy of such assumptions to account for the orientational distribution of MTSSL spin probes emerges from our study; analogous conclusions were reached by Budil and co-workers on the basis of the analysis of MD trajectories.[25] We speculate that the features of the nitroxide distribution can influence the ESR line shapes, especially at high frequency. An accurate line shape analysis is beyond our present purpose; however, model calculations can be useful to illustrate this point. The ESR spectrum of a spin label in a protein results from the superposition of a variety of motions; for the sake of simplicity, we have assumed the fast motional approximation for the side chain dynamics, and other motions are simply modeled as isotropic rotational diffusion with an effective correlation time. Thus the ESR spectrum can be calculated by solving the SLE[49] for a rotating body with partially averaged magnetic tensors. Figure 6 shows a series of ESR spectra calculated for the C13 conformer of the R2 spin label at increasing frequencies, with and without account of the biaxiality of order. An isotropic diffusion coefficient has been used, $D_0 = 10^8\ s^{-1}$. The partially averaged tensors reported Table 5 have been taken for C13; for the axial case, tensors with identical *X* and *Y* components, equal to the average of the values reported in the table, have been assumed. It clearly appears that, while the 9 GHz spectra obtained in the two cases are hardly distinguishable, the differences between spectra become significant at higher frequency.

IV. Discussion and Conclusions

A conformational analysis has been performed for the flexible chain of the MTSSL spin label at a solvent-exposed α-helix site. Knowledge of the chain energetics and evaluation of steric constraints, along with a realistic account of the friction opposing bond rotations in a viscous environment, has led to quantitative insight on amplitude and rates of the side chain motions. A small number of sterically allowed conformers has been identified, and the isomerization rates, provided by the kinetic analysis, support the experimental observation of a rather stiff nitroxide tether.[46,48,50] Chain motions are described as jumps between stable conformers and librations about the minima of the chain potential energy. Rotations around the χ_1 to χ_3 bonds are very unlikely due to the presence of high torsional barriers and/or steric constraints. So, chain motions relevant for ESR relaxation can be taken as torsional oscillations of all bonds and χ_4 and χ_5 conformational transitions. The former are characterized by small amplitudes, of the order of 10° for each bond; for the χ_5 dihedral, wider fluctuations are possible, with their exact features probably depending on the local environment of the spin probe. Thus, the results of our analysis support the so-called "χ_4,χ_5" model, which has been suggested by a number of experimental studies[46,48,51] and by MD simulations.[24,25]

In our approach, we have focused on a simple model, which can be worked out in detail, and it offers the advantage of an easier interpretation of the determining factors of the conformational dynamics. Our description of the conformational dynamics of the side chain, although approximate, contains substantial realistic features, and it has led to some rather general results on the geometry and kinetics of such motions. More detailed descriptions can be carried out by MD[20−25,28] or Monte Carlo simulations.[26,27] These techniques can provide a picture of a spin label in its environment in a given protein, so in principle, it should be possible to extract from trajectories the information needed to relate ESR line shape and structural or dynamic characteristics of the different labeling sites. However, our analysis allowed us to single out some key features that should be considered in applying these techniques for the interpretation of ESR experiments. Since the relevant motions fall in the nanosecond time scale, there is the obvious requirement that trajectories should not be shorter than tens of nanoseconds. A less obvious caveat derives from the subtle features of the averaging of magnetic tensors produced by tether motions; in particular, our investigation highlights the importance of the pattern of substituents in the pyrroline ring and that of the characteristics of the χ_5 torsional potential. Therefore, simulations adopting simplified labels cannot provide adequate

information that is useful for the analysis of ESR spectra;[23] moreover, the parameters appropriate for the spin label, which are not contained in the available force fields, need to be accurately assessed.

The results of our analysis can be exploited to introduce the features of the spin label structure and dynamics into the framework of a line shape theory. Such a study is presented in a companion paper.[29] However, here we simply summarize the implication of the results of our investigation for the interpretation and the simulation of ESR spectra. We have found that, in general, the simultaneous presence of different conformers, undergoing different motions, has to be taken into account. Conformational transitions for the R1 spin label have characteristic times of the order of 1 ns or slower for a protein in water; only χ_4 and χ_5 jumps are fast on the time scale of X-band ESR experiments, whereas at higher frequencies, the shorter experimental time scales render the fast motional limit as questionable, even for such motions. Torsional oscillations occur over time scales shorter than about a nanosecond, and especially in view of their small amplitude, they are likely to fall in the fast motional regime, even at higher frequency.

We have seen that chain motions produce a limited extent of averaging of magnetic tensors, especially when only torsional oscillations are possible. An anisotropic orientational distribution of the N-p_z orbital has been obtained, which is not surprising for the five-bond side chain of MTSSL, under the further constraints deriving from the presence of the α-helix backbone and the tails of the nearby residues. Namely, in the case of an alkyl chain, it is well-known that, due to the geometrical bond constraints, conformational motions cannot produce an isotropic distribution of the terminal end unless the chain is very long.[18,52] The presence of three ordering axes, characterized by different degrees of order, emerges from the analysis, in contrast to the common assumption of axial symmetry of the orientational distribution in the protein diffusion frame, e.g., in the popular model of diffusion in a cone.[53,54] As we have shown, biaxiality in the ordering could have have nonnegligible effects on line shapes at high frequency;[55,56] moreover, it might influence the distance distribution between pairs of nitroxides in doubly labeled systems.[4,57]

A significant difference between the R1 and R2 spin labels has been found, which could be exploited for different purposes. For R1, rotamers with different mobility are simultaneously present, and nontrivial effects on ESR spectra are expected. The presence of the methyl substituent at the 4-position of the pyrroline ring reduces the conformational freedom in R2, so only *noninterconverting* conformers are possible. Because the torsional oscillations experienced by such conformers are shown to have just small averaging effects on the magnetic tensor, and are similar for all conformers, a smaller impact of the chain dynamics on EPR spectra is predicted. In this respect, R2 appears to be a more suitable spin label to probe the protein dynamics. On the other hand, the higher mobility of R1 can make it a more sensitive probe of the environment.

Acknowledgment. A.F. and F.T. have been supported by MIUR (PRIN-2005) and Università di Padova (CPDA057391). J.H.F. acknowledges support of this project by grant number P41RR16292 from the National Center for Research Resources (NCRR), a component of the National Institutes of Health (NIH), and its contents are solely the responsibility of the authors and do not necessarily represent the official view of NCRR or NIH.

Appendix: Order Parameters

The order parameters $\overline{D^2_{q,k}(\Omega_M)}$ defined in eq 17 are complex scalars, quantifying the degree of order which characterizes the distribution of magnetic axes (MF frame) in the AF frame, produced by side chain motions. The two indices q and k have different meaning; they refer to a frame fixed in the protein and another frame moving with the magnetic tensors, respectively.[37] This point will be illustrated by some considerations.

The components $\overline{D^2_{q,0}(\Omega_M)}$ specify the distribution of the magnetic z_M axis in the AF frame. Going from the irreducible spherical to the Cartesian representation, we can write:

$$S_{zz}^{ZZ} = \overline{D^2_{0,0}}$$

$$S_{zz}^{XX} - S_{zz}^{YY} = \mathrm{Re}\,\overline{D^2_{2,0}}/\sqrt{6}$$

$$S_{zz}^{XY} = -\sqrt{3/2}\,\mathrm{Im}\,\overline{D^2_{2,0}}$$

$$S_{zz}^{XZ} = -\sqrt{3/2}\,\mathrm{Re}\,\overline{D^2_{1,0}}$$

$$S_{zz}^{YZ} = \sqrt{3/2}\,\mathrm{Im}\,\overline{D^2_{1,0}}$$

where S_{zz}^{KI} ($K, I = X, Y, Z$) are the elements of a second-rank, traceless tensor ($S_{zz}^{XX} + S_{zz}^{YY} + S_{zz}^{ZZ} = 0$), usually denoted as the *ordering tensor*. The value of S_{zz}^{KK} gives the degree of order of the z_M axis with respect to the K axis, with $-0.5 \le S_{zz}^{KK} \le 1$; $S_{zz}^{KK} = 1$ for perfect alignment of z_M to the K axis, while $S_{zz}^{KK} = -0.5$ if z_M is perfectly ordered perpendicular to the K axis. The ordering tensor $\mathbf{S_{zz}}$ is generally expressed in its PAS (*ordering frame*, SF in Figure 2), whose axes are designed as *directors*. For a generic orientational distribution of the z_M axis, the three principal values of $\mathbf{S_{zz}}$ are different; for axial symmetry, the relation $S_{zz}^{XX} = S_{zz}^{YY} = -S_{zz}^{ZZ}/2$ holds (having chosen the Z principal axis parallel to C_∞).

The $\overline{D^2_{0,k}(\Omega_M)}$ components specify the distribution of the Z director in the magnetic frame. The following relations hold between Cartesian and irreducible spherical components:

$$S_{xx}^{ZZ} - S_{yy}^{ZZ} = \mathrm{Re}\,\overline{D^2_{2,0}}/\sqrt{6}$$

$$S_{xy}^{ZZ} = \sqrt{3/2}\,\mathrm{Im}\,\overline{D^2_{0,2}}$$

$$S_{xz}^{ZZ} = -\sqrt{3/2}\,\mathrm{Re}\,\overline{D^2_{0,1}}$$

$$S_{yz}^{ZZ} = -\sqrt{3/2}\,\mathrm{Im}\,\overline{D^2_{0,1}}$$

Again, S_{ki}^{ZZ} ($k,i = x_M, y_M, z_M$) are the elements of a second-rank, traceless tensor, which accounts for the alignment of the magnetic axes to the Z director. The value of S_{kk}^{ZZ} quantifies the degree of alignment of the k axis to the Z director, and $-0.5 \le S_{kk}^{ZZ} \le 1$; $S_{kk}^{ZZ} = 1$ for perfect alignment of the k axis to the Z director, while $S_{kk}^{ZZ} = -0.5$ if the k axis is perfectly ordered perpendicular to the Z director. In general, the axes of the magnetic frame will have different propensity to align with respect to the Z director, i.e., $S_{xx}^{ZZ} \neq S_{yy}^{ZZ} \neq S_{zz}^{ZZ}$.

References and Notes

(1) Hubbell, W. L.; Altenbach, C. *Curr. Opin. Struct. Biol.* **1994**, *4*, 566.

(2) Hubbell, W. L.; Gross, A.; Langen, R.; Lietzow, M. *Curr. Opin. Struct. Biol.* **1998**, *8*, 649.

(3) *Biological Magnetic Resonance: the Next Millenium*; Berliner L. J., Ed.; Plenum Press: New York, 1998; Vol. 14.
(4) *Biological Magnetic Resonance: Distance Measurements in Biological Systems by EPR*; Berliner, L. J., Eaton, S. S., Eaton, G. R., Eds.; Kluwer Academic: New York, 2000; Vol. 19.
(5) Borbat, P. P.; Costa-Filho, A. J.; Earle, K. A.; Moscicki, J. K.; Freed, J. H *Science* **2001**, *291*, 266.
(6) Perozo, E.; Cortes, D. M.; Cuello, L. G. *Science* **1999**, *285*, 73.
(7) Perozo, E.; Cortes, D. M.; Sompornpisut, P.; Kloda, A.; Martinac, B. *Nature (London)* **2002**, *418*, 942.
(8) Xu, Y.; Zhang, F.; Su, Z.; McNew, J. A.; Shin, Y.-K. *Nat. Struct. Mol. Biol.* **2005**, *12*, 417.
(9) Jao, C. C.; Der-Sarkissian, A.; Chen, J.; Langen, R. *Proc. Natl. Acad. Sci. U.S.A.* **2004**, *101*, 8331.
(10) Borbat, P.; Ramlall, T. F.; Freed, J. H.; Eliezer, D. *J. Am. Chem. Soc.* **2006**, *128*, 10004.
(11) Radzwill, N.; Gerwert, K.; Steinhoff, H. J. *Biophys. J.* **2001**, *80*, 2856.
(12) Altenbach, C.; Yang, K.; Farrens, D. L.; Farahbakhsh, Z. T.; Khorana, H. G.; Hubbell, W. L. *Biochemstry* **1996**, *35*, 12470.
(13) Cai, K. W.; Langen, R.; Hubbell, W. L.; Khorana, H. G. *Proc. Natl. Acad. Sci. U.S.A.* **1997**, *94*, 14267.
(14) Park, S.; Borbat, P. P.; Gonzalez-Bonet, G.; Bhatnagar, J.; Pollard, A. M.; Freed, J. H.; Bilwes, A. M.; Crane, B. R. *Nat. Struct. Mol. Biol.* **2006**, *13*, 400.
(15) Ferrarini, A.; Moro, G.; Nordio, P. L. *Mol. Phys.* **1988**, *63*, 225.
(16) Moro, G. J.; Ferrarini, A.; Polimeno, A.; Nordio, P. L. In *Reactive and Flexible Molecules in Liquids*; Dorfmüller, Th., Ed.; Kluwer Academic: Dordrecht, 1989; p 107.
(17) Ferrarini, A.; Moro, G. J.; Nordio, P. L.; Crepeau, R. H.; Freed, J. H. *J. Chem. Phys.* **1989**, *91*, 5707.
(18) Cassol, R.; Ferrarini, A.; Nordio, P. L. *J. Phys.: Condens. Matter* **1994**, *6*, A279.
(19) Mchaourab, M. S.; Lietzow, M. A.; Hideg, K.; Hubbell, W. L. *Biochemistry* **1996**, *35*, 7692.
(20) Robinson, B. H.; Slutsky, L. J.; Auteri, F. P. *J. Chem. Phys.* **1992**, *96*, 2609.
(21) Steinhoff, H.-J.; Hubbell, W. L. *Biophys. J.* **1996**, *71*, 2201.
(22) LaConte, L. E. W.; Voelz, V.; Nelson, W.; Enz, M.; Thomas, D. D. *Biophys. J.* **2002**, *83*, 1854.
(23) Stoica, I. *J. Phys. Chem. B* **2004**, *108*, 1771.
(24) Murzyn, K.; Rg, T.; Blicharski, W.; Dutka, M.; Pyka, J.; Szytula, S.; Froncisz, W. *Proteins* **2006**, *62*, 1088.
(25) Budil, D. E.; Sale, K. L.; Khairy, K. A.; Fajer, P. J. *J. Phys. Chem. B* **2006**, *110*, 3703.
(26) Sale, K.; Sr, C.; Sharp, K. A.; Hideg, K. A.; Fajer P. G. *J. Magn. Reson.* **2002**, *156*, 104.
(27) Sale, K.; Song, L.; Liu, Y.-S.; Perozo, E.; Fajer P. J. *J. Am. Chem. Soc.* **2005**, *127*, 9334.
(28) Timofeev, V. P.; Nikolsky, D. O. *J. Biomol. Struct. Dyn.* **2003**, *21*, 367.
(29) Tombolato, F.; Ferrarini, A.; Freed, J. H. *J. Chem, Phys. B* **2006**, *110*, 26260.
(30) Flory P. J. *Statistical Mechanics of Chain Molecules*; Interscience: New York, 1969.
(31) Karplus, M.; Kushick, J. N. *Macromolecules* **1981**, *14*, 325.
(32) Moro, G. J. *J. Chem. Phys.* **1991**, *94*, 8577.
(33) Kramers, H. A. *Physica* **1940**, *7*, 284.
(34) Langer, J. S. *Ann. Phys.* **1969**, *54*, 258.
(35) Shore, J. E.; Zwanzig R *J. Chem. Phys.* **1975**, *63*, 5445.
(36) Zientara, G. P.; Freed, J. H. *J. Chem. Phys.* **1983**, *69*, 3077.
(37) Zannoni, C., in *The Molecular Physics of Liquid Crystals*; Luckhurst, G. R., Gray, G. W., Eds.; Academic Press: New York, 1979; p 51.
(38) Zare N. R. *Angular Momentum*; Wiley: New York, 1987.
(39) Frisch, M. J.; Trucks, G. W.; Schlegel, H. B.; Scuseria, G. E.; Robb, M. A.; Cheeseman, J. R.; Montgomery, J. A., Jr.; Vreven, T.; Kudin, K. N.; Burant, J. C.; Millam, J. M.; Iyengar, S. S.; Tomasi, J.; Barone, V.; Mennucci, B.; Cossi, M.; Scalmani, G.; Rega, N.; Petersson, G. A.; Nakatsuji, H.; Hada, M.; Ehara, M.; Toyota, K.; Fukuda, R.; Hasegawa, J.; Ishida, M.; Nakajima, T.; Honda, Y.; Kitao, O.; Nakai, H.; Klene, M.; Li, X.; Knox, J. E.; Hratchian, H. P.; Cross, J. B.; Bakken, V.; Adamo, C.; Jaramillo, J.; Gomperts, R.; Stratmann, R. E.; Yazyev, O.; Austin, A. J.; Cammi, R.; Pomelli, C.; Ochterski, J. W.; Ayala, P. Y.; Morokuma, K.; Voth, G. A.; Salvador, P.; Dannenberg, J. J.; Zakrzewski, V. G.; Dapprich, S.; Daniels, A. D.; Strain, M. C.; Farkas, O.; Malick, D. K.; Rabuck, A. D.; Raghavachari, K.; Foresman, J. B.; Ortiz, J. V.; Cui, Q.; Baboul, A. G.; Clifford, S.; Cioslowski, J.; Stefanov, B. B.; Liu, G.; Liashenko, A.; Piskorz, P.; Komaromi, I.; Martin, R. L.; Fox, D. J.; Keith, T.; Al-Laham, M. A.; Peng, C. Y.; Nanayakkara, A.; Challacombe, M.; Gill, P. M. W.; Johnson, B.; Chen, W.; Wong, M. W.; Gonzalez, C.; Pople, J. A. *Gaussian 03*; Gaussian, Inc.: Wallingford, CT, 2004.
(40) Pal, D.; Chakrabarti, P. *J. Biomol. Struct. Dyn.* **1998**, *13*, 1059.
(41) Note that the state that we label as $g_+(g_-)$ corresponds to the state labeled as $g_-(g_+)$ in refs 40, 42.
(42) Langen, R.; Joon, Oh, K.; Cascio, D.; Hubbell, W. L. *Biochemistry* **2000**, *39*, 8396.
(43) Lovell, S. C.; Word, J..M.; Richardson, J. S.; Richardson, D. C. *Proteins* **2000**, *40*, 389.
(44) Happel, J.; Brenner, H. In *Low Reynolds Number Hydrodynamics*; Prentice Hall: Englewood Cliffs, NJ, 1965.
(45) In the context of magnetic resonance, the word "rhombicity" is commonly used rather than "biaxiality".
(46) Columbus, L.: Kámás, T.; Jekö, J.; Hideg, K.; Hubbell, W. L. *Biochemistry* **2001**, *40*, 3828.
(47) Liang, Z.; Lou, Y.; Freed, J. H.; Columbus, L.; Hubbell, W. L. *J. Phys. Chem. B* **2004**, *108*, 17649.
(48) Jacobsen, K.; Oga, S.; Hubbell, W. L.; Risse, T. *Biophys. J.* **2005**, *88*, 4351.
(49) Budil, D. E.; Lee, S.; Saxena, S.; Freed, J. H. *J. Magn. Reson.* **1996**, *120*, 155.
(50) Barnes, J. P.; Liang, Z.; Mchaourab, H. S.; Freed, J. H.; Hubbell, W. L. *Biophys. J.* **1999**, *76*, 3298.
(51) Pyka, J.; Iinicki, J.; Altenbach, C.; Hubbell, W. L., Froncisz, W. *Biophys. J.* **2005**, *89*, 2059.
(52) Ferrarini, A.; Luckhurst, G. R.; Nordio, P. L. *Mol. Phys.* **1995**, *85*, 131; Stocchero, M.; Ferrarini, A.; Moro, G. J.; Dunmur, D. A.; Luckhurst, G. R. *J. Chem. Phys.* **2004**, *121*, 8079.
(53) Columbus, L.; Hubbell, W. L. *Trends Biochem. Sci.* **2002**, *27*, 288.
(54) Hustedt, E. J.; Stein, R. A.; Sethaphong, L.; Brandon, S.; Zhou, Z.; DeSensi, S. C. *Biophys. J.* **2006**, *90*, 340.
(55) Barnes, J. P.; Freed, J. H. *Biophys. J.* **1998**, *75*, 2532.
(56) Gaffney, B. J.; Marsh, D. *Proc. Natl. Acad. Sci. U.S.A.* **1998**, *95*, 12940.
(57) Borbat P. P.; Mchaourab, H. S.; Freed, J. H. *J. Am. Chem. Soc.* **2002**, *124*, 5304.

Chapter 7

Modeling the effects of structure and dynamics of the nitroxide side chain on the ESR spectra of spin-labeled proteins

Modeling the Effects of Structure and Dynamics of the Nitroxide Side Chain on the ESR Spectra of Spin-Labeled Proteins

Fabio Tombolato and Alberta Ferrarini*

Dipartimento di Scienze Chimiche, Via Marzolo 1, Università di Padova, 35131 Padova, Italy

Jack H. Freed

Baker Laboratory of Chemistry and Chemical Biology, Cornell University, Ithaca, New York 14853-1301

Received: May 15, 2006; In Final Form: October 5, 2006

In the companion paper (*J. Phys. Chem. B* **2006**, *110*, jp0629487), a study of the conformational dynamics of methanethiosulfonate spin probes linked at a surface-exposed α-helix has been presented. Here, on the basis of this analysis, X-band ESR spectra of these spin labels are simulated within the framework of the Stochastic Liouville equation (SLE) methodology. Slow reorientations of the whole protein are superimposed on fast chain motions, which have been identified with conformational jumps and fluctuations in the minima of the chain torsional potential. Fast chain motions are introduced in the SLE for the protein reorientations through partially averaged magnetic tensors and relaxation times calculated according to the motional narrowing theory. The 72R1 and 72R2 mutants of T4 lysozyme, which bear the spin label at a solvent-exposed helix site, have been taken as test systems. For the side chain of the R2 spin label, only a few noninterconverting conformers are possible, whose mobility is limited to torsional fluctuations, yielding almost identical spectra, typical of slightly mobile nitroxides. In the case of R1, more complex spectra result from the simultaneous presence of constrained and mobile chain conformers, with relative weights that can depend on the local environment. The model provides an explanation for the experimentally observed dependence of the spectral line shapes on temperature, solvent, and pattern of substituents in the pyrroline ring. The relatively simple methodology presented here allows the introduction of realistic features of the spin probe dynamics into the simulation of ESR spectra of spin-labeled proteins; moreover, it provides suggestions for a proper account of such dynamics in more sophisticated approaches.

I. Introduction

Different kinds of ESR experiments have been devised to probe the structural features of proteins, as well as the properties of different protein environments and the dynamical processes occurring in these systems, which are characterized by a wide range of time scales.[1,2] The X-band (9 GHz) spectra have typical shapes, usually three broadened lines, indicating the absence of enough fast and large amplitude motion to fully average out the anisotropy of the **g** and **A** hyperfine tensors. Simple inspection of the spectra can provide an insight into the mobility of the spin probe, at least at a qualitative level; so, for example, differences in line broadening observed for spin labels at different sites are taken as indicators of low or high mobility at the local site of the spin label. On the other hand, accurate line shape analysis, which is capable of providing quantitative information, is not a simple task in the presence of complex dynamics. Namely, a variety of processes can produce nitroxide reorientation: they range from overall protein tumbling and refolding processes to backbone fluctuations and motions of the tether.

The analysis of ESR line shapes can be carried out by the stochastic Liouville equation (SLE) formalism to describe the time evolution of the density matrix for the spin degrees of freedom, treated quantum mechanically, coupled to the probability density for the orientational degrees of freedom, described as classical stochastic variables.[3−5] Efficient implementations make use of the expansion on a complete basis set, which is the direct product of basis sets for the spin and the classical variables. This methodology has been widely used, and software packages are available for the simulation of ESR line shapes of spin probes undergoing Brownian rotational motion.[6] In principle, there is no restriction on the number of classical stochastic variables, and multivariate Fokker−Planck equations for various kinds of motional models can be formulated. In practice, however, the rapidly growing dimension of the stochastic Liouville matrix needed to represent many stochastic variables, and the increase in computational time, pose substantial limits to the complexity of motions that can be treated. So, only simplified or approximate treatments of the variety of processes affecting the spin relaxation of nitroxide spin labels attached to proteins are currently feasible. Thus some approaches have been proposed that include some key features of the systems and still circumvent the computational limits.

(a) When the overall motions are so slow that their dynamic effects can be neglected, the so-called microscopic order macroscopic disorder model (MOMD) can be used.[7] Here the spectrum is calculated for a static isotropic distribution of rotors, undergoing Brownian motion in an ordered environment. The nitroxide spin probe is identified with the rotor and the constraints deriving from the chain geometry and from the steric hindrance of the environment are taken into account through an orienting potential. The MOMD approach has been used for

* Corresponding author. E-mail: alberta.ferrarini@unipd.it.

10.1021/jp062949z CCC: $33.50
Published on Web 12/21/2006

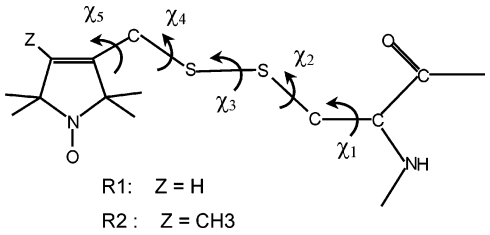

Figure 1. Structure of the spin labels considered in this study. They are obtained by reaction of the sulfhydryl group of a cysteine with 1-oxyl-2,2,5,5-tetramethyl-3-pyrroline-3-(methyl)methanethiosulfonate (R1) and 1-oxyl-2,2,4,5,5-pentamethyl-3-pyrroline-3-(methyl)-methanethiosulfonate (R2). The five dihedral angles defining the chain conformation are shown.

proteins in high viscosity media and/or low temperature,[8] as well as for very high-frequency ESR,[9] but of course it is no longer suitable when the rigid limit cannot be assumed for the protein motions.

(b) The overall protein reorientation can be taken into account by a more sophisticated approach, known as the slowly relaxing local structure (SRLS) model, wherein the rotational diffusion of a rotor, identified with the spin probe, is superimposed onto protein rotations.[10−12] Even in this case, local constraints are introduced through an orienting potential. This model has been used for the simultaneous simulations of 9 and 250 GHz spectra of T4 lysozyme (T4L) in water.[13] A large number of parameters enter the model: the diffusion tensor of the protein and that of the nitroxide in the protein frame, in addition to the coefficients specifying the orienting potential experienced by the spin probe. It follows that a large set of experimental data are needed.

A valuable feature of the SLE methodology is that it provides a relatively simple description of a complex system, in terms of a few physical properties, that are introduced in a parametric way. These parameters can then be optimized by simulating experimental spectra with best-fitting procedures. The drastic reduction in the dimension of the problem deriving from a suitable selection of the variables deemed relevant, which characterizes standard SLE methods, has the drawback that mapping the results into precise information on the protein is not necessarily straightforward. So, for instance, the interpretation of diffusion coefficients and order parameters for the spin probe in terms of specific molecular motions and local constraints can remain rather vague, especially given the limited sensitivity to the details of the dynamics provided by conventional ESR.[9,13,14]

Alternative approaches have been proposed to obtain a more detailed modeling of the systems. The dynamics of the classical degrees of freedom can be obtained in the form of trajectories by molecular dynamics (MD) or Brownian dynamics simulations.[15−19] A detailed picture of the local environment probed by the spin label and of the various processes modulating its orientations can be attained at a computational cost, which can be very high due to the huge number of degrees of freedom. Conformational transitions in the side chain occur on the nanosecond time scale, therefore, long trajectories are needed, even to just sample a few conformational sites. The computational demand can be significantly reduced if strong constraints are introduced, as in MD simulations where all degrees of freedom but those of the spin label are frozen.[20]

In the companion paper,[21] we have examined the internal motions of methanethiosulfonate (MTSSL), a typical spin label whose structure is shown in Figure 1, attached to a model α-helix. We have found that the system can be described in terms of a limited number of conformers. They undergo fast, small-amplitude torsional oscillations and side chain isomerizations. In water at room temperature, the former are estimated to have characteristic times shorter than a nanosecond. The latter occur on a range of time scales that can be of the order of 1 ns if rotations of the terminal chain bonds are involved, but are significantly slower for the bonds closer to the protein backbone. Thus, on the time scale of ESR spectra, we can distinguish two kinds of conformers: ones that are connected to other conformers by fast rotations around the terminal chain bonds, while the others are linked only by very slow transitions involving internal bonds, so they can be considered as isolated.

Here, the information derived from this analysis is used to investigate the effects of conformational dynamics on X-band (9 GHz) ESR line shapes. A simplified approach has been used, exploiting the time scale separation between the various processes producing reorientation of nitroxide. Fast motions, identified with torsional oscillations and isomerizations of the terminal side chain bonds, are treated according to the fast motional ESR relaxation theory.[22,23] Spectral line shapes are then obtained by introducing partially averaged magnetic tensors and T_2 relaxation times, obtained in this way, into the SLE for slow protein tumblings.[3,24−26] The 72R1 and 72R2 mutants of T4L, for which experimental data are available in the literature,[8,9,13] are taken as test cases; the effects of side chain dynamics on the spectral line shape have been analyzed as a function of temperature and solvent. This approach is shown to be satisfactory for 9 GHz ESR spectra, and the generalizations needed to interpret high-frequency spectra (250 GHz) are considered in the Discussion Section below.

The paper is organized in the following way. In the next section, an approximate treatment for the ESR spectrum of a nitroxide spin probe in the presence of fast side chain motions and slow overall protein reorientations is presented. Then the effects of the chain dynamics on ESR spectra of the 72R1 and the 72R2 mutants of T4L are presented. In the final section, the results of our investigation are discussed, the conclusions of this work are summarized, and future outlooks are sketched.

II. ESR Spectrum of a Nitroxide Spin Label

According to linear response theory, the absorbed power in an ESR experiment is the imaginary part of the Fourier−Laplace transform of the time-dependent complex magnetization, $M_+ = M_X + iM_Y$:

$$M_+(t) \propto \mathrm{Tr}\overline{\mathcal{J}_+\rho(\Omega,t)} \tag{1}$$

where Tr indicates the trace over the spin variables and the bar implies an orientational average; $\mathcal{J}_+ = \mathcal{J}_X + i\mathcal{J}_Y$ is an electronic spin operator, and $\rho(\Omega, t)$ is the spin density matrix, whose time evolution is described by the SLE:[3−5]

$$\frac{\partial\rho(\Omega,t)}{\partial t} = -i\mathbf{L}(\Omega)\rho(\Omega,t) - \Gamma(\Omega)\rho(\Omega,t) \tag{2}$$

Here $\mathbf{L}(\Omega)$ is the Liouville superoperator associated with the spin Hamiltonian and $\Gamma(\Omega)$ is a stochastic operator accounting for the orientational dynamics of the spin label. It describes the time dependence of the Euler angles $\Omega = (\alpha, \beta, \gamma)$, specifying the orientation of the magnetic frame, MF, in the laboratory frame, LF.

The spin Hamiltonian of a nitroxide radical has the form:

$$H(\Omega, t) = \mathcal{J}\cdot\mathbf{g}\cdot\mathbf{B}_0 + \mathcal{J}\cdot\mathbf{A}\cdot\mathcal{I} \tag{3}$$

with the Zeeman and hyperfine terms, which contain the **g** tensor

and the hyperfine tensor **A**, respectively. Here $\mathcal{S}$ and $\mathcal{I}$ are the electronic and nuclear spin operators, and B_0 represents the static magnetic field, whose orientation is chosen as the Z axis of the laboratory frame (LF). The spin Hamiltonian can be expressed as the sum of a contribution, H_{iso}, independent of the orientation of the spin probe, and an orientation dependent part, δH, which fluctuates in time due to rotations of the nitroxide:

$$H(\Omega,t) = H_{iso} + \delta H(\Omega,t) \tag{4}$$

It is convenient to make use of the irreducible spherical tensor formalism:[27]

$$H_{iso} = \sum_{\mu} F^{(00)}_{\mu;LF}\, T^{(00)}_{\mu;LF} \tag{5}$$

$$\delta H(\Omega, t) = \sum_{\mu,m} F^{(2m)*}_{\mu;LF}\, T^{(2m)}_{\mu;LF} \tag{6}$$

where $\mu = g, A$ is used to denote the Zeeman and hyperfine terms, and $F^{l,m}_{\mu}$, $T^{l,m}_{\mu}$ are components of the magnetic tensors and the electronic or nuclear spin operators, respectively, all expressed in the laboratory frame: $\mathbf{T}_g = \mathcal{S} \otimes \mathbf{B}_0$, $\mathbf{T}_A = \mathcal{S} \otimes \mathcal{I}$. It is convenient to express the magnetic tensors in the magnetic frame, MF; then, the orientation-dependent part of the Hamiltonian can be rewritten as

$$\delta H(\Omega,t) = \sum_{\mu} \sum_{m,k} D^{2}_{m,k}(\Omega,t) F^{(2k)*}_{\mu;MF}\, T^{(2,m)}_{\mu;LF} \tag{7}$$

where $D^{2}_{m,k}$ are Wigner rotation matrices having as their argument the Euler angles for the rotation from the laboratory to the magnetic frame.[27]

A. Superposition of Fast and Slow Motions. The orientation with respect to the laboratory frame of a spin label attached to a protein varies in time under the effect of several motions: dynamics of the chain linking the probe to the protein, fluctuations of the backbone, overall protein tumbling, domain motions, etc. Thus, the stochastic operator Γ in eq 2 should depend on a large number of variables, which would render the SLE too complex to treat. A simplified approach can be adopted, under the condition of time scale separation between motions, if some of these can be assumed to be fast on the ESR time scale.[24−26] The dynamics of a given variable is assumed to be fast if its characteristic frequency, $1/\tau$, is larger than the magnetic anisotropy it modulates, $\Delta\omega$, i.e. $1/\tau \gg \Delta\omega$. In the case of X-band (9 GHz) ESR experiments, such a condition is satisfied by motions with correlation times shorter than about 1 ns. If the fast-motional regime can be assumed for the side chain motion, the ESR spectrum of a nitroxide spin label, in a protein at the orientation Ω_D in the laboratory frame, is given by three lines whose positions are determined by the spin Hamiltonian eq 4, partially averaged by the side chain dynamics:

$$\overline{H(\Omega_D,t)} = H_{iso} + \overline{\delta H}\,(\Omega_D,t) = H_{iso} + \sum_{\mu} \sum_{m,k} \overline{D^{2}_{m,k}(\Omega,t)}\, F^{(2,k)*}_{\mu;MF}\, T^{(2,m)}_{\mu;LF} \tag{8}$$

where the upper bar denotes the average over the fast motions.

The spectral linewidths can be calculated according to the motional narrowing theory:[22,23]

$$T^{-1}_{2,MM'} = A(\Omega_D) + (1/2)B(\Omega_D)[M + M'] + (1/4)C'(\Omega_D)[M + M']^2 + (1/2)C''(\Omega_D)[M^2 + M'^2] \tag{9}$$

with $M,M' = 0,\pm1$ indicating nuclear spin states for the electron spin states connected by electronic spin transitions. The coefficients $A(\Omega_D)$, $B(\Omega_D)$, $C(\Omega_D)$ are defined as:

$$A(\Omega_D) = \frac{2}{3}J^{gg}_0 + \frac{1}{2}J^{AA}_1 \tag{10}$$

$$B(\Omega_D) = \frac{2}{3}(J^{gA}_0 + J^{Ag}_0) = \frac{4}{3}J^{gA}_0 \tag{11}$$

$$C(\Omega_D) = \frac{2}{3}J^{AA}_0 - \frac{1}{4}J^{AA}_1 \tag{12}$$

where $J^{\mu\mu'}_m$ is the zero-frequency spectral density:

$$J^{\mu\mu'}_m = \int_0^{\infty} \overline{\delta F^{(2,m)}_{\mu;LF}(0)\, \delta F^{(2,m)*}_{\mu';LF}(t)}\, dt \tag{13}$$

Here $\delta F^{(2,m)}_{\mu;LF}$ represents fluctuations of tensor components with respect to their partially averaged values, $\delta F^{(2,m)}_{\mu;LF} = F^{(2,m)}_{\mu;LF} - \overline{F^{(2,m)}_{\mu;LF}}$. If fast side chain dynamics is superimposed to slow overall motions, the former can be included in the modified SLE:[25]

$$\frac{\partial \rho(\Omega_D,t)}{\partial t} = -i\,\bar{\mathbf{L}}(\Omega_D)\rho(\Omega_D,t) - [T_2^{-1}(\Omega_D) + \Gamma(\Omega_D)]\rho(\Omega_D,t) \tag{14}$$

where $\bar{\mathbf{L}}(\Omega_D)$ is the Liouville superoperator associated to the Hamiltonian partially averaged by the chain dynamics, eq 8, $T_2^{-1}(\Omega_D)$ is the orientation-dependent line width defined in eq 9, and $\Gamma(\Omega_D)$ is the stochastic operator describing the slow protein tumbling.

B. Fast Side Chain Motions: Average Magnetic Tensors and Spectral Linewidths. Explicit expressions for the partially averaged quantities entering the spin Hamiltonian, eq 8, and the coefficients A, B, C, eqs 10−12, can be obtained on the basis of a model for the side chain motions. Considering the case of the MTSSL spin label linked to an α-helix, we have shown in ref 21 that a restricted number of possible conformers can be identified. All undergo fast and small-amplitude torsional oscillations, and only some of them can be connected by conformational jumps. These are characterized by transition frequencies occurring on a range of time scales; the fastest, of the order of 1 ns^{-1} in water, involve rotations around the S_δ−C bond (χ_4 jumps), whereas rotations around the C_β−S_γ bond (χ_2 jumps) are about an order of magnitude slower, and those involving the χ_1 dihedral and the disulfide bond (χ_3 transitions) are even slower. For the sake of simplicity, the approximation will be adopted that, according to their rate, conformational transitions can be assumed to be either fast or frozen. So, a spectrum will be calculated as a sum of contributions, each due to a single conformer, or to a set of conformers whose interconversion is fast on the time scale of the experiment under examination. A contribution is obtained by solving a modified SLE, eq 14, with partially averaged Hamiltonian and spectral line width calculated for a given conformer or set of conformers. In the following, expressions for the quantities appearing in the SLE will be derived.

For this purpose, the rotation from the laboratory (LF) to the molecular (MF) frame is conveniently decomposed into a series of transformations, as shown in Figure 2. The DF frame is the principal axis system (PAS) of the protein diffusion tensor, and AF is a frame fixed on the spin-labeled amino acid residue, with the origin on the C_α carbon. The reference systems designated as L_i are local frames with the origin on the side

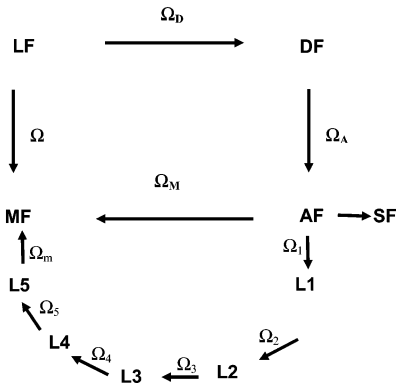

Figure 2. Reference frames considered in this work. LF: laboratory frame, with the Z_L axis parallel to the magnetic field B_0. DF: PAS of the rotational diffusion tensor of the protein. AF: frame of the amino acid residue, with the origin on the C_α bringing the nitroxide side chain, the z_A axis perpendicular to the plane of the N−C_α−CO atoms, and the x_A axis on the plane containing the z_A axis and C_α−C_β bond. L_i: local frame, with the z_{L_i} axis parallel to the ith chain bond and x_{L_i} in the plane of the preceding chain bond for the eclipsed configuration with $\chi_{i-1} = 0°$. MF: magnetic frame, with the origin on the nitroxide N nucleus, the z_M axis along the N-$p_z$orbital, and the x_M axis parallel to the N−O bond.

chain carbons, whose orientation changes with the configuration of the side chain. Finally, the MF frame is fixed in the nitroxide moiety, with the origin on the N nucleus, the z_M axis along the N-$p_z$orbital, and the x_M axis parallel to the N−O bond. Here we are focusing on the case of labeled sites in α-helices; neglecting the possibility of significant changes in the protein shape, as could be brought about by domain reorientation, and that of fluctuations of the protein backbone, the protein diffusion tensor and the orientation of AF with respect to DF will be assumed to be time independent. The validity of this assumption will be assessed by comparing theoretical and experimental results.

The averaged Wigner rotation matrices appearing in eq 8 can be expressed as:

$$\overline{D^2_{m,k}(\Omega)} = \sum_{p,q} D^2_{m,p}(\Omega_D)\, D^2_{p,q}(\Omega_A) \overline{D^2_{q,k}(\Omega_M)} \qquad (15)$$

where the addition theorem of Wigner rotation matrices[27] has been used to made explicit the dependence on variables that are assumed to be independent of the motions in the side chain, i.e., Ω_D and Ω_A, and the average has been taken only over the fast chain motions. The matrix elements $\overline{D^2_{q,k}(\Omega_M)}$, which will be designated as order parameters, reflect the orientational distribution of the magnetic frame in the frame of the amino acid residue. They are related to the magnetic tensors partially averaged by chain motions:

$$\overline{F^{(2,q)}_{\mu;\mathrm{AF}}} = \sum_k \overline{D^2_{q,k}{}^*(\Omega_M)}\, F^{(2,k)}_{\mu;\mathrm{MF}} \qquad (16)$$

Even for the evaluation of the spectral densities, eq 13, it is convenient to make explicit the dependence upon the variables that are modulated by chain motions; the following form is obtained:

$$J^{\mu\mu'}_m = \sum_{p,q,k,p',q',k'} F^{(2,k)}_{\mu;FM} F^{(2,k')}_{\mu';FM}{}^* j_{q,k,q',k'} \times D^2_{m,p}{}^*(\Omega_D)\, D^2_{m,p'}(\Omega_D)\, D^2_{p,q}{}^*(\Omega_A)\, D^2_{p',q'}(\Omega_A) \qquad (17)$$

where $j_{q,k,q',k'}$ is the reduced zero-frequency spectral density:

$$j_{q,k,q',k'} = \int_0^\infty \overline{\delta D^2_{q,k}{}^*(\Omega_M,0)\, \delta D^2_{q',k'}(\Omega_M,t)}\, \mathrm{d}t \qquad (18)$$

with $\delta D^2_{q,k}(\Omega_M) = D^2_{q,k}(\Omega_M) - \overline{D^2_{q,k}(\Omega_M)}$.

Partially averaged magnetic tensors and reduced spectral densities for torsional oscillations and conformational jumps can be calculated as explained in ref 21; the expressions to be used will be summarized in the following.

Torsional Oscillations. The order parameters $\overline{D^2_{qk}(\Omega^J_M)}$, accounting for nitroxide reorientation produced by bond fluctuations about the configuration of the Jth chain conformer, are obtained by integrating over the probability distribution $p(\delta\boldsymbol{\chi}^J)$, with $\delta\boldsymbol{\chi}^J = \boldsymbol{\chi} - \boldsymbol{\chi}^J$ being the displacements from the equilibrium dihedral angles, $\boldsymbol{\chi}^J$. Under the assumption of independent bond contributions, the torsional probability can be factorized into single bond contributions; using the harmonic approximation for the torsional potential about a minimum, these can be expressed as:

$$p(\delta\chi^J_i) = \frac{\exp[-V^{(2)}_{J,i}(\delta\chi_i{}^J)^2/2k_\mathrm{B}T]}{(2\pi k_\mathrm{B}T/V^{(2)}_{J,i})^{1/2}} \qquad (19)$$

where $V^{(2)}_{J,i}$ is the curvature of the torsional potential for the χ_i dihedral, calculated at $\chi_i = \chi^J_i$. Then, the order parameters can be calculated as:[21]

$$\overline{D^2_{q,k}(\Omega^J_M)} = \sum_{q_1,q_2,q_3,q_4,q_5} D^2_{q,q_1}(\Omega^J_1)\, D^2_{q_1,q_2}(\Omega^J_2) \ldots \times D^2_{q_4,q_5}(\Omega^J_5) D^2_{q_5,k}(\Omega_m) \exp\left[-\frac{k_\mathrm{B}T}{2}\left(\frac{q_1{}^2}{V^{(2)}_{J,1}} + \ldots \frac{q_5{}^2}{V^{(2)}_{J,5}}\right)\right] \qquad (20)$$

where $\Omega^J_{i+1} = (\chi^J_i, \beta^J_{i+1}, \gamma^J_{i+1})$ are the Euler angles for the local transformation $L_i \rightarrow L_{i+1}$. Under the same conditions, the following form is obtained for the reduced spectral density eq 18:

$$j_{q,k,q',k'} = \int_0^\infty \overline{\delta D^2_{q,k}{}^*(\Omega_M, 0)\delta D^2_{q'k'}(\Omega_M, t)}\, \mathrm{d}t = \sum_{q_1,q_2,q_3,q_4,q_5} D^2_{q,q_1}(\Omega^J_1)\, D^2_{q_1,q_2}(\Omega^J_2) \ldots D^2_{q_4,q_5}(\Omega^J_5)\, D^2_{q_5,k}(\Omega_m) \times \sum_{q'_1,q'_2,q'_3,q'_4,q'_5} D^2_{q',q'_1}(\Omega^J_1)\, D^2_{q'_1,q'_2}(\Omega^J_2) \ldots D^2_{q'_4,q'_5}(\Omega^J_5)\, D^2_{q'_5,k'}(\Omega_m) \times \int_0^\infty \overline{\exp\{i[q_1\, \delta\chi^J_1(0) + q_2\, \delta\chi^J_2(0) \ldots + q_5\, \delta\chi^J_5(0) + -q'_1\, \delta\chi^J_1(t) - q'_2\, \delta\chi^J_2(t) \ldots - q'_5\, \delta\chi^J_5(t)]\}} \qquad (21)$$

The torsional angle fluctuations can be described by a Fokker−Planck−Smoluchowski equation, which is conveniently solved by the normal mode transformation: $\delta\boldsymbol{\chi}^J = \mathbf{U}\mathbf{y}$.[28−30] The transformation matrix $\mathbf{U}$ is defined by $\mathbf{U}^{-1}\mathbf{D}_J\mathbf{V}^{(2)}_J\mathbf{U} = k_\mathrm{B}T\boldsymbol{\Lambda}^J$, where $\mathbf{D}_J$ is the diffusion tensor for the side chain in the Jth conformation. It is related to the friction matrix opposing bond rotations, $\boldsymbol{\xi}_J$, by the Stokes−Einstein relation $\mathbf{D}_j = k_\mathrm{B}T\boldsymbol{\xi}^{-1}_J$. The presence of this matrix, which couples all torsional angles, makes it impossible to factorize the correlation function appearing in the last row of eq 21 into single bond contributions. However, the correlation function can be easily calculated in terms of the normal modes:

$$\overline{\exp\{i[q_1\,\delta\chi_1^J(0) + q_2\,\delta\chi_2^J(0) \ldots + q_5\,\delta\chi_5^J(0) - q_1'\,\delta\chi_1^J(t) - q_2'\,\delta\chi_2^J(t) \ldots - q_5'\,\delta\chi_5^J(t)]\}} = \prod \overline{\exp\{i[a_i y_i(0) - b_i y_i(t)]\}} \quad (22)$$

where $a_i = \sum_j q_j U_{ji}$, $b_i = \sum_j q_j' U_{ji}$. By truncating the Taylor series expansion of the exponentials at the first terms, the following expression is obtained for the correlation functions appearing in the product:

$$\overline{\exp\{i[a_i y_i(0) - b_i y_i(t)]\}} \approx C_0 + C_1\, e^{-\Lambda_i^J t} + C_2\, e^{-2_i^J t} \quad (23)$$

with $C_0 = (1 - a_i^2/2\Lambda_i^J)(1 - b_i^2/2\Lambda_i^J)$, $C_1 = a_i b_i/\Lambda_i^J$, and $C_2 = a_i^2\, b_i^2/2(\Lambda_i^J)^2$. Thus the reduced spectral density eq 21 can be easily calculated using the expression:

$$\int_0^\infty \overline{\exp\{i[q_1\delta\chi_1^J(0) + q_2\delta\chi_2^J(0) \ldots + q_5\delta\chi_5^J(0) - q_1'\delta\chi_1^J(t) - q_2'\delta\chi_2^J(t) \ldots - q_5'\,\delta\chi_5^J(t)]\}} = \sum_{\alpha_1=0,1,2}{}' \ldots \sum_{\alpha_2=0,1,2}{}' \frac{\prod_{i-1}^{5} C_{\alpha_i}^{(i)}}{\sum_{i-1}^{5} \alpha_i \Lambda_i^J} \quad (24)$$

where the prime indicates that the term with all α_i values equal to zero is excluded from the summations.

Conformational Jumps. For conformers which, in addition to torsional oscillations, undergo also conformational jumps, the order parameters in eq 15 can be approximated as[21]

$$\overline{D_{q,k}^2(\Omega_M)} = \sum_J P_J \overline{D_{q,k}^2(\Omega_M^J)} \quad (25)$$

where the sum is extended to all the interconverting conformers, $\overline{D_{q,k}^2(\Omega_M^J)}$ are order parameters calculated by averaging over the torsional fluctuations of the Jth conformer, eq 20, and P_J is the conformer probability. This is defined as $P_J = \exp(-V_J/k_B T)(\det \mathbf{V}_J^{(2)})^{-1/2}/\sum_J \exp(-V_J/k_B T)(\det \mathbf{V}_J^{(2)})^{-1/2}$, where V_J and $\mathbf{V}_J^{(2)}$ are the potential energy and the matrix of the second derivatives of the potential energy for the Jth conformer, respectively.[21]

Spectral densities can be obtained as[31]

$$j_{q1,k1,q2,k2} = \mathbf{v}^* \cdot \tilde{\mathbf{W}}^{-1} \cdot \mathbf{v} \quad (26)$$

where $\tilde{\mathbf{W}}$ is the symmetrized transition matrix for conformational jumps. Its elements are defined as $\tilde{W}_{JJ'} = P_J^{-1/2} W_{JJ'} P_{J'}^{1/2}$, where $-W_{JJ'}$ is the $J' \rightarrow J$ transition rate.[21] The vector $\mathbf{v}$ in eq 26 has the Jth element defined as $v_J = P_J^{1/2}[D_{q,p}^2(\Omega_M^J) - \overline{D_{q,p}^2(\Omega_M^J)}]$. Conformer probabilities can be evaluated in terms of the chain energetics, while transition probabilities have been determined on the basis of torsional potentials and friction opposing bond rotations[21,31] within the framework of the multidimensional Kramers theory.[32,33]

III. Results

With the information derived from the conformational dynamics of the side chain, we have calculated the ESR spectra of the R1 and R2 mutants of T4L, with the spin probe linked at site 72, which is solvent-exposed and located in the middle of a 5-turn α-helix, as shown in Figure 3. The theoretical results are compared with experimental spectra recorded at different temperatures and in different solvents, which are available in the literature.[8,13]

A spectrum has been obtained as the sum of contributions, each due to an independent set of conformers with suitable weights. Each spectral component is calculated as explained in the previous section. Partially averaged magnetic tensors and spectral densities modulated by chain dynamics are introduced into the slow-motion simulation programs of the NLLS software package,[6] which has been modified to adapt to the present model (see Appendix). The Brownian diffusion model has been used for overall protein reorientation.

The input parameters for the calculation of each spectral contribution can be summarized: (1) **g** and **A** tensors of the spin label, (2) intrinsic line width, (3) rotational diffusion tensor $\mathbf{D}_0$ of the protein, and (4) Euler angles Ω_A, defining the orientation of the amino acid residue frame (AF) with respect to the diffusion frame (DF).

All parameters are obtained either by modeling or from experimental data. Magnetic tensors, expressed in the MF frame for the 72R1 mutant of T4L, are taken from the literature;[13] they are reported in Table 1. The diffusion tensor $\mathbf{D}_0$ has been calculated with a hydrodynamic model,[34] on the basis of the crystal structure of wild type T4L (3LZM.pdb).[35] Also the values of the Euler angles Ω_A have been obtained from the X-ray structure. Principal values of the diffusion tensor in water solution at $T = 298$ K ($\eta = 0.9$ mPa·s) are reported in Table 1, along with the Ω_A Euler angles. A slightly anisotropic diffusion tensor is obtained, in agreement with the protein shape. An intrinsic Lorentzian line width of 1 G has been used in all line shape calculations,[13] in addition to the line width contribution deriving from chain motions, calculated as explained in the previous sections.

A. R2 Spin Probe. For the R2 spin label, large amplitude χ_4 and χ_5 rotations are hampered by the steric hindrance deriving from the methyl substituent at the 4-position in the pyrroline ring. So, within our approximation, only isolated conformers are possible, which undergo fast and small-amplitude torsional fluctuations.[21] Ten conformers can be identified, which are listed in Table 2. A spectrum is calculated as the sum of ten independent contributions, each due to a single conformer, with a weight, P_J, estimated on the basis of the torsional potential.[21] For a given conformer, reorientation of the nitroxide with respect to the magnetic field is produced by rotational diffusion of the whole protein and librations in the minima of the torsional potential.

Parts A−C of Figure 4 show the spectra calculated for 72R2-T4L in a 30 wt % sucrose solution at the temperatures of 277, 298, and 312 K. The overall diffusion tensor of the protein has been estimated by scaling the values reported in Table 1 according to the change in viscosity of the medium.[36] Thus, the following values have been assumed: $D_{0,\perp} = 0.3 \times 10^7\ s^{-1}$ and $D_{0,\parallel} = 0.47 \times 10^7\ s^{-1}$ ($T = 277$ K), $D_{0,\perp} = 0.6 \times 10^7\ s^{-1}$ and $D_{0,\parallel} = 0.95 \times 10^7\ s^{-1}$ ($T = 298$ K), and $D_{0,\perp} = 0.8 \times 10^7\ s^{-1}$ and $D_{0,\parallel} = 1.35 \times 10^7\ s^{-1}$ ($T = 312$ K). Because of the limited amplitude (about 10° for each bond)[21] and the short correlation times of such motions, the reduced spectral densities, defined in eq 18, are small, of the order of 10^{-11} s. This yields very small spectral densities, given by eq 17, corresponding to a 10 mG line width contribution at X-band. Even at frequencies as high as 250 GHz, such values remain smaller than the inverse of the magnetic anisotropies that they average out, thereby

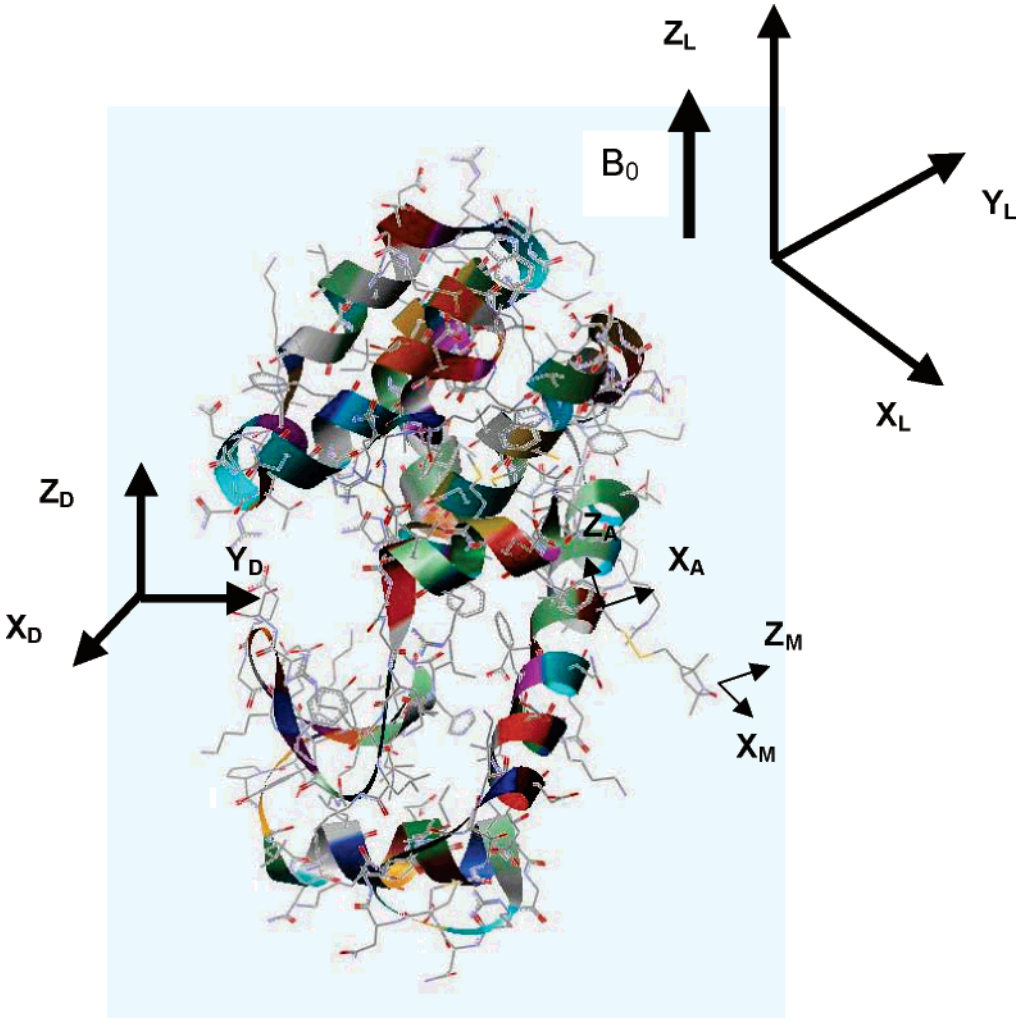

Figure 3. Structure of T4L (3LZM.pdb)[35] with the nitroxide probe linked at site 72. Some of the reference frames defined in this study are shown: laboratory frame (LF), diffusion frame (DF), frame of the amino acid residue (AF), magnetic frame (MF).

TABLE 1: Magnetic Tensors for the Nitroxide in the 72R1 Mutant of T4L;[13] Components of the Rotational Diffusion Tensor Calculated for T4L in Water at $T = 298$ K ($\eta = 0.9$ mPa·s) and Angles from the DF to the AF Frame[34]

$g_{xx} = 2.00803$	$g_{yy} = 2.00582$	$g_{zz} = 2.00218$
$A_{xx} = 6.42$ G	$A_{yy} = 5.95$ G	$A_{zz} = 35.83$ G
$D_{0,\|\|} = 1.2 \times 10^7$ s^{-1}		$D_{0,\perp} = 1.9 \times 10^7$ s^{-1}
$\alpha_A = -68°$	$\beta_A = 166°$	$\gamma_A = -89°$

justifying the fast-motional approximation for the torsional motions. The rotational diffusion coefficients of the protein in the viscous medium are quite small; the spectra of the ten conformers are similar and not very different from the spectrum of a powder sample of a nitroxide spin probe with the **g** and **A** tensors partially averaged by torsional oscillations.

Although of small amplitude, the torsional oscillations are sufficient to produce sizable effects on the spectral line shapes via partial averaging of the magnetic tensors. This clearly appears from comparison of the spectrum calculated at $T = 298$ K, in Figure 4B, with that obtained without any averaging, which is shown in Figure 4D. The differences between the two line shapes match those experimentally found between the spectra recorded for 72R2-T4L and for another mutant, having an MTSSL derivative with a bulky substituent at the 4-position of the pyrroline ring, which is likely to freeze almost completely the chain motions (see Figure 6g in ref 8). The small differences experimentally observed between the spectra of 72R2 at various temperatures (see Figure 5a in ref 8) are also reflected by the line shapes reported in Figure 4A−C. In our model, changes result from: (i) the decrease of viscosity, which brings about a twofold increase in the overall diffusion rate of the protein and the reduction, by a factor of 2, of the spectral densities for chain oscillations (actually, the latter effect is scarcely detectable in view of the small magnitude of such spectral densities); (ii) the increase in amplitude of torsional oscillations, which for each angle is of the order of 1° for a 20° temperature increase. We can see that the main features of the experimental spectra are well predicted without requiring a significant role of the other processes, which we have not taken into account in our model. In addition to transitions involving χ_2 to χ_5 rotations in the side chain, which we found to be very slow,[21] these could include local backbone fluctuations and other interesting dynamical modes of the protein. Thus, our results suggest that backbone motions at sites which, like 72 in T4L, are located at the center of a well-structured α-helix will not be major contributors to the 9 GHz ESR spectra.[8,13] In the future, the approach presented here could be extended to include local fluctuations and protein dynamics, e.g., in the form of normal modes,[37,38] for a more general analysis of ESR spectra. Further investigation, combining theoretical and experimental work, possibly with the use of multifrequency experiments and analysis, could provide new insights into the dynamics of proteins.

B. R1 Spin Probe. The side chain of the R1 spin probe is less sterically hindered than that of R2, and its dynamics becomes more complex due to the possibility of conformational

TABLE 2: Torsional Angles and Probabilities for the Sterically Allowed Conformers of the Nitroxide Side Chain of the R1 Spin Label, at a Site Located in the Middle of a Poly-Ala Helix[a]

conformer	χ_1 (deg)	χ_2 (deg)	χ_3 (deg)	χ_4 (deg)	χ_5 (deg)	P_J
C1*	−60	−75	−90	180	+77 (+85)	0.143 (0.201)
*C*2*	−60	−75	−90	180	−77 (−85)	0.143 (0.201)
C3	−60	−75	−90	−75	+100	0.045
C4	−60	−75	−90	−75	−8	0.074
C5*	−60	180	90	180	+77 (+85)	0.187 (0.263)
C6*	−60	180	90	180	−77 (−85)	0.187 (0.263)
C7	−60	180	90	+75	−100	0.059
C8	−60	180	90	+75	+8	0.098
C9*	180	180	−90	180	+77 (+85)	0.009 (0.013)
C10*	180	180	−90	180	−77 (−85)	0.009 (0.013)
C11	180	180	−90	−75	+100	0.003
C12	180	180	−90	−75	−8	0.005
C13*	180	180	90	180	+77 (+85)	0.009 (0.013)
C14*	180	180	90	180	−77 (−85)	0.009 (0.013)
C15*	180	75	90	180	+77 (+85)	0.007 (0.010)
C16*	180	75	90	180	−77 (−85)	0.007 (0.010)
C17	180	75	90	+75	−100	0.002
C18	180	75	90	+75	+8	0.004

[a] Statistical weights were calculated at $T = 298$ K on the basis of the single bond torsional potential, V' in eq 1. Conformers allowed for the R2 spin probe are denoted by an asterisk; probability and χ_5 values for these are reported in parentheses.

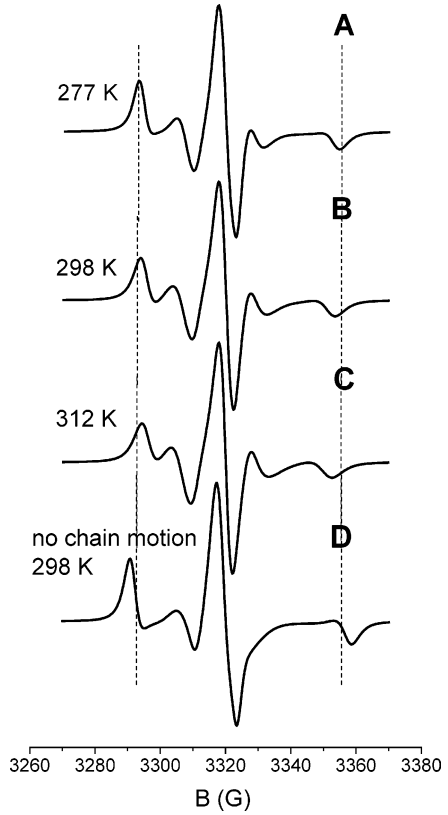

Figure 4. Spectra calculated for the 72R2 mutant of T4L in a 30 wt % sucrose solution at different temperatures (A−C). The spectrum calculated at $T = 298$ K in the absence of chain motions is shown in (D). Experimental spectra are reported in Figure 5b of ref 8. The dashed vertical lines are drawn as a guide to the eye for comparison.

transitions.[21] For the sake of simplicity, the fast-motional approximation has been assumed for torsional librations and χ_4 and χ_5 jumps, whereas conformational transitions involving the χ_1, χ_2, and χ_3 dihedrals are considered to be slow enough that they could be been neglected. This choice can be justified by

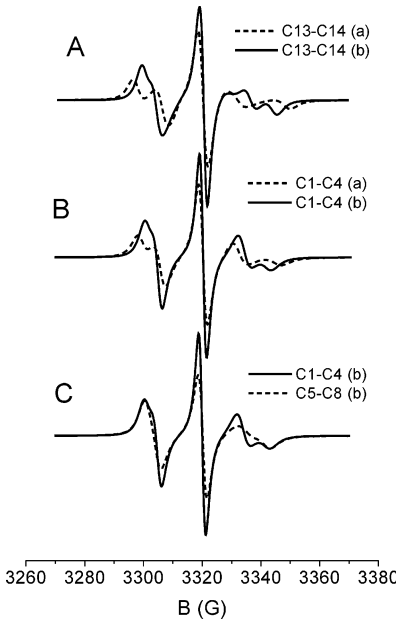

Figure 5. Contributions to the spectrum of R1 spin label deriving from different sets of conformers, as indicated in the labels, and under different conditions for the $\chi_5|_{\chi_4=t}$ distribution. (a): Gaussian distribution about the minima, with root-mean-square amplitude $\overline{(\delta\chi_5)^2}^{1/2} = 20°$; (b): distribution derived from the calculated torsional potential (ROHF/6-31G**),[21] in the range 0° to ±120°. Parameters suitable for the 72R1-T4L mutant in 30 wt % sucrose solution at $T = 298$ K are used.

the observation that conformational jumps occurring through rotations of internal bonds are slower by virtue of the higher friction opposing them; moreover, because they involve the displacement of larger chain portions, they are more likely to be hampered by neighboring chains. Thus, five independent blocks of conformers can be identified, which will be designated according to the notation reported in Table 2. The two conformers in the block C13−C14 interconvert through χ_5 jumps, whereas the four conformers in each of the blocks C1−C4, C5−C8, C9−C2, and C14−C18 are connected by χ_4 and χ_5 rotations. In 30 wt % sucrose solutions at $T = 298$ K, reduced spectral densities are of the order of 5×10^{-11} s. Thus, given the magnitude of the magnetic anisotropies averaged by the two kinds of side chain motions, the motional narrowing approximation can be adopted for them in the case of 9 GHz ESR spectra;[21] however, at higher frequency, such an approximation is likely inappropriate.

An important difference with the case of R2 is that the independent blocks of conformers of R1 yield significantly different spectra. The situation is made even more complicated by the possible effects of local interactions on the conformer distribution and the uncertainty in the torsional potential $V(\chi_5)$ when χ_4 is in the trans state, $(\chi_5|_{\chi_4=t})$. Actually, a barrier of the order of k_BT is predicted from ab initio calculations at the ROHF/6-31G** level;[21] however, such a value is sensitive to the level of the calculations and also the possibility exists that it can be affected by interactions involving the pyrroline ring.[39] Examples of the spectra which can be obtained are shown in Figure 5. In all cases, the values $D_{0,\perp} = 0.6 \times 10^7$ s^{-1} and $D_{0,\parallel} = 0.95 \times 10^7$ s^{-1}, appropriate for a 30 wt % sucrose solution at $T = 298$ K, are used. Given the uncertainty in the torsional profile for $\chi_5|_{\chi_4=t}$ and the fact that adoption of Gaussian distributions centered at the minima is not fully justified if barriers are not sufficiently high, we have considered two different torsional distributions for the $\chi_5|_{\chi_4=t}$ dihedral angle. In case (a) Gaussian distributions with oscillations of root-mean-

square amplitude $\overline{(\delta\chi_5)^2}^{1/2} = 20°$ about the minima at $\pm 77°$ are assumed; this value has been derived from the curvature of the torsional potential in the minima. In case (b), a wider distribution has been assumed, obtained from the calculated $V(\chi_5)$ torsional potential in the range 0° to ±120°. The exact form of the distribution is not relevant; analogous results would be obtained with a Gaussian distribution centered in the minima, of root-mean-square amplitude $\overline{(\delta\chi_5)^2}^{1/2} \approx 35°$ to ±40°. Figure 5A shows the spectra calculated for the C13−C14 pair of conformers with the two choices; they look quite different, with case (b) exhibiting a higher degree of averaging, as expected. Figure 5B shows the line shapes obtained for the block of conformers C1−C4, with the same choices, (a) and (b), for the $\chi_5|_{\chi_4=t}$ distribution. A similarity to the spectra obtained for the C13−C14 pair clearly appears, although the presence of χ_4 jumps produces here somewhat more averaging. Finally, Figure 5C displays the spectra calculated for the C1−C4 and the C5−C8 blocks; the main reason for the differences between the two line shapes is the difference in chain isomerization rates,[21] which reflects different friction opposing bond rotations, as a consequence of differences in the chain geometry. The spectra obtained for the C15−18 and the C9−C12 blocks are very similar to those shown in Figure 5C for the C1−C4 and the C5−C8 blocks, respectively.

The examples reported in Figure 5 clearly show that the chain conformational dynamics is sufficient to produce a variety of spectra for the R1 spin label. The weight of the various contributions to the line shape is likely to depend on the location of the spin label and on the nature of the neighboring amino acid residues. This consideration is confirmed by ESR experiments on T4L mutants with R1 linked at different solvent exposed α-helix sites, or on mutants having R1 at a given site and different nearby residues.[41] Such spectra have a common structure, with minor differences which can be ascribed to the different weight of the same contributing components. Having distinguished the possible spectral components, we have tried to make the spectral analysis more manageable, retaining a minimal number of independent of contributions. Taking as a reference the spectrum of 72R1-T4L recorded at $T = 298$ in 30 wt % sucrose solution,[8] these have been identified as: (i) a constrained component, deriving from pairs of conformers with χ_4 in the *t* state, in which the χ_5 dihedral undergoes $-77° \rightleftharpoons +77°$ jumps and torsional oscillations of root-mean-square amplitude $\overline{(\delta\chi_5)^2}^{1/2} = 20°$ (case (a) in Figure 5A); (ii) a mobile component, originating from groups of four conformers experiencing χ_4 and χ_5 transitions, with a wide $\chi_5|_{\chi_4=t}$ distribution (case (b) in Figure 5B); (iii) an intermediate contribution, which differs from the latter only in the assumption of a more confined $\chi_5|_{\chi_4=t}$ distribution around the minima of the torsional potential, with root-mean-square amplitude $\overline{(\delta\chi_5)^2}^{1/2} = 20°$ (case (a) in Figure 5B).

Calculations have been performed giving the three components the weights 0.4, 0.3, and 0.3, respectively, which have been adjusted to reproduce the experimental line shape of 72R1-T4L in 30 wt % sucrose solution at $T = 298$ K.[8] The effect of temperature on fluctuation amplitudes and rates of conformational transitions have been taken into account. Dynamic parameters, like the overall diffusion tensor of the protein and rates of internal motions, have been scaled according to the change in solution viscosity.[36] The diffusion tensor components used are: $D_{0,\perp} = 0.4 \times 10^7 s^{-1}$ and $D_{0,\parallel} = 0.63 \times 10^7\ s^{-1}$ ($T = 283$ K), $D_{0,\perp} = 0.6 \times 10^7\ s^{-1}$ and $D_{0,\parallel} = 0.95 \times 10^7\ s^{-1}$ ($T = 298$ K), and $D_{0,\perp} = 0.8 \times 10^7\ s^{-1}$ and $D_{0,\parallel} = 1.35 \times 10^7\ s^{-1}$ ($T = 312$ K). The temperature dependence of the rates of internal motion are found to be due to both the activated processes (33%) and the decreased viscosity (67%) as the temperature is raised. Figure 6 shows the calculated spectra at temperatures of 283, 298, and 312 K, superimposed on the experimental spectra, taken from Figure 5a in ref 8. We can see that the main features of the spectra and their temperature dependence are well reproduced by the simulation. Some discrepancies are observed at the lowest temperature ($T = 283$ K); they probably reflect the inadequacy of the fast motional assumption for the chain dynamics in the highly viscous sucrose solution at this low temperature.

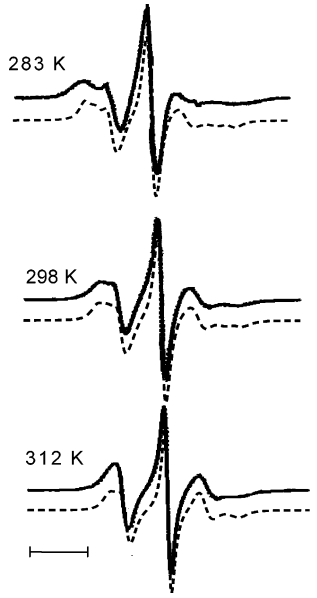

Figure 6. Spectra calculated for the 72R1 mutant of T4L in 30 wt % sucrose solution at different temperatures (dashed) and the corresponding experimental spectra taken from Figure 5a in ref 8 (solid). A small vertical offset between calculated and experimental spectra is introduced to help their comparison. The bar corresponds to a field scan of 20 G.

We have also calculated the 9 GHz spectra of 72R1 in water at different temperatures, giving again the weights 0.4, 0.3, and 0.3 to the three spectral components. At a given temperature, differences from the spectra in sucrose solution only arise from the change in viscosity, which affects both transition rates and the protein diffusion tensor. For the latter, the values reported in Table 1 have been used for $T = 298$ K, while the values at the other temperatures have been scaled according to the change in solution viscosity.[36] The following values have been used: $D_{0,\perp} = 0.8 \times 10^7\ s^{-1}$ and $D_{0,\parallel} = 1.35 \times 10^7\ s^{-1}$ ($T = 283$ K), and $D_{0,\perp} = 1.2 \times 10^7\ s^{-1}$ and $D_{0,\parallel} = 1.9 \times 10^7\ s^{-1}$ ($T = 312$ K). Calculated and experimental line shapes are shown in Figure 7; the good quality of the simulations as compared to experiment can be recognized. Interestingly, the observed disappearance, at higher temperatures, of a less mobile component, clearly recognizable at low temperature, naturally emerges from the calculations.

To summarize, we have seen that the spectra of 72R1-T4L can be simulated as the superposition of three components, obtained from modeling of the side chain dynamics. The only adjustable parameters are the weights of such components; the choice of all the other parameters is justified not by spectral fitting, but rather by independent experimental findings and theoretical considerations. In addition to torsional oscillations involving all the dihedral angles, the majority of conformers can undergo both χ_4 and χ_5 transitions; for a smaller number of conformers, $t \rightarrow g$ transitions of the χ_4 dihedral are forbidden

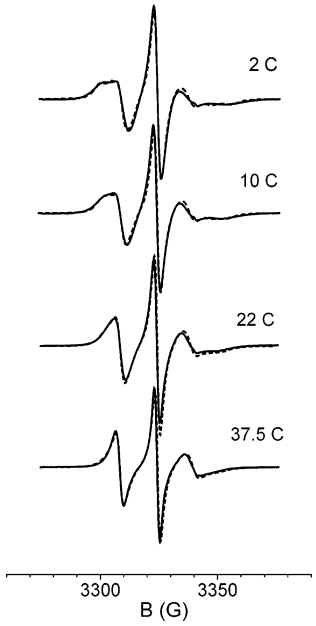

Figure 7. Experimental[13] (solid) and calculated (dashed) spectra of the 72R1 mutant of T4L in water at different temperatures.

for sterical reasons, and only χ_5 jumps remain possible. The value of 40% obtained for the constrained component from spectral analysis is much greater than the value of the calculated probability for just the C13−C14 pair, which are the only conformers that do not permit rotations of the χ_4 dihedral (see Table 2). We thus infer that in the real system the number of conformers that only undergo χ_5 jumps is actually larger than just the C13−C14 pair. A plausible explanation for such behavior could be the hampering of χ_4 transitions by the neighboring side chains in the real system; effects of this kind, which depend on the structure and conformation of the nearby residues, were only partially taken into account in our model of a poly-Ala α-helix used to derive the conformer distribution. If we take, for example, the C1−C4 block, it is likely that, due to the constraints of the specific protein environment, χ_4 interconversion between some of the four conformers becomes highly hindered; so the four conformers of the C1−C4 block would in practice behave as two blocks of conformers connected by χ_5 jumps, whose contribution to the ESR spectra would be similar to that of the C13−C14 pair. Similar comments could apply to other blocks. Moreover, the physical significance of the fitted weights of the spectral components should be taken with care because even small variations in the contributing line shapes can bring about significant changes in the relative weights estimated from spectral fitting. This matter is exacerbated when, as in the present case, just a few components are taken as representative of a more extensive collection of states. Thus, for example, the 30% weights estimated for the (ii) and (iii) components should be better interpreted as an indication of the simultaneous presence of conformers experiencing oscillations of different amplitudes about the $\chi_5|_{\chi 4} = t$ stable states.

In view of our analysis, we now wish to reconsider the results of simulation of the multifrequency spectra of 72R1-T4L in water.[13] The uncertainty in the molecular interpretation of the best fit parameters of Liang et al.,[13] and the differences in the present approach from that previously used by them,[13] limit somewhat the comparison that can be made.

(a) The presence of two components with different mobility emerged from fitting of multifrequency ESR experiments on 72R1-T4L, at least at the lower temperatures.[13] Dominance of the less-mobile contribution was inferred, in agreement with our result. A quantitative comparison of the weights obtained in the two cases is not really meaningful, for the reason mentioned above: the separation of sharp and broad spectral components is not straightforward and can be strongly affected by the assumptions of the underlying model. The sensitivity of spectral weights to model assumptions was also pointed out in ref 13, where different values were obtained from separate fitting of spectra at different frequencies.

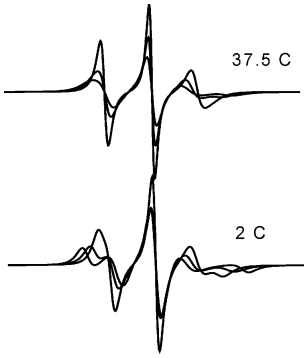

Figure 8. Constrained and mobile contributions to the spectra of 72R1-T4L in water at $T = 2$ °C and $T = 37.5$ °C.

TABLE 3: Order Parameters for the Magnetic Frame of MTSSL in the 72R1 Mutant of T4L in Water at $T = 10$ °C, as Obtained from This Work and from the Simultaneous Fit of Multifrequency Spectra[13] [a]

	S_{xx}^{ZZ}	S_{yy}^{ZZ}	S_{zz}^{ZZ}
constrained	−0.44	−0.24	0.68
	−0.29	−0.23	0.52
	−0.33	−0.23	0.56 (ref 13)
mobile	−0.41	0.04	0.37
	−0.37	+0.01	0.36 (ref 13)

[a] Order parameters for the constrained and the mobile spectral components are reported. The *x*, *y*, *z* axes define the principal frame of the ordering matrix S^{ZZ};[43] *z* is parallel to the N-p_z orbital.

(b) In ref 13, two spectral components were detected at low temperatures, but only one at higher temperatures; thus, the possibility of dynamic exchange between two conformers was suggested. Here, from the modeling of the side chain dynamics, we have shown that merging of the two components naturally results with increasing temperature from the increase in overall protein mobility and in amplitude of torsional fluctuations. The change of spectral components with temperature is shown in Figure 8. The possibility of exchange narrowing cannot be ruled out, but this is not necessary to explain the observed behavior.

(c) Table 3 reports the order parameters calculated in this work and those obtained in ref 13. The values obtained for the more mobile component are similar, although in the present case, higher biaxiality of order is predicted, i.e., a larger difference in the propensity of the *x* and *y* principal axes of the magnetic frame to align along the *Z* director. The order parameters derived in ref 13 for the more constrained component are roughly between those obtained here for the two constrained contributions. In ref 13, the alignment axes were assumed to be parallel to the principal axes of the magnetic **A** and **g** tensors; from our modeling of the side chain motions, only the *z* axis comes out to be roughly parallel to the N-p_z orbital.

(d) Let us now consider the parameters characterizing the chain dynamics. In ref 13, a higher rotational mobility perpendicular than along the N-p_Z orbital was found for both components; a particularly high value of the perpendicular diffusion coefficient was obtained for the mobile component. The physical interpretation of the motional parameters derived

from fitting of spectra with more or less sophisticated models of rotational diffusion has been a matter of concern.[9] Our modeling of the side chain motions offers this interpretation: the fastest motions are χ_5 rotations, which produce reorientations of the magnetic tensors roughly perpendicular to the N-p_Z orbital. Such motions are expected to be particularly fast in conformers with wider $\chi_5|_{\chi_4=t}$ distribution around the stable states, i.e., lower $g_+ \rightleftharpoons g_-$ barrier for the χ_5 dihedral.

IV. Discussion and Conclusions

The main objective of this work has been the identification of the general features introduced into the ESR line shape of spin-labeled proteins by the structure and intrinsic dynamics of the nitroxide side chain. For this purpose, a methodology for the simulation of spectra of MTSSL spin labels linked at an "ideal" α -helix has been developed. It has been assumed that the reorientation of the magnetic tensors with respect to the static magnetic field is modulated by the conformational dynamics of the nitroxide side chain, superimposed on overall reorientations of the protein. The latter, which fall in the slow time scale for the experiments under examination, have been treated in the framework of the SLE. A detailed description of the chain dynamics has been adopted on the basis of the results of the conformational analysis.[21] For the sake of simplicity, a separation has been taken between sufficiently fast chain motions, whose effect is approximated by the fast motional theory,[22,23] and slower bond rotations, which have been assumed to be frozen on the ESR time scale. The fast motions are described as jumps between stable conformers and librations about the minima of the chain torsional potential. Our approach, although approximate, contains key realistic features that have led to some rather general results on the geometry and kinetics of such motions.

This methodology has been used to analyze X-band (9GHz) spectra of T4L with two variants of the MTSSL spin probe at the 72 residue. The spectra calculated with our modeling approach, utilizing a limited number of parameters (either derived from experiments or from theory), are in very good agreement with experiment. Details of protein dynamics are not included in the model at this stage, and from our results, it can be inferred that they probably do not significantly affect the line shape of a spin probe located on a rather rigid α-helix.

The case of the 72R2 mutants was first considered. It is actually simpler because the presence of the methyl substituent at the 4-position of the pyrroline ring freezes out almost completely the MTSSL side chain dynamics. Actually, 10 noninterconverting conformers turn out to be possible, which only undergo small-amplitude torsional oscillations. We have shown that the main features of the spectra recorded in sucrose solution at different temperatures can be explained as the sum of contributions calculated for each of these conformers, with magnetic tensors partially averaged by oscillations about the minima of the torsional potential and an overall diffusion tensor estimated on the basis of the protein structure. Spectral changes with temperature are simply accounted for through the thermal change in oscillation amplitude and the solution viscosity, i.e., protein diffusion tensor.

The 72R1 mutants have greater torsional freedom and present more complex dynamics. All conformers also undergo, in addition to small-amplitude torsional oscillations of the $\chi_1-\chi_4$ dihedrals, conformational jumps and wider amplitude fluctuations involving the χ_5 dihedral. Moreover, some of the conformers can also experience χ_4 conformational transitions. As a consequence, the dynamics of the side chain is expected to yield complex spectra, resulting from the superposition of a variety of contributions. A key result of our analysis is the identification of the simultaneous presence of "constrained" and "mobile" components in the spectra. From the modeling of the chain dynamics, the former is ascribed to conformers, which, in addition to rather confined fluctuations about all the minima of the torsional potential, can only undergo χ_5 jumps. On the other hand, the most mobile component is attributed to sets of conformers experiencing χ_4 and χ_5 conformational jumps, together with wider amplitude χ_5 fluctuations about the minima. To make the spectral analysis simpler, three components are taken as a minimal number sufficient to account for the experimental behavior; in this way, good simulations of the 9 GHz ESR spectra at different temperatures in different solvents have been obtained, with only the spectral weights as free parameters.

The presence of different components is a feature displayed in many cases by the spectra of spin-labeled proteins, and several reasons for it have been proposed.[8,9,13] The simultaneous presence of different conformers has been hypothesized,[39,40] as well as that of different local environments,[8] and the possibility of a temperature-dependent dynamic exchange mechanism;[13] the two-state nature of the disulfide bond has also been indicated as a possible explanation.[18,39] On the basis of our model, we suggest here that the multicomponent character is an intrinsic feature of the ESR spectra of the R1 spin label, which derives from the simultaneous presence of conformers with different mobilities. Depending on the experimental conditions and the labeling site, the spectral components can sometimes be more or less well resolved, and sometimes only a single component can be inferred from the analysis of a single spectrum.

It is of interest to compare the spectra of the 72R1 mutant of T4L with those obtained for 131R1, which are also reported in refs 8 and 13. Despite a little larger anisotropy of the magnetic tensors,[13] less anisotropic line shapes are obtained for 131R1 than for 72R1, which cannot be simply obtained by adjusting the weights of the components considered for 72R1. Because of its location, the spin probe in 131R1 is more solvent exposed than in 72R1; this hypothesis is supported by the larger hyperfine tensor components. Accordingly, less hindrance to conformational jumps is expected, together with larger amplitude χ_5 motions, even for isolated conformers. But most likely this is not the main reason behind the narrowing of the spectra; actually, the presence of a constrained component can be detected for 131R1 in 30 wt % sucrose solution at sufficiently low temperatures. This suggests that the backbone dynamics is likely to be the main reason for the observed differences between the spectra for 72R1 and 131R1.[8,13] In fact, we notice that 131R1 is located on a small two-and-a-half turn helix, which is expected to provide less rigidity to the motion.[13]

A clear distinction between the R1 and R2 spin labels emerges from our analysis. In the latter case, the chain dynamics is very restricted. Therefore, it has small effects on the line shapes and can be easily accounted for. Moreover, it can be treated under the fast-motional approximation up to higher frequencies, and different conformers of the side chain yield very similar spectral components. These features turn out to be very advantageous for the interpretation of experiments and make R2 a very useful spin probe for the investigation of protein dynamics. Namely, the possibility of accounting in a simple way for the side chain dynamics opens up the prospect of introducing into the stochastic Liouville equation the protein dynamics, e.g., by relatively simple approaches like the Gaussian (or elastic network) model.[37,38] The situation is less straightforward in the case of

the R1 spin label, which is more mobile and has an intrinsic multicomponent nature; for these reasons, spectral analysis and disentanglement of the various motions become harder. On the other hand, the possibility of exploring more extended regions make R1 more suitable to distinguish different local environments through their effects on the probe mobility.

The methodology presented here can be used as long as the fast motional regime can be assumed for the side chain motions; a more general description, which would also be suitable for high field experiments, would require relaxing the motional narrowing approximation for the nitroxide side chain dynamics. (Our preliminary analysis of 72R-T4L spectra obtained at 250 GHz[13] has indicated that the fast motional approximation is no longer appropriate.) To this purpose, the spectral contribution of a set of interconverting conformers could be described by explicitly including in the SLE the dynamics of the χ_4 and χ_5 dihedral angles, characterized by their torsional potentials and their frictional effects, in addition to the overall protein reorientation. Solution of the problem should remain feasible at a resonable computational cost, even after the inclusion of these two further degrees of freedom. The description of the conformational dynamics would not require the introduction of new parameters because the relevant quantities, i.e., torsional potentials and friction opposing bond rotations, could be calculated as we have shown in this report. Only the height of the χ_5 torsional barrier, which is likely to be strongly dependent on the specific environment experienced by the spin probe, could be taken as an adjustable parameter. This could be obtained through the best fit of experimental line shapes, together with the weights of the spectral components and the diffusion tensor of the whole protein. The advantage of such an approach over other approaches would be the clear physical interpretation of the parameters, and, as a consequence, a better characterization of structural and dynamic features of the protein.

An alternative methodology for the introduction of the side chain dynamics of R1 in the SLE framework could be based on the use of the SRLS model,[12] together with MD simulations. From these, the parameters for internal motions and orienting potential of the spin probe in its specific environment could be derived. As shown here and in the companion paper,[21] the presently available version of the SRLS model could be conveniently improved by introducing a more flexible form of the orienting potential suitable to account for the orientational distribution of the spin probe. Of course, an important requirement of trajectories is a representative sampling of the conformational space explored by the spin probe. We have seen that the constraints imposed by a generic α-helix environment lead to sets of noninterconverting conformers. This means that, in a given trajectory, the spin probe could remain trapped in a subspace, which depends on the starting condition; this point should be carefully considered in order to obtain reliable information from MD.

Acknowledgment. A.F. and F.T. have been supported by MIUR (PRIN-2005) and Università di Padova (CPDA057391). They gratefully Anna Lisa Maniero, Lorenzo Franco, and Antonio Toffoletti for stimulating discussions. J.H.F. acknowledges support of this project by grant no. P41RR16292 from the National Center for Research Resources (NCRR), a component of the National Institutes of Health (NIH), and its contents are solely the responsibility of the authors an do not necessarily represent the official view of NCRR or NIH.

Appendix: Introduction of Fast Internal Motions in the SLE

Extension of the slow-motional ESR theory[42] to include fast internal motions has been performed in the following way.

(a) The partially averaged magnetic tensors, which are used in place of the nitroxide magnetic tensors, are obtained from these and from the calculated order parameters according to eq 16.

(b) An orientation-dependent line width is assumed, defined by eqs 9−13 and eq 17. Equation 9 is expressed in the form:

$$T_{2,MM'}{}^{-1} = \sum_{m=0,1}\sum_{p,p'} D^2_{m,p}{}^*(\Omega_D)\, D^2_{m,p'}(\Omega_D) T_{M,M',m,m',p,p'} \quad (27)$$

where $T_{M,M',m,m',p,p'} = \sum_{\mu,\mu'} c_{M,M',m,m,\mu,\mu'} \sum_{q,k,q',k'} F^{(2,k)}_{\mu;\mathrm{MF}} F^{(2,k')*}_{\mu';\mathrm{MF}} j_{q,k,q',k'} D^2_{p,q}{}^*(\Omega_A) D^2_{p',q'}(\Omega_A)$, with $c_{M,M',m,m,\mu,\mu'}$ being suitable coefficients. Thus, additional elements of the following form have to be introduced into the matrix representation of the stochastic Liouville operator:[42]

$$\langle LMK|D^2_{m,p}{}^*(\Omega_D) D^2_{m,p'}(\Omega_D)|L'M'K'\rangle = \sqrt{(2L+1)(2L'+1)}\,\delta_{M,M'}\,\delta_{K+p,K'+p'}\,\delta_{mm'}\sum_J (2J+1)^{-1}$$

$$\begin{pmatrix} L & 2 & & J \\ M & m & -M & -m \end{pmatrix}\begin{pmatrix} L' & 2 & & J \\ M' & m' & -M' & -m' \end{pmatrix}\begin{pmatrix} L & 2 & & J \\ K & p & -K & -p \end{pmatrix}\begin{pmatrix} L' & 2 & & J \\ K' & p' & -K' & -p' \end{pmatrix} \quad (28)$$

where $|LMK\rangle = \sqrt{(2L+1)/8\pi^2} D^L_{MK}(\Omega_D)$ and (...) are 3j symbols.[27]

The introduction of the side chain fast motions does not appreciably increase the computing time required for line shape simulations.

References and Notes

(1) Hubbell, W. L.; Gross, A.; Langen, R.; Lietzow, M. *Curr. Opin. Struct. Biol.* **1998**, *8*, 649.
(2) Borbat, P. P.; Costa-Filho, A. J.; Earle, K. A.; Moscicki, J. K.; Freed, J. H *Science* **2001**, *291*, 266.
(3) Freed, J. H. In *Spin Labeling: Theory and Application*; Berliner, L. J., Ed.; Academic Press: New York, 1976; p 53.
(4) Schwartz, L. J.; Stillman, A. E.; Freed, J. H. *J. Chem. Phys.* **1982**, *77*, 5410.
(5) Schneider, D. J.; Freed, J. H. *Adv. Chem. Phys.* **1989**, *73*, 387.
(6) Budil, D. E.; Lee, S.; Saxena, S.; Freed, J. H. *J. Magn. Res.* **1996**, *120*, 155; programs available at www.acert.cornell.edu.
(7) Meirovitch, E.; Nayeem, A.; Freed, J. H. *J. Phys. Chem.* **1984**, *88*, 3454.
(8) Columbus, L.; Kámás, T.; Jekö, J.; Hideg, K.; Hubbell, W. L. *Biochemistry* **2001**, *40*, 3828.
(9) Barnes, J. P.; Liang, Z.; Mchaourab, H. S.; Freed, J. H.; Hubbell, W. L. *Biophys. J.* **1999**, *76*, 3298.
(10) Polnaszek, C. F.; Freed, J. H. *J. Phys. Chem.* **1975**, *79*, 2283.
(11) Freed, J. H. *J. Chem. Phys.* **1977**, *66*, 4183.
(12) Polimeno, A.; Freed, J. H. *J. Phys. Chem.* **1995**, *99*, 10995.
(13) Liang, Z.; Lou, Y.; Freed, J. H.; Columbus, L.; Hubbell, W. L. *J. Phys. Chem. B* **2004**, *108*, 17649.
(14) Jacobsen, K.; Oga, S.; Hubbell, W. L.; Risse, T. *Biophys. J.* **2005**, *88*, 4351.
(15) Steinhoff, H.-J.; Hubbell, W. L. *Biophys. J.* **1996**, *71*, 2201.
(16) Robinson, B. H.; Slutsky, L. J.; Auteri, F. P. *J. Chem. Phys.* **1992**, *96*, 2609.
(17) Stoica, I. *J. Phys. Chem. B* **2004**, *108*, 1771.
(18) Murzyn, K.; Rg, T.; Blicharski, W.; Dutka, M.; Pyka, J.; Szytula, S.; Froncisz, W. *Proteins* **2006**, *62*, 1088.
(19) Budil, D. E.; Sale, K. L.; Khairy, K. A.; Fajer, P. J. *J. Phys. Chem. B* **2006**, *110*, 3703.
(20) Timofeev, V. P.; Nikolsky, D. O. *J. Biomol. Struct. Dyn.* **2003**, *21*, 367.

(21) Tombolato, F.; Ferrarini, A.; Freed, J. H. *J. Phys. Chem. B* **2006**, *110*, 26248.
(22) Redfield, A. G. *Adv. Magn. Reson.* **1965**, 1.
(23) Freed, J. H.; Fraenkel, G. K. *J. Chem. Phys.* **1963**, *39*, 326.
(24) Cassol, R.; Ferrarini, A.; Nordio, P. L. *J. Phys. Chem.* **1993**, *97*, 2933.
(25) Cassol, R.; Ge, M.-T.; Ferrarini, A.; Freed, J. H. *J. Phys. Chem. B* **1997**, *101*, 8782.
(26) Liang, Z.; Freed, J. H. *J. Phys. Chem. B* **1999**, *103*, 6384.
(27) Zare, R. N. *Angular Momentum*; Wiley: New York, 1987.
(28) Shore, J. E.; Zwanzig, R. *J. Chem. Phys.* **1975**, *63*, 5445.
(29) Zientara, G. P.; Freed, J. H. *J. Chem. Phys.* **1983**, *69*, 3077.
(30) Risken H. *The Fokker−Planck Equation*; Springer-Verlag: Berlin, 1984.
(31) Ferrarini, A.; Moro, G.; Nordio, P. L. *Mol. Phys.* **1988**, *63*, 225.
(32) Kramers, H. A. *Physica* **1940**, *7*, 284.
(33) Langer, J. S. *Ann. Phys.* **1969**, *54*, 258.
(34) Garcia de la Torre, J.; Huertas, M. L.; Carrasco, B. *J. Magn. Res.* **2000**, *147*, 138.
(35) Matsumura, M.; Wozniak, J. A.; Dao-pin, S.; Mattews, B. W. *J. Biol. Chem.* **1989**, *264*, 16059.
(36) Weast R. C. *Handbook of Chemistry and Physics*; CRC Press: Cleveland, 1975.
(37) Tirion, M. M. *Phys. Rev. Lett.* **1996**, *77*, 1905.
(38) Bahar, I.; Atilgan, A. R.; Erman, B. *Fold. Des.* **1997**, *2*, 173.
(39) Langen, R.; Oh, K. J.; Cascio, D.; Hubbell, W. L. *Biochemistry* **2000**, *39*, 8396.
(40) Pyka, J.; Iinicki, J.; Altenbach, C.; Hubbell, W. L.; Froncisz, W. *Biophys. J.* **2005**, *89*, 2059.
(41) Mchaourab, M. S.; Lietzow, M. A.; Hideg, K.; Hubbell, W. L. *Biochemistry* **1996**, *35*, 7692.
(42) Meirovitch, E.; Igner, E.; Igner, D.; Moro, G.; Freed, J. H. *J. Chem. Phys.* **1982**, *77*, 3915.
(43) Zannoni, C. In *The Molecular Physics of Liquid Crystals*; Luckhurst, G. R., Gray, G. W., Eds.; Academic Press: New York, 1979; p 51.

Chapter 8

MD simulation of the 31-52 fragment of α-synuclein with lipid bilayer

8.1 Introduction

α-Synuclein (*aS*) is 140 amino acid protein that is concentrated at the presynaptic termini of the central nervous system [Maroteaux, 1988]. Although not yet fully understood, the physiological function of *aS* is likely to involve a role in modulating synaptic plasticity [George, 1995], presynaptic vesicle pool size, and neurotransmitter release [Abeliovich, 2000], as well as vesicle recycling. *aS* is commonly believed to play a role in diseases such as Parkinson's disease [Spillantini, 1997], Alzheimer's disease [Ueda, 1993] and Hallervorden-Spatz syndrome. For instance, a large population of *aS* is found in Lewy body filaments (amyloid fibrils) that are a distinctive pathological characteristics of these diseases. However, the role of the protein in the etiopathogenesis remains elusive.

aS has been shown to interact with liposomes [Davidson, 1998] and micelles [Chandra, 2003] *in vitro*. On the basis of sequence analysis, it was recognized that the N-terminal portion of *aS* was likely to mediate lipid interactions. The N-terminus of *aS* contains seven repeats, each of which is made of 11 amino acids. This region is a positively charged lysine-rich region that can interact by electrostatically with negatively charged lipids. According to Circular Dichroism analysis, this interaction causes *aS* to undergo a conformational change from an unstructured monomer in solution to an α-helical, membrane bound protein. On the contrary, the negatively charged glutamate-rich C-terminal region is not involved in membrane interactions and remains unfolded. Micelle-bound *aS* has been thoroughly investigated, and there is a general consensus on the presence of two helical portions [Bisaglia, 2005; Ulmer, 2005; Borbat, 2006], with a break in the 38-44 region. On the contrary, the structure of *aS* bound to lipid vesicles, likely to be physiologically more relevant, is still a matter of debate. An uninterrupted helix was proposed from SDSL-EPR experiments with small unilamellar vesicles (SUV) comparable in size and composition to synaptic vesicles [Jao, 2004]. The presence of a break was also hypothesized [Bussell, 2005], as well as the possibility of switching of the helix connector between conformations in an environment-dependent manner [Ulmer, 2005; Zakharov, 2007].

Another aspect that remains unclear is that binding of *aS* seems to be lipid specific and dependent on vesicle size [Davidson, 1998; Zhu, 2003]. On the basis of available data, several experiments reported that the presence of anionic lipids is necessary for binding of *aS* to membranes [Chandra, 2003; Ramakrishnan, 2003]. However, binding of wild-type or truncated protein to zwitterionic lipids has been recently observed [Rhoades, 2006]. Furthermore, NMR spectra of phospholipids multilamellar vesicles (MLV) revealed that *aS* can disrupt the integrity of the lipid bilayer when associated with membrane containing lipids with anionic headgroups, but the protein has little effect on membranes of zwitterionic phosphatidylcholine [Madine, 2006]. On the contrary, binding of the *aS* fragment 10-48, which corresponds to the lysine-rich N-terminal region, or fragment 120-140, which corresponds to the glutamate-rich C-terminal

region, do not disrupt the lamellar structure of membranes, but both peptides appear to induce lateral segregation the lipids into clusters of acidic lipid-enriched and acidic lipid-deficient domains.

The structural properties of *aS* in the presence of a lipidic environment have been investigated also by computational methods. Molecular Dynamics simulations (MD) have been performed on the 1-95 fragment of *aS* [Mihajlovic, 2007] with an implicit membrane model. This work shows that *aS* preferentially binds to anionic, but also marginally to neutral membranes. Furthermore, MD simulations on the 1-95 fragment evidenced that *aS* presents an instability in the region near residue 47, and forms a bent helix. This work hypothesizes that bending of the helix is not due to the protein sequence or membrane binding, but to collective motions of the long helix. The choice of an implicit membrane model let the possibility to obtain various MD trajectories with a low computational cost and relatively short time. The authors performed a series of MD simulations changing the relative orientation of the helix with respect to the dielectric slab which mimics the bilayer and showed that *aS* has a preferential binding face. Furthermore, they found that the most stable helical conformation is a 11/3 conformation (11 amino acids per helical turn) Rather than the classical α-helix (18/5). Despite some interesting results, there can be some doubts on the particular approach used to describe lipid bilayer in these works. The implicit membrane model considers the lipid bilayer as a continuum medium, neglecting molecular details. Hydrophobic interactions between protein and bilayer are calculated according to functions that depend on the exposed area of each amino acid, while electrostatic interactions are treated within the Poisson-Boltzmann approximation [Im, 2003]. This methodology has given good results when applied to transmembrane proteins, but its use appears more critical in the case peripheral membrane proteins[1]. For example, the predicted immersion depth [Mihajlovich, 2007] does not correspond to the experimental findings [Jao, 2004]. Binding dynamics and binding equilibrium properties can strongly depend on details of molecular interactions, especially when this process involves charged region of lipid bilayer headgroups. To treat the bilayer at the molecular level, it is possible to perform all-atom MD simulations [Patra, 2003]. Within this approach, all the atoms of lipids are treated explicitly. Patches of bilayers consisting of about 128-256 lipids are used, solvated by a number of water molecules of the order of a few thousand. Of course, this method is more expensive and time consuming, but the detailed information that can be reached on protein-lipid binding justifies this choice [Kandt, 2007]. Due to the reduced dimensions of a bilayer patch, often it is not possible to perform long MD simulations of a whole protein. So the usual strategy is to perform MD simulations on fragments of the protein. Standard computational resources permit MD simulations of 20-30 amino acid peptides on a bilayer of 128 lipids for trajectory lengths up to 40-50ns [Kandasamy, 2004; Kandasamy 2006; Lague 2005; Shepherd, 2003]. The most

[1] Peripheral proteins: proteins that adhere to the surface of a membrane and penetrate into the phosphate region, but scarcely into the hyrdrophobic tail region.

important information that can be obtained from an all-atom MD simulation of a peptide in the presence of a bilayer are, in addition to the structure of the peptide, the immersion depth, the preferential orientation of binding, the effect of the peptide on the bilayer order, the effect of interactions between amino acid side chains and specific lipid atoms, the effect of specific interactions like hydrogen bonds, etc. Most of this information is not accessible with an implicit membrane model. In this chapter, we report an all-atom MD simulation of fragment 31-52 of *aS* in the presence of a 128 lipids bilayer and water solvent. The fragment was selected from amino acid 31 to amino acid 52 because it contains two of the imperfect repeats that characterise the primary sequence of *aS* and comprises a whose structure is controversial for membrane-bound *aS*. A MD trajectory of 120 ns was performed, that is twice as long as the MD simulations which have been performed on analogous peptide-bilayer systems [Kandasamy, 2004; Kandasamy 2006; Shepherd, 2003]. This study is aimed at shedding light on various issues: in addition to the stability of a helical structure of the L38-T44 region of *aS*, the penetration and anchoring of the protein into the bilayer and the effects of binding on the membrane, the mobility and flexibility of the protein, the role of residues and the specific interactions involving the side chains.

The simulation has been performed in the presence of a 128 POPC bilayer and about 6500 water molecules, with two copies of the G31-V52 fragment of *aS*, with different geometry, placed at either side of the bilayer in the starting configuration: one in the α-helical structure, the other in the average structure proposed from NMR experiments in SDS micelle environment (PDB id: 1XQ8). A POPC (1,2-dioleoyl-sn-glycero-3-phosphocholine) bilayer (see fig. 8.2) has been considered, for which a well tested force field[2] is available [Zhao, 2007]. This has already been used for Molecular Dynamics investigations of the interaction between amphipathic peptides and membranes [Kandasamy, 2004; 2006], which makes possible a comparison with our system. We have also performed a short simulation with the anionic POPS (1,2-dioleoyl-sn-glycero-3-phosphoserine), which would be preferable in view of the strong binding affinity of *aS* for acidic membranes. We have used a new version of the force field for this lipid, which is intended to replace the previous one [Mukhopadhyay, 2004] and is still under development [Monticelli, 2007]. However we have found some inconsistencies, therefore we have preferred to use POPC.

In the next chapter the information obtained from MD simulations will been exploited, together with the theoretical methodology presented in chapters 6 and 7, to interpret SDSL-EPR spectra of mutants of *aS* bound to small unilamellar vesicles.

[2] In Molecular Dynamics a system is defined by its topology and its force field. The topology is simply a list of atom types, bonds, angles and dihedrals that are used to define a molecular configuration. The force field comprises the functional form and the parameter set used to define the potential energy of a system, i terms of intra- and inter-molecular interactions. These are derived from fitting of experimental data and quantum mechanical calculations. The reliability of a force field can be assessed on the basis of its capability of reproducing experimental results.

8.2 Methods

System A pre-equilibrated bilayer was made of 128 POPC molecules (64 lipids in each leaflet) and 3655 water molecules. First, to ensure that the distance between the lipid bilayer and its periodic image was large enough to allow insertions of the fragment, 2859 water molecules were added to the system, so reaching a total number of about 6500 water molecules. This new system was further equilibrated for 10 ns, and no appreciable change in the area per lipid was found [Zhao,2007]. Then, the G31-V52 fragment of *aS* was placed at each side of the bilaye, with different geometry: the bent structure taken from the average NMR conformation in SDS micelle [Ulmer, 2005], hereafter referred to as *B*), and ideal α-helix, henceforth denoted by *H*. The two fragments were placed with their centre of mass at a distance of about 3 nm from the middle plane of the bilayer, in the water-bilayer interface region. In this configuration there was no overlap between lipid and fragments, and overlapping water was removed. The starting orientation of *B* fragment was chosen according to the binding model of *aS* on SDS micelles [Ulmer, 2005], while the starting orientation of the *H* structure was taken so as to maximise the number of hydrophobic and hydrophilic residues facing the lipid bilayer and the water solution, respectively (see fig 8.1.b). For each peptide, 5 Cl^- and 2 Na^+ ions were added at random positions to neutralize the positive charges of 4 lysines and one histidine and the negative charge of 2 glutamates.
First, a 5 ns equilibration of the whole system was made, during which all atoms of the fragments were restrained in position (with a force constant of 1000 kJ mol^{-1} nm^{-1}). Then, all constrains were released and a 120 ns trajectory was generated.

Simulation method Simulations have been performed using the GROMACS simulation tool [Lindahl 2001] on a 16 processor Linux cluster. One nanosecond simulation took about 3.6 hours. The GROMOS (ffgmx) force field was used for fragments, counterions and water, while the lipid parameters provided by Berger *et al* [Berger, 1997] were employed for POPC. The starting configuration of the POPC was downloaded from http://www.softsimu.org/downloads.shtml, while the corresponding topology file (popc.itp) was taken from http://moose.bio.ucalgary.ca/downloads. The SPC model was used for water. The G31-V52 fragments of *aS* was terminated with ACE and NH_2 as the N- and C- blocking groups, respectively; the starting α-helical (*H*) structure was built with Molden [Molden]. Periodic boundary conditions were applied in all three dimensions. The LINCS algorithm was used to constrain all bonds. Simulation were performed in the NpT ensemble, with an integration timestep i of 2 fs. For the production run, an anisotropic pressure was adopted, with a 1 bar Berendsen barostat with a coupling constant of 1 ps and a compressibility of 4.5×10^{-5} bar^{-1}. Temperature was kept at 310 K using a Berendsen thermostat; each component of the system (lipid, solvent and fragment) was coupled separately to a temperature bath with a relaxation

time of 0.1 ps. Van der Waals and short-range Coulomb interactions were cut-off at 1.0 nm. Long-range electrostatic interactions were computed using the Particle Mesh Ewald (PME) method on a 0.12nm reciprocal space grid with sixth-order spline interpolation. Rendering and visualization was made with PyMOL [PyMOL].

Analysis The trajectories were analyzed using GROMACS tools and home made codes. In particular, the latter were developed for the analysis of ordering matrices.

The elements of the ordering Saupe matrix for a given bond are defined as

$$S^{IJ}{}_{bond} = (1/2) < 3\cos\beta_I \cos\beta_J - 1 >$$

where β_J is the angle between the bond and the J axis of a frame fixed in the molecule or in the laboratory. Brackets denote averaging over the trajectory. The order parameters describe the symmetry ad confinement of the orientational distribution of the bond in the reference frame. The following relations hold: $S^{XX}{}_{bond} + S^{YY}{}_{bond} + S^{ZZ}{}_{bond} = 0$ ad $-0.5 \le S^{JJ}{}_{od} \le 1$, with $S^{JJ}{}_{bond} = 1$ ad $S^{JJ}{}_{bond} = -0.5$ for perfect alignment on the bond parallel ad perpendicular to the Jth axis, respectively. By diagonalization of the ordering matrix, the principal alignment axes of the bond in the molecule or in the laboratory are found. Let us label such axes such that $S^{ZZ}{}_{bond} \ge S^{XX}{}_{bond} \ge S^{YY}{}_{bond}$. For an axially symmetric distribution of bond orientations about the Z axis, $S^{XX}{}_{bond} = S^{YY}{}_{bond} = - S^{ZZ}{}_{bond}$; thus, the difference $S^{XX}{}_{od} = S^{YY}{}_{od}$ can be taken as a measure of the biaxiality of the distribution. The $S^2{}_{od}$ order parameter appearing in the Lipari-Szabo model [Lipari, 1982], which is usually derived from NMR relaxation experiments, is defined as $S^2{}_{bond} = S^{ZZ}{}_{bond} + (S^{XX}{}_{bond} - S^{YY}{}_{bond})^2/3$.

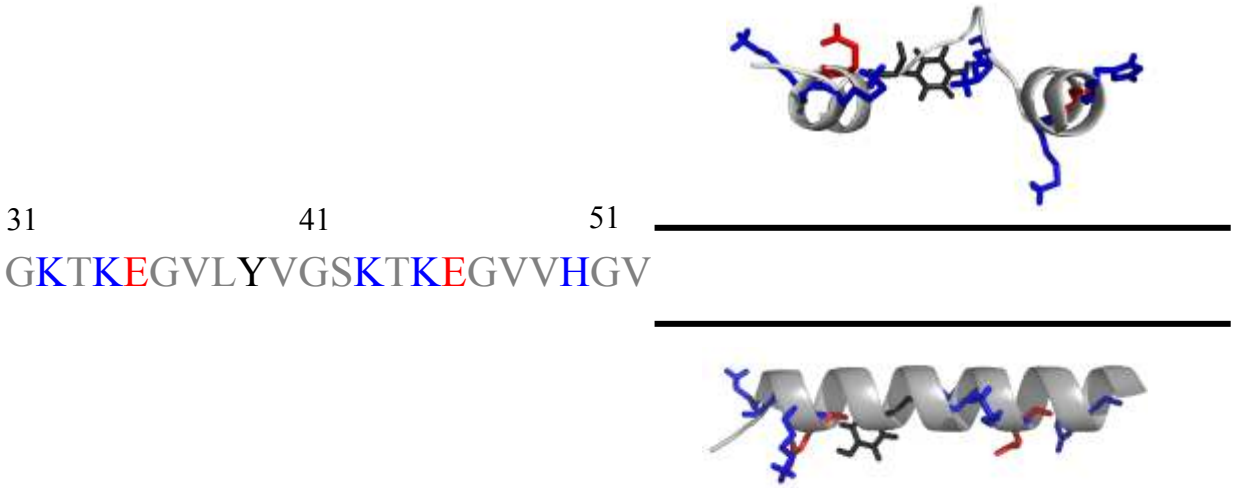

Figure 8.1 a) G31-V52 fragment of *aS* considered in the MD simulation (single letter amino acid code)[3]. Blue (red) letters correspond to positively (negatively) charged residues. b) Starting configuration, with the fragment in the *B* and *H* geometry placed on bot and bottom, respectively. The black line represent the average plane of phosphates.

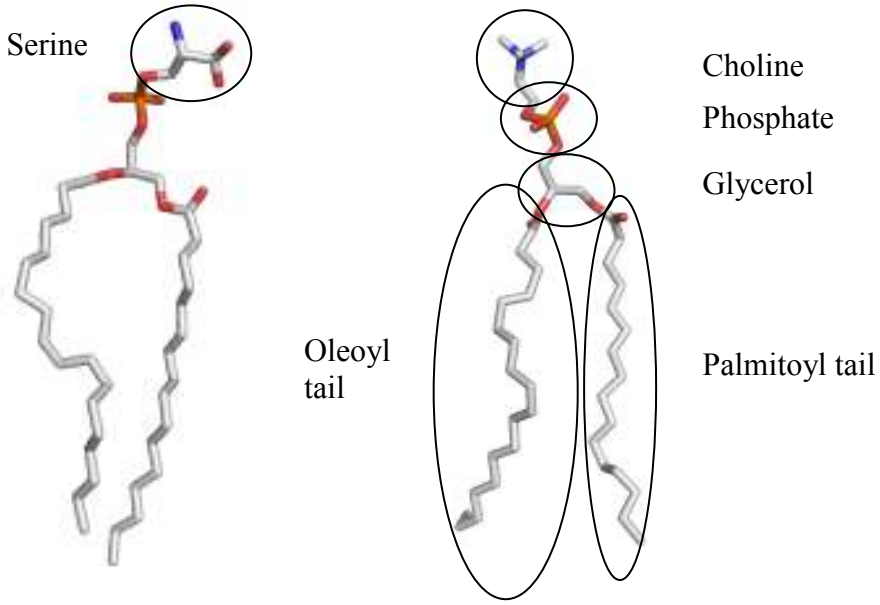

Figure 8.2 Structure of POPS (left) and POPC (right).

[3] G: glycine; V: valine; T: threonine; L: leucine; Y: tyrosine; S: serine; K: lysine; E: glutamate; H:histidine.

8.3 Results and Discussion

Structure of fragments and penetration into the bilayer Fig. 8.3. shows snapshots of the system taken at regular times along the trajectory. We can see that both fragments penetrate into the bilayer, and already at t=10 ns strong interactions with the bilayer take place. The fragments have partially changed their structure and lysines play an important role in this process. The disorder of the bilayer and the imperfect packing of the headgroups seem to be essential consitions for the insertion to occur. After about 60 ns of simulation time, both fragments have substantially settled in the region of the lipid head groups, and in the following time they do not undergo dramatic changes. On the contrary, the bilayer exhibits higher mobility, and seems to rearrange even at the end of the 120 ns trajectory.

The average position of the center of mass of the fragments relative to the average middle plane of the bilayer is shown in fig. 8.4 In this plot, the average position of phosphate groups is at ~1.92nm. We can see that during the first 40 ns the two fragments insert at roughly the same rate. Then the *H* structure decreases its insertion rate and slowly reaches an immersion depth of about 1.9 nm, which is maintained. On the contrary, the *B* structure did not change insertion rate for about 60 ns. After this time, the *B* fragment remains at approximately 1.5 nm of immersion depth.

Fig. 8.5 shows the density distribution of the various lipid moieties and of the fragments during the last 10 ns of the trajectory. The *H* fragment penetrates the bilayer but lies preferentially in the headgroup region, mainly between the choline and phosphate groups; *B* penetrates deeply, and is located beyond the phosphate group region, with a tendency to extend into the aliphatic tails.

Fig. 8.6 shows the *B* structure at the beginning and the end of the MD simulation. Fig.8.6.c shows the RMSD of this structure at different times, with the starting geometry taken as reference. RMSDs quantify the difference between molecular structures at times t_0 ad t; they are calculated as $\mathrm{RMSD}(t_0,t)=\left[(1/N^2)\sum_{i=1}^{N}|\mathbf{r}_i(t_0)-\mathbf{r}_i(t)|^2\right]^{1/2}$, where N is the number of backbone atoms and $\mathbf{r}_i$ is the position of the *i*th atom.. As we can see, the *B* fragment undergoes strong reorganisation during the first 10 ns; then the new structure is stabilised with an RMSD value of about 0.5nm. During the following 110 ns, the *B* fragment reaches a stable conformation, with only small fluctuations. The main changes can be described as fraying of the short N- and C-terminal helices, while the central region undergoes only small reorganisation. This observation can be quantified by the analysis of the RMSD of each amino-acid from the starting structure, during the last 110-120 ns of the trajectory (fig 8.7). The loop region near Y39 exhibits small fluctuations, between 0.2 nm and 0.3 nm, while the amino acids in the helical regions are characterised by higher values, between 0.5 nm and 0.8 nm.

The central part of the *B* fragment is in a loop conformation and the C- and N-terminal parts face each other in antiparallel arrangement. The C terminal part, K43-V52, retains helical character, whereas on the opposite end helix fraying is observed, in agreement with the low order parameters observed by NMR for this region [Ulmer, 2005].

$t = 0ns$

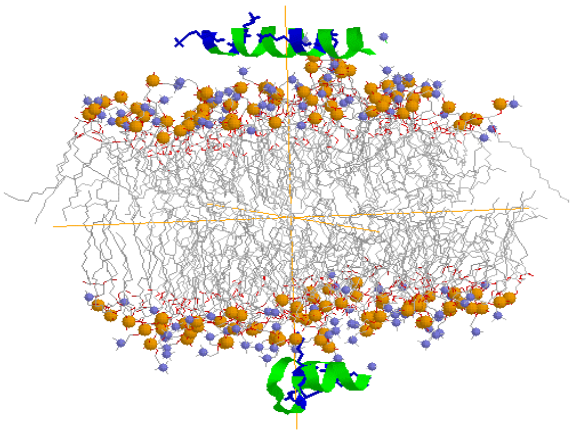

$t = 10ns$

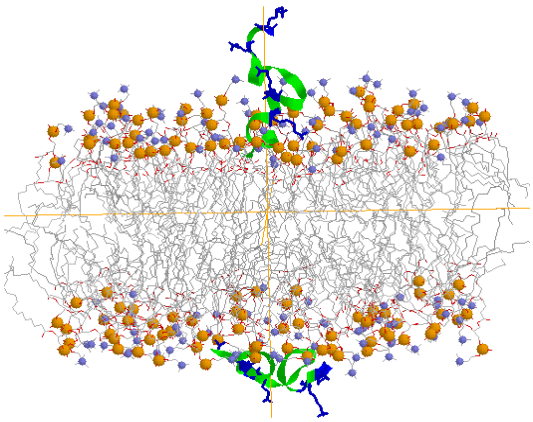

$t = 20ns$

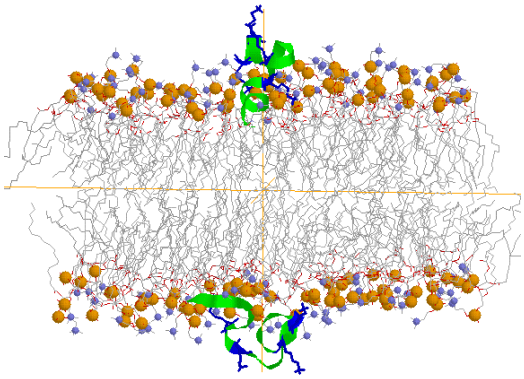

$t = 30ns$

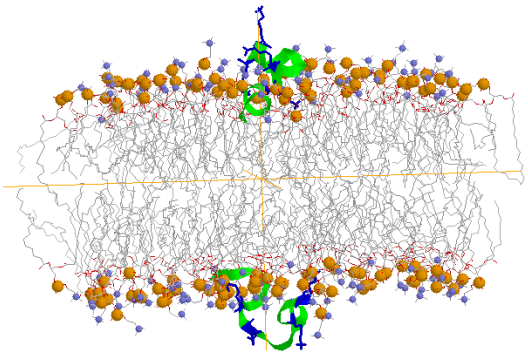

$t = 40ns$

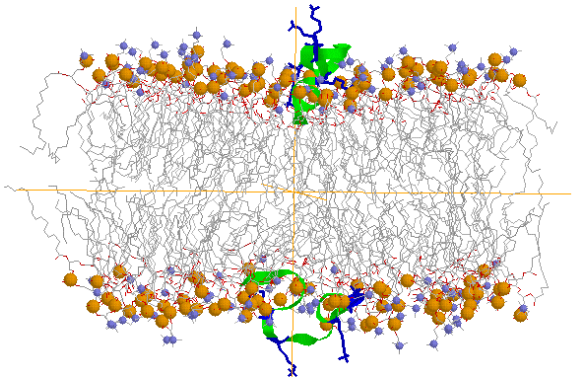

$t = 50ns$

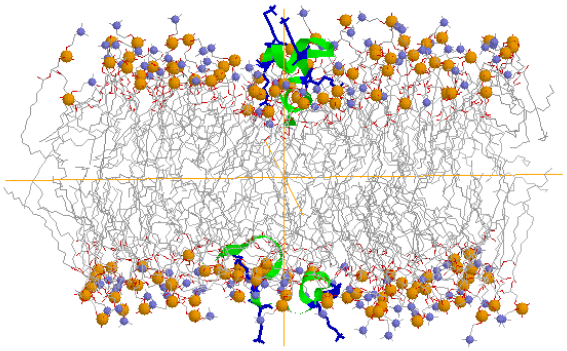

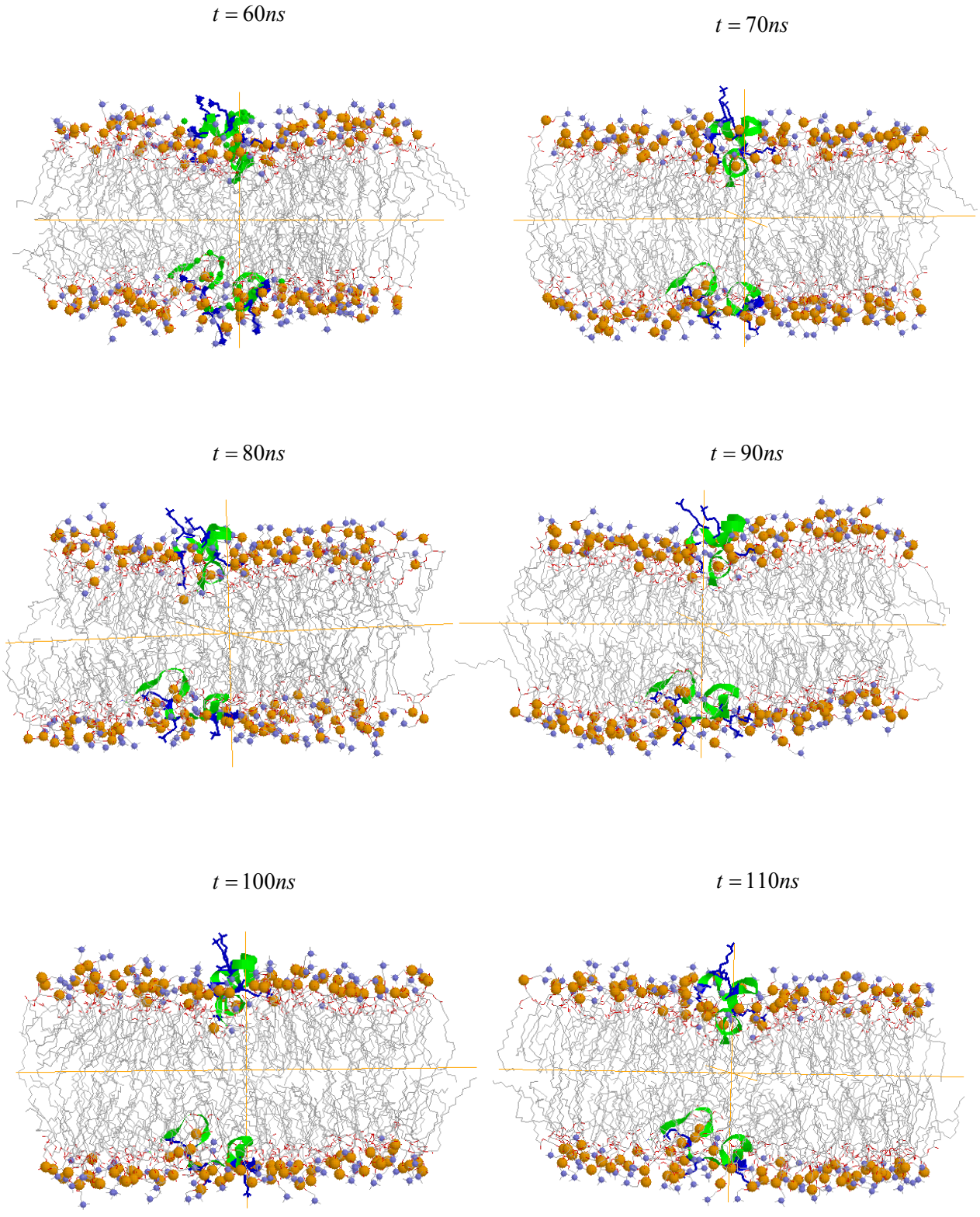

Figure 8.3 Snapshots of the system taken at different times. The backbone is represented as a green ribbon. Orange (blue) spheres represent phosphorous (nitrogen) atoms of POPC bilayer. Lysines are shown as blue sticks. Water molecules are removed for clarity.

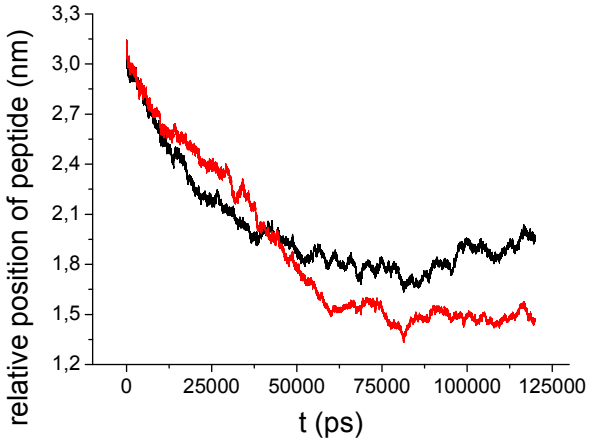

Figure 8.4 Distance of center of mass of the *B* (red) and *H* (black) fragments from the middle of the lipid bilayer. Only backbone atoms were considered for this calculation. In this plot the average position of phosphate groups is at ~1.92 nm.

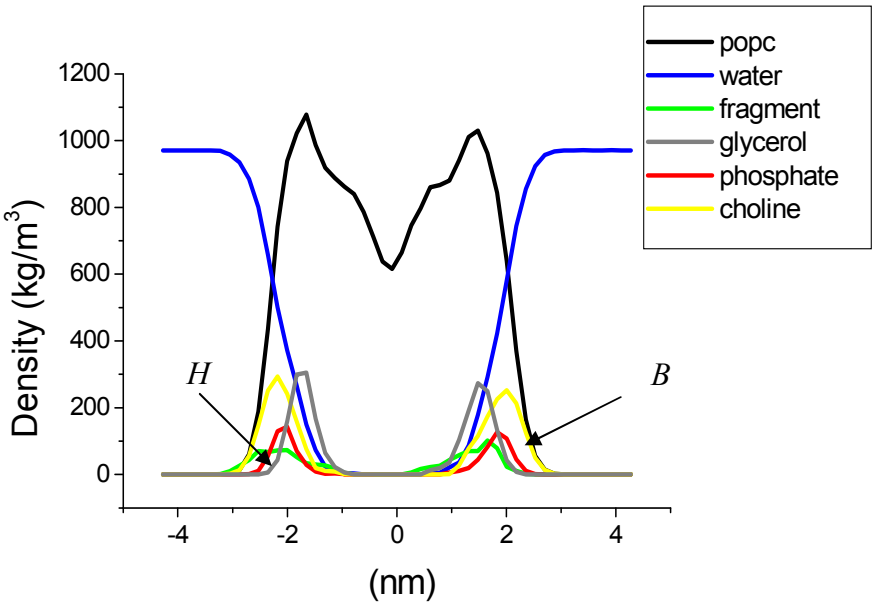

Figure 8.5 Density profiles for lipid moieties and aS fragments averaged over the last 10 ns of the MD trajectory. Lipid groups are defined in fig. 8.2.

Fig.8.11 shows the structure of the *H* fragment at the beginning and the end of the MD simulation and fig.8.11.c reports the RMSD of the *H* structure along the trajectory with respect to the starting structure. As we can see from Fig.8.11.b, the *H* fragment breaks near Y39 and a loop appears. The helical structure is not stable: the *H* fragment undergoes strong reorganization during the first 20 ns; then the structure stabilizes to an RMSD value of about 0.65nm. This new structure is stable during the last 50 ns MD simulations, as shown by the RMSD plot.

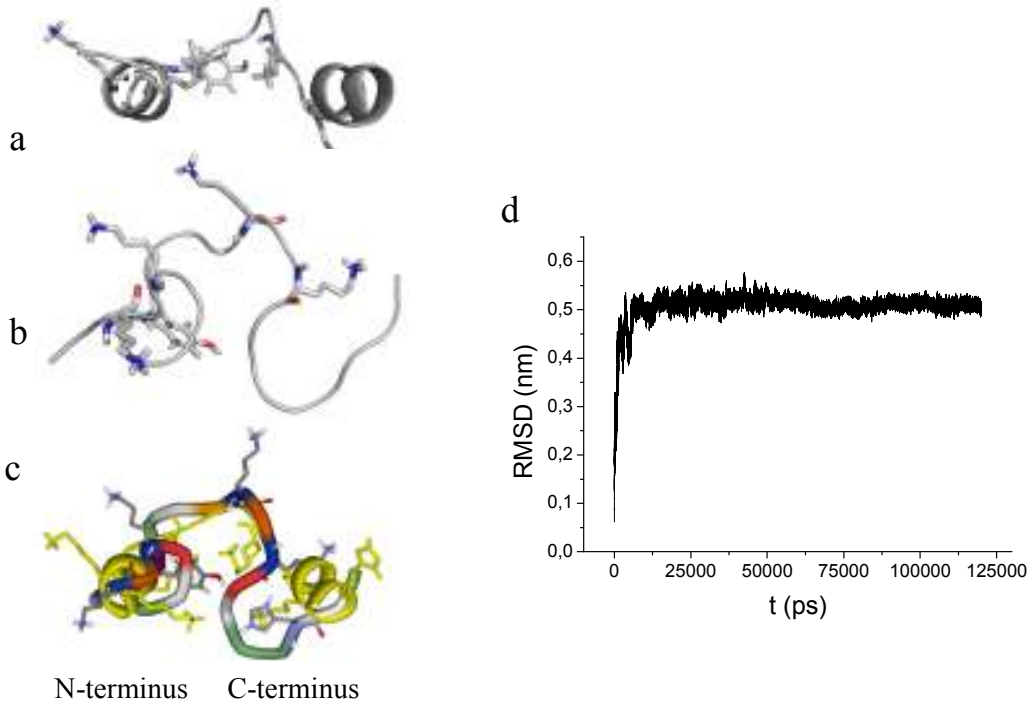

Figure 8.6 Structure of the *B* fragment (a) at beginning and (b) after 120 ns of the MD trajectory. The backbone is shown as grey ribbon. A stick representation is used for lysines and tyrosine 39. (c) RMSD of the *B* fragment over the simulation with respect to the starting structure.

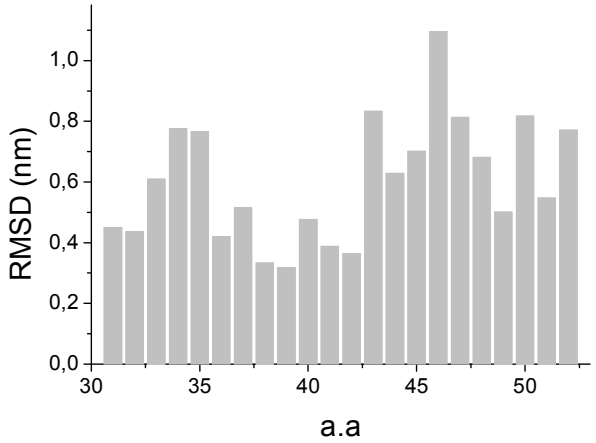

Figure 8.7 Root mean square deviations (RMSD) of the *B* fragment from the starting configuration, calculated for the backbone atoms.

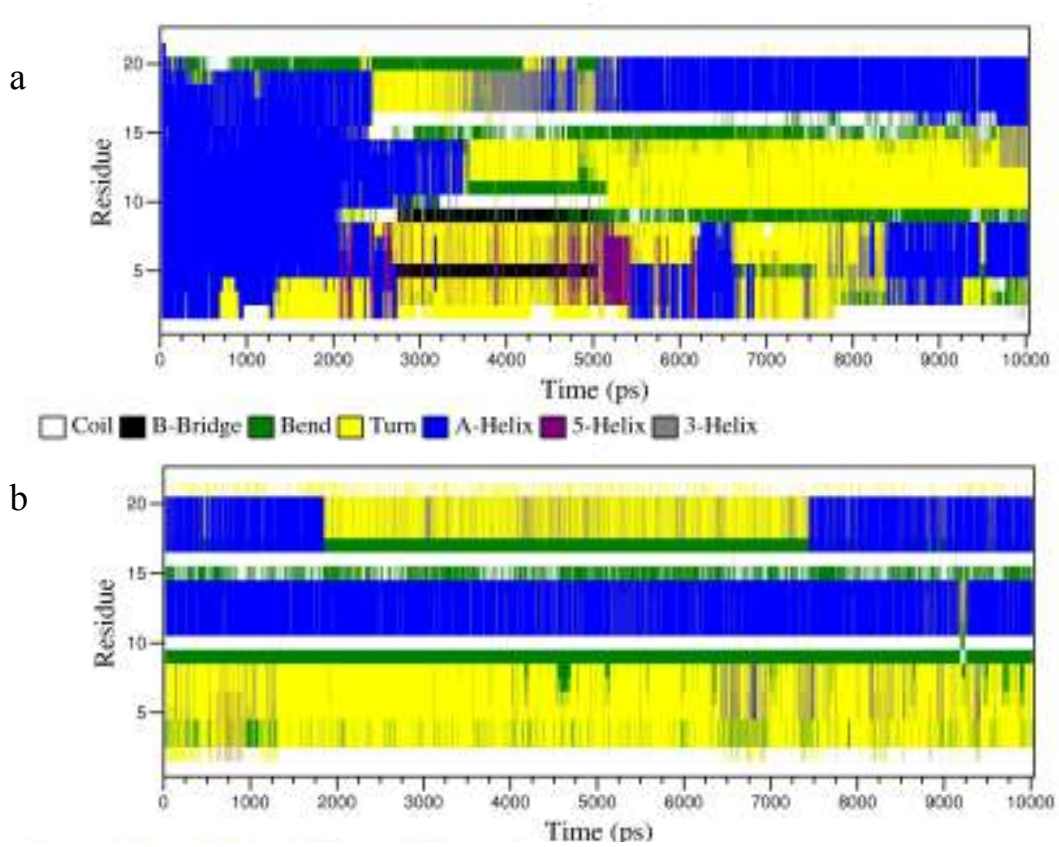

Figure 8.8 Secondary structure of the *H* fragment (a) at the beginning (t=0-10 ns) and (b) the end (t=110-120 ns) of the MD simulation. Tyr39 corresponds to residue number 9. **Bend**: residue at the centre of a high curvature region of five amino acids. **Turn**: H-bond between CO of *i* residue and HN of *i*+*n* residue (*n* =3,4,5). **A-Helix**: at least 2 H-bonds between CO of *i* residue and HN of *i*+4 residue (α-helix). **5-Helix**: at least 2 H-bonds between CO of *i* residue and HN of *i*+5 residue (π-helix). **3-Helix**: at least 2 H-bonds between CO of *i* residue and HN of *i*+3 residue (3_{10}-helix). **β-bridge**: two H-bonds characteristic of β structure.

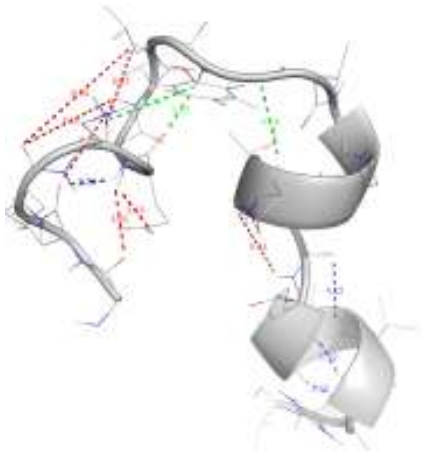

Figure 8.9 Intramolecular hydrogen bonds in the *H* fragment. Blue dotted lines show hydrogen bonds that persist at the end of the 120 ns trajectory. Red dotted lines show hydrogen bonds that persist for long times, but break during the last 10 ns MD simulations. Green dotted lines show hydrogen bonds made by Tyr39 .

The secondary structure analysis of the *H* fragment during the course of the first 10 ns and the last 10 ns is shown in Fig.8.12. From these plots, we can see that helical breakage process starts at t=3ns near amino-acid Y39, thereafter the unfolding process extends to the neighbouring residues: a loop appears, which evolves during the following about 10 ns. From 20 to 120 ns of simulation time the fragment undergoes only small fluctuations about this partially unfolded structure, without dramatic transformations. At the end of the simulation (120 ns), *H* fragment is partially embedded into the headgroup region of the bilayer (see fig.8.14). The central part of the fragment is in a loop conformation and the C- and N-terminal parts face each other in antiparallel arrangement. The C terminal part, K43-V52, retains helical character, whereas on the opposite end helix fraying is observed. Only lysines 32 and 45 are embedded in the bilayer and interact via hydrogen bonds with the phosphate groups (see analysis below). Tyr39 faces the lipid-water interface and is located in the water region.

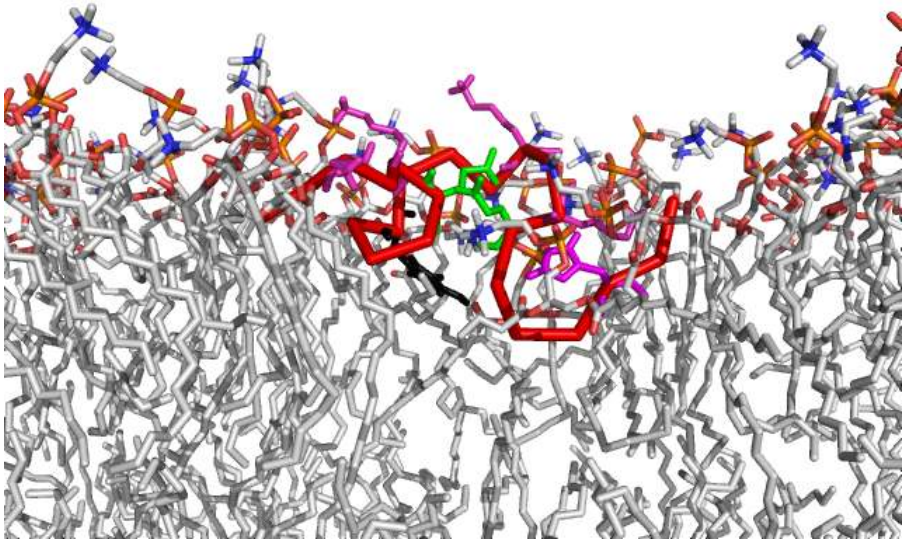

Figure 8.10 Snapshot of the *B* fragment at t=120ns. Backbone is shown as cartoon. Magenta is used for lysines and histidine, green for glutamate and lack for tyrosine 39. For clarity, some lipids molecules overlapping the fragment view have been removed. In this structure, only two lysines (32 and 45) are embedded in the lipid headgroup region, while lysine 34 and 43 are exposed to solvent.

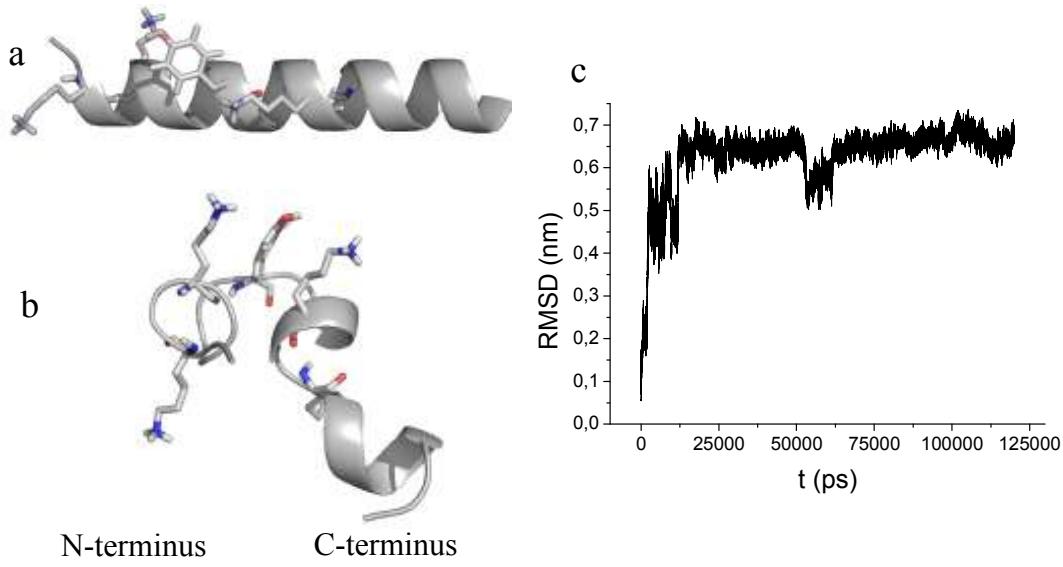

Figure 8.11 Structure of the *H* fragment at the beginning (a) and after 120 ns of the MD simulation (b). The backbone is shown as ribbon. A stick representation of lysines and tyrosine 39 is used. (c) Overlapped structures of the *B* fragment at the beginning (t=0 ns, yellow) and the end (t=120 ns) MD trajectory. (d) RMSD of the *B* structure during the simulation with respect to the starting structure.

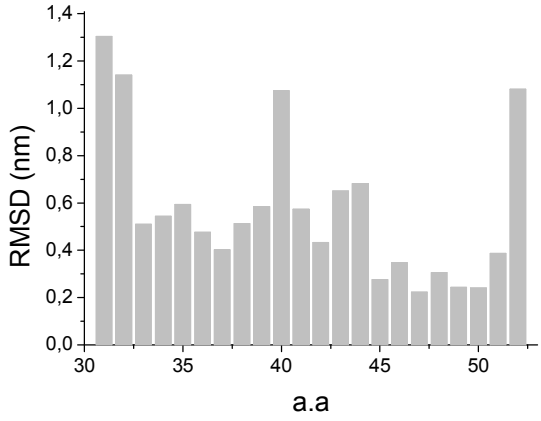

Figure 8.12 Root mean square deviations (RMSD) of the *H* fragment from the starting configuration, calculated for the backbone atoms.

The secondary structure of the *H* fragment during the course of the first 10 ns and the last 10 ns (from 110 to 120 ns), as defined by the Dictionary of Secondary Structure of Proteins (DSSP) [Kabsch, 1983], is shown in fig. 8.8. From these plots, again we can see a fast frying of the N-

and C-terminal helices during the first 2 ns, with the latter appearing slightly more stable than the former. During the 110-120 ns period, we can see the presence of a pseudo-helical region towards the N-terminus and a weakly structured region towards the C-terminus. It is interesting to note that during all 120ns MD simulations, the central region near Y39 never exhibits any structure.

At the end of the simulation (120 ns), the *B* fragment is deeply embedded in the lipid bilayer (see Fig.8.10), and the backbone preferentially lies under the average plane of phosphates. Charged residues (lysines, histidine and glutamate) are located in the headgroup region and there are strong interactions via hydrogen bonds (see analysis below) between positively charged lysines and negatively charged phosphate groups. Tyr39 is deeply embedded between the hydrophobic lipid tails.

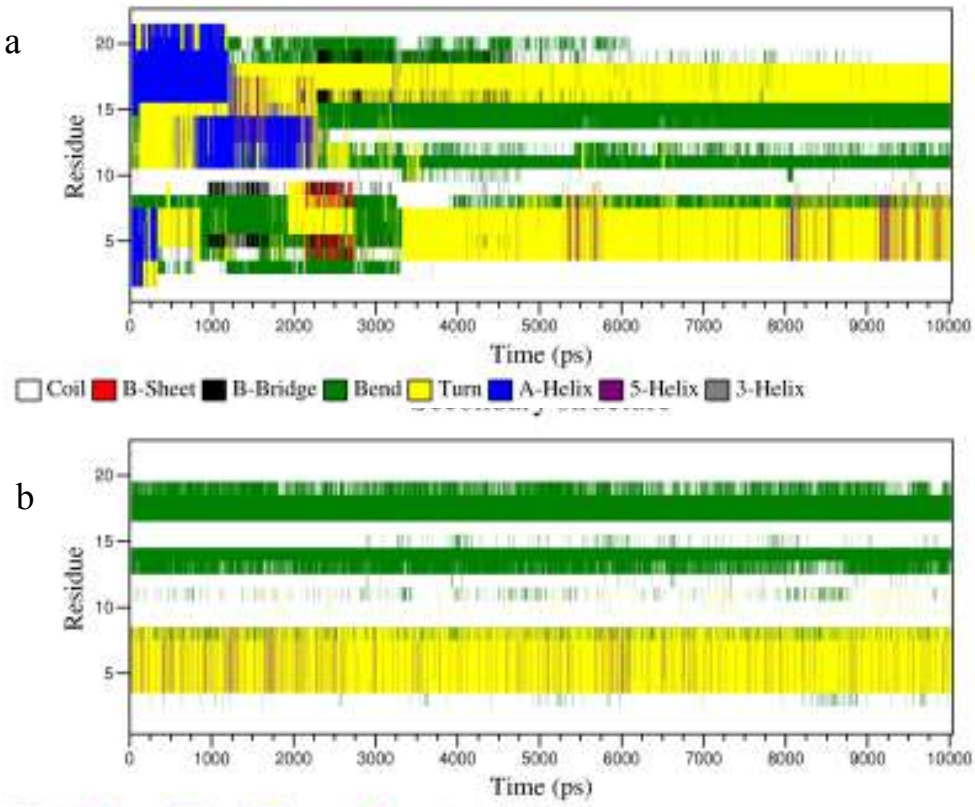

Figure 8.13 Secondary structure of the *B* fragment from DSSP analysis, (a) at the beginning (t=0-10 ns) and (b) the end (t=110-120 ns) of the MD simulation. Tyr39 corresponds to residue number 9. The DSSP code is reported in the caption to fig. 8.8

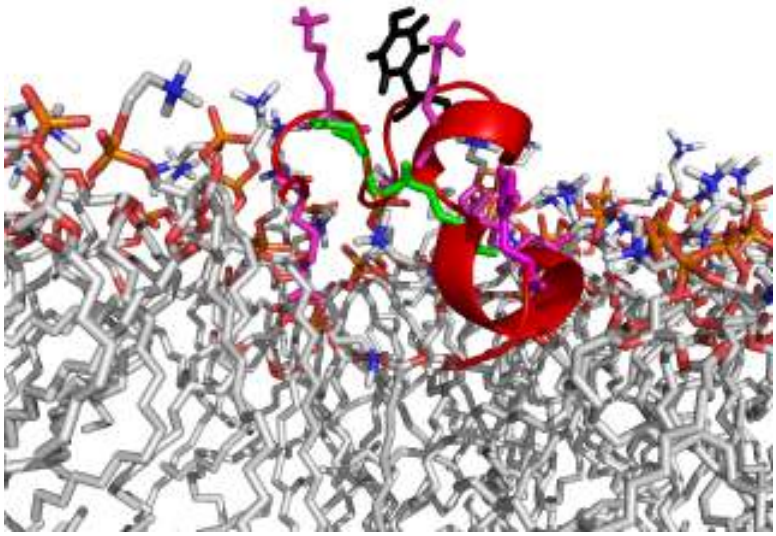

Figure 8.14 *H* fragment in the bilayer at t=120ns. The protein backbone is shown as ribbon. Magenta is used for lysines and histidines, green for glutamates and black for tyrosine. For clarity, some lipids overlapping the fragment have been removed. Lysines lie on the phosphate plane and interact via hydrogen bond with the phosphate oxygen. Tyr39 is deeply embedded in the bilayer, in the region of hydrophobic tails.

The results presented above all seem to be in favour of a loop region centred approximately to residue Y39. We can now compare the two loops after 120ns of MD simulation. The main differences between the two loops are insertion depth and orientation of phenol ring of tyrosine 39. The *H* fragment loop is only partially embedded into the bilayer and preferentially lies on the phosphate region; in this loop tyrosine 39 exposes the phenol ring to water. On the contrary, the loop in the *B* fragment sits more deeply in the bilayer, and exposes the phenyl ring to the lipid hydrophobic tails.

Hydrogen bonds between amino acids and bilayer Now we can analyze more in details the insertion mechanism of the two fragments. It is well known that lysines contribute significantly to the binding process and also to determine the stability of fragments on lipid bilayers with a so called 'snorkel' mechanism [Kandasamy, 2004; Kandasamy, Kandasamy, 2006]. Lysine side chains act as anchoring elements via hydrogen bonds with phosphate and glycerol oxygen of lipid bilayers. A lysine residue has three donor hydrogens (NH_3^+), while each lipid has eight acceptor atoms (based on partial point charges on oxygens of lipid molecules, we assume that all eight oxygens, four on the phosphate group and four on the glycerol group, are capable of accepting hydrogen bonds). Hence, a lysine side chain group in

the vicinity of a lipid head-group can form a theoretical maximum of 24 hydrogen bonds with a specific lipid. In all of our simulations we observed that a lysine side chain that is close to the lipid bilayer interface typically interacts with an average of 3-4 neighbouring lipid molecules, and hydrogen bonds are more often with phosphate than glycerol oxygens.

Fig. 8.15 shows the hydrogen-bond existence map for the four lysines of the *B* fragment. Since the early stages of the simulations, lysine 45 comes into contact with the lipid head group region, forming the earliest hydrogen bonds. This interaction is favoured by the position of lysine 45, that faces the lipid bilayer since the first ps of simulation. This anchoring effect brings the C-terminal region to interact as first with the POPC bilayer. On the contrary, the other three lysines start to interact with the bilayer later during the simulation. In particular, lysine 32 forms hydrogen bonds after 10 ns, when the *B* fragment approaches more deeply the bilayer. Lysine 34 forms hydrogen bonds after long time, only during the last 50 ns MD simulations. Lysines 32 and 34 lie on the N-terminal part of the *B* fragment. We can see from the first 10 ns of the MD trajectory (as well as from the DSSP plots) that the N-terminal region appears less stable than the C-terminal one. It starts fraying very early during the simulation. This strong secondary structure fluctuations probably disturb a possible interaction between the two lysines and the POPC bilayer. On the other hands, the absence of these two interactions raise the secondary structure instability of this region. Lysine 43 practically never shows hydrogen bonding with the POPC bilayer. Its position in the *B* fragment, facing the water solution, does not favour this kind of interactions. As we can see from the plots in fig 8.15, hydrogen bonds once established ,appear quite stable in time.

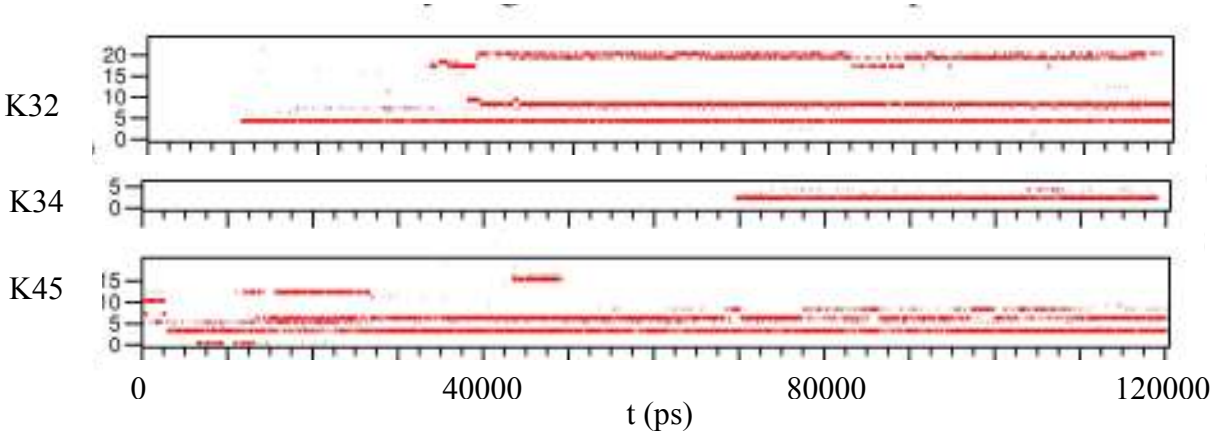

Figure 8.15 Hydrogen-bond existence map for the four lysines of the *B* fragment. Red indicates the presence of an H-bond. Each hydrogen bond index refers to unique donor-hydrogen-acceptor triplet.

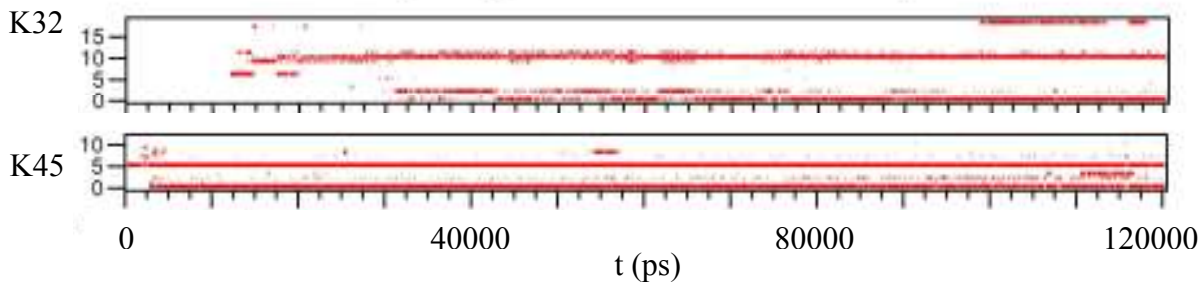

Figure 8.16 Hydrogen-bond existence map for two lysines of the *H* fragment. Red indicates the presence of an H-bond. Each hydrogen bond index refers to unique donor-hydrogen-acceptor triplet.

Fig. 8.15 shows the hydrogen-bond existence map for the two lysines of the *H* fragment that show such bonds. Again, since the early stages of the simulation lysine 45 interacts strongly with the POPC bilayer. This anchoring effect promotes the interaction between the C-terminal region and the POPC bilayer. On the contrary, during the first 10 ns of the simulation, the other three lysines never exhibit hydrogen bonds. The *H* fragment undergoes the following insertion mechanism: it approaches the bilayer and starts interacting with the lipid headgroups through the C-terminal region. The helical axis changes its inclination with respect to the bilayer surface and brings the N-terminal region through water solution. After 3 ns the helix breaks in the proximity of Tyr39, thereafter the unfolding process extends to the neighbouring residues: a loop appears, which evolves during the following about 10 ns. The two helical fragments in the fragment move towards each other, and hydrogen bonds between lysine 32 and the POPC bilayer appear. From 20 to 120 ns of the simulation the fragment penetrates into the bilayer, undergoing fluctuations about this partially unfolded structure. In this new structure, lysines 34 and lysine 43 never form hydrogen bonds with the POPC bilayer.

There are experimental evidences that suggest a role of certain hydrophobic residues in anchoring to the bilayer, in particular tyrosine and tryptophan, in membrane proteins and peptides [Lu, 2005]. So, we have analyzed the hydrogen existence map between the oxydril group of tyrosine 39 and POPC in both the *B* and the *H* fragment. As clearly shown in fig. 8.14 tyrosine 39 in the *H* fragment does not interact with the POPC bilayer, due to its position. On the contrary, in the *B* fragment tyrosine 39 forms one stable hydrogen bond with the carbonyl oxygen of the oleyl tail of POPC, at t= 35ns (see fig. 8.17).

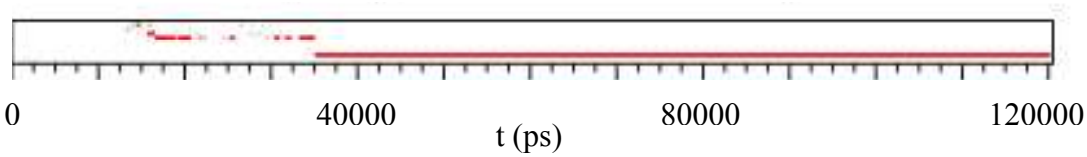

Figure 8.17 Hydrogen-bond existence map for the tyrosine of the *B* fragment. Red indicates the presence of an H-bond. Each hydrogen bond index refers to unique donor-hydrohgen-acceptor triplet.

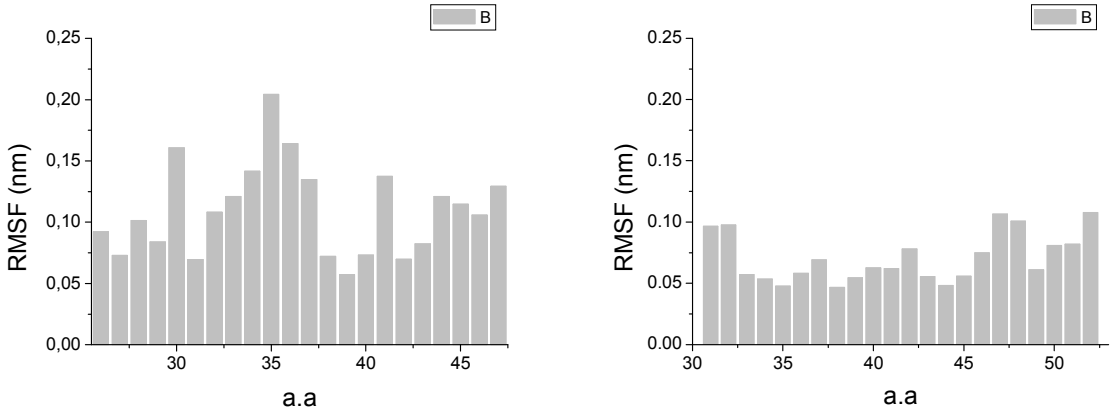

Figure 8.18 RMSF of the residues of the (a) *B* and (b) *H* fragment (calculated for backbone atoms).

Backbone flexibility and side chain mobility of the embedded fragments To characterise the confinement and mobility of the protein fragments in the bilayer, we have calculated the RMSF [4] of residues and the order parameters for the NH bonds of the backbone, averaged over the 90-120 ns time interval. RMSFs are shown in figure 8.18, whereas figure 8.19 reports the major order parameter S_{NH}^{ZZ} ad the difference S_{NH}^{XX}- S_{NH}^{YY} (see section 8.2). A correspondence between RMSFs and order parameters appears. S_{NH}^{ZZ} is high, which is in agreement with the low mobility and the limited flexibility of the fragments when embedded in the bilayer. We can recognize some more disorder in the *H* than in the *B* fragment, in particular in the central zone, which in *H* is mostly exposed to the solvent. On the contrary, the whole *B* fragment is embedded in the bilayer, and the confining behaviour of the latter is probably responsible for this difference. Relatively small order parameters were found for the NH bonds in the 30-37 region by NMR relaxation experiments on *aS* bound to SDS-micelles [Ulmer,

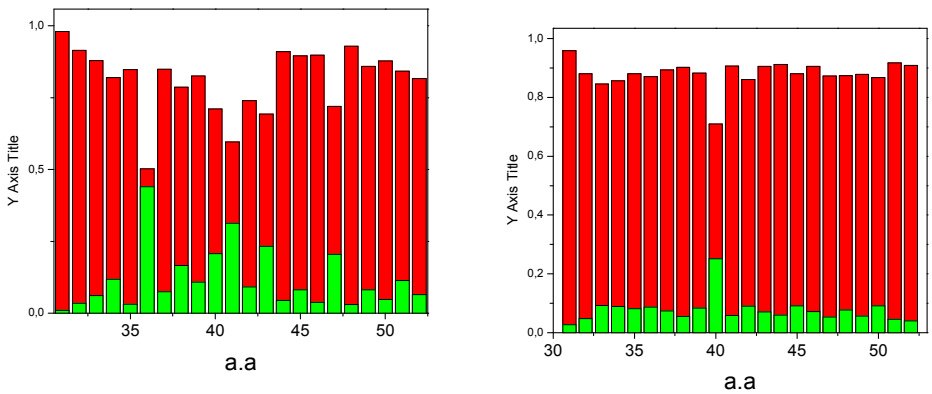

Figure 8.19 Order parameters for the NH bonds of the (a) *B* and (b) *H* fragment.

2004]. Although caution should be paid in comparing the whole micelle-bound protein and a small fragment in a lipid bilayer, this similarity of behaviour might be a sign of an intrinsic propensity the 30-40 region of the aS for disorder (which in this context is probably related to the extent of insertion).

We can see in figure 8.19 that in all cases a decrease of S_{NH}^{ZZ} is accompanied by an increase of the biaxiality of order: in other words, the orientational distribution of NH bonds is axially symmetric only when these have extremely low mobility. As they become less confined, they tend to move on a plane.

To further investigate the mobility of the fragments when inserted in the bilayer, we have calculated the time autocorrelation function for the torsional angles (θ) of side chains. These are defined as:

$$g(t) = \langle \cos\theta(0) \cdot \cos\theta(t) \rangle$$

where the brackets denote averaging over the trajectory. We did not find any common feature deriving from the location of chains in the lipid or the water or the headgroup; on the contrary, the chain dynamics appears to strongly depend upon the nature of the neighbouring chains and on the backbone conformation. Moreover, strong effects of hydrogen bonds could be recognised. To illustrate this point, we show in figures 8.20 and 8.21 the autocorrelation functions obtained for lysines: the almost complete absence of motions clearly appears for those residues that have been shown above to be strongly involved in hydrogen bonds with lipids.

[4] Root Mean Square Fluctuation

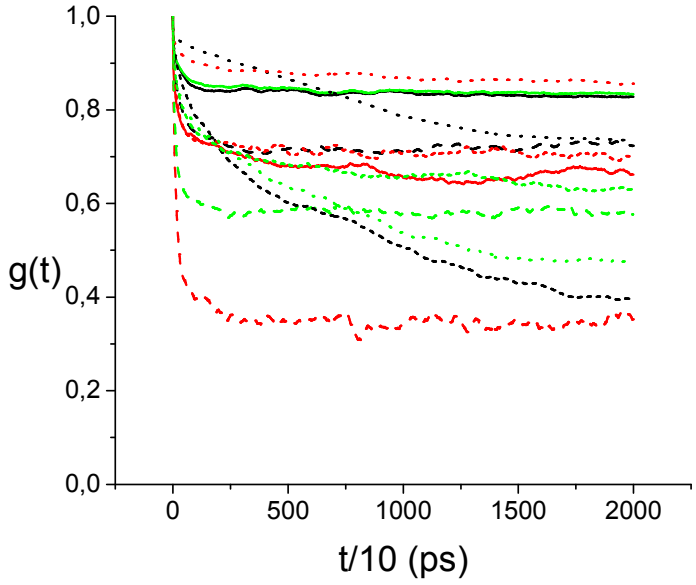

Figure 8.20 Autocorrelation functions g(t), defined in the text, for the dihedral angles of lysines in the *B* fragment. Black: C_α-C_β; red: C_β-C_γ; green: C_γ-C_δ. Solid: K32; dash: K34; short dash: K43; dash-dot: K45.

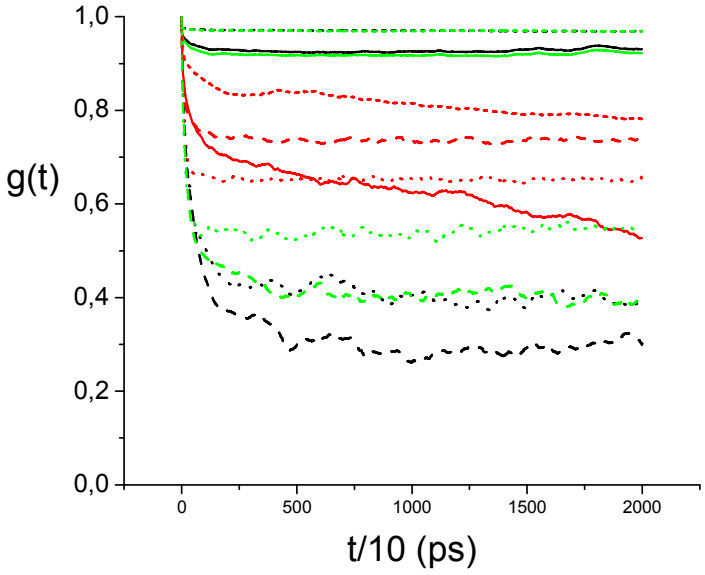

Figure 8.21 Autocorrelation functions g(t), defined in the text, for the dihedral angles of lysines in the *H* fragment. Black: C_α-C_β; red C_β-C_γ; green: C_γ-C_δ. Solid: K32; dash: K34; short dash: K43; dash-dot: K45.

Effect of the G31-V52 fragment on the bilayer We shall now analyse the effect of the *H* and *B* fragments on the lipid bilayer, in particular on the order parameters of the lipid tails. The order parameters of the lipid tails is defined by $S_{CH} =< 3/2\left(\cos^2 \beta - 1\right) >$, where β is the angle between the CH bond and the director, which often coincides with the normal to the bilayer. The order parameters have been calculated as explained in section 8.2.

In our simulation box, each leaflet contains 64 lipids and the fragments do not interact with all the lipids in the same way. The lipids in each leaflet can be distinguished on the basis of their spatial proximity to the embedded fragment [Kandasamy, 2006]. If the distance between any portion of a given lipid and any of the backbone atoms of the fragment is closer than 15 Å at any time in the simulation, that lipid is labelled as 'associating'. All the other lipids are labelled as 'non associating' lipids. This distance-based classification yields approximately equal numbers of associating and non associating lipids per leaflet. We have calculated separately the order parameters of associating and non associating lipids.

In fig. 8.21 the order parameters of the palmitoyl chain in each individual leaflet, averaged over the last 10 ns of the trajectory, are compared with those calculated for pure POPC, either distinguishing associating and non associating lipids and taking all together. The order parameters for pure POPC were averaged over 10 ns of the MD simulation performed for such system. We can see in the figure that in all cases the order parameter profile has the general shape exhibited by the data obtained by ^{2}H-NMR experiments on aligned samples of fully hydrated bilayers [Seelig, 1977], with a plateau near the top of the chains and a gradual decrease proceeding towards the methyl group. As we can see from fig. 8.21.a, both leaflets show order parameters slightly higher than pure POPC bilayer. The stronger effect is displayed by the leaflet containing the *B* fragment. This results seems to be in contrast with those obtained for anitimicrobial peptides with approximately the same number of amino acids as our fragment and a predominant helical structure [Kandasamy, 2004; Shepherd, 2003]; in those cases the peptide had a disordering effect on the bilayer. In both leaflets, associating lipids are less ordered than non-associating lipids, with a higher effect on carbon atoms close to the headgroup region; analogous behaviour was found in other MD simulations of POPC bilayers embedding helical peptides [Kandasamy, 2004, Kandasamy, 2006]. This reflects non-homogeneity of the lipid leaflet in the presence of a peptide.

With the purpose of shedding light on the unexpected ordering effect in the presence of fragments, that seems to be in contrast with experiments and other MD simulations, we repeated this analysis for the last 30 ns of the trajectory, from 90 ns to 120 ns, averaging over time intervals of 10 ns. The results are shown in fig. 8.22. We can see that, particularly in the case of the leaflet containing the *B* fragment, the order parameters exhibit strong fluctuations. For these reasons we cannot say that the differences between the order parameters calculated with and without the fragments are really meaningful.

Another consideration can be derived form the analysis of fig. 8.22. The strongest variations of order parameters are shown by the leaflet containing the *B* fragment. Yet, if we take the insertion profile and RMSD of the molecular structure as indicators, we can say that the *B* fragment reaches an equilibrium situation earlier than the *H* fragment. Its insertion profile does not change during last approximately 40 ns of the MD simulation, and its RMSD has only small fluctuations. On the contrary, the *H* fragment seems to be less stable and its RMSD exhibits wider fluctuations also during the last 20 ns. We can explain the effect on the order parameters considering that the *H* fragment penetrates only superficially the bilayer, so it probably has a weaker disordering effect. On the contrary, the *B* fragment penetrates deeper into the bilayer: probably even small structure fluctuations or side chains partial reorganizations could have a strong effect on the order within the bilayer.

Concluding, from our 120 ns long MD simulations (longer than those generally carried for analogous systems) we infer that, in lipid-peptide simulations, it should not be taken for granted that also the bilayer has equilibrated when the peptide seems to have reached a stationary condition. The collective reorganisation of the lipid bilayer might require longer equilibration times.

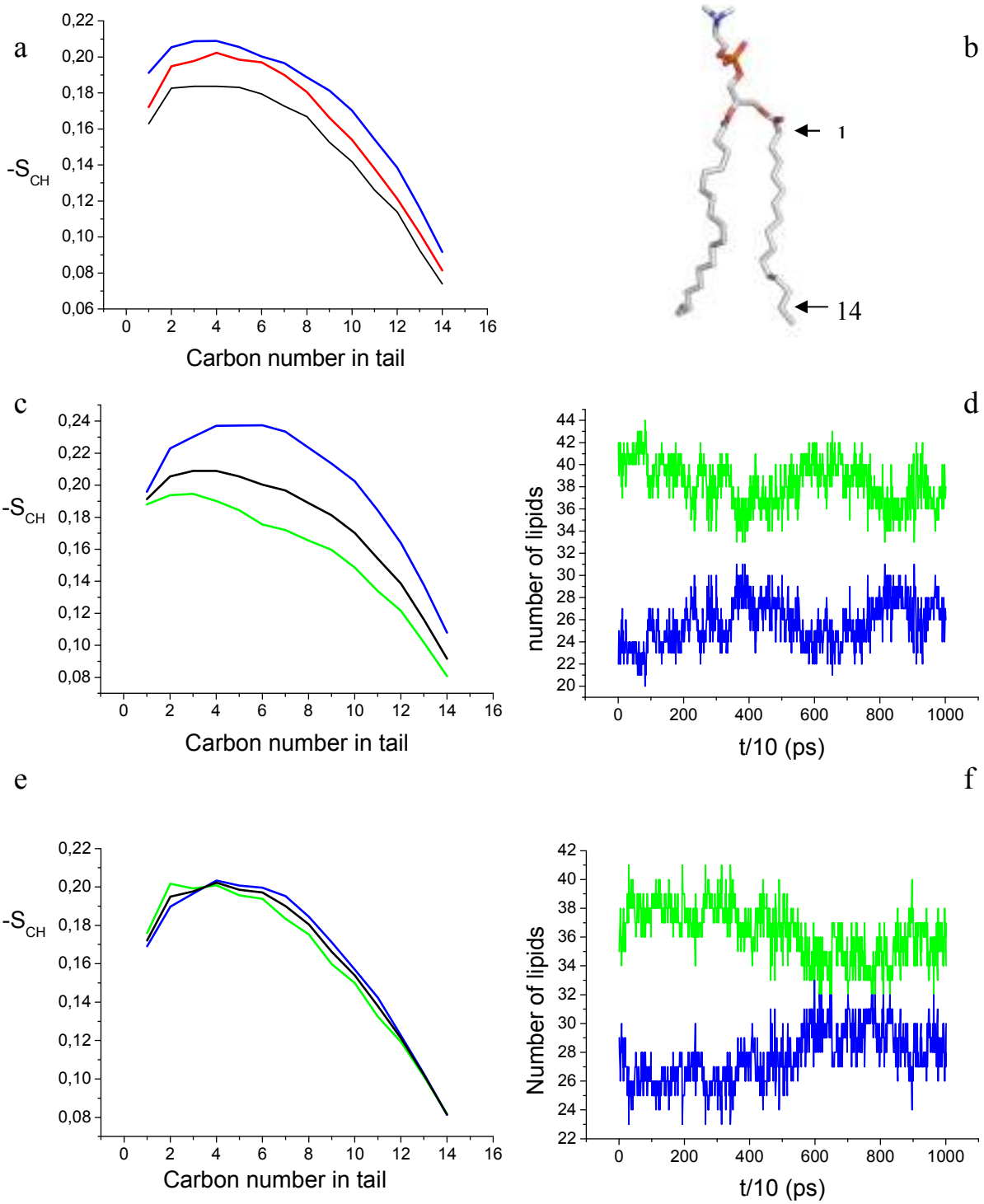

Figure 8.21 a) Order parameters of palmitoyl chain for leaflet containing *H* structure (red) and leaflet containing *B* structure (blue) averaged over last 10 ns MD simulations. Black line refer to pure POPC, averaged over 10 ns MD simulation of pure bilayer. b) POPC molecule. The arrows show carbon 1 and 14 of palmitoyl chain. c,e) order parameters of associating (green) and non associating (blue) lipids for

leaflet containing respectively (c) the *B* and (e) the *H* fragment. Black lines show order parameter of the relative leaflets. Number of associating (green) and non associating (blue) lipids for leaflet containing (d) *B* and (f) the *H* fragment.

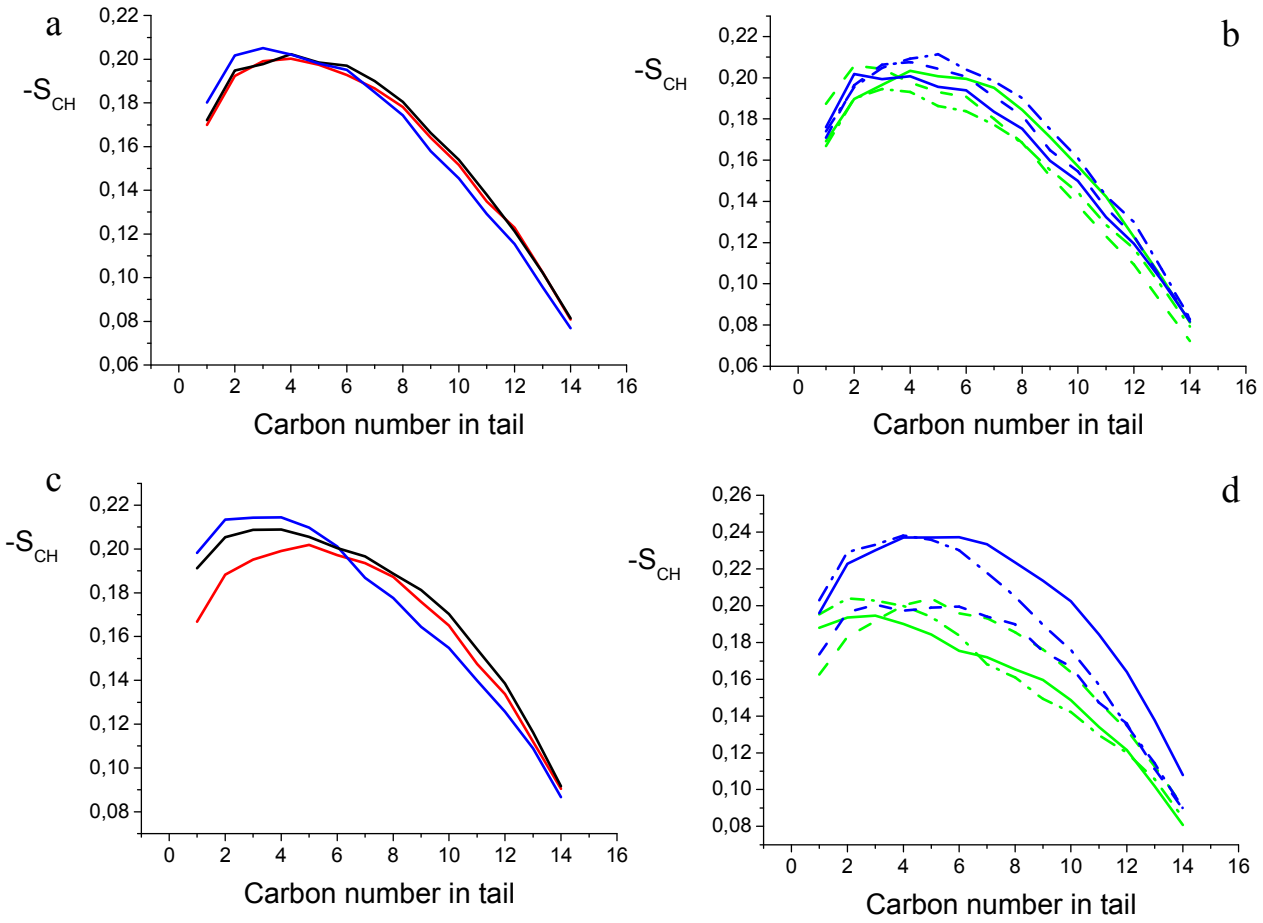

Figure 8.22 Order parameters calculated for palmitoyl chain averaging over 90-100ns (red), 100-110ns (blue), 110-120ns (black) for leaflets containing (a) the *H* peptide and (c) the *B* fragment. b, c) Order parameters of associating (green) and non associating (blue) averaged over 90-100ns (dash line), 100-110ns (dash-dot line), 110-120ns (solid line) for leaflets containing (b) the *H* and (d) the *B* fragment.

8.4 Conclusion

We have investigated the interaction between a-Synuclein ad a lipid bilayer, focussing on the G31-V52 region whose structure remains unknown and has been widely discussed. A 120 ns MD simulation with explicit water and POPC bilayer has been carried out, starting from selected configurations of the fragment, placed in water, in proximity of the lipid headgroups. Of course, given the reduced dimension of the fragment and the still limited trajectory length, this model study is far from an exhaustive description of the mechanism of *aS* folding in membrane environment. However, suitable choices of the fragment and initial conditions allow us to highlight some specific issues: new insights into the interaction between *aS* and phospholipid bilayers are reached; moreover, some general hints on the behaviour of peripheral proteins can be derived.

First of all, we have seen that the fragment penetrates into the bilayer and, due to its amphipathic character, remains at the bilayer-water interface. As already inferred from experiments and simulations [Kandasamy, 2004], a major role in the insertion process is played by lysines, through their interactions with the lipid headgroups. Indeed, under many respects the *aS* fragment behaves as on amphipathic peptides; there are, however some peculiar features.

Interestingly, we have found that a starting helical conformation breaks roughly in the middle, forming a loop which connects between two antiparallel more structured moieties. This behaviour seems to be specific of the amino acid sequence of the fragment: in analogous simulations on amphipathic peptides with the same bilayer, the helix was found to be either disrupted or retained, with no more than some gentle bending, when entering the bilayer [Kandasamy, 2004; 2006].

Of course, due to the short length of the investigated fragment, caution must be used in comparing the structure obtained from the simulation with experimental data on *aS*. Nevertheless, some similarity of the structure obtained at the end of our simulation to the average conformation derived from NMR experiments on micelle-bound *aS* [Ulmer, 2005] can be recognised. Considering the fragment with starting helical structure, we can see that the C-terminal part of the fragment, K43-V52, retains helical character, whereas on the opposite end helix fraying is observed. This can be compared with the results of NMR experiments, indicating the tendency to helical structuring of the 38-46 region and lower order parameters for the 30-37 residues [Ulmer, 2005].

The results of the simulation allow us to address a central issue on the structure of *aS* bound to lipid bilayers, suggesting that the helix breaking in the 38-48 region derives from an intrinsic propensity of the bound protein, rather than being a mere result of the constraints imposed by the small dimension of the micelle. The presence of the break gives the protein some more flexibility which allows it to adjust to the binding surface [Rhoades, 2006], while retaining the two amphipathic helices, which are essential for the binding process.

For the reasons explained in the Introduction, our simulations have been performed for the *aS* fragment in the presence of a flat POPC bilayer, whereas *aS* has been reported to preferentially bind to small acidic vesicles [Davidson, 1998]. So, the role of charge and curvature of the bilayer has been been proposed. We tried a simulation with POPS, using a preliminary version of the force field [Monticelli, 2007], but without success. The starting helical structure of the fragment remained practically undisturbed on top of the bilayer even after 30 ns, anchored to the interface by lysines. Penetration was prevented by the unrealistic compactness of the bilayer, which made the plane of phosphates like an impenetrable barrier. Comparison of the behaviour of the fragment in the presence of the two lipids suggests that membrane insertion can only take place if the bilayer is sufficiently floppy ; this might be the reason for the preference of *aS*, as of other peripheral proteins, for high curvature vesicles, bilayers, or defect rich monolayers. We also suggest that a negatively charged surface could be important for attracting the positively charged *aS*, but might not play a significant role in the insertion process, once *aS* lies in its proximity.

The importance of hydrogen bonds, already singled out in previous atomistic simulations of membrane-protein systems [Kandasamy, 2004], clearly emerges from this study. In addition to the network of intramolecular connections, which mainly involves backbone atom and has a major responsibility for the protein structure, H-bonds provide protein-lipid interactions which play a fundamental role for the insertion of the protein and its location in the interface region. The latter generally involve side chains and mostly, but not exclusively, lysines. As a consequence of this ensemble of inter- ad intramolecular constraints, the protein holds its conformation and location without significant changes, once embedded in the bilayer, even in the absence of secondary structure. On the contrary, the bilayer exhibits high deformability and capability of readjusting to accommodate the guest. This collective a reorganisation takes rather long times, as evidenced by the slow convergence of the order parameters for the lipid tails. In the equilibrated system the latter do not exhibit large deviations from the profile obtained for the pure lipid. This is in agreement with the findings of EPR experiments on spin-labeled lipids in model bilayers in the presence of bound *aS* [Ramakrishnan, 2003].

To further characterise the embedded fragment, we have examined the mobility of the side chains; this property, in addition to their H-bond capability, polarity and polarizability, is likely to play a role for the stabilisation of proteins and peptides at the membrane interface, but is often disregarded in this respect. Moreover, the mobility of side chains is of interest in relation to the observables of NMR, EPR and other spectroscopic techniques. We have not found differences ascribable to the chain exposure to lipids or water; on the contrary, the chain dynamics seems to be strongly conditioned by the local interactions and constraints, mostly deriving from backbone and neighbouring chains.

Recently, MD simulations of *aS* in implicit solvent have been reported [Mihajlovic, 2007]. The speeding up resulting from the reduced number of degrees of freedom made it possible to investigate a substantial portion of the protein, comprising the 1-95 residues, under different

conditions. A strict comparison with our short fragment does not make sense; however it might be worth highlighting some general differences. In ref. [Mihajlovic, 2007], membrane bound *aS* was found to adopt a helical structure, which slightly bends around residue 47 in the case of a neutral bilayer. This was interpreted as the manifestation of a general bending tendency of long helixes, independent of their primary sequence. This is in clear contrast to the result we have obtained for a short protein portion. Moreover, from the implicit environment simulation, the helix was predicted to lay on top of the bilayer, a few Ångstroms above the plane of phosphates. On the contrary, the axis of the short helix , resulting from the *H* configuration in our simulation, resides a few Ångstroms below the phosphate plane (this can be seen for instance in fig. 8.10), which is in good agreement with the immersion depth of the *aS*, as measured by ESR. Indeed, our simulations pose the question of the suitability of an implicit representation of the bilayer environment. The simple model of a dielectric slab cannot account for the heterogeneity and the anisotropy of the bilayer. The latter becomes important if the elastic response of the membrane playes a role in its interaction with the protein. The former seems to be particularly critical in the case of peripheral proteins, whose structure, location and dynamics is so strictly related to the features of the water-bilayer interface.

8.5 References

Abeliovich A., Schmitz Y., Farinas I., Choi-Lundberg D., Ho W.H., Castillo P.E. Shinsky N., Verdugo J.M., Armanini M., Ryan A. **25**, 239 (2000).

Berger O., Edholm O., Jahnig F. *Biophys. J.* **72** 2002 (1997).

Bisaglia M., Tessari I., Pinato L., Bellanda M., Girando. S., Fasano M., Bergantino E., Bubacco L., Mammi S. *Biochemistry* **44**, 329 (2005).

Borbat P., Ramlall T.F., Freed J.H., Eliezer D. *J. Am. Chem. Soc.* **128**, 10004 (2006).

Bussell R., Ramlall T.F., Eliezer D. *Prot. Sci.* **14**, 862 (2005).

Chandra S., Chen X., Rizo J., Jahn R., Sudhof T.C. *J. Biol. Chem.* **278** , 15313 (2003).

Davidson W.S., Jonas A., Clayton D.F., George J.M. *J. Biol. Chem.* **273**, 9443 (1998).

George J.M., Jin H., Woods W.S. Clayton D.F. *Neuron* **15**, 361 (1995).

Im W., Feig M., Brooks C.L. *Biophys. J.* **85**, 2900 (2003).

Jao C.C., Der-Sarkissian A., Chen J., Langen R. *PNAS* **101**, 8331 (2004).

Kabsch W., Sander C. *Biopolymers* **22** 2577 (1983)

Kandasamy S.K., Larson R.G., *C.P.L* **132**, 113 (2004).

Kandasamy S.K., Larson R.G., *Biochim. Biophys. Acta* **1758**, 1274 (2006).

Kandt C., Ash W.L., Tieleman D.P. *Struc. Biol. Membr. Prot.* **41**, 475 (2007).

Lague P., Roux B., Pastor R.W. *J.M.B.* **354**, 1129 (2005).

Lindahl E., Hess B., van der Spoel D., *J. Mol. Model.* **7**, 306 (2001).

Lipari G., Szabo A. *J. Am. Chem. Soc.* **104** 4546 (1982).

Lu J.X., Damodaran J.B., Lorigan G.A. *Biochemistry* **44** 10208 (2005).

Madine J., Doig A.J., Middleton D.A. *Biochemistry* **45**, 5783 (2006).

Maroteaux L., Campanelli J.T., Scheller R.H. *J. Neurosci.* **8** 2804 (1988).

Mihajlovic M., Lazaridis T. *Proteins* **21558**, 1 (2007).

Molden: http://www.cmbi.ru.nl/molden/molden.html

Monticelli L., personanl communication (2007).

Mukhopadhyay P., Monticelli L., Tieleman P.D., *Biophys. J.* **86**, 1601 (2004).

Patra M., Karttunen M., Hyvonen M.T., Falck E., Lindqvist P., Vattulainen I. *Biophys. J.* **84**, 3636 (2003).

PyMOL: http://pymol.sourceforge.net/

Ramakrishnan M., Jensen P.H., Marsh D. *Biochemistry* **42**, 12919 (2003).

Rhoades E., Ramlall T.F., Webb W.W., Eliezer D. *Biophys. J.* **90**, 4692 (2006).

Seelig A., Seelig J. *Biochemistry* **16**, 45 (1977)

Shepherd C.M., Vogel H.J., Tieleman D.P. *Biochem. J.* **370**, 233 (2003).

Spillantini M.G., Schmidt M.L., Lee V.M.Y., Trojanowski J.Q., Jakes R., Goedert M. *Nature* **388**, 839 (1997).

Ueda K., Fukushima H., Masliah E., Xia Y., Iwai A., Yoshimoto M., Otero D.A.C., Kondo J., Ihara Y., Saitoh T. *P.N.A.S.* **90**, 11282 (1993).

Ulmer T.S., Bax A., Cole N.B., Nussbaum R.L. *J. Biol. Chem.* **280**, 9595 (2005).
Zakharov S.D., Hulleman J.D., Dutseva E.A., Antonenko Y.N., Rochet J.C., Cramer W.A. *Biochemistry* **46**, 14369 (2007)**.**
Zhao W., Rog T., Gurtovenko A.A., Vattulainen I., Karttunen M. *Biophys. J.* **92**, 1114 (2007).
Zhu M., Li J., Fink A.L. *J. Biol. Chem.* **278**, 40186 (2003).

Chapter 9

ESR study of α-Synuclein in membrano-mimetic environment

9.1 Introduction

Recently, a systematic SDSL-ESR study of monomeric *aS* in small unilamellar vesicle (SUV) environment was reported [Jao, 2004]. A set of singly labelled mutants of the protein, with the spin probe in the region between amino acid 9 and 90, were synthesised. Information on the secondary structure of the protein and on its orientation in the bilayer was obtained from the analysis of the accessibility of the spin probe to paramagnetic colliders, in the region between amino acid 59 and 89. This region was found to have a helical secondary structure with 11/3 periodicity, and to lie at the water-lipid interface, with the centre of the helix at an immersion depth of ≈ 1-4 Å. Ignoring some peculiarities in the spectral lineshapes of mutants in the region between amino acids 35 and 43, the authors proposed the structure of an interrupted helix for the whole 1-90 segment of *aS* bound to SUV.

SDSL-ESR experiments on a series of *aS* double mutants bound to SDS and LPPG [1] micelles have been reported [Borbat, 2006]. They essentially confirm the structural information obtained by NMR for SDS-bound *aS* [Ulmer, 2005], with the presence of two antiparallel helices connected by a linker.

With the purpose of shedding light on this subject, we have performed an ESR study on selected mutants of *aS*, i.e. the single mutants E35R1[2], Y39R1 and K43R1 and the double mutants E35R1-Y39R1, E35R1-K43R1, Y39R1-K43R1, in the presence of SUV of POPS [3] and mixed POPS-POPC [4]. These mutants were chosen for the crucial location of the spin label in the region between the well established helices of *aS*: in particular, the i+4 and i+8 sites were selected in view of the typical helix periodicity. For the sake of comparison, the same experiments on *aS* bound to SDS micelles have been carried out.[5]

In the next section the methods will be reported; then, the spectra of double and single mutants will be presented and discussed. Conclusions of this analysis and future outlooks will be summarised in the final section.

[1] Lyso-1-PalmitoylPhosphotidylGlycerol.
[2] Code used for mutants: E35R1 refers to the mutant obtained by replacement of the E amino acid (single letter code) at site 35 with the spin label R1.
[3] 1-Palmitoyl-2-Oleoyl-*sn*-Glycero-3-[Phospho-L-Serine].
[4] 1-Palmitoyl-2-Oleoyl-*sn*-Glycero-3-[Phosphocholine].
[5] This work has been carried out in collaboration with L. Bubacco, I. Tessari (preparation of *aS* mutants), A.L. Maniero, M. Bortolus (ESR experiments) and S. Mammi (NMR study of *aS*).

9.2 Methods

Sample Preparation Site–directed mutagenesis was used to obtain *aS* mutants, which were expressed and purified according to previously published protocols [Huang, 2005] MTSSL labeling was performed as described in literature [Jao, 2004]; the quantitative reaction of the protein was verified RP HPLC and mass spectrometry. The small unilamellar vesicles (SUV) used in this study were prepared from POPC and POPS. The lipids were purchased from Avanti Polar Lipids and used as is, without any further purification. The lipids in the desired ratio were dissolved in chloroform and a homogeneous lipid film was obtained by drying the solution in a rotavapor; the film was left overnight under vacuum in a desiccator to remove any trace of solvent. The following day the film was resuspended in the same buffer used for the protein (10 mM HEPES [6], 100 mM NaCl, pH 7.4) to obtain a lipid concentration of 38-45 mM. The preparation then followed two different routes. SUV in the 70 nm diameter range were prepared by extrusion: the lipid suspension was passed through a large pore filter (500 nm) and extruded through a small pore filter (70 nm); this process was repeated several times. SUV in the 30 nm range were prepared by sonication: the lipid suspension was immersed in a water bath and sonicated until the solution started to become clear. Vesicle dimension were checked during preparation by Dynamic Light Scattering using a NICOMP Model 370 Submicron Particle Sizer by Pacific Scientific. Vesicles were used fresh after preparation or up to five days after the preparation, stored above the gel transition temperature. The protein solution and the SUV were mixed and buffer was added as needed to obtain the desired protein:lipid molar ratios of 1:500 or 1:1450. Samples in micellar solution of SDS were prepared by diluting a stock solution of SDS to the desired protein:detergent molar ratio (1:150 or 1:500).

ESR experiments For all measurements a volume of 50 μl of sample in micellar or vesicle solution was placed in 2x1 mm quartz tubes. ESR spectra were obtained in a Bruker ER 200D equipped with a rectangular cavity ST9112 and the relative cryostat, and a variable-temperature controller Bruker ER 4111 VT. Spectra were obtained using the following parameters: 20 mW power, 1.55 G modulation amplitude, 40 ms time constant, 80 ms conversion time, 180 G scan width, and 1024 points. Measurement on vesicles solutions were done at 290 K for vesicles in the liquid crystalline phase and at 240 K, in frozen solution, for vesicles in the gel phase; micellar solutions were measured at 290 K and 220 K respectively. SUV samples were frozen without any cryoprotection, whereas 30% glycerol by volume was added to SDS and solution samples prior to freezing. ESR spectra at X-band were taken in a standard rectangular ESR cavity at 240 K. The distance analysis of the spectra has been performed by the convolution method (see Appendix), assuming a Gaussian distribution [Rabenstein, 1995]

[6] 4-(2-hydroxyethyl)-1-piperazine-ethanesulfonic acid.

Generation of rotamers of MTSSL and calculation of inter-spin distances for double mutants Rotamers of MTSSL[7] (fig. 9.1) in a given protein structure are generated assuming the geometry defined as in chapter 6, on the basis of the torsional profiles calculated *ab-initio* for the chain bonds. Considering the minima of single bond torsional potentials, a total number of 108 rotamers can be estimated; however, this number is strongly reduced when the effect of the protein environment is taken into account, in terms of excluded volume between spin label and backbone or side-chains of neighbouring residues.

Inter-spin distances in double mutants of *aS* have been calculated for selected structures of the backbone, by considering all the sterically allowed rotamers of MTSSL. Spin-spin distances in double mutants have to be intended as those between the Nitrogen atoms of the pyrroline rings, as shown in fig. 9.2.

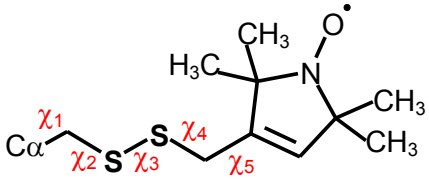

Figure 9.1 Structure of MTSSL with the five dihedral angles χ_i which define rotamers.

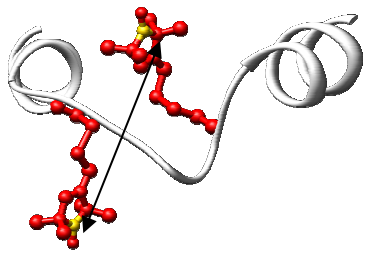

Figure 9.2 Pair of MTSSL rotamers in the E35R1-K43R1 double mutant, inserted into to the 1XQ8.pdb structure [Ulmer, 2005]. Red is used for the spin labels, while the Nitrogen atoms of the pyrroline rings, that are considered for the distance calculation, are shown in yellow. Here the pair of rotamers which put Nitrogens farther away from each other (distance equal to 1.43 nm) are shown.

[7] 1-oxyl-2,2,5,5-tetramethylpyrrolinyl-3-(methyl)-methanethiosulfonate spin label.

9.3 Results and discussion

Double mutants To rationalise the experimental data, the interspin distance distributions were also obtained by modeling, taking into account the chain flexibility of MTSSL, for selected conformations of *aS*: all possible rotamers of the spin labels were generated, with the geometry determined in chapter 6 ; only those rotamers were retained, which are sterically allowed by the structure of the backbone and of the nearby side-chains. For the sake of comparison, ESR lineshapes of double mutants were then calculated, using the computed distance distributions.

The experimental spectra of the double mutants in SUV and SDS look similar (Figure 1a/b); then, also the distance distributions are almost identical (Figure 1c), with only slightly wider distributions for micelle-bound *aS*. This is in clear disagreement with the hypothesis of two different structures of the studied region of *aS* in SDS and SUV. Our spectra appear different from those reported in the literature for MTSSL linked to i-i+4 and i-i+8 sites of long α-helices [Rabenstein, 1995; Altenbach, 2001], and our analysis leads to much wider distance distributions. Indeed, the main feature of all our experimental distributions appears their broadness, clearly evident if compared with the distance distributions modeled either for the α-helix or the 1XQ8 structure (Figure 1c, histograms). Therefore, also the ESR lineshapes calculated using such distributions do not reproduce our experimental spectra. As far as SDS is concerned, the unsatisfactory comparison between experimental results and calculations based on the single 1XQ8 structure can be explained by the conformational disorder in the 30-56 region found by NMR studies of *aS* in this environment [Ulmer, 2005; Bisaglia, 2005]. Also the wider distance distributions determined for E35C-Y39C and E35C-K43C, in comparison to Y39C-K43C, is in accord with the NMR results for SDS-bound *aS*, which indicated for the 30-37 region a greater flexibility than for the 38-46 region [Ulmer, 2005]. The similarity of the results we have obtained in the two environments suggests that a distribution of backbone conformations for the linker region, particularly in the 30-37 zone, can be extended to SUV-bound *aS*. Some flexibility of the linker region, which allows it to fit to the environment while maintaining two antiparallel helices, is also consistent with possible changes in its local conformation as a function of the binding surface, which was hypothesized from pulsed ESR experiments in SDS and LPPG micelles [Borbat, 2006].

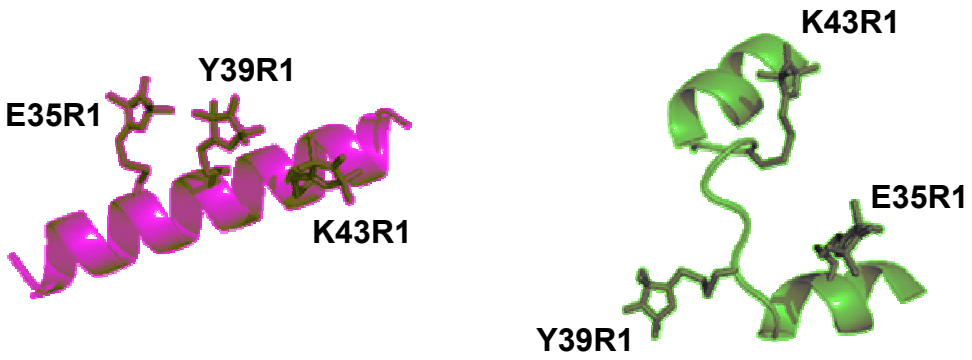

Figure 9.3 The spin labels considered in this study, in two different structures of *aS*: α-helix (pink) and 1XQ8.pdb (green).

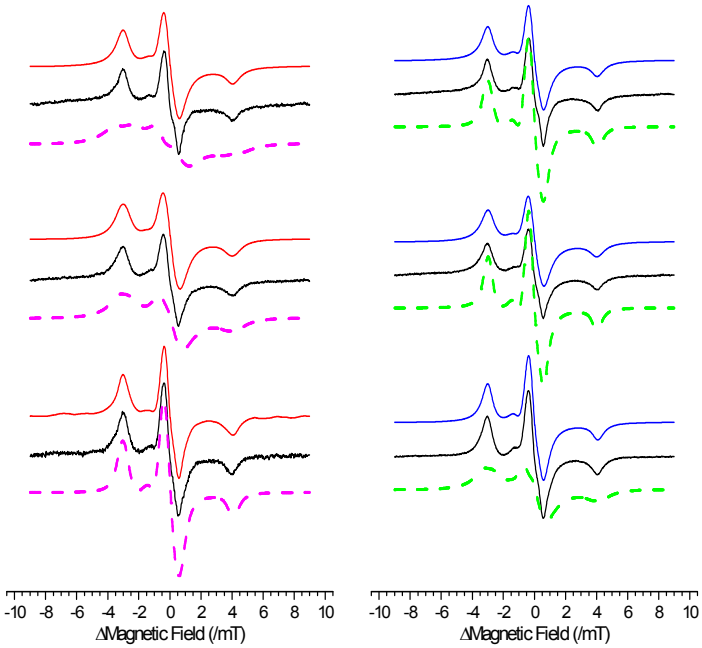

Figure 9.4 (a) The ESR spectra of the double mutants of *aS* bound to SUV (black), the spectral simulation obtained by convolution method (red) and the spectra calculated using the distance distribution for an α-helix (pink). (b) The spectra of the double mutants bound to SDS (black), the spectral simulation by the convolution method (blue) and the spectra calculated using the distance distribution for the 1XQ8.pdb structure (green).

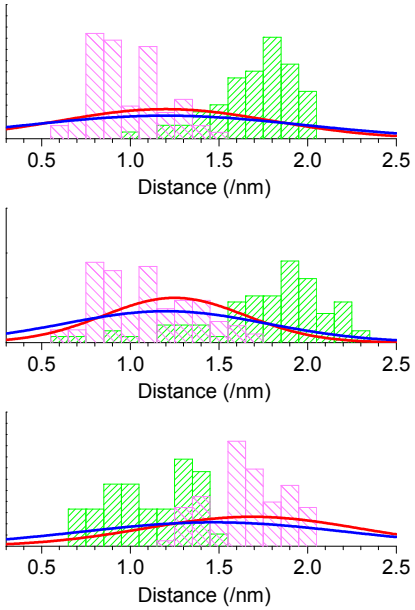

Figure 9.5 Gaussian distribution of spin-spin distances in double mutants, as obtained from fitting of the spectra in SUV (red) and in SDS (blue), and distance distribution calculated from the rotamers of MTSL in the helical structure (pink) and in the 1XQ8.pdb structure (green).

Single mutants The spectra of the E35R1, Y39R1, K43R1 mutants of *aS*, obtained in the presence of SUV (100% POPS - diameter equal to 70 nm) at T=290 K, are displayed in fig. 6. The spectra have complex shapes, deriving from the superposition of various components. A first, sharp contribution comes from unbound protein, which is present in solution as random coil [Davidson, 1998; Jao, 2004]. A further, even sharper component is due to traces of free radicals that detach from the protein as a consequence of breaking of the disulphide bond. We have focused on a third, broader component, which comes from *aS* mutants bound to SUV.

The spectral analysis is based on the model reported in chapters 6 and 7. Spectral lineshapes for bound *aS* were simulated according the Stochastic Liouville Equation approach [Freed, 1976], with the reorientational motion of the spin probe described in terms of conformational dynamics of the spin label, superimposed to overall rotational diffusion. This should account for rotation of the whole protein and backbone fluctuations. In chapter 7 it was shown that the X-band cw-ESR spectrum of MTSSL in a protein can be considered as the sum of contributions, each deriving from a set of rotamers which can interconvert with each other through χ_4 and χ_5 rotations. Interconversion between rotamers belonging to different sets, if any, is so slow on the ESR timescale that its effect on the lineshape can be neglected. The rotamer population, and then the contribution of each independent set to the lineshape, depends on the local environment of the spin label, therefore it is largely determined by the backbone arrangement and the nature

of the neighbouring residues. The rotamer sets can be collected into two groups: (i) rather constrained structures which, in addition to small amplitude oscillations in the minima of the torsional potential for the χ_1-χ_4 dihedrals, can only undergo more or less wide χ_5 rotations (henceforth denoted as **S**); (i) more mobile rotamers, which can also interconvert through jumps between the minima of the χ_4 torsional potential (henceforth called **F**). All the sets within a given group give similar contributions to the lineshape; for this reason, we have simulated the broad component of the spectra of SUV-bound α-synuclein as the sum of two components, deriving one from **S,** the other from **F** rotamers. The weight of each component has been taken as a free parameter, to be determined by comparison with the experimental data. Additional parameters entering the calculations are the root-mean-square fluctuations of the χ_1-χ_4 dihedrals around the minima of the torsional potential and the diffusion tensor of the overall rotation. The former have been given the values 8.0°, 12.0°,8.0°, 12.0°, respectively, which can be estimated at T=290 K on the basis of the curvature of the torsional potentials (see chapter 6). The choice of the rotational diffusion tensor will be discussed below. The **g** and **A** magnetic tensors used in the simulations were obtained from frozen spectra; their values are reported Table 9.I. An intrinsic linewidth of 1.5 G was assumed .

The **S** contribution is discernible in all the spectra reported in fig. 9.6, and is particularly evident in the case of E35R1 and Y39R1. Its width is considerably high, not far from what would be obtained for a powder spectrum, and this indicates a very low mobility of the spin label in the **S** rotamers of MTSSL for the three mutants of bound *aS*. This is only compatible with very restricted χ_5 motion and the absence of significant effect of overall dynamics. The **S** contribution to the spectra has been reproduced assuming for χ_5 only restricted oscillation around the minima, of root-mean-square amplitude $\overline{(\delta\chi_5)^2}^{1/2} = 12.5°$ for E35R1 and Y39R1 and $\overline{(\delta\chi_5)^2}^{1/2} = 25.0°$ for K43R1. This means that jumps between the two minima ($-77° \leftrightarrow +77°$) of the χ_5 torsional potential, which in principle should be possible for MTSSL and in fact were found in the model system previously considered (see fig.3 in chapter 6 and Results-Section B in chapter 7), are hindered for the **S** rotamers of the mutants under investigation. Negligible overall rotational diffusion was assumed, with a diffusion coefficient equal to 10^5 s^{-1}; this value, to be compared with the estimate (~10^4 s^{-1}) from the Stokes-Einstein equation for a spherical vesicle of diameter of 50 nm in water at T=290 K, indicates that the region of *aS* under investigation is strongly bound to the vesicle, and backbone fluctuations or other dynamic modes of the protein are absent or extremely slow.

The faster **F** component, which is also present in the spectra of all the three mutants, was simulated assuming again a diffusion coefficient equal to 10^5 s^{-1} for overall rotation, in addition to χ_4 jumps and wide χ_5 oscillations in the range 0° to ±130°. The **S** and **F** components contribute differently to the spectra of the three mutants, i.e. 50: 50 for E35R1 and Y39R1, and 30:70 for K43R1.

Mutant	g_{xx}	g_{yy}	g_{zz}	A_{xx} (Gauss)	A_{yy} (Gauss)	A_{zz} (Gauss)
E35R1	2.008	2.0067	2.0026	6.58	5.02	35.86
Y39R1	2.0085	2.0067	2.003	6.9	5.3	34.9
K43R1	2.0083	2.0067	2.0027	6.64	5.12	35.4

Table 9.I Principal components of the **g** and **A** magnetic tensors determined for the three single mutants of *aS*.

Figure 9.6 Spectra of the single mutants of *aS* in the presence of SUV (100% POPS - diameter of 70 nm) at T=290K (black). Each spectrum is the sum of contributions from free spin label, *aS* in solution and bound *aS*. The red line shows the simulation of the bound component.

To rationalise the results of the lineshape simulations, we have examined the possible rotamers of MTSSL at sites 35, 39 and 43. The spin label was introduced in *aS*, assuming different protein structures: (a) that derived from NMR (PDB id:1XQ8); (b) an α-helix; (c) the structure of the H fragment at the end of the MD simulation described in the previous chapter. For an α-helix, a similar distribution of rotamers was obtained for the three sites, analogous to that reported in chapter 6 and scarcely dependent on the nature of the neighbouring side chains. But effects of the environment were found for the (a) and (c) structures. In E35R1 the spin label is strongly confined: the number of allowed rotamers is reduced, together with the possibility of interconversion between them. In Y39R1 and K43R1, the spin label is located in a different and more free environment (see fig. 9.3), and a higher number of interconverting rotamers is predicted. The results of lineshape simulation are not compatible with *aS* being structured as a continuous helix. For E35R1, they would be consistent with a bent structure of *aS*, but this could not explain the results obtained for K43R1, neither those for Y39R1. There is still the possibility that the reduced mobility of the **S** conformers inferred from the ESR spectra of these mutants might be caused by the bilayer, which is not taken into account in our rotamer analysis. We suggest that hydrogen bonds between the nitroxide oxygen and amine hydrogen in the lipid headgroups could be responsible. Electrostatic interactions were found between the nitroxide oxygen and the choline methyl groups in MD simulations of spin labeled lipids [Stimson, 2007]. The analysis of the MD trajectories for the G31-V52 fragment of *aS*, reported in the previous chapter, has shown that hydrogen bonds strongly reduce the mobility of the side chains.

In the light of the results of our detailed analysis, we can now look at the series of spectra for single mutants of *aS* bound to POPS:POPC SUVs (3:7), that were reported in ref. [Jao, 2004] without any attempt of interpretation. In all of the spectra we can distinguish a similar **F**-like component; for some mutants, mostly located in sites which, according to the accessibility measures reported in the article, should be water exposed, this is accompanied by an **S**-like contribution. The latter has essentially the same features, though quite different intensity, in the various cases. The series of spectra is consistent with our interpretation of the lineshape features in terms of independent contributions from sets of conformers interconverting through χ_4- χ_5 rotations and from more constrained conformers. These would give a weak contribution, mainly depending on the nature of the neighbouring side-chains, for the sites embedded in the lipid tail region of the bilayer. The stronger contribution, generally recognisable in the case of water exposed sites, and characterised be highly restricted dynamics, could be explained by the presence of hydrogen bonds involving the nitroxide spin label. Within this framework we can also provide an explanation for the high contribution of the low mobility component in the spectra of mutants with the spin label in the 35-43 region. Namely, some peculiarity in this region was noticed also by the authors of ref. [Jao, 2004], who invoked the occurrence of

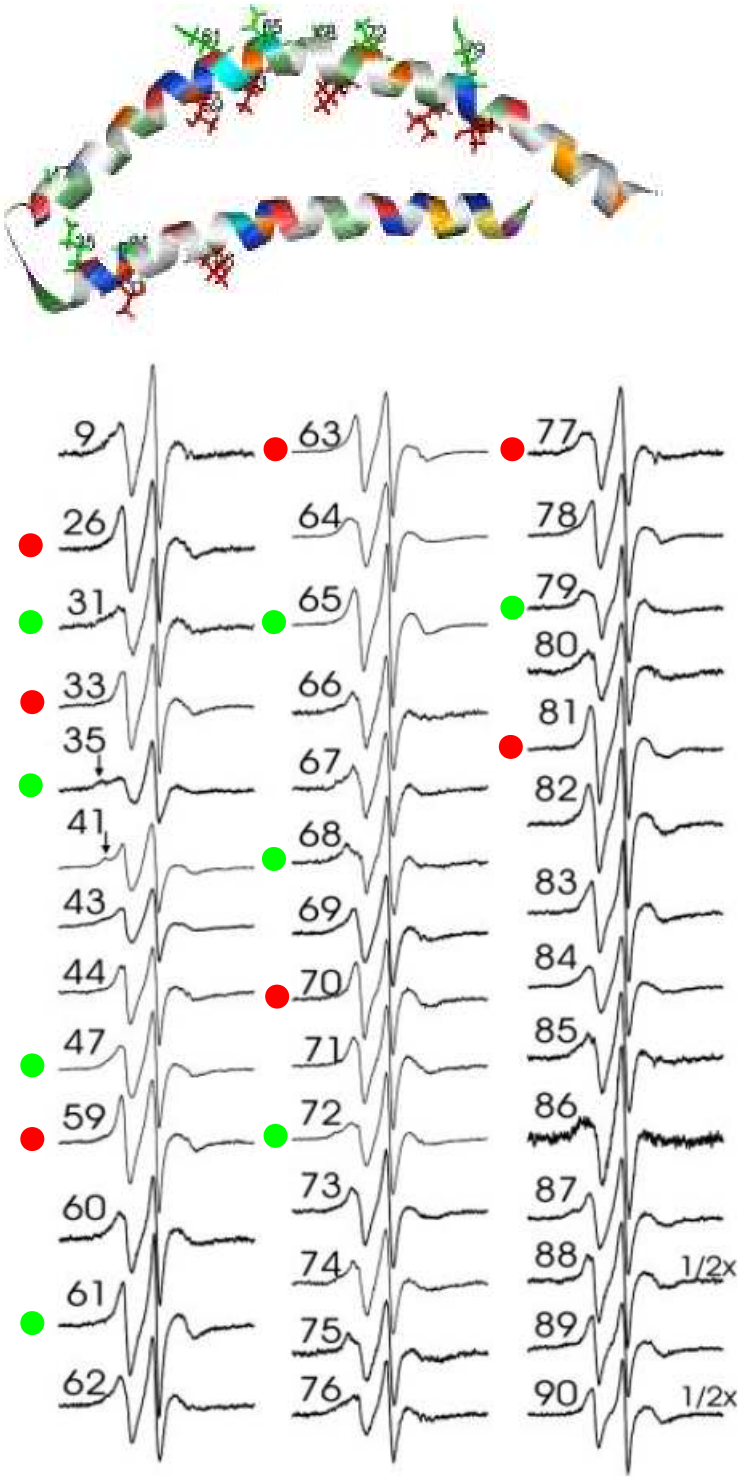

Figure 9.7 Cw-ESR spectra of single mutants of *aS* bound to POPS:POPC (3:7) SUVs [Jao, 2004]. Red and green spots indicate sites which, according to according to accessibility measures, should be embedded in the lipid tail region of the bilayer and exposed to water, respectively. The location of these sites in the NMR structure of *aS* (1XQ8.pdb) is shown on top.

occasional collisions between proteins as a questionable explanation. Furthermore, the special behaviour of the 35-43 region would be hardly understandable, especially within the model of a continuous helix proposed by the authors. We suggest that the peculiarity in the spectra reported for the 35-43 region, which is confirmed by our experiments on this zone, reflects the presence of helix breaking. The unstructured linker region would reside in the interface zone of the bilayer (see the snapshots from the MD trajectories shown in fig. 8.10), making possible the onset of hydrogen bonds between the attached spin label and lipid headgroups.

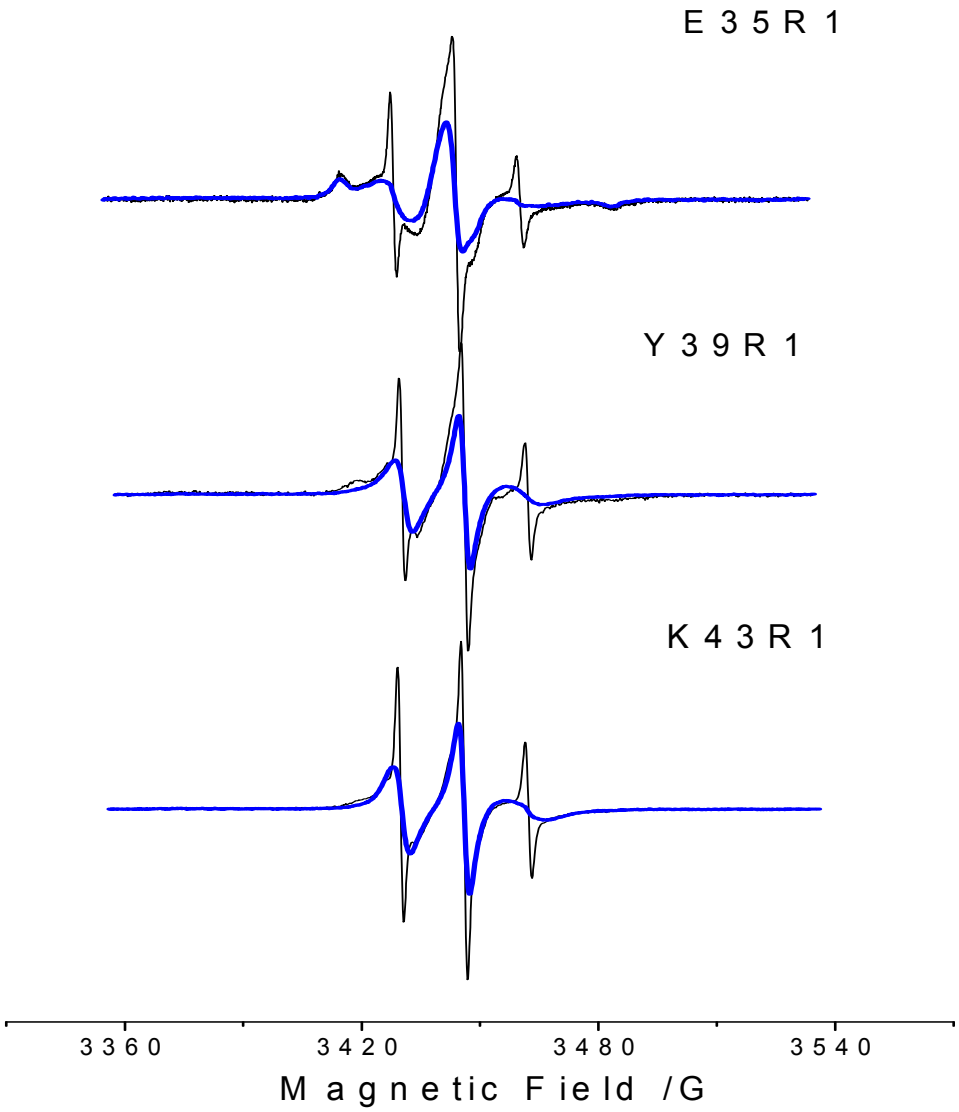

Figure 9.8 Spectra of α-synuclein bound to SDS micelles (blue line), superimposed to the spectra recorded in the presence of POPS SUV (black line). The spectra have been arbitrarily scaled for the sake of comparison.

In Fig. 7 the ESR spectra of the E35R1, Y39R1, K43R1 mutants of *aS*, recorded in the presence of pure POPS SUVs and SDS micelles are compared. The spectra of E35R1 are very similar in the two environments; on the contrary, the spectra of SDS-bound Y39R1 and K43R1 do not show the more constrained component observed in SUV environment. Although further investigation, with new experiments, is required to confirm our view, a possible explanation can be attempted, on the basis of the considerations presented above. The rotamer analysis showed that, as a consequence of its location, MTSSL linked to site 35 is highly confined in bent conformations of α-synuclein, as is the structure reported for the protein bound to SDS micelles [Ulmer,2005]. Therefore, the presence of an intense component with very low mobility in the ESR spectra can be expected, independently of the nature of the amphiphilic environment. On the contrary, for Y39R1 and K43R1 the low mobility spectral component would originate from rotamers of the spin label involved in hydrogen bonds with the lipid headgroups, which are sensitive to the environment, and might be absent when the protein is bound to SDS micelles.

9.4 Conclusions

The analysis of cw-ESR lineshapes, based on a model which takes explicitly into account the conformational dynamics of the spin label, accompanied by modeling of the rotamer distribution and supported by Molecular Dynamics simulations, has allowed us to get an insight intocontroversial aspects of the structure and dynamics of α-synuclein bound to lipid bilayers.

The main result of our investigation, obtained from the study of double mutants and confirmed by the investigation of singly labeled *aS*, is that SUV-bound *aS* bears most of the features reported for it in micellar environment [Chandra, 2003; Bisaglia 2005; Ulmer 2005]: in particular an unbroken helical structure of the region between the N- and C-termini can be ruled out. Helix breaking does not appear to be a mere consequence of the constraints imposed by the small micellar dimensions [Jao, 2004], but as an intrinsic feature of *aS*, when bound to amphiphilic interfaces. Furthermore, we can confirm the picture of the inter-helix region as characterized by conformational disorder, rather than exhibiting a single structure. This disorder might play a role in *aS* binding to synaptic vesicles, by allowing the protein to fit into amphiphilic aggregates with different degrees of lipid packing strain [Zakharov, 2007].

We have shown that detailed information can be obtained from the accurate analysis of the spectral lineshape for single labeled mutants, which can lead to a consistent description of the interactions and dynamics of the protein in the amphiphilic environment. Particularly informative is the low mobility component, which can be found in the spectra of some of the mutants, and is ascribed to the presence of highly constrained rotamers of the spin label. From lineshape simulation we infer that *aS* is strongly anchored to the surface of vesicles and micelles and the effect of backbone fluctuation is negligible on the ESR timescale; the lineshape essentially reflects the internal dynamics of the spin label and the constraints experienced by

this. On the basis of the present investigation and the Molecular Dynamics simulation reported in the previous chapter, we suggest that the low mobility spectral component might be the signature of hydrogen bonds between the nitroxide oxygens and the amine groups of lipids, which could be correlated to the insertion depth of the spin labels in proteins and peptides lying at the lipid-water interface. Further experiments are presently under way to confirm the interpretation proposed here.

Appendix

Distance Analysis The spin-spin distance distributions were obtained from the frozen solution spectra following a procedure analogous to the one presented in [Rabenstein, 1995]. The experimental spectrum of the double mutant (*D(B)*) was fitted as the convolution (⊗) of the sum of the spectra of the single mutants (*S(B)*) with a dipolar broadening function (*Broad(r,B)*) that depends on the interspin distance *r*:

$$D(B) = S(B) \otimes Broad(r, B) \tag{A.1}$$

where *B* is the magnetic field, and *Broad(r,B)* is the Pake doublet function.

The flexibility of the protein and of the nitroxide side chain imply that a weighted sum of interspin distances (r_i) rather than a single distance should be used: $D(B) = S(B) \otimes \left\{ \sum_{i=3\,\text{Å}}^{50\,\text{Å}} P(r_i) Broad(r_i, B) \right\}$ (A.2)

where $P(r_i)$ represents the weight for each interspin distance, and the distance lower limit of 3 Å represents van der Waals contact between the spin labels. Therefore, the broadening function is treated as the weighted sum of Pake doublet functions. In the literature the choice for the weight function $P(r_i)$ ranges from an arbitrary distribution [Altenbach, 2001] to a complex model for the tether [Hustedt, 2006]. We chose, when fitting the spectra, to use a single Gaussian function, centered at a distance r_0 and with a width σ:

$$D(B) = \int_{-\infty}^{\infty} dB' S(B') \sum_{i=3\,\text{Å}}^{50\,\text{Å}} Gauss_{r_0,\sigma}(r_i) Pake(r_i, B - B') \tag{A.3}$$

Therefore, the fitting parameters are the center (r_0) and width (σ) of the Gaussian function; when the Gaussian is plotted as a function of the interspin distance (r_i) the interspin distance distribution is obtained. The choice of a Gaussian function was made for its simplicity, and was justified by the featurelessness of the spectra that implied a broad distribution of interspin distances. In the paper we report the use of interspin distributions calculated from the allowed rotamers of the spin label.

To obtain the spectra on the basis of the interspin distributions derived from modeling, eq. (A.2) was used, with the calculated weights $P(r_i)$.

9.5 References

Altenbach C., Oh K.-J., Trabanino R.J., Hideg K., Hubbell, W.L. *Biochemistry* **40**, 15471 (2001).

Bisaglia M., Tessari I., Pinato L., Bellanda M., Giraudo S., Fasano M., Bergantino E., Bubacco L., Mammi S. *Biochemistry* **44**, 329 (2005).

Borbat P., Ramlall T.F., Freed J.H., Eliezer D. *J. Am. Chem. Soc.* **128**, 10004 (2006).

Chandra S., Chen X., Rizo J., Jahn R., Sudhof T.C. *J. Biol. Chem.* **278** , 15313 (2003).

Davidson W.S., Jonas A., Clayton D.F., George J.M. *J. Biol. Chem.* **273**, 9443 (1998).

Freed J.H. in *'Spin Labeling: Theoy and Application.'* (Berliner, L.J., ed., Academic Press, New York, 1976)

Huang C., Ren G., Zhou H., Wang C.C. *Protein Expr. Purif.* 42, 173 (2005).

Hustedt E.J., Stein R.A., Sethaphong L., Brandon S., Zhou Z., DeSensi S.C. *Biophys. J.* **90**, 340 (2006).

Jao C.C., Der-Sarkissian A., Chen J., Langen R. *PNAS* **101**, 8331 (2004).

Rabenstein M.D., Shin Y.-K. *PNAS* **92,** 8239 (1995).

Stimson L., Dong L., Karttunen M., Wisniewska A., Dutka M., Rog T. *J. Phys. Chem B* **111**, 12447, (2007).

Ulmer T.S., Bax A., Cole N.B., Nussbaum R.L. *J. Biol. Chem.* **280**, 9595 (2005).

Zakharov S.D., Hulleman J.D., Dutseva E.A., Antonenko Y.N., Rochet J.C., Cramer W.A. *Biochemistry* **46**, 14369 (2007)**.**

Chapter 10

Summary

10.1 Summary

The present thesis deals with the development and implementation of models for problems in soft condensed matter, at the interface between biology and material science. In particular, two projects have been carried out. The first focuses on the molecular origin of chirality in liquid crystalline solutions of semiflexible polyelectrolytes like DNA, columnar aggregates of deoxyguanosine tetramers (G-wires) and filamentous becteriophages. The second project deals with the integration between theoretical and experimental methods for the study of membrane-proteins systems, starting from the analysis of ESR spectra of spin labelled proteins. Both projects have been carried out in collaboration with experimental groups.

In **Chapter 1** the phenomenon of chiral amplification is introduced and the main properties of liquid crystals are summarised. In particular, the case of charged polymers is described with two examples: DNA and *fd*-M13 viruses. Both exhibit a particular kind of chiral amplification, with chirality transferred from molecules to liquid crystal phases. The theoretical investigation of the correlation between molecular and phase chirality in these systems and in general in solutions of semiflexible charged polymers has been one of the subjects of this PhD thesis. One major difficulty in these problems comes from the smallness of the chiral contribution to intermolecular interactions and its strong and subtle dependence on structural details. A further complication in the case of polyelectrolyte solutions derives from the intrinsic multicomponent nature of the systems, which are characterized by a variety of interactions covering a wide range of length-scales.

In **Chapter 2** the theoretical method and the numerical procedure are presented which, starting from the structure of polyelectrolytes, leads to the prediction of the cholesteric pitch. Molecular expressions for the free energy of the system are obtained on the basis of steric and electrostatic interactions between polymers; the former are described in terms of excluded volume, while the Poisson-Boltzmann theory is used for the latter, within a mean field approximation. This model has been applied to the study of the cholesteric phase formed by solutions of short B-DNA fragments (130 base pairs). The main results of this work can be summarized as follows. (1) The connection between phase chirality on one side, and structure of polyelectrolytes and pair interactions in solutions is established, on a clear theoretical framework. (2) A model based on steric and electrostatic interactions between polyelectrolytes correctly predicts the organization of the cholesteric phase of B-DNA solutions. It provides an explanation for the observed left-handed helicity of the phase and for the temperature dependence of the cholesteric pitch. The shape chirality of B-DNA molecule plays a crucial role in our description. Not only it is at the origin of the steric contribution to the cholesteric phase, but it is also responsible for the emergence of the electrostatic contribution. Calculations show that in the case of B-DNA steric and electrostatic interactions have a counteracting effect, which can be simply explained in the following way: steric interactions would lead to the formation of a right-handed cholesteric phase, because packing is optimised when double

helices fit into each other grooves. However, such configurations are also characterized by strong repulsions between the charges of polyelectrolytes. Since for B-DNA solutions the latter effect prevails, a left-handed cholesteric phase results.

Chapter 3 reports on the application of the model developed in Chapter 2 to the chiral nematic phases formed by suspensions of a rodlike virus (M13) . The complexity of this system derives from the simultaneous presence of different sources of chirality at a molecular level, ranging from the subnanometer to the micrometer length-scale, that could be responsible for the phase chirality. In this work we propose the helical arrangement of coat proteins on the virus surface as an explation.. Again, as for the case of B-DNA, the phase organization is explained as the results of the competition between contributions of opposite handedness, deriving from best packing of viral partices and electrostatic interparticle repulsions. This model, as for the case of B-DNA, requires a coarse-grained representation of the virus, simplest enough to hallow numerical caculations, but able to reproduce the relevant molecular features that originate phase chirality.

The model presented in chapters 2 and 3 neglects the effects of molecular flexibility. If this can be an acceptable approximation for 130 base-pair B-DNA fragments, viruses on the contrary are better described as semiflexible polymers. Molecular flexibility has also been invoked as the molecular origin of chirality in liquid crystal phases of M13 and *fd* viruses. In **chapter 4**, we presented the theoretical method we developed to investigate the role of shape fluctuations in formation of cholesteric phases is solution of semiflexible polymers. The model associates a Monte Carlo method sampling of configurations of the polymer, described as a worm-like polymer, to a mean field model for its orientational distribution in the chiral nematic phase. The crucial point of the model is the description of molecular flexibility. In our model, we used an expression for the beding free energy that depends on four parameters: the isotropic bending constant κ_{iso}, the anisotropic bending constant κ_{aniso}, the local stability parameter m and the bending periodicity j. The first parameter, κ_{iso}, describes the isotropic contribution of bending energy, and is the only term of the classic WLC model. The second parameter, κ_{aniso}, quantifies anisotropic bending effects due to anisotropic molecular shape. The third parameter, m, describes the number of local preferred directions of bending, while the fourth, j, describes the pattern of local preferred directions of bending proceeding along polymer axis. Even if our results strongly depend on our choices for these values, we can make some general considerations. As already pointed out in chapters 2 and 3, twist elastic constant K_{22} is rather insensitive to molecular details, and for the model that considers molecules as rigid can be calculated using a very simple molecular representation of fused spheres. Also in this work, where we consider molecular flexibility explicitly, we saw that the twist elastic constant is rather independent on molecular details. On the contrary, the chiral strength K_t (and then wave number q) is strongly dependent on molecular details and on our choices for bending

parameters. In a statistical sample, virus conformers that could give a chiral phase are present. The range of possible q values for the wave number of the phase can be very large, and grows increasing virus flexibility. However, the global effect can be strongly washed out by the simultaneous presence of conformers with opposite twisting power (that will give opposite values of wave numbers q). In the case of absence of chiral anisotropic terms into molecular bending energy ($\kappa_{aniso} = 0$), we obtained a racemic statistical sample of virus conformers, and a final value of wave number $q = 0\,\mu m^{-1}$. Introduction of chiral anisotropic terms into bending breaks down this symmetry, and, for suitable values of bending parameters, the displacement between virus conformers with opposite twisting power can stabilize the existence of a cholesteric phase with a wave number q comparable with that obtained for *fd* and M13.

In **Chapter 6** the dynamics of the tether linking methanethiosulfonate (MTSSL) spin probes to α-helices is investigated, with the purpose of rationalizing its effects on ESR line shapes. Torsional profiles for the chain bonds have been calculated ab initio, and steric interactions with the α-helix and the neighboring residues have been introduced at an excluded volume level. As a consequence of the restrictions deriving from chain geometry and local constraints, a limited number of allowed conformers has been identified that undergo torsional oscillations and conformational jumps. Torsional fluctuations are described as damped oscillations, while transition rates between conformers are calculated according to Langer multidimensional extension of the Kramers theory. The time scale and amplitude of the different motions are compared; the major role played by rotations of the outermost bonds of the side chain emerges, along with the effects of substituents in the pyrroline ring on the conformer distribution and dynamics. The extent and symmetry of magnetic tensor averaging produced by the side chain motions are estimated and the implications on the ESR spectra of spin-labeled proteins are discussed.

In **Chapter 7** the results of the conformational analysis presented in chapter 6 are exploited to introduce a realistic description of the structure and dynamics of the spin probe in the simulation of their X-band ESR spectra, within the framework of the Stochastic Liouville equation (SLE) methodology. Slow reorientations of the whole protein are superimposed to fast chain motions, which have been identified with conformational jumps and fluctuations in the minima of the chain torsional potential. Fast chain motions are introduced in the SLE for the protein reorientations through partially averaged magnetic tensors and relaxation times calculated according to the motional narrowing theory. The 72R1 and 72R2 mutants of T4 lysozyme, which bear the spin label at a solvent-exposed helix site, have been taken as test systems. For the side chain of the R2 spin label, only a few noninterconverting conformers are possible, whose mobility is limited to torsional fluctuations, yielding almost identical spectra, typical of slightly mobile nitroxides. In the case of R1, more complex spectra result from the simultaneous presence of constrained and mobile chain conformers, with relative weights that can depend on the local environment. The model provides an explanation for the experimentally

observed dependence of the spectral line shapes on temperature, solvent and pattern of substituents in the pyrroline ring. This relatively simple methodology allows the introduction of realistic features of the spin probe dynamics into the simulation of ESR spectra of spin-labeled proteins.

The model presented in chapters 6 and 7 can be applied to the interpretation of SDSL-ESR experiments of membrane bound proteins containing an aminoacidic spin probe. As already pointed out in chapter 5, SDSL is a powerful technique to access informations about membrane protein structure, where other techniques like NMR and X-ray diffraction fail. In **chapters 8** and **9** we reported a joint experimental and theoretical approach to the study of membrane binding of an important peripheral protein: α-synuclein (*aS*). *aS* is a 140 amino acids protein, which function is related to synaptic vesicle regulation. The damage of this protein is hypothesized to play a role in diseases such as Parkinson's disease and Alzheimer's disease. The structure of the protein upon membrane binding is yet unclear. Two hypotheses exist: NMR experiments on SDS micelles bound *aS* show the existence of two helical regions linked by a loop in the region between amino acid 38 and 44, while SDSL-ESR experiments on small unilamellar vesicles (SUV) bound *aS* hypothesize the existence of a continuous helix. With the purpose of shedding light on this subject, we performed a 120 ns Molecular Dynamics (MD) simulation of the controversial region between amino acids G31 and V52 with explicit water and POPC bilayer, starting from selected configurations of the fragment. Contemporaneously, we have performed an ESR study of *aS* mutants with spin label in the controversial region, i.e. E35R1, Y39R1 and K43R1, and double mutants E35R1-Y39R1, E35R1-K43R1, Y39R1-K43R1, bound to SUV of POPS, mixed POPS-POPC and SDS micelles.

We performed MD simulations of two fragments of α-synuclein with different geometry: the bent structure taken from the average NMR conformation in SDS micelles and ideal α-helix. The main results can be summarized as follow. The two fragments penetrate into bilayer and, due to their amphipathic character, remain at the bilayer water interface. A crucial role in the insertion mechanism is played by positively charged lysine residues. From our simulations, we saw that a negatively charged membrane surface is not necessary for peptide insertion but could be relevant in the process of attracting the positively charged *aS* near membrane surface. The starting helical conformation breaks roughly in the middle, forming a loop region between two antiparallel structured moieties. This behaviour seems to be specific of the amino acid sequence of the fragment rather then a consequence of constraints imposed by the membrano-mimetic system. The importance of hydrogen bonds clearly appears from this study not only in determining peptide structure. Hydrogen bonds provide protein-lipid interactions which play a fundamental role for the insertion of the peptide and its location in the interface region. As a consequence of this intramolecular and intermolecular constraints, peptides hold their conformation and location without significant changes once embedded into the bilayer. On the contrary, the bilayer exhibits high deformability and capability of readjusting to accommodate to the guest. This collective reorganization takes rather long times. At the equilibrium, however,

order of aliphatic tails does not differ significantly from that of pure bilayer. Comparing our results with those present in literature about MD simulations of *aS* in implicit solvent and implicit bilayer, we pointed out the relevance of using an all-atom model for the bilayer to obtain reliable results, especially in the case of peripheral proteins, whose structure, location and dynamics is strictly related to the features of water-bilayer interface.

The hypothesis of a loop region in *aS*, between residues 35 and 45 is confirmed also by ESR spectra analysis. The analysis of double mutants spectra show that SUV-bound *aS* bears most of the features reported for this system in micellar environment. Furthermore, the analysis confirms the idea of a loop region characterized by conformational disorder. Detailed information can be obtained from single labelled mutant spectra analysis. From lineshape simulation, we infer that *aS* is strongly anchored to the surface of vesicles and micelles and backbone fluctuation is negligible on ESR timescale.

10.2 Sommario

Il progetto sviluppato in questa tesi riguarda lo sviluppo e l'implementazione di modelli teorici per problemi di "soft matter" che si collocano all'interfaccia tra la biologia e la scienza dei materiali.. In particolare, sono stati sviluppati due progetti. Il primo riguarda lo studio dell'amplificazione della chiralità in soluzioni liquido-cristalline di polielettroliti semiflessibili come DNA, aggregati colonnari di guanosine (G-wires) e virus filamentosi. Il secondo progetto riguarda invece lo sviluppo di una metodologia per lo studio di sistemi membrana-proteina, partendo dall'analisi degli spettri ESR di proteine contenenti sonde paramagnetiche.

Nel **Capitolo 1** viene presentato il fenomeno dell'amplificazione della chiralità. In chimica supramolecolare l'amplificazione della chiralità è definita come la trasmissione della chiralità a diverse scale di lunghezza. Nel capitolo vengono presentati due esempi: l'amplificazione della chiralità nel DNA e nei virus *fd* e M13. In questi sistemi la chiralità è trasmessa da un livello atomico (sulla scala degli Ångstrom) all'organizzazione supramolecolare, su scala nanometrica, fino anche ad una scala micrometrica. Sia il DNA che i virus presentano una particolare forma di amplificazione della chiralità; la chiralità cioè viene trasferita dalle molecole alle fasi liquido-cristalline che essi formano. Questi sistemi, ad opportune concentrazioni, danno origine alle fasi liquido-cristalline nematiche chirali (colesteriche). Lo studio teorico della correlazione tra chiralità a livello molecolare e la chiralità della fase in soluzioni liquido-cristalline di polielettroliti è uno dei soggetti sviluppati in questa tesi di dottorato. La complessità di studiare queste fasi deriva dal fatto che il contributo chirale alle interazioni intermolecolari (responsabile della formazione di queste fasi), può cambiare drammaticamente per piccole variazioni strutturali, e il poter fare predizioni necessita di una modellizzazione accurata del sistema. Le soluzioni di polielettroliti sono sistemi intrinsecamente complicati da studiare, a causa del fatto che sono sistemi multicomponente caratterizzati da una varietà di interazioni intermolecolari che coprono un ampio intervallo di scale di lunghezza.

Nel **Capitolo 2** è presentato il modello teorico e la procedura numerica che abbiamo sviluppato il quale, partendo dalla struttura del polielettrolita, porta alla predizione del passo della fase colesterica. Le espressioni per l'energia libera in funzione di grandezze molecolari sono state ricavate sulla base delle interazioni tra i polielettroliti. Le interazioni considerate sono interazioni steriche, descritte in termini di volume escluso, ed elettrostatiche, modellizzate attraverso un'approssimazione di campo medio. Questo modello è stato applicato allo studio delle fasi colesteriche in soluzioni di molecole di B-DNA di 130 coppie di basi. Il modello fornisce un'interpretazione del comportamento di queste fasi, e mostra il diverso ruolo giocato dalla forma e dalla distribuzione di carica della molecola. I risultati più importanti che emergono da questo studio vengono qui riassunti. Un modello che si basa su interazioni steriche ed elettrostatiche tra polielettroliti è in grado di giustificare l'organizzazione chirale delle soluzioni liquido-cristalline di B-DNA. Esso fornisce una spiegazione del verso sinistrorso dell'elicità della fase ed è in grado di spiegare la dipendenza dalla temperatura del passo della fase colesterica. La chiralità della forma delle molecole di B-DNA gioca un ruolo cruciale. Essa

non è solo all'origine del contributo di tipo sterico alla chiralità della fase, ma è anche responsabile dell'emergere del contributo elettrostatico. I calcoli effettuati hanno mostrato che, nel caso del B-DNA, le interazioni steriche ed elettrostatiche hanno un effetto opposto sul termine chirale, che può essere spiegato nel modo seguente: le interazioni steriche darebbero origine ad una fase destrorsa, come conseguenza di un migliore impiccamento delle eliche molecolari in soluzione. Però queste sono le configurazioni per cui sono massimizzate le repulsioni elettrostatiche tra le molecole. Poiché nel caso del B-DNA l'effetto delle interazioni elettrostatiche prevale, si ha la formazione di una fase colesterica sinistrorsa.

Nel **Capitolo 3** è riportato lo studio da noi effettuato sulle fasi nematiche chirali di sospensioni del virus M13. La complessità di questo sistema è dovuta alla presenza simultanea di diverse 'fonti' di chiralità a livello molecolare, che vanno da una scala subnanometrica fino ad una scala micrometrica, che potrebbero essere responsabili della chirallità della fase. In questo lavoro viene proposta una spiegazione per l'origine microscopica dell'organizzazione chirale della fase; quest'ultima sarebbe dovuta all'organizzazione chirale delle proteine che formano il capside del virus. Questa disposizione origina sulla superficie del virus dei solchi di forma elicoidale e di verso destrorso nelle cui vicinanze sono concentrate le cariche negative presenti sul capside. Ancora, come nel caso del B-DNA, l'organizzazione chirale della fase è interpretata in base alla competizione tra contributi di segno opposto derivanti dalle interazioni steriche ed elettrostatiche. Anche in questo caso le interazioni elettrostatiche prevalgono e danno origine ad una fase chirale sinistrorsa. Come per il B-DNA, è necessaria una rappresentazione di tipo corse-grained del virus, abbastanza semplice da permettere calcoli numerici, ma in grado di riprodurre i dettagli molecolari più rilevanti.

Il modello presentato nel capitolo 2 ed applicato allo studio delle fasi colesteriche di B-DNA e virus M13 di fatto trascura l'effetto della flessibilità molecolare. Questa approssimazione può essere giustificata nel caso di frammenti di B-DNA di 130 coppie di basi, ma può risultare troppo forte nel caso del virus M13. Nel **capitolo 4** è presentato il modello teorico che abbiamo sviluppato per indagare il ruolo della fluttuazioni di forma sulla chiralità della fase in soluzioni di polimeri semiflessibili. Il modello accoppia un campionamento Monte Carlo delle conformazioni del polimero, descritto utilizzando il modello 'worm-like' (WLC), ad un trattamento di campo medio per la sua distribuzione orientazionale nella fase colesterica. Un punto cruciale del modello risulta essere la descrizione della flessibilità molecolare. Nel nostro modello, l'energia che descrive il bending di un polimero è scritta in funzione di quattro parametri: la costante isotropa di bending κ_{iso}, la costante anisotropa di bending κ_{aniso}, il parametro di simmetria locale m e la periodicità del bending j. Il primo parametro, κ_{iso}, descrive il contributo isotropo all'energia di bending, e rappresenta l'unico termine nel modello WLC classico. Il secondo parametro, κ_{aniso}, quantifica il contributo anisotropo al bending dovuto all'anisotropia di forma eventualmente presente nel polimero. Il terzo parametro, m, descrive localmente il numero di direzioni preferenziali del bending, mentre il quarto, j, descrive la geometria secondo cui evolvono le direzioni preferenziali del bending procedendo lungo l'asse del polimero. Anche se i risultati ottenuti dipendono fortemente dalla scelta dei

valori per questi parametri, possiamo ugualmente fare delle considerazioni generali. Come già evidenziato nei capitoli 2 e 3, il valore della costante elastica di twist K_{22} è poco sensibile ai dettagli molecolari. Nel modello per sistemi rigidi, si è visto che buoni risultati si ottengono utilizzando un modello estremamente semplice in cui la molecola è rappresentata da una serie di sfere fuse. Anche in questo lavoro, in cui abbiamo considerato esplicitamente l'effetto della flessibilità molecolare, si è visto che la costante elastica risulta essere insensibile alle diverse scelte fatte per i parametri di flessibilità. Al contrario il termine K_t (e di conseguenza il numero d'onda della fase) è fortemente dipendente dai dettagli molecolari e dalle nostre scelte per i parametri di flessibilità. In un campione statistico di possibili conformazioni, emergono delle strutture che darebbero origine a fasi chirali. L'intervallo dei possibili valori di numero d'onda ottenibili può essere molto ampio, e cresce al crescere della flessibilità molecolare. Però l'effetto globale può essere notevolmente ridotto dalla presenza simultanea di strutture che darebbero fasi di segno opposto. Nel caso in cui non ci sia contributo anisotropo all'energia del bending, otteniamo una soluzione racema di conformazioni e il valore finale del numero d'onda risulta nullo. L'introduzione di un contributo anisotropo rompe questa simmetria, e per opportuni valori dei parametri di elasticità sviene stabilizzata una fase colesterica con un numero d'onda paragonabile a quello ottenuto per i virus *fd* e M13. Sfortunatamente, la mancanza di dati sperimentali dettagliati sulla flessibilità di singola molecola permettono solo un confronto qualitativo tra predizioni teoriche e dati sperimentali, per quanto riguarda le fasi colesteriche di questi virus.

Nel **Capitolo 6** abbiamo investigato la dinamica della catena che lega la sonda paramagnetica MTSSL ad un' α-elica con lo scopo di razionalizzare il suo effetto sulla forma di riga di uno spettro ESR. I profili di energia torsionale per i vari legami della catena sono stati calcolati ab-initio, e le interazioni steriche con il backbone dell'α-elica e le catene laterali dei residui vicini sono state introdotte al livello di volume escluso. Come conseguenza delle restrizioni derivanti dalla geometria della catena e dall'intorno, solo un numero limitato di conformeri è permesso. La dinamica di questi ultimi è descritta da oscillazioni torsionali e salti conformazionali. Le fluttuazioni torsionali sono descritte come oscillazioni smorzate, mentre le velocità di transizione tra conformeri sono descritte utilizzando la teoria di Kramer estesa al caso multidimensionale. Le scale dei tempi e l'ampiezza delle oscillazioni dei differenti moti sono state confrontate; da questa analisi emerge il ruolo principale giocato dalle rotazioni che coinvolgono i legami più esterni. Notevole effetto sia sui possibili conformeri sia sulla dinamica della catena è dovuto ai sostituenti presenti nell'anello pirrolinico. Questa analisi ha permesso di valutare l'effetto della dinamica della catena sulla modulazione dei tensori magnetici e quindi valutarne l'effetto sulla forma di riga degli spettri ESR.

Nel **Capitolo 7**, siamo andati a simulare gli spettri ESR delle sonde paramagnetiche sulla base della dinamica conformazionale presentata nel capitolo 6, facendo uso del formalismo dell'equazione Stocastica di Liouville (SLE). L'effetto dovuto alla lenta riorientazione della proteina è sommato all'effetto dovuto ai moti della catena, cioè salti conformazionali e oscillazioni attorno ai valori di minimo dei potenziali torsionali, che avvengono su una scala

dei tempi più veloce. I moti veloci della catena sono introdotti nell'equazione SLE che descrive l'effetto della riorientazione della proteina attraverso tensori parzialmente mediati e tempi di rilassamento calcolati. Come sistemi di prova sono stati presi i mutanti 72R1 e 72R2 della proteina T4 lisozima, in cui lo spin label si trova in un intorno di α-elica ed esposto al solvente. Nel caso dello spin label R2, sono possibili solo conformeri che non interconvertono, la cui mobilità è limitata a fluttuazioni torsionali. Questi conformeri danno origine a spettri praticamente identici, tipici delle sonde nitrossidiche poco mobili. Nel caso della sonda R1, gli spettri ESR risultano più complicati per la presenza simultanea di conformeri mobili e conformeri costretti, il cui peso statistico relativo dipende dall'intorno. Il modello è in grado di fornire una spiegazione della dipendenza della firma di riga dalla temperatura, tipo di solvente e tipi di sostituenti nell'anello pirrolinico. La metodologia sviluppata permette di introdurre in maniera realistica gli effetti della dinamica della sonda paramagnetica nella simulazione degli spettri ESR di proteine labellate.

Il modello presentato nei capitoli 6 e 7 può essere utilizzato per l'interpretazione di esperimenti di Site Directed Spin Labeling (SDSL) di proteine, contenenti una sonda paramagnetica, che interagiscono con membrane fosfolipidiche. Come già messo in luce nel capitolo 5, la tecnica SDSL-ESR è estremamente potente per ottenere informazioni sulla struttura e dinamica di proteine legate a membrane, informazioni che risultano difficili da ottenere con altre tecniche quali NMR e diffrazione ai raggi X. Nei **capitoli 8** e **9** abbiamo riportato uno studio sperimentale e teorico relativo al binding su membrane fosfolipidiche di una importante proteina periferica: l'α-sinucleina (*aS*). L'*aS* è una proteina di 140 aminoacidi la cui funzione è legata all'effetto regolatiorio che esercita sulle vescicole sinaptiche. E' stato ipotizzato che il danneggiamento di questa proteina giochi un ruolo importante in malattie quali il Parkinson a l'Azheimer. La struttura della proteina a s seguito del binding su membrana risulta ancora poco chiara. Sono state proposte due possibili strutture: esperimenti NMR condotti sulla proteina legata a micelle di SDS mostrano l'esistenza di due region strutturate in elica, legate da una regione di loop tra gli aminoacidi 38 e 44, mentre esperimenti SDSL-ESR sulla proteina legata a vescicole unilamellari (SUV) ipotizzano l'esistenza di un'elica continua. Con lo scopo di far luce su questa controversia, abbiamo condotto una Dinamica Molecolare (MD) su una traiettoria di 120 ns su un frammento della proteina G31-V52 contenente la presunta regione di loop in presenza di acqua di solvatazione e doppio strato lipidico di POPC descritti in maniera esplicita. Nella simulazione, abbiamo considerato due possibili configurazioni per il peptide. Contemporaneamente, abbiamo condotto uno studio ESR su mutanti dell' *aS* contenenti sonde paramagnetiche nella regione controversa; sono stati analizzati i singoli mutanti E35R1, Y39R1 e K43R1 e i doppi mutanti E35R1-Y39R1, E35R1-K43R1, Y39R1-K43R1, legati a vescicole di POPS, POPS/POPC e micelle di SDS.

Le simulazioni MD sono state condotte su due frammenti con geometria differente: l'uno presenta la struttura ripiegata (loop) proposta come media delle strutture ottenute da esperimenti NMR, l'altro è strutturato in α-elica. I risultati più importanti sono riportati di seguito. I due frammenti penetrano nel doppio strato e, grazie alla loro struttura antipatica, restano nella zona

di interfaccia tra acqua e doppio strato lipidico. Un ruolo cruciale nel processo di immersione è sicuramente quello dei residui lisina carichi positivamente. Le nostre simulazioni mostrano come una carica netta negativa sulla membrana non sia un requisito necessario per l'immersione, ma potrebbe essere rilevante per attirare verso il doppio strato la proteina in soluzione. Un altro dato rilevante che emerge dalle simulazioni è costituito dal fatto che il frammento in elica si rompe approssimativamente nel mezzo, dando origine a d una regione di loop tre due zone strutturate. Questo comportamento sembra essere una proprietà intrinseca del frammento più che un fenomeno dovuto all'interazione con il sistema membrano-mimetico. L'analisi evidenzia l'importanza dei legami ad idrogeno sia intramolecolari che con il doppio strato lipidico, e giocano un ruolo rilevante sia nel processo di inserimento sia nel determinare la profondità di immersione dei peptidi. Questi vincoli intra e intermolecolari stabilizzano la struttura peptidica che una volta terminato il processo di inserimento, praticamente non cambia. Al contrario, il doppio strato mostra una grande deformabilità e capacità di riarrangiarsi attorno ai due peptidi. Questa riorganizzazione avviene su scale dei tempi lunghe. All'equilibrio, comunque, le proprietà d'ordine del doppio strato con immersi i due peptidi non differiscono di molto da quelle del sistema puro. Confrontando i nostri risultati con quelli presenti in letteratura, ottenuti da simulazioni MD di *aS* con solvente e doppio strato lipidico trattati in maniera implicita, possiamo affermare, l'importanza di utilizzare una rappresentazione all-atom per il doppio strato lipidico per avere dei risultati credibili che riproducano i dati sperimentali, specialmente quando si studiano proteine periferiche, la cui struttura, immersione e dinamica sono fortemente legate alle caratteristiche della regione di interfaccia.

L'ipotesi di una regione non strutturata nell'*aS*, tra i residui 35 e 45 è avvalorata anche dall'analisi degli pettri ESR. L'analisi degli spettri dei doppi mutanti mostrano come l'*aS* legata alle SUV mantenga molte delle caratteristiche strutturali del sistema quando è legato a micelle. L'analisi inoltre conferma l'ipotesi dell'esistenza di una regione di loop caratterizzata da un disordine conformazionale. Altre informazioni dettagliate arrivano dall'analisi degli spettri dei singoli mutanti. Dalla simulazione delle forme di riga, possiamo dedurre come l'*aS* sia fortemente ancorata alla superficie delle vescicole e delle micelle, ed eventuali fluttuazioni del backbone sono trascurabili sulla scala dei tempi dell'ESR.

10.3 List of publications

- Tombolato F., Ferrarini A. *J. Chem. Phys.* **122** 054908 (2005).
- Tombolato F., Ferrarini A., Grelet E. *Phys. Rev. Lett.* **96** 258302 (2006).
- Tombolato F., Ferrarini A., Freed J.H. *J. Chem. Phys. B* **110** 26248 (2006).
- Tombolato F., Ferrarini A., Freed J.H. *J. Chem. Phys. B* **110** 26260 (2006).

Manuscripts in preparation

- Bortolus M., Tombolato F., Tessari I., Siragusa P., Bergantino E., Bubacco L., Ferrarini A., Mammi S., Maniero A.L. "*Broken helix in vesicle and micelle-bound α-Synuclein: insights from SDSL-EPR experiments and MD simulations.*"